

# **CFD AND NEURO-FUZZY MODELLING OF FUEL CELLS**

**Yasemin Vural**

Submitted in accordance with the requirements for the  
degree of Doctor of Philosophy

The University of Leeds  
Centre for Computational Fluid Dynamics

November, 2010

"The candidate confirms that the work submitted is his/her own and that appropriate credit has been given where reference has been made to the works of others."

"This copy has been supplied on the understanding that it is copyright material and that no quotation from the thesis may be published without proper acknowledgement."

"The right of Yasemin Vural to be identified as Author of this work has been asserted by her in accordance with the Copyright, Designs and Patents Act 1988."

©2010 The University of Leeds and Yasemin Vural

## **ACKNOWLEDGEMENTS**

In this part of my thesis, I would like to express my great gratitude to those that provide me with the constant motivation and support during my PhD studies.

First of all, I would like to express my deep appreciation for Prof. Mohamed Pourkashanian who gives me the opportunity and encourages me to work in an area that I absolutely love and his constant support in every part I need during the period of my studies. I would like to express my earnest gratitude to Prof. Derek Ingham, for his encouragement and fruitful discussions. His enthusiasm in research has always given me power throughout my studies. I would like to thank Dr. Lin Ma, for his support on the computational side of my research and for his friendship. I also thank all the members of the CFD group, Kevin Hughes and Duncan Borman for the helpful discussions. I am thankful to my colleagues for the pleasant atmosphere in the Centre for CFD and their friendship. I thank James McKay who deals with many challenging administrative issues and organizes perfect events for us.

For the generous bursary, I would like to acknowledge the European Union, European Research Commission, that is fully supporting the research work through the award of a Marie Curie EST Research Fellowship in the Centre for Computational Fluid Dynamics at the University of Leeds.

Finally, I would like to express my eternal gratitude to my parents, Muserref and Mecit Vural, and my brother Yalcin Vural for their everlasting love, support and encouragement.

## Abstract

This thesis presents some model developments for the simulation and optimization of the design of fuel cells, in particular for the Solid Oxide Fuel Cell (SOFC) and Proton Exchange Membrane Fuel Cell (PEMFC). However, the approaches and models presented can be basically applied to any type of fuel cell. In this study, the multicomponent diffusion processes in the porous medium of a SOFC anode has been investigated through comparison of the Stefan Maxwell Model, Dusty Gas Model and Binary Friction Model in terms of their prediction performance of the concentration polarization of a SOFC anode to mainly investigate the effect of the Knudsen diffusion on the predictions. The model equations are first solved in 1D using an in-house code developed in MATLAB. Then the diffusion models have been implemented into COMSOL to obtain 2D and 3D solutions. The model predictions have been evaluated for different parameters and operating conditions for an isothermal system and assuming that reaction kinetics are not rate limiting. The results show that the predictions of the models are similar and the differences in the predictions of the models reported previously are mainly due to the definition of the effective diffusion coefficient, i.e. the tortuosity parameter, and with a tortuosity parameter fitted for each model, the models that take into account the Knudsen diffusion and that do not predict similar concentration polarization. Moreover, in this research, the application of an Adaptive Neuro-Fuzzy Inference System (ANFIS) to predict the performance of an Intermediate Temperature Solid Oxide Fuel Cell and a Proton Exchange Membrane Fuel Cell (PEMFC) have been presented. The results show that a well trained and tested ANFIS model can be used as a viable tool to predict the performance of the fuel cell under different operational conditions to facilitate the understanding of the combined effect of various operational conditions on the performance of the fuel cell and this can assist in reducing the experimentation and associated costs.

# LIST OF PUBLICATIONS

## JOURNAL PUBLICATIONS

**Yasemin Vural**, Lin Ma, Derek B. Ingham, Mohamed Pourkashanian. Comparison of the Multi-component Mass Transfer Models for Prediction of the Concentration Overpotential for Solid Oxide Fuel Cell Anodes. *Journal of Power Sources*, 195 (2010), 4893-4904. (**Impact factor=3.792**).

**Yasemin Vural**, Mohamed Pourkashanian, Derek B. Ingham. Performance Prediction of the Proton Exchange Membrane Fuel Cell using the ANFIS model. *International Journal of Hydrogen Energy*, 34 (22), 2009, 9181-9187. (**Impact factor=3.945**).

**Yasemin Vural**, Diyar Akay, Mohamed Pourkashanian, Derek B. Ingham. Modeling of an Intermediate Temperature Solid Oxide Fuel Cell using the Adaptive Neuro-Fuzzy Inference Systems. *Journal of Fuel Cell Science and Technology*, doi:10.1115/1.3207873. (**Impact factor=1.167**).

**Yasemin Vural**, Mohamed Pourkashanian, Derek B. Ingham, Lin Ma. Three-dimensional CFD modeling of a Solid Oxide Fuel Cell with special emphasis on the multicomponent mass transfer in porous anode. In preparation, to be submitted to the *Journal of Power Sources* (**Impact factor=3.792**).

## CONFERENCE PROCEEDINGS

**Yasemin Vural**, Mohamed Pourkashanian, Derek B. Ingham, "Performance Prediction of the Proton Exchange Membrane Fuel Cell using the ANFIS model", In Proceedings of the International Conference on Automotive Technologies (ICAT'08), Istanbul, Turkey, 2008, 254-265.

**Yasemin Vural**, Lin Ma, Mohamed Pourkashanian, Derek B. Ingham, "On the Multicomponent Mass Transport in an Anode-supported Solid Oxide Fuel Cell", In Proceedings of the Third European Fuel Cell Technology and Applications Conference - Piero Lunghi Conference, Italy, 2009, 185-186.

# Contents

<b>Nomenclature</b>	<b>xxi</b>
<b>1 INTRODUCTION</b>	<b>1</b>
1.1 Fuel Cells . . . . .	2
1.1.1 SOFC . . . . .	2
1.1.2 PEMFC . . . . .	8
1.1.3 Electrochemistry . . . . .	10
1.2 Problem Definition and Objectives of the Study . . . . .	14
1.3 Thesis Structure . . . . .	17
<b>2 LITERATURE REVIEW</b>	<b>20</b>
2.1 CFD modelling of SOFC . . . . .	21
2.1.1 Diffusion Models in Fuel Cell Models . . . . .	25
2.2 Neuro-fuzzy modelling . . . . .	28
<b>3 CFD AND NEURO-FUZZY MODELLING CONCEPT</b>	<b>31</b>
3.1 CFD Modelling Concept . . . . .	32
3.1.1 Mathematical Model . . . . .	32

3.1.2	Numerical Model . . . . .	38
3.2	Neuro-Fuzzy Modelling Concept . . . . .	40
3.2.1	Artificial Neural Network (ANN) . . . . .	40
3.2.2	Fuzzy Logic . . . . .	43
3.2.3	Artificial Neuro-Fuzzy Inference System (ANFIS) . . . . .	46
3.2.4	Hybrid Learning . . . . .	49
3.2.5	Performance Criteria . . . . .	50
<b>4</b>	<b>MULTICOMPONENT MASS TRANSFER IN POROUS MEDIA</b>	<b>51</b>
4.1	Physical Definitions . . . . .	51
4.2	Mathematical Definitions . . . . .	54
4.2.1	Special cases . . . . .	56
4.2.2	Conversion from mole into mass fraction . . . . .	56
4.2.3	Conversion from mole fraction gradient into mass fraction gradient . . . . .	56
4.3	Mass Diffusion Model Approaches . . . . .	57
4.3.1	Fick Model (FM) . . . . .	57
4.3.2	Stefan Maxwell Model (SMM) . . . . .	60
4.3.3	Dusty Gas Model (DGM) . . . . .	61
4.3.4	Binary Friction Model (BFM) . . . . .	63
4.4	Summary . . . . .	65
<b>5</b>	<b>PERFORMANCE OF DIFFUSION MODELS - 1D RESULTS</b>	<b>69</b>
5.1	Definition of the system . . . . .	70

5.1.1	Simplifications of the experiments to the 1D, 2D and 3D models . . . . .	71
5.2	Methodology . . . . .	73
5.2.1	Conservation Equation . . . . .	73
5.2.2	Multicomponent Diffusion Models . . . . .	74
5.3	Results and Discussion . . . . .	84
5.3.1	Results at Uniform Pressure . . . . .	84
5.3.2	Effect of Pore Radius . . . . .	91
5.3.3	Results at a non-uniform pressure (Effect of the partial pressures in the DGM and the BFM) . . . . .	102
5.3.4	Further Remarks and Discussions on the tortuosity . . . . .	102
5.4	Conclusions . . . . .	106
<b>6</b>	<b>TWO AND THREE DIMENSIONAL RESULTS</b>	<b>109</b>
6.1	Implementation of the diffusion models into COMSOL . . . . .	110
6.1.1	DGM . . . . .	111
6.1.2	BFM . . . . .	113
6.2	Verification of the implementation of diffusion models into COMSOL	115
6.3	Simplification of the 2D model . . . . .	117
6.4	Two-Dimensional Model Domain and Boundary Conditions . . . . .	119
6.5	Three-Dimensional Model Domain and Boundary Conditions . . . . .	122
6.6	Pre-processing . . . . .	125
6.6.1	Grid Independency Analysis . . . . .	125

6.7	Two-Dimensional Results . . . . .	126
6.8	Three Dimensional Results . . . . .	128
6.9	Comparison of the 1D, 2D and 3D Results . . . . .	138
6.9.1	Evaluation of the Constant Current Density Assumption . . . . .	143
6.10	Further Discussion . . . . .	149
6.11	Conclusions . . . . .	159
<b>7</b>	<b>NEURO-FUZZY MODELLING RESULTS</b>	<b>162</b>
7.1	ANFIS Modelling of SOFC . . . . .	163
7.1.1	Experimental Data . . . . .	163
7.1.2	Preprocessing . . . . .	164
7.1.3	ANFIS modelling of SOFC . . . . .	170
7.1.4	Results and Discussion . . . . .	171
7.1.5	Extrapolation capability of the ANFIS model . . . . .	173
7.2	Performance Prediction of a PEMFC using the ANFIS model . . . . .	176
7.2.1	Experimental Data . . . . .	176
7.2.2	Preprocessing . . . . .	176
7.2.3	ANFIS modelling of the PEMFC . . . . .	177
7.2.4	Results and Discussion . . . . .	178
7.2.5	Performance of ANFIS at various operational conditions . . . . .	179
7.2.6	Further Remarks on the ANFIS Model . . . . .	184
7.2.7	Conclusions . . . . .	186
<b>8</b>	<b>GENERAL CONCLUSIONS AND FUTURE WORK</b>	<b>188</b>

8.1	General Conclusions . . . . .	188
8.2	Future Work . . . . .	192
<b>A</b>	<b>Source codes</b>	<b>210</b>
A.1	IMPLEMENTATION OF THE DGM AND BFM INTO COMSOL . . .	210
A.1.1	Implementation of the DGM into COMSOL . . . . .	210
A.1.2	Implementation of the BFM into COMSOL . . . . .	216

# List of Figures

1.1	Schematic of the basic operational principle of a SOFC [59]. . . .	5
1.2	Typical SEM image of a cross-sectional microstructure of the single cell [84]. . . . .	7
1.3	Schematic of the basic operational principle of a PEMFC [10]. . .	9
1.4	Typical current-voltage distribution curve for many hydrogen fuel cells [79]. . . . .	13
3.1	Typical structure of a neural network. . . . .	41
3.2	Triangular membership function . . . . .	44
3.3	Block diagram of a fuzzy inference system. . . . .	45
3.4	A typical ANFIS Architecture. . . . .	47
5.1	Schematic diagram of the one cell stack and the single-unit cell model for the anode-supported SOFC [130]. . . . .	70
5.2	Schematic diagram of the 3D SOFC geometry used in the experiment of Yakabe et al. [130] (left) and its simplification to the 1D geometry used in this analysis (right). . . . .	72
5.3	Schematic diagram of the 1D model domain. . . . .	80

5.4	DGM, SMM and BFM predictions for (a) CO-CO <sub>2</sub> system at 0.1, 0.3 and 0.5 A/cm <sup>2</sup> , and (b) H <sub>2</sub> /(H <sub>2</sub> +H <sub>2</sub> O+Ar) system at 0.3, 0.7 and 1.0 A/cm <sup>2</sup> , and comparison with the experimental data ( $\tau$ is 4.5 in DGM and SMM, and $\tau^2$ is 4.5 in the BFM).	86
5.5	The DGM, SMM and BFM predictions for (a) CO-CO <sub>2</sub> system at 0.1, 0.3 and 0.5 A/cm <sup>2</sup> and (b) H <sub>2</sub> -H <sub>2</sub> O-Ar system at 0.3, 0.7 and 1.0 A/cm <sup>2</sup> , and comparison with the experimental data with fitted tortuosity values for each model.	88
5.6	The ( $\eta_c - \eta_o$ ) predictions of the SMM and the DGM for the H <sub>2</sub> /(H <sub>2</sub> +H <sub>2</sub> O+Ar) system at 1 A/cm <sup>2</sup> ; (a) for pore diameter 2.6 $\mu$ m, respectively, and $\tau = 4.5$ and (b) same system for the optimized tortuosity parameters which are 5.0, 5.4 for the SMM and DGM, respectively.	92
5.7	The ( $\eta_c - \eta_o$ ) predictions of the SMM and the DGM for the H <sub>2</sub> /(H <sub>2</sub> +H <sub>2</sub> O+Ar) system at 1 A/cm <sup>2</sup> ; (a) for pore diameter 1.6 $\mu$ m, respectively, and $\tau = 4.5$ and (b) same system for the optimized tortuosity parameters which are 5.0, 5.4 for the SMM and DGM, respectively.	93
5.8	The ( $\eta_c - \eta_o$ ) predictions of the SMM and the DGM for the H <sub>2</sub> /(H <sub>2</sub> +H <sub>2</sub> O+Ar) system at 1 A/cm <sup>2</sup> ; (a) for pore diameter 0.26 $\mu$ m, respectively, and $\tau = 4.5$ and (b) same system for the optimized tortuosity parameters which are 5.0, 5.4 for the SMM and DGM, respectively.	94

5.9	The $(\eta_c - \eta_0)$ predictions of the SMM and the DGM for the $H_2/(H_2+H_2O+Ar)$ system at 0.05, 1, and 1.5 $A/cm^2$ and average pore diameter= $2.6 \mu m$ (a) for $\tau= 4.5$ and (b) the same system for the optimized tortuosity parameters. . . . .	97
5.10	The $(\eta_c - \eta_0)$ predictions of the SMM and the DGM for the $H_2/(H_2+H_2O+Ar)$ system at 0.05, 1, and 1.5 $A/cm^2$ and average pore diameter= $1.6 \mu m$ (a) for $\tau= 4.5$ and (b) the same system for the optimized tortuosity parameters. . . . .	98
5.11	The $(\eta_c - \eta_0)$ predictions of the SMM and the DGM for the $H_2/(H_2+H_2O+Ar)$ system at 0.05, 1, and 1.5 $A/cm^2$ and average pore diameter= $0.26 \mu m$ (a) for $\tau= 4.5$ and (b) the same system for the optimized tortuosity parameters. . . . .	99
5.12	The $(\eta_c - \eta_0)$ predictions of the DGM and the BFM for the $H_2/(H_2+H_2O+Ar)$ system at 0.05, 1, and 1.5 $A/cm^2$ for pore diameters $2.6 \mu m$ (a) for $\tau=4.5$ (b) for the optimized tortuosity parameter.	100
5.13	The $(\eta_c - \eta_0)$ predictions of the DGM and the BFM for the $H_2/(H_2+H_2O+Ar)$ system at 0.05, 1, and 1.5 $A/cm^2$ for pore diameters $0.26 \mu m$ (a) for $\tau=4.5$ (b) for the optimized tortuosity parameter.	101
5.14	$(\eta_c - \eta_0)$ predictions of the (a) DGM and (b) BFM with and without the additional pressure gradient term, labelled as (1) and (2), respectively for the $H_2/(H_2+H_2O+Ar)$ system at 0.3, 0.7, and 1 $A/cm^2$ ; for pore diameter $2.6 \mu m$ . . . . .	103
6.1	The experimental set-up of Evans et al. [29] that is used to measure the counter diffusion flux of He and Ar in a porous septum. . . . .	116

6.2	A comparison of the predictions of the $N_{H_e}$ and $N_{Ar}$ for the uniform pressure system at different pressure between the experimental data and (a) present study, and Krishna [67] for the DGM and (b) present study, and Kerkhof et al.[61] for the BFM. . . . .	118
6.3	The domain for the 2D SOFC model. . . . .	120
6.4	The domain of the 3D SOFC model. . . . .	124
6.5	The variations of the $w_{H_2}$ along the catalyst length ( $x$ -direction) for the inlet $w_{H_2}=0.0202$ and current density $1.0 \text{ A/cm}^2$ for different number of cells for the (a) 2D, and (b) 3D model. . . . .	127
6.6	A comparison of the 2D models of the SMM, DGM and the BFM and the comparison with the experimental data at (a) 0.3, (b) 0.7 and (c) $1.0 \text{ A/cm}^2$ . . . . .	129
6.7	The 2D concentration polarization predictions of the SMM, DGM and the BFM for different inlet mole fractions of $H_2$ with the adjusted tortuosity parameter at (a) 0.3 (b) 0.7 (c) $1.0 \text{ A/cm}^2$ . . . . .	130
6.8	A comparison of the 3D predictions of the concentration polarization, $(\eta_c - \eta_0)$ , of the SMM, DGM and the BFM when using a constant tortuosity parameter at $0.3 \text{ A/cm}^2$ for (a) $\tau=4.5$ and (b) the adjusted tortuosity parameter (see Table 6.5). . . . .	132
6.9	A comparison of the 3D predictions of the concentration polarization, $(\eta_c - \eta_0)$ of the SMM, DGM and the BFM with using a constant tortuosity parameter at $0.7 \text{ A/cm}^2$ for (a) $\tau=4.5$ and (b) adjusted tortuosity parameter (see Table 6.5). . . . .	133

6.10 A comparison of the 3D predictions of the concentration polarization, $(\eta_c - \eta_0)$ of the SMM, DGM and the BFM with using a constant tortuosity parameter at 1.0 A/cm <sup>2</sup> for (a) $\tau=4.5$ and (b) adjusted tortuosity parameter (see Table 6.5). . . . .	134
6.11 The H <sub>2</sub> mass fraction distribution over the SOFC anode for at 0.3 A/cm <sup>2</sup> for (a) SMM, (c) DGM and (e) BFM, and at 1.0 A/cm <sup>2</sup> for (b) SMM, (d) DGM, and (f) BFM. The inlet $w_{H_2}$ is 0.0202. . . . .	139
6.12 A comparison of the SMM, DGM and BFM predictions of the H <sub>2</sub> mass fraction distribution over the length of the catalyst layer at $y = 0, z = 0$ at (a) 0.3 A/cm <sup>2</sup> , and (b) 1.0 A/cm <sup>2</sup> , and $w_{H_2}=0.0202$ . . . . .	140
6.13 A comparison of the SMM, DGM and BFM predictions of the H <sub>2</sub> mass fraction distribution over the height of the anode and catalyst at the midpoint of the length of the anode ( $x = 0.01, y = 0$ ) at (a) 0.3 A/cm <sup>2</sup> , and (b) 1.0 A/cm <sup>2</sup> , and $w_{H_2}=0.0202$ . . . . .	141
6.14 A comparison of the 1D, 2D and 3D concentration polarization predictions of the SMM at the current densities (a) 0.3, (b) 0.7, and (c) 1.0 A/cm <sup>2</sup> . . . . .	142
6.15 A comparison of the 1D, 2D and 3D concentration polarization predictions of the DGM at the current densities at (a) 0.3, (b) 0.7, and (c) 1.0 A/cm <sup>2</sup> . . . . .	144
6.16 A comparison of the 1D, 2D and 3D concentration polarization predictions of the BFM at the current densities at (a) 0.3, (b) 0.7, and (c) 1.0 A/cm <sup>2</sup> . . . . .	145
6.17 Current density distribution in the active area of a cross flow planer SOFC stack [98]. . . . .	146

6.18	A comparison of the 3D concentration polarization predictions of the SMM with the constant and the linear variations in the current density distribution at (a) $i=0.3 \text{ A/cm}^2$ , and (b) $1.0 \text{ A/cm}^2$ . . . . .	150
6.19	A comparison of the distribution of mass fraction of $\text{H}_2$ along the length of the catalyst layer with the constant and linear variations in the current density distribution at (a) $i=1.0 \text{ A/cm}^2$ , and (b) $0.3 \text{ A/cm}^2$ , for the SMM. . . . .	151
6.20	A comparison of the 3D concentration polarization predictions of the DGM with the constant and the linear variations in the current density distribution at (a) $i=0.3 \text{ A/cm}^2$ , and (b) $1.0 \text{ A/cm}^2$ . . . . .	152
6.21	A comparison of the distribution of mass fraction of $\text{H}_2$ along the length of the catalyst layer with the constant and linear variations in the current density distribution at (a) $i=1.0 \text{ A/cm}^2$ , and (b) $0.3 \text{ A/cm}^2$ , for the DGM. . . . .	153
6.22	A comparison of the 3D concentration polarization predictions of the BFM with the constant and the linear variations in the current density distribution at (a) $i=0.3 \text{ A/cm}^2$ , and (b) $1.0 \text{ A/cm}^2$ . . . . .	154
6.23	A comparison of the distribution of mass fraction of $\text{H}_2$ along the length of the catalyst layer with the constant and linear variations in the current density distribution at (a) $i=1.0 \text{ A/cm}^2$ , and (b) $0.3 \text{ A/cm}^2$ , for the BFM. . . . .	155
6.24	A comparison of the 3D concentration polarization predictions of the BFM, both with and without $\kappa/K_i$ , at the current densities (a) $0.3$ (b) $0.7$ , and (c) $1.0 \text{ A/cm}^2$ . . . . .	157
7.1	Fuel cell geometry (view from the top; lengths in mm) [13]. . . . .	163

7.2	The IT-SOFC cross section [13]. . . . .	164
7.3	The input data distribution (a) before and (b) after, the data reduction.	168
7.4	RMSE for a different number of experimental data. . . . .	169
7.5	Training data versus the ANFIS output. . . . .	171
7.6	Test data versus the ANFIS output. . . . .	172
7.7	Current-voltage curve as a function of the fuel mass flow rate. The volumetric H <sub>2</sub> content is 53%, and the temperature is 800°C. . . . .	173
7.8	Current-voltage curve as a function of the volumetric H <sub>2</sub> rate (%). The mass flow inlet rate is 0.00756 g/s, and the temperature is 800°C. . . . .	174
7.9	The training and test data distribution chosen to test the extrapolation capability of ANFIS. . . . .	175
7.10	The structure of the ANFIS for the PEMFC model with 5 inputs, 2 input membership functions for each input, constructed 32 rules and the output of the model. . . . .	178
7.11	The RMSE values of the test and training data sets for each epoch. The black dot indicates the point where the test RMSE reaches its minimum value and hence the training is terminated. . . . .	179
7.12	Scatter diagrams showing the correlation between the ANFIS output and (a) the training data, and (b) the test data. . . . .	180
7.13	The ANFIS prediction of the voltage-current density curve as a function of the cell temperature. The anode and cathode humidification temperatures are 70 °C, backpressures are 3 atm on both the anode and cathode sides, and the flow rates are 1200 sccm on the anode side and 2200 sccm on the cathode side. . . . .	182

7.14	The ANFIS prediction of the voltage-current density curve as a function of the anode humidification temperature. The cell temperature and cathode humidification temperatures are 70 °C, backpressures are 3 atm on the both anode and cathode sides, and the flow rates are 1200 sccm on the anode side and 2200 sccm on the cathode side. . . . .	183
7.15	The ANFIS prediction of the voltage-current density curve as a function of the cathode humidification temperature. The cell temperature and anode humidification temperatures are 70 °C, backpressures are 3 atm on both the anode and cathode sides, and the flow rates are 1200 sccm on the anode side and 2200 sccm on the cathode side. . . . .	184
7.16	The ANFIS prediction of the voltage-current density curve as a function of the backpressure. The fuel cell temperature and anode and cathode humidification temperatures are 70 °C, and the flow rates are 1200 sccm on the anode side and 2200 sccm on the cathode side. . . . .	185

# List of Tables

3.1	Forward and backward passes in the hybrid learning procedure for ANFIS [52]. . . . .	50
5.1	Model parameters [130]. . . . .	81
5.2	Calculated viscosities of different gas components at different temperatures. . . . .	84
5.3	Tortuosity fitted values for the SMM, DGM and the BFM for CO-CO <sub>2</sub> and H <sub>2</sub> -H <sub>2</sub> O-Ar systems. . . . .	90
6.1	Parameters used in Kerkhof [61] (DGM) and Krishna [67] (DGM) to predict the flux of He and Ar in the porous septum at uniform pressure. . . . .	116
6.2	Dimensions of the SOFC anode. . . . .	119
6.3	The average mass fraction of H <sub>2</sub> and H <sub>2</sub> O at the anode-electrolyte interface for different number of cells for the 2D model. . . . .	126
6.4	The average mass fraction of H <sub>2</sub> and H <sub>2</sub> O at the anode-electrolyte interface for different number of cells for the 3D model. . . . .	126
6.5	Optimized tortuosity parameters for each diffusion model for the 2D and 3D analysis. . . . .	128

7.1	Fuel mass flow rate and fuel composition (the water content is complementary to 100%) used for the experimental characterization of the fuel cell [13]. . . . .	165
7.2	Performance of the ANFIS model for the SOFC using fifteen different input combinations. . . . .	167
7.3	RMSE of the training and test data sets chosen to test the extrapolation capability of ANFIS. . . . .	175
7.4	The training and test performances of ANFIS. . . . .	178

# Nomenclature

## Abbreviations

BFM	Binary Friction Model
CFD	Computational Fluid Dynamics
CHP	Combined Heat and Power
CPIM	Cylindrical Pore Interpolation Model
DGM	Dusty Gas Model
DMFC	Direct Methanol Fuel Cell
FEM	Finite Element Method
FM	Fick Model
FVM	Finite Volume Method
GDL	Gas Diffusion Layer
ILU	Incomplete Lower and Upper algorithm
IT-SOFC	Intermediate temperature SOFC
IP-SOFC	Integrated planar SOFC
LU	Lower and Upper algorithm
LSM	Strontium-doped Lanthanum Manganite
MAPE	Mean Absolute Percentage Error
MTPM	Mean Transport Pore Model

PEN	Positive electrode-Electrolyte-Negative electrode
PEMFC	Polymer Electrolyte Membrane Fuel Cell
RMSE	Root Mean Square Error
SMM	Stefan Maxwell Model
SOFC	Solid Oxide Fuel Cell
STP	Standard Temperature and Pressure
TPB	Triple Phase Boundary
YSZ	Yttria Stabilized Zirconia

## Roman Letters

$A$ (and $B$ )	linguistic labels	—
$A_i$	activation function	—
$a_i$	actual value of the sample $i$	—
$a, b$ and $c$	premise parameters of bell-shaped membership functions	—
$c_T$	total concentration of gas mixture	$kg/m^3$
$D_{i,m}$	mass diffusion coefficient for component $i$ in the mixture	$m^2/s$
$D_{ij}$	binary molecular diffusion coefficient	$m^2/s$
$D_{ij}^e$	effective binary molecular diffusion coefficient	$m^2/s$
$D_{i,Kn}^e$	effective Knudsen diffusion coefficient for species $i$	$m^2/s$
$E$	actual cell voltage	$V$
$E_{Nernst}$	Nernst potential	$V$
$E^0$	Open Circuit Voltage (OCV) at STP	$V$

$F$	Faraday constant	$C/mol$
$\mathbf{f}$	body force	$m/s^2$
$G$	Gibbs free energy	$Jl$
$G^0$	standard Gibbs free energy	$J$
$\Delta G$	change in the Gibbs free energy	$J$
$\Delta G^0$	change in the standard Gibbs free energy	$J$
$\bar{g}_f$	Gibbs free energy per mole	$J/mol$
$H$	enthalpy	$J/mol$
$I$	current	$A$
$i$	current density	$A/cm^2$
$i_{ref}^a$	exchange current density of anode	$A/cm^2$
$i_{ref}^c$	exchange current density of cathode	$A/cm^2$
$\mathbf{J}_i$	molar diffusion flux of component $i$	$mol/m^2/s$
$\mathbf{j}_i$	mass diffusion flux of component $i$	$kg/m^2/s$
$Kn$	Knudsen number	–
$l$	length of the conductor	$m$
$L_e$	average pore length	$m$
$L$	actual pore length	$m$
$M_{w,i}$	molar weight of component $i$	$kg/mol$
$n$	number density of molecules	$molecules/m^3$
$n_e$	mole of electrons	$mol$
$\mathbf{n}_i$	mass total flux of component $i$	$kg/m^2/s$
$N$	number of components in a gas mixture	–
$\mathbf{N}_i$	molar total flux of component $i$	$mol/m^2/s$

$P$	static pressure	$Pa$
$p_i$	predicted value of the sample $i$	–
$p, q$ and $r$	consequent parameters of the ANFIS model	–
$Q_i^n$	output of the $n^{th}$ layer of ANFIS	–
$r_o$	mean pore radius	$m$
$R_g$	universal gas constant	$J/mol/K$
$R_g$	universal gas constant	$J/mol/K$
$R_{ohm}$	resistance	$ohm$
$S$	entropy	$J/K$
$T$	temperature	$K$
$u$	mixture velocity	$m/s$
$V$	volume	$m^3$
$w_i$	mass fraction of species $i$	–
$x_1$ (and $x_2$ )	input of the ANFIS model	–
$x_i$	mole fraction of component $i$	–
$y$	output of the ANFIS model	

## Greek Letters

$\alpha$	charge transfer coefficient	–
$\epsilon$	porosity	–
$\lambda$	path length	$m$
$\mu_A^i, \mu_B^j$	fuzzy membership functions	–
$\mu$	fluid mixture viscosity	$kg/m/s$

$\rho$	fluid density	$kg/m^3$
$\rho_i$	species mass density	$kg/m^3$
$\sigma_{12}$	collision diameter of 1-2 molecule pair	$A^o$
$\sigma_{ion}$	ionic conductance	<i>siemens</i>
$\Omega_D$	diffusion collision integral	—
$\sigma$	electrical conductance	$1/ohm/m$
$\tau$	tortuosity	—
$\eta_{ohmic}$	ohmic losses	$V$
$\eta_{act.a}$	activation losses at anode	$V$
$\eta_{act.c}$	activation losses at cathode	$V$
$\eta_c$	concentration losses	$V$
$\eta$	dynamic viscosity	$kg/m/s$
$\eta_i^0$	pure component viscosity of species $i$	$kg/m/s$
$\phi_e$	electric potential	$V$
$\phi_{ion}$	ionic potential	$V$

# Chapter 1

## INTRODUCTION

Over the last decade, both the increase in the energy demand and concerns about the global warming due to the industrialization has forced governments to take precautions to meet the increasing energy demand and prevent the global warming.

In this sense, fuel cells offer the prospect that the world is looking for, namely, power generation with zero or low emissions and high efficiency (usually up to 50-60 %, and even more when combined with other systems). Therefore, they are represented as strong candidates for the next generation of power systems. They offer endless possibilities for application, ranging from the automobile industry to power stations, cellular phones to laptops. Although commercialization has been initiated for some types of fuel cells, there are still problems that should be overcome before their widespread use. The success of the fuel cells as competitive power generation devices depends on the advances made in their designs; therefore much research is needed in this area.

## **1.1 Fuel Cells**

Fuel cells are electrochemical devices that convert the chemical energy of a fuel directly into electricity. The electrochemical conversion process of the fuel into energy is clean, quiet and more efficient compared to other energy generation processes, such as combustion.

There are different types of fuel cells. One classification can be made according to the electrolyte type used, i.e. Proton Exchange Membrane Fuel Cell (PEMFC), Solid Oxide Fuel Cell (SOFC), Direct Methanol Fuel Cell (DMFC), Alkaline Fuel Cell (AFC), Phosphoric Acid Fuel Cell (PAFC), etc. In addition to the diversities in electrolyte type, they differ in their areas of application, operating temperatures and efficiencies. This section gives a general overview on the two types of fuel cells investigated in this thesis, namely SOFC and PEMFC and their components, operating principles and kinetics.

### **1.1.1 SOFC**

High temperature Solid Oxide Fuel Cells (SOFCs) operate usually between 600 – 1000 °C. The basic idea was first proposed by Nernst and his colleagues in 1899 using zirconia ( $ZrO_2$ ) as an oxygen ion conductor. The reader can refer to [105] for comprehensive background information.

A high temperature is a requirement for the electrolyte type used to promote ionic conductivity. Operating at high temperatures brings them some advantages mainly due to: (i) heat produced at a high temperature can be used in a variety of fields, such as in combined heat and power (CHP) systems, to drive turbines

that can drive generators to produce further energy and to reform other fuels such as natural gas, (ii) electrochemical reaction rates are accelerated due to high temperatures and therefore expensive catalysts are not required to promote the reactions, (iii) activation losses are less than low temperature fuel cells which makes them more efficient, and (iv) CO poisoning of the electrodes is not a problem. Therefore there is the opportunity to reform hydrocarbons within the system directly on the anode of the cell.

Although the high temperature heat can be used in a variety of areas, the main disadvantages of operating at elevated temperatures are the high cost, mainly due to precious materials for interconnects and construction materials, thermal stresses, unwanted sintering, i.e any chemical interaction between the electrodes and electrolyte during the cell fabrication [105] and corrosion. Operation at a reduced temperature can overcome these problems and bring additional benefits. Therefore, intermediate temperature (IT) SOFC has gained importance over the last few years. They can operate at temperatures as low as 500 °C, and this means that low cost metallic materials can be used. This makes both the stack and the balance of the plant which includes the thermal insulation, pipe work, pumps, heat exchangers, heat utilization plant, fuel processors, control system, start-up heater and power conditioning cheaper. In addition to the cost, IT SOFC offers other advantages such as a more rapid start up and shut down procedure, simpler design, reduction in corrosion, etc.

In the fuel cell concept, a single cell generates a limited voltage. Therefore more than one cell is connected together to increase the voltage and accordingly the power. The combination of more than one cell is called a "stack". The basic designs used for the SOFC technology are planar, tubular and monolithic de-

signs. The tubular SOFC was developed by Siemens-Westinghouse to overcome the sealing problems related to the planar design. Fuel and air is supplied to the outside and the inside, respectively, of the solid oxide tubes closed at one end. The main problems with the tubular design are the manufacturing and assembling difficulties. Therefore, the planar SOFC systems have been receiving attention lately because manufacturing is comparatively easy and higher performance are obtained compared to the tubular types [130]. Planar SOFCs are generally manufactured in three different configurations according to their operating temperatures as anode supported, cathode supported and electrolyte supported. For SOFC operating at lower operating temperatures, anode- or cathode-supported cell configurations are preferred, while for cells operating around 1000°C, the electrolyte-supported cell configuration is preferred. In addition to the two most widely used planar and tubular designs, Rolls-Royce have developed integrated planar designs which use both the advantage of the planar design (ease of manufacturing) and tubular design (to overcome the sealing problem) called Integrated Planar SOFC (IP- SOFC). IP-SOFC is a family of integrated system concepts supporting product flexibility with evolutionary stretch potential from a common SOFC module [34].

The applications of high and intermediate temperature SOFCs range from large scale distributed power generation to small-scale domestic heat and power. In addition, many automotive manufacturers are investigating whether small SOFC stacks (3-5 kW) can be developed to supply the electrical power for auxiliary functions such as air conditioning in vehicles [107].

### 1.1.1.1 Operation Principle

Figure 1.1 illustrates the basic operational principle of a SOFC. It consists of two electrodes (anode and cathode) and an electrolyte between. Electrodes are the porous materials which enables gas transport through the electrolyte/electrode/gas interface where electrochemical reactions take place.

If pure hydrogen and air are fed into the fuel cell as the fuel and oxidant sources, respectively, the following reactions takes place at the anode and cathode sides:

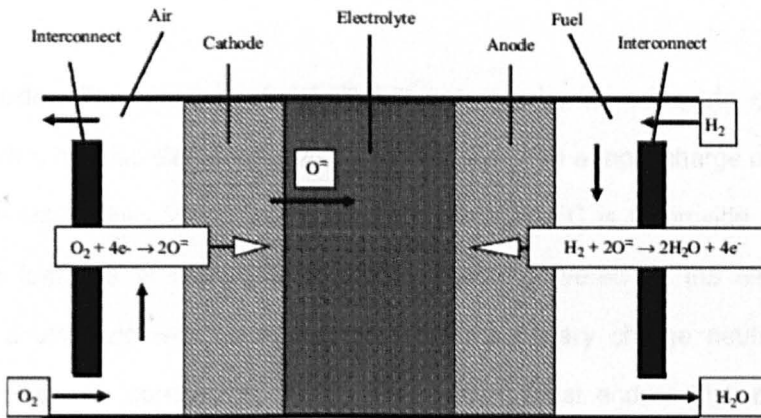
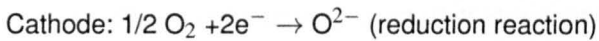
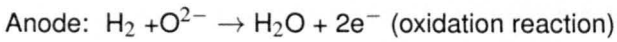


Figure 1.1: Schematic of the basic operational principle of a SOFC [59].

### 1.1.1.2 SOFC Components

A single cell is mainly composed of five components: an electrolyte, two electrodes and two interconnects. In Fig. 1.2, the Scanning Electron Microscope (SEM) image of a SOFC anode is presented. In the following these components are discussed.

**Electrolyte:** The electrolyte is the ion conducting unit of the fuel cells. The ideal electrolyte should have high ionic and low electronic conductivity. They must be stable in an oxidizing and reducing environment. In addition, the material must be able to be formed into a thin, strong film and with no gas leaks [105]. Zirconia doped with a small percentage, usually between 8-10 % yttria (YSZ) is the most effective electrolyte for the high temperature SOFC and some other materials have been investigated, including  $\text{Bi}_2\text{O}_3$ ,  $\text{CeO}_2$  and  $\text{Ta}_2\text{O}_5$ . Zirconia is highly stable in both reducing and oxidizing environments [73].

**Anode:** The anode material should not only be an adequate electronic conductor, but also electro-catalytically active such that a rapid charge exchange can be established. The role of an anode in a SOFC is to provide the sites for the fuel gas to react with the oxygen ions delivered by the electrolyte, within a structure which also facilitates the necessary charge neutralisation by its electronic conductivity [105]. Moreover, it must endure high operating temperatures, and must have redox stability. Nickel-zirconia cermet is the most common anode used in SOFCs.

**Cathode:** The cathode must have high electrical conductivity, high catalytic activity for oxygen reduction, and compatibility (with other cell components).

Many materials have been tested for use as a cathode material. For intermediate temperature SOFCs, a composite consisting of strontium-doped lanthanum manganite (LSM) and YSZ have been shown to have a good performance [84].

**Interconnect:** Two major roles of interconnects are to provide the anode and cathode with fuel and oxidant, respectively, and conduct electrons between the neighbouring fuel cells, i.e. connections between neighbouring fuel cells. In planar fuel cells, this is the bipolar plate, but the arrangement is different for tubular geometries (see [73]). Metals can be used as an interconnect, but these tend to be expensive type stainless steels, particularly for stacks that need to operate at 800 to 1000°C. Conventional steels also have a mismatch in the thermal expansion coefficient with the YSZ electrolyte. To overcome this, Siemens and others have attempted to develop new alloys [73].

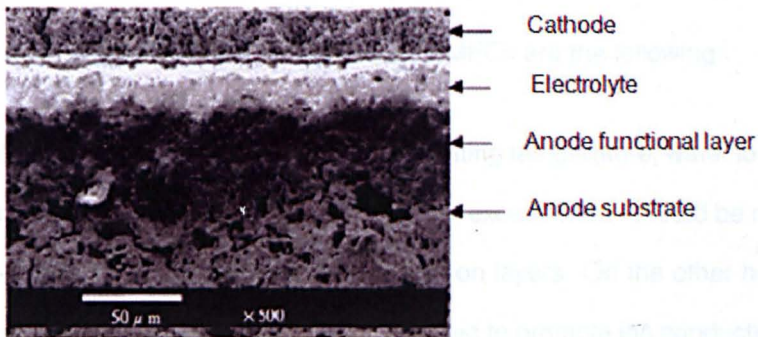


Figure 1.2: Typical SEM image of a cross-sectional microstructure of the single cell [84].

### 1.1.2 PEMFC

As compared to the SOFC, the low temperature PEMFCs operate usually between temperatures 60-90 °C. This low operating temperature is a requirement to promote the hydrogen ion (proton) conductance of the membrane electrolyte. In recent years, there have been advances in the high temperature PEMFCs which are promising alternatives in terms of overcoming the water management problems. However in this chapter the discussion will be restricted to the low temperature PEMFCs that has been investigated in this thesis.

The main advantages of PEMFCs are as follows: (i) easy operation due to low operating temperature, (ii) thermal stability is not an important issue and therefore low cost material can be used for Gas Diffusion Layers (GDLs) through which reactants diffuse from flow channel to catalyst, and (iii) low start up time.

The main problems in low temperature PEMFCs are the following:

- (i) Water management: due to the low operating temperature, water formed on the cathode is in a liquid form. Therefore, excess water should be removed to prevent the clogging of the gas diffusion layers. On the other hand, the membrane electrolyte should be humidified to promote ion conduction. Due to this critical balance related to the amount of water, the cell operates in a narrow range and the effective operational conditions should be determined carefully for a specific cell.
- (ii) Since their activation losses are higher than that of SOFCs, their efficiency is usually lower than that of the SOFC.

Due to the low start up time associated with the low operational temperature,

the main application areas are the automotive industry and in portable industries such as laptops and cellular phones.

### 1.1.2.1 Operational Principles

Figure 1.3 shows a schematic of the operation principle of a single cell PEMFC. It consists of anode and cathode GDLs, electrolyte, catalyst layers and an anode and cathode bipolar plates which conduct electrons and supply fuels to the cell. Different from the SOFC, for the hydrogen fed PEMFC,  $H^+$  ions are transferred from the anode to the cathode and  $H_2O$  is formed on the cathode side.

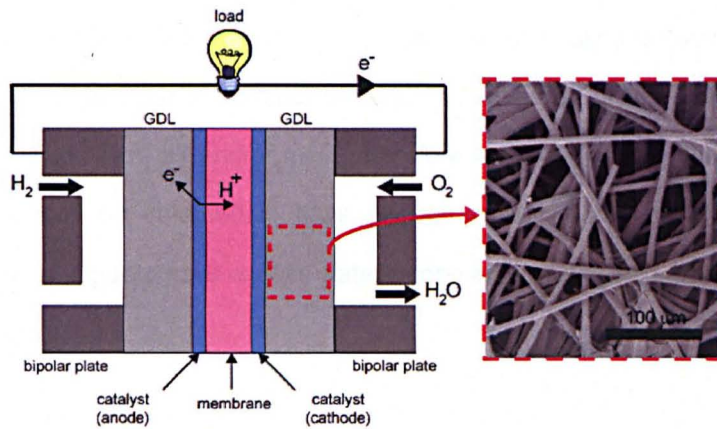
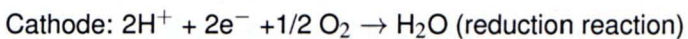
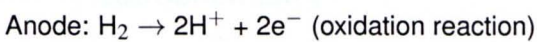


Figure 1.3: Schematic of the basic operational principle of a PEMFC [10].

The overall reactions on the anode and cathode are as follows:



For the reduction of  $H_2$  on the anode, the catalyst layer is required and the most widely used catalyst for low PEMFC is platinum. Platinum is a precious material which is the main source of the cost in a PEMFC.

### 1.1.2.2 PEMFC Components

The components of a PEMFC are as follows:

**Anodes and Cathode Electrodes (Gas Diffusion Layers):** In the PEMFC literature, the anode and cathode electrodes are often called as Gas Diffusion Layers (GDLs). As in a SOFC, electrodes should be good electron conductors and ion insulators. The traditional and most widely used GDL is polytetrafluoroethylene (PTFE).

**Electrolyte:** The most widely used membrane electrolyte is Nafion. Nafion needs to be humidified to conduct protons and one way of this is to feed the fuel with a humidified air and/or fuel. Therefore in the fuel cell system, a water balance should be obtained to have enough water needed to humidify the electrolytes and not to have excess water to prevent flooding and clogging of the electrolytes.

**Catalyst:** Platinum is the most widely used catalyst material on the anode site for hydrogen reduction. It is an expensive material and is the main cost factor in the early development of fuel cells.

### 1.1.3 Electrochemistry

In a hydrogen fuel cell, electricity is produced due to the exothermic process in the formation of water from hydrogen and oxygen. Eqn. (1.1) gives the electrical work done moving  $n_e$  mole of electrons through the circuit that produces  $E^0$  volts of voltage, where  $-n_e F$  is the charge carried by  $n_e$  mole of electrons,

$$\text{Electrical work done} = -n_e F E^0 \quad (1.1)$$

where  $n_e$  is mole of electrons transferred per mole of hydrogen (mole of  $e^-$ /mole of hydrogen),  $F$  is the Faradays constant (charge transferred per mole of  $e^- = 96834 \text{ C/mole of } e^-$ ), and  $E^0$  is the reversible open circuit voltage (OCV) (V).

The Gibbs energy ( $G$ ) is the "energy available to do external work", neglecting any work done by changes in pressure or volume, namely,

$$G = H - TS \quad (1.2)$$

where  $G$  is Gibbs free energy (J),  $H$  is enthalpy (J),  $S$  is entropy (J/K), and  $T$  is temperature (K).

The second part on the right-hand-side of Eqn. (1.2) indicates the loss of energy in the form of heat (energy that cannot be converted into work). The Gibbs free energy of formation changes with temperature and state (liquid or gas). In a fuel cell, it is the change in the Gibbs free energy of formation,  $\Delta G_f$ , that gives the energy released. This change is the difference between the Gibbs free energy of the products and the Gibbs free energy of the reactant [73], namely:

$$\Delta \bar{g}_f = \bar{g}_{f,H_2O} - \bar{g}_{f,H_2} - \frac{1}{2} \bar{g}_{f,O_2} \quad (1.3)$$

Note that to make comparisons easier, it is most convenient to consider these quantities in their 'per mole' form and therefore these are indicated by the  $\bar{\quad}$  over the lower case letter in Eqn. 1.3.

In a fuel cell, the external work involves moving electrons round an electrical circuit. Hence, the Gibbs free energy is equal to the electrical energy as follows:

$$\Delta\bar{g}_f = -n_e F E^0 \quad (1.4)$$

$$E^0 = -\frac{\Delta\bar{g}_f}{n_e F} \quad (1.5)$$

where  $E^0$  is the reversible open circuit voltage (OCV) (V), and  $n_e$  is the moles of electrons transferred per mole of hydrogen molecule.

### 1.1.3.1 Kinetics

**Operational Losses:** The performance of an operating fuel cell is reduced by activation (kinetics), ohmic resistance and mass transfer losses. At low current density, activation losses are the main cause of voltage reduction, at intermediate voltages, ohmic losses within the electrolyte are dominant, while at high current densities, mass transfer effects predominate. Figure 1.4 shows a typical current-voltage distribution curve for many hydrogen fuel cells. At an open circuit condition, some of hydrogen (fuel) is separated from anode and diffuses to catalyst, then it crosses-over from catalyst to cathode and reacts with oxygen directly and produces water. It should be noticed, no output current exists in this case, and this type of losses fuel is called fuel cross over or internal currents [36].

**Activation losses** are due to the slowness of the reactions on the anode and cathode sides. The high temperature fuel cells have less activation losses than the low temperature ones due to the increase in the rate of chemical reactions at higher temperatures.

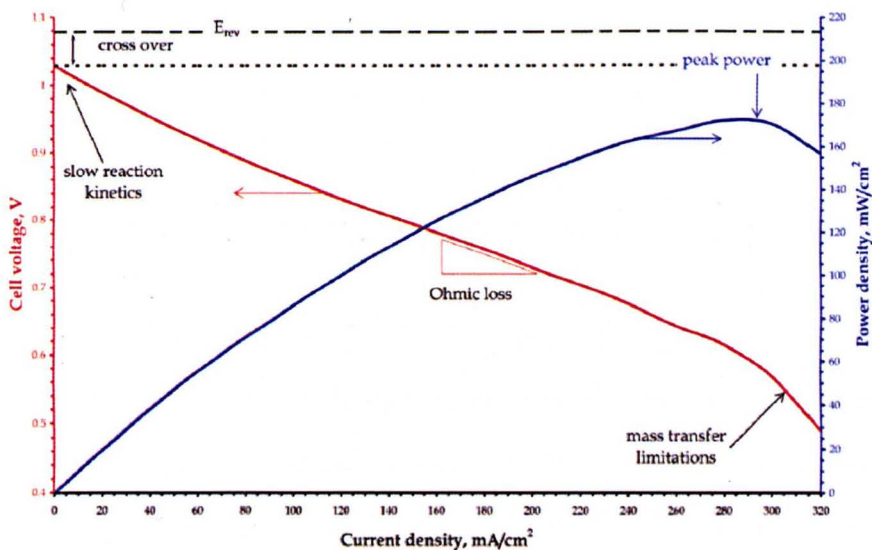


Figure 1.4: Typical current-voltage distribution curve for many hydrogen fuel cells [79].

**Ohmic losses** are due to resistance of the electrodes and interconnects to the flow of electrons and resistance of the electrolyte to the flow of ions. Ohmic losses in the electrolyte are generally much higher than the losses in the other components of the fuel cell.

**Concentration losses** are due to the decrease in concentration as the reactants (fuel and oxygen) are used up. Concentration losses are the predominant losses for high temperature fuel cells.

The mathematical definition of these voltage losses are discussed in Chapter 3. The cell voltage,  $E$ , is usually calculated by subtracting these losses from the open circuit voltage,  $E^0$  as follows:

$$E = E^0 - \eta_{ohmic} - \eta_{act,a} - \eta_{act,c} - \eta_c \quad (1.6)$$

where "a" and "c" refer to as anode and cathode, respectively,  $\eta_{ohmic}$  is the ohmic losses,  $\eta_{act}$  is the activation losses (V), and  $\eta_c$  is the concentration losses (V).

## 1.2 Problem Definition and Objectives of the Study

Conducting experiments on fuel cells are often expensive, time consuming and constrained by the adequate measurement techniques. In particular, measurements within the fuel cell are extremely difficult to perform, due to the compactness and complexities in the design of fuel cells. Therefore, comprehensive and well-validated mathematical and numerical models can be important tools in the design purposes and in assisting in the development of fuel cells as an alternative to performing numerous very expensive experimental investigations to provide detailed information [78]. A number of developments and applications of mathematical models for fuel cells in 1D, 2D and 3D can be found in the literature.

The modelling may take place at different levels, ranging from the molecular level, the cell level to the stack level, and to the system level. At the cell level to the stack level, the flow distribution and the related electrochemical transport simulations are performed by Computational Fluid Dynamics (CFD) tools. In order to build a comprehensive, multi-component CFD model, and obtain accurate numerical solutions for the fuel cells, a fundamental understanding of the fuel cell processes is essential. This ranges from the understanding of the various macro-fluid flows and heat transfer, and the material, physical and chemical properties, to the significant insight into the micro-processes of the species transport and charge transfer reactions. From the recent publications it has been observed that the majority of the published fuel cell CFD models are developed under substantially simplified conditions [78].

In general, the main purpose of this study is the development and improvement of the CFD models which will accordingly assist in the design improvements of the fuel cells with a special emphasis on the investigation of the multicomponent mass diffusion modelling in porous medium of a SOFC.

Multicomponent mass diffusion processes, especially in porous electrodes of fuel cells, plays a critical role in the performance of the cells. In particular, accurate prediction of the diffusion in the porous medium of the electrodes is important in the overall performance prediction, and in turn in the design optimization of fuel cells. The ordinary and the Knudsen diffusion are the two types of diffusion that generally dominate in a porous medium that has a small pore diameter. In ordinary diffusion, molecule-molecule interactions are important, while for the Knudsen diffusion, wall-molecule collision dominates and the effect of the molecule-molecule collisions are negligible. In fuel cells, the electrodes which have a pore diameter of the order of a couple of micrometers, it is expected that both the Knudsen diffusion and the ordinary diffusion have an important effect.

There are different multicomponent diffusion models in the chemical engineering literature. However, on the other hand, there is still no extensive research that shows the advantages of one model for the prediction of the diffusion flux in porous medium. It is still an open question as to which multicomponent mass transfer model should be used to accurately predict the multicomponent diffusion in the porous electrodes as well as in the gas channels of the fuel cells. In the existing work in the literature, the effect of some averaged parameters on the model performance has not been investigated in detail (see [110], [118]).

Moreover in the diffusion literature, a very serious problem is the complexity of the understanding on the set of equations derived and assumptions made. In addition, a through analysis and comparison of the models with each other and with the experimental data is still missing. Therefore it is still not clear which model predictions produce the best results and under which conditions for even a simple diffusion process in porous medium.

The main motivation of this research, in addition to a detailed background discussion and theoretical evaluation of the existing multicomponent diffusion models, is to investigate and evaluate the models in terms of their prediction performance of the species concentration and in turn the concentration polarization of a Solid Oxide Fuel Cell. The ultimate purpose is to identify a multicomponent diffusion model that is physically sound, and mathematically and computationally acceptable in predicting the multicomponent diffusion in the porous medium of a SOFC and previously this has not been investigated in detail.

Although CFD modelling is a useful tool to investigate the effect of the governing parameters and operational conditions on the cell performance for the design optimization purposes, it should be noted that CFD modelling of fuel cell design is still not in a state of the art condition for making accurate predictions without fitting some parameters to the experimental data and hence validating the model over a large range of operational conditions. This is mainly due to the limited accuracy in the definitions of the nature of the physical processes. Although very recently, the research has been shifted on the coupling of the macroscopic approach with the microscopic approaches and determining macroscopic parameters from the microscopic scale information, this is com-

putationally very demanding and the accuracy of the results are still questionable.

On the other hand, soft computing techniques, including Artificial Neural Networks (ANN), Fuzzy Logic (FL), neuro fuzzy systems, can be used as an alternative to physical models, especially for complex nonlinear systems. They can be used as an alternative to mathematical models (e.g. CFD) in order to predict fuel cell performance under different operating conditions in an efficient and easy way. A neuro-fuzzy technique, namely an Adaptive Neuro-Fuzzy Inference System (ANFIS) combines the learning and generalization capability of ANNs with the approximate reasoning capability of the FL to make predictions without any prior knowledge of the system. This innovative technique is still in its infancy in the fuel cell research area and this will be investigated as a part of this study in terms of its prediction capability in predicting the fuel cell performance for two of the main types of fuel cells, namely a SOFC and a PEMFC.

### **1.3 Thesis Structure**

This thesis consists of 8 main chapters:

- Chapter 2 starts with the physical concept and mathematical modelling of multicomponent gas diffusion in porous medium. Then the different multicomponent diffusion models are theoretically evaluated. The basic history of the development of the models are also reviewed in this chapter.
- Chapter 3 discusses the methodology of the CFD modelling for SOFC and the neuro-fuzzy modeling concept. First, the mathematical equations that govern the multi-physic processes of the SOFC, as well as numerical solution techniques used are discussed in this chapter. Then the methodology

of the ANFIS modelling is discussed.

- Chapter 4 starts with a general literature review on the CFD modelling of SOFC, and then the discussion is mainly restricted to a literature review on the treatment of the mass transport in the SOFC and then the modeling approaches on the neuro-fuzzy modelling of the fuel cells are discussed.
- Chapter 5 presents the results of the prediction capability of the multicomponent mass diffusion models, namely the Stefan Maxwell Model (SMM), the Dusty Gas Model (DGM) and the Binary Friction Model (BFM) for their capability in predicting the concentration polarization of an anode supported SOFC anode. The effect of the pore diameter, current density and concentration of reactants and tortuosity (or porosity/tortuosity) term on the model predictions are investigated in detail. Moreover, in this chapter, the effect of the pressure gradient term in the DGM and the BFM are investigated by including and excluding this term from the model equations. The results are compared with the experimental data.
- Chapter 6 presents the 2D and 3D results of the case investigated in the previous chapter. The implementation of the diffusion models, namely the BFM and the DGM, into COMSOL Multiphysics are discussed in detail. The velocity and pressure distribution on the anode, as well as the effect of the current distribution on the predictions, are presented in this chapter. A 1D, 2D and 3D comparison of the results are also presented and discussed.
- Chapter 7 presents the ANFIS modeling strategies and its performance prediction for an intermediate temperature tubular SOFC and a PEMFC for different operational conditions. The applicability and the limitation of the model in the fuel cell applications are discussed.

- Chapter 8 concludes the thesis by summarizing the results discussed. Further recommendations are also given in this chapter.

## Chapter 2

# LITERATURE REVIEW

The number of articles on the modelling and simulation of the fuel cells have rapidly increased over the last decade. The macro scale continuum model approaches can range from zero- to three-dimensional, can be for different geometries, e.g. planar, tubular etc., can consider or ignore various phenomena such as temperature distribution, internal reforming etc., can analyze steady state or dynamic cell performance. In this chapter, the review of the literature on the CFD modelling of SOFCs will be restricted to the steady state and isothermal multi-dimensional models, since this is the main focus of the investigation in this thesis. First a general literature review on the steady state, and multi-dimensional CFD modelling of SOFC will be given, then the discussion on the CFD modelling of SOFCs will be mainly restricted to the modelling of the multicomponent mass transport in a porous and non-porous components of a SOFC. Then the application of the artificial intelligence methods, such as Fuzzy Logic (FL), Neural Network (NN) and neuro-fuzzy modelling which is the combination of the FL and NN for the two main type of fuel cells, namely SOFC and PEMFC will be discussed.

## 2.1 CFD modelling of SOFC

The macro-scale continuum CFD modelling approach of SOFC may range from zero-dimensional to three-dimensional models. A zero-dimensional model is the simplest one where the fuel cell is modelled as a lumped parameter system. The main advantage of a zero-dimensional model over the one-, two- and three-dimensional models are their small computational time requirements. Zero-dimensional models are especially appropriate for use in system modelling applications where the fuel cell interacts with other devices, such as heat exchangers, combustors, turbines, etc. [17]. However its main limitation is that the distribution of the variables, such as the species mass fraction, velocity, temperature and the pressure distribution in a cell cannot be predicted using a zero-dimensional model. This means that the design of a particular section of a cell by focusing on the distribution of the variables under consideration is not possible using a zero-dimensional model.

In one-dimensional models in the SOFC literature, e.g. Gemmen and Trembly [35], Lehnert et al. [74], Hussain et al. [46], the variations of the variables such as the species concentration, velocity, temperature are modelled in the selected direction. Generally, the direction which is normal to the gas flow direction in the fuel cell channel is selected as the principle direction in order to account for the effect of the consumption at the catalyst layer on the variations of the variables such as species concentration, velocity, temperature. Gemmen and Trembly [35] presented modelling of the half cell SOFC operating with coal syngas in 1D. In the simulations, only the porous anode and catalyst has been into account and transport of the species in the fuel channel has been ignored. Lehnert et al. [74] investigated the mass transport phenomena in the porous cermet, such

as diffusion and permeation, accompanied by chemical and electrochemical reactions. The anode half cell has been modelled by taking into account the gas channel, anode interlayer and the catalyst layer. Hussain et al. [46] presents steady state one-dimensional model of mass transport inside the porous anode of an anode-supported SOFC. The transport of the gas species in the porous anode has been neglected, assuming that the transport of reactant species to the reaction sites in the reaction zone layer is predominated by diffusion.

In the two-dimensional model approaches, e.g. Burt et al. [16], Suwanwarangkul et al. [111], the changes of variables such as species mass fraction, current density, etc. in the transverse direction normal to the gas flow direction has been neglected and the variations in the gas flow direction and in the direction normal to the gas-flow, i.e. the primary current flow direction were considered. In Burt et al. [15], in the fuel cell anode gas channel, electrolyte plate, cathode gas channel, and the separator plate, the variations in the streamwise direction are explicitly calculated, while those in the vertical directions are accounted for via integral approximations, and those in the transverse directions have been neglected. In Suwanwarangkul et al. [111], a two-dimensional model of a button cell SOFC operating with a syngas fuel was presented. Momentum, mass and charge transport coupled with electrochemical and chemical reactions. The button cell consists of an anode feed tube, air channel, fuel channel and electrochemical cell and two-dimensional cylindrical coordinates (radial and vertical directions) were used in the simulations.

Some studies used three-dimensional approaches to model the whole cell/stack, e.g. Achenbach [1], Recknagle et al. [98], Yakabe et al. [131], Zhu et al. [137]). In such studies the main objective is to investigate the effect of the

configuration of the cell and operating conditions, e.g. fuel and air inlets, on the overall performance of the cell/stack. Achenbach [1] studied various effects of the configuration of the co-, counter-, and cross-flow on the efficiency of planar SOFC with internal reforming of methane fuel. However, in his model, the charge transport in the interconnect has been neglected and it was assumed that the electrodes are the only conducting units. Recknagle et al. [98] predicted the distributions of temperature, current density, and fuel species, the flow of anode and cathode gases and fuel utilization. The effect of the co-flow, cross-flow, and counter-flow configuration have been investigated. It was pointed out that the co-flow SOFC configuration produces a more uniform temperature distribution over the cell. Yakabe et al. [131] examined the concentration polarization as the principal polarization in an anode of an anode-supported SOFC. The three-dimensional model of the flow in a SOFC operating with the  $H_2$ - $H_2O$ -Ar, and  $CO$ - $CO_2$ , and the methane reformed gas system were simulated, and the concentration overpotential at the anode was calculated. In Zhu et al. [137], a planar, anode-supported SOFC has been modelled in three-dimension in order to investigate chemically reacting flow mechanism in the cell. The gas transport in the porous anode has been predicted by the combination of the Fickian, Knudsen and the Darcy flow. The gas flow in the fuel and air channel is considered to be one-dimensional and laminar, and the variations of the gas composition transport transverse to the flow direction has been neglected. The main reason for this assumption was that Reynolds number was calculated to be less than 100 and consequently the flow was incompressible and hence it was assumed that a fully developed velocity profile was established very near to the channel entrance. It should be noted that the main disadvantage of three-dimensional modelling is its higher computational effort and computational time demand compared to the zero-, one- and the two-dimensional models.

In order to reduce the computational time and effort required to model the fuel cell as a whole, some of the reported modelling studies focus on modelling of a specific part of the cell which is the most important for the mechanism in their investigations, e.g. Lehnert et al. [74] and, Hao and Goodwin [41]. Such an approach does not only save the computational time but it also saves the computational effort. Lehnert et al. [74] and, Hao and Goodwin [41] have focused on the modelling of the transport mechanism at the porous electrode. Lehnert et al. [74] modelled the mass transport of gases inside the SOFC anode due to diffusion, permeation, accompanied by the chemical and electrochemical reactions. Only the reactions and transport mechanism on the anode side has been considered. Hao and Goodwin [41] numerically investigated the heterogeneous catalytic reactions in the anode of an anode-supported SOFC running on methane fuel with added oxygen. The model accounts for the catalytic chemistry, porous media transport, and electrochemistry at the anode/electrolyte interface.

The recent review papers on the CFD modelling of SOFC are written by Ma et al. [78], Young [133], Kakac et al. [59], Colpan et al. [20], Bhattacharyya et al. [11]. Among those, Ma et al. [78] and Young [133] reviewed the recent advances in CFD modelling of both SOFC and PEMFC and pointed out the major problems. Kakac et al. [59] and Colpan et al. [20] have made an extensive review on the CFD models of SOFC. Most recently Bhattacharyya et al. [11] have reviewed and compared the dynamics model of the SOFC. According to these reviews, one of the common discussion is on the need for the validation of the models, as most of the published modelling work have not been validated at all. Moreover, despite the increasing number of articles on the mathematical and numerical modelling,

there are not many reported research on the investigation of the different model approaches used in the models and the focus in most of these studies is on using the models as design optimization tools by searching the effect of operational conditions and geometrical properties on the fuel cell performance.

### **2.1.1 Diffusion Models in Fuel Cell Models**

In the fuel cell literature, Ni et al. [90], Hernandez et al. [42], and Suwanwarangkul et al. [110] have used the modified version of the FM with the Bosanquet formulation in their model in order to predict the diffusion flux. The Stefan-Maxwell equation is one of the most widely used equations for multicomponent mass transfer problems. In the fuel cell literature, the general trend is to use the SMM by coupling the ordinary diffusion coefficient with the Knudsen diffusion coefficient using the Bosanquet formulation in order to account for the effect of the Knudsen diffusion. One of the reasons for the extensive use of this method is its computational ease in comparison to the other models which take into account the Knudsen diffusion, such as the Dusty Gas Model. However there is no physical justification behind the use of the Bosanquet formulation to model the Knudsen effect and this approach has not been validated against the experimental data.

On the other hand, in the chemical engineering literature there is an ongoing debate on the completeness and the correctness of the developed diffusion models for the porous medium. For example in recent years, Kerkhof [61] criticized the DGM and argued that the addition of a viscous flux to the flux equations, as performed in the DGM, is erroneous because the viscous friction has already been accounted for in the equations before the addition [61]. Based

on the discussion, he derived a new multicomponent model, namely the Binary Friction Model (BFM). The computational requirement for the BFM is much more extensive than the DGM, and that of the DGM is more demanding than the SMM.

In recent years, in the fuel cell literature, BFM has also gained increasingly more attention and this work was modified and extended for fuel cells by Young and Todd [132] and Fimrite et al. [33]. However, there is still no extensive research that shows the advantages of the BFM over the DGM in comparison with the experimental data in porous medium. It is still an open question as to which multicomponent mass transfer model to use to accurately predict the multicomponent diffusion in the porous electrodes as well as in the gas channels of fuel cells.

In the fuel cell literature, one of the methods listed above has been selected and used without stating any particular reason for this choice. The main argument in the literature is that the Knudsen diffusion should be taken into account as it is as important as the ordinary diffusion due to the small pore size in the porous medium. In the fuel cell literature, the first attempt to compare the diffusion models was made by Suwanwarangkul et al. [110] in order to compare three selected models, namely the modified FM, SMM and the DGM for their predictive capabilities of the models in terms of their prediction of the concentration overpotential for an anode supported planar type SOFC anode for the binary CO-CO<sub>2</sub> and the ternary H<sub>2</sub>-H<sub>2</sub>O-Ar components. The solution was made in 1D using MATLAB. They compared the models using the experimental data of Yakabe et al. [130]. To the authors knowledge, this is the only available experimental data for the measurement of the concentration overpotential for SOFCs. Their conclusion was that DGM predicts the model results the best,

especially for the small pore diameter medium, at high current densities and low reactant concentration. They presented the results in table form, indicating the pore diameters only for the CO-CO<sub>2</sub> system and not for the H<sub>2</sub>-H<sub>2</sub>O-Ar system. However, the solution for the ternary mixtures appears to be problematic as the presented prediction of the models fail to accurately predict the concentration polarization and also a detailed discussion of the results is not given for ternary mixtures. The work of Suwawarankul et al. [110] can be criticized on two accounts. Firstly, for the solution of the ternary mixtures equations for SMM and DGM, the mole fraction of Ar was assumed constant in the solution. In fact, the change in the mole fractions of the other species causes a change in Ar, even if Ar is an inert gas and its molar flux is zero at the triple phase boundary (TPB) and through the anode and gas channel domain in the one-dimensional solution. Secondly, the tortuosity parameter, which is used as a fit parameter following the work of Yakabe et al. [130] was assumed to take the same value in all the models. In fact, since it is a fit parameter it must be fitted to the best value for each model individually. It was concluded that the current density, pore diameter and concentration are three key parameters to choose one method over the others. Tseronis et al. [118] extended the study of Suwawarankul et al. [110] to the two-dimensional case. They compared the SMM and DGM for the 1D and 2D cases for the H<sub>2</sub>-H<sub>2</sub>O-Ar ternary system. Their results were in agreement with the results of Suwawarankul et al. [110] and also they showed that the 2D predictions improve compared with the 1D result, especially at high current densities and low inlet H<sub>2</sub> concentration regions. In their work, they again ignored the effect of the tortuosity parameter on the results and the same value of this parameter was used as in [110].

Djilali [26] discussed the transport phenomena in fuel cells by evaluating both

the microscale and macroscale approaches. The main attention of this study is on the PEMFC but the issues that were highlighted is also important for the SOFC transport processes. Djilali [26] stated the ambiguity in the determination of the average transport properties and appropriate parametrisation of the medium. From the analysis in the fuel cell literature, it is observed that the CFD models are still not in the state-of-art in making accurate predictions without fitting some parameters to the experimental data. For example, for the transport equations, the parameter that is important is the effective diffusion coefficient, and hence the porosity and tortuosity. In recent years, the approaches of Direct Numerical Simulation (DNS) and the Lattice Boltzmann Model (LBM) has gained attention in determining the microscopic parameters. The LBM which is originated from the Lattice Gas Automata (LGA) is a discrete particle kinetic method based on discrete time and lattice. The LBM is constructed based on the simplified kinetic models that incorporate the essential physics of microscopic processes so that the macroscopic averaged properties obey the desired macroscopic equations. However Djilali [26] pointed out that the usefulness of the microscopic simulations is currently restricted to the determination of the transport parameters, such as the effective diffusion coefficients in the fuel cell electrodes.

## **2.2 Neuro-fuzzy modelling**

Arriagada et al. [6], Wu et al. [126] and Ou et al. [91] have reported on the application of ANN on fuel cell applications. Arriagada et al. [6] have trained and tested the ANN model for SOFC with the data obtained from a physical model. They concluded that the ANN showed a good consistency with the physical model with the average values of the errors being less than 1%, and the maximum errors being less than 4%. Wu et al. [126] have used the Genetic Algorithm (GA) Radial

Basis Function (RBF) neural network model to predict the voltage of a SOFC at different operational conditions, such as the pressure and current density. They have used the data generated by a physically based CFD model for training and testing the model. The use of the data from the physical model in the ANN model is trivial, especially for the unvalidated physical models. The results and reliability of the ANN models are dependent on the reliability of the physical models and this decreases the reliability of the ANN models. Ou et al. [91] have used ANN in order to model the PEMFC. Specifically they investigated the effect of the Platinum (Pt) loading on the cell voltage. They concluded that the model gives a good approximation to the cell voltage. They proposed a hybrid model which combines the ANN with a physically based CFD model. Their results have showed that the hybrid model provided a modest improvement in the accuracy, compared to the pure ANN model. Jurado [58] has used a fuzzy Hammerstein model to predict the SOFC voltage (output) at different temperatures, currents and fuel flow rates (input). In order to build the rules of the fuzzy model, the user must have a *priori* knowledge of the system, i.e. how the output varies with the input. Entchev et al. [27] have both applied and compared the the ANN and an Artificial Neuro Fuzzy Inference System (ANFIS) for the prediction of the current and voltage of a SOFC stack. They concluded that the SOFC system can be modelled with high accuracy using the ANN and ANFIS techniques and it is faster in comparison to the conventional physical models. However, in their model, both the current and voltage were predicted, while in the physical models, the voltage is a function of the current and vice versa and hence their models are incompatible with the actual physical processes in this sense. Wang et al. [121] have modelled the DMFC stack using the polynomial, ANN and ANFIS methods. It was concluded that among these three kinds of models, the ANFIS based model was the best. As a result, due to its better prediction capability in comparison to the ANN and

the FL [121], in this study ANFIS will be used. In contrast to most of the previous studies which use the data obtained from the physically based models for training and testing of the neuro-fuzzy models, in this study experimental data obtained from the literature are used. The capability of ANFIS is investigated for the tubular SOFC and the PEMFC for multi input and output variables and this has not been investigated before. The effect of the operational conditions on the cell performance will be discussed, as well as the extrapolation capability of the ANFIS model beyond the experimental data is investigated.

## **Chapter 3**

### **CFD AND NEURO-FUZZY**

### **MODELLING CONCEPT**

This chapter discusses the theoretical concept of the CFD modelling of SOFCs and the neuro-fuzzy modelling, namely an Artificial Neuro Fuzzy Inference System (ANFIS). The CFD modelling is based on the solution of the conservation equations, i.e. mass, momentum, electrical and energy balance equations coupled with the appropriate constitutive equations. The governing balance equations which are in partial differential equation forms, are solved using one of the numerical techniques, namely the Finite Element Method (FEM), Finite Volume Method (FVM), etc. On the other hand, ANFIS which is a soft computing technique is the combination of both Artificial Neural Network (ANN) and Fuzzy Logic (FL) and in order to understand the structure of ANFIS, it is important to have a basic knowledge of the ANN and FL fundamentals. This chapter starts with the governing balance equations to model a SOFC and the numerical solution used in this thesis. It then continues with a description of three types of soft computing techniques, namely ANN, FL, and ANFIS.

## 3.1 CFD Modelling Concept

### 3.1.1 Mathematical Model

The mathematical model of fuel cells consist of the governing balance equations, i.e. mass, momentum, and charge balance equations supplemented with appropriate constitutive equations. In what follows these balance equations are explained in detail.

#### 3.1.1.1 Mass Balance

The gas mixture in a SOFC usually consist of more than two species. Hence the mass transport of species in the gas channel and porous electrodes of a SOFC is a multicomponent transport problem. This requires the solution of the mass balance equations for each species in order to define the distribution of the species concentration inside the cell and to predict the performance of the cell.

The mass balance equation for each species  $i$  in the air and fuel channel may be written as follows [119]:

$$\frac{\partial(\rho w_i)}{\partial t} + \nabla \cdot (\rho \mathbf{u} w_i) = -\nabla \cdot (\mathbf{j}_i) + S_i \quad (3.1)$$

where  $\rho$  is the fluid density ( $kg/m^3$ ),  $w_i$  is the mass fraction of species  $i$ ,  $\mathbf{u}$  is the velocity vector of the gas mixture (m/s),  $\mathbf{j}_i$  is the mass diffusion flux ( $kg/m^2/s$ ), and  $S_i$  is the source term of species  $i$  ( $kg/m^3/s$ ). There are different models to predict the diffusion flux term,  $\mathbf{j}_i$ , and these models are discussed in detail in Chapter 4. In the air and fuel channels,  $\mathbf{j}$  is usually neglected assuming that the diffusion is negligible compared to the convection in the gas channels [119].

The summation of the Eqn. (3.1) over each species  $i$  gives the mass balance equations for the mixture, namely:

$$\frac{\partial \rho}{\partial t} + \nabla \cdot (\rho \mathbf{u}) = \mathbf{S} \quad (3.2)$$

In the porous electrodes, Eqn. (3.1) is usually corrected using the porosity,  $\varepsilon$  term as follows [119]:

$$\frac{\partial(\varepsilon \rho w_i)}{\partial t} + \nabla \cdot (\varepsilon \rho \mathbf{u} w_i) = -\nabla \cdot (\mathbf{j}_i) + \mathbf{S}_i \quad (3.3)$$

The overall mass balance equation in porous medium is given as follows:

$$\frac{\partial(\varepsilon \rho)}{\partial t} + \nabla \cdot (\varepsilon \rho \mathbf{u}) = \mathbf{S}_i \quad (3.4)$$

In fuel cells, the mass of the reactants decrease and that of the products increase as a result of the electrochemical reactions that take place at the electrode-electrolyte-gaseous Triple Phase Boundaries (TPB). The consumption and production of the reactants and products are proportional to the electrical current produced by the electrochemical reaction in the cell. As a result, the source term in Eqn. (3.3) may be expressed as follows [78]:

$$\mathbf{S}_i = -\frac{\mathbf{i}}{nF} M_{w,i} \quad (3.5)$$

where  $\mathbf{S}_i$  is the source term of species  $i$  ( $kg/m^3s$ ),  $\mathbf{i}$  is the current density ( $A/m^3$ ),  $n$  is mole of  $e^-$  transferred per mole of reactant,  $F$  is the Faraday's constant ( $C/mol$  of  $e^-$ ), and  $M_{w,i}$  is the molar weight of species  $i$  ( $kg/mol$ ).

Specifically for species H<sub>2</sub>, O<sub>2</sub> and H<sub>2</sub>O, Eqn. (3.5) can be rewritten as follows [78]:

$$\mathbf{S}_{H_2} = -\frac{\mathbf{i}}{2F}M_{w,H_2}; \quad \mathbf{S}_{O_2} = -\frac{\mathbf{i}}{4F}M_{w,O_2}; \quad \mathbf{S}_{H_2O} = +\frac{\mathbf{i}}{2F}M_{w,H_2O} \quad (3.6)$$

### 3.1.1.2 Momentum Balance

The momentum balance or the force balance equation for a moving gas is [119]:

$$\rho \frac{\partial \mathbf{u}}{\partial t} + \rho \mathbf{u} \nabla \cdot \mathbf{u} = -\nabla P + \mu \nabla^2 \mathbf{u} + \rho \mathbf{f} \quad (3.7)$$

where  $\mathbf{f}$  is the body force ( $m/s^2$ ), i.e. gravity,  $\mu$  is the dynamic viscosity ( $kg/m/s$ ). Eqn. (3.7) is a simplified version of the Navier-Stokes equation in the incompressible limit which is a valid assumption for the gas flow in the non-porous medium, i.e. gas channel, at low Mach number [119].

For the fluid flow in the porous electrodes and catalysts of the cell, the momentum conservation is often substituted by the phenomenologically derived constitutive equations, such as Darcy's Law which is given by [119]:

$$\mathbf{u} = -\frac{k}{\mu} \nabla P \quad (3.8)$$

where  $k$  is the permeability of the medium ( $m^2$ ).

### 3.1.1.3 Charge Balance

For the electric and ionic current flow that is generated in the fuel cell, the conservation equation of charge may be employed and it governs the current density distribution and overall potential in the fuel cell as follows [78]:

$$\nabla \cdot (\sigma_e \nabla \phi_e) + \mathbf{S}_e = 0 \quad (3.9)$$

$$\nabla \cdot (\sigma_{ion} \nabla \phi_{ion}) + \mathbf{S}_{ion} = 0 \quad (3.10)$$

where  $\sigma_e$  and  $\sigma_{ion}$  are the electrical and ionic conductances, respectively (1/ohm/m) and  $\phi_e$  and  $\phi_{ion}$  are the electric and ionic potentials, respectively (V),  $\mathbf{S}_e$  and  $\mathbf{S}_{ion}$  are the volumetric transfer currents of the electrons and ions, respectively due to the electrochemical reactions. The magnitude of  $\mathbf{S}_e$  and  $\mathbf{S}_{ion}$  are non-zero only in the catalyst layers and equal to the local transfer current density,  $i$ , i.e.  $\mathbf{S}_e = -\mathbf{i}$  and  $\mathbf{S}_{ion} = \mathbf{i}$  at the catalyst layer and  $\mathbf{S}_e = 0$  and  $\mathbf{S}_{ion} = 0$  in the other regions of the fuel cell.  $i$  can be calculated from the Butler-Volmer equations for anode and cathode sides as follows [17]:

$$\mathbf{i}_a = \mathbf{i}_{ref}^a \left( \frac{[H_2]}{[H_2]_{ref}} \right)^{\gamma_a} \left[ \exp \left( \frac{\alpha_a n F \eta_{act,a}}{RT} \right) - \exp \left( \frac{-\alpha_c n F \eta_{act,a}}{RT} \right) \right] \quad (3.11)$$

$$\mathbf{i}_c = \mathbf{i}_{ref}^c \left( \frac{[O_2]}{[O_2]_{ref}} \right)^{\gamma_c} \left[ \exp \left( \frac{\alpha_c n F \eta_{act,c}}{RT} \right) - \exp \left( \frac{-\alpha_a n F \eta_{act,c}}{RT} \right) \right] \quad (3.12)$$

where the subscripts and superscripts "a" and "c" denote the anode and cathode respectively,  $i_{ref}$  is the exchange current density,  $\alpha$  is the transfer coefficient,  $n$  is the number of electrons transferred per reaction,  $\gamma$  is the concentration dependence exponent,  $[ ]$  and  $[ ]_{ref}$  represent the local species concentration and its reference concentration, respectively, and  $\eta_{act}$  is the activation overpotential.  $i_{ref}$  depends on the catalyst material and its operational condition, and usually it

is obtained experimentally [78]. The activation overpotential in Eqn. (3.11) and (3.12) are given by [78]:

$$\eta_{act,a} = \phi_e - \phi_{ion} \quad (3.13)$$

$$\eta_{act,c} = \phi_e - \phi_{ion} - V_{oc} \quad (3.14)$$

where  $\phi_e$  and  $\phi_{ion}$  are the electronic and ionic potentials respectively, at the interface of the electrode and electrolyte, and  $V_{oc}$  is the open circuit voltage ( $V$ ). The Eqns. (3.13) and (3.14) basically state that the overpotential is the difference between the electrode potential and the ideal potential based on the Nernst equation [78].

With the assumption that there is no electronic transport within the electrolyte, and no gas passage from one electrode to another,  $V_{oc}$  can be calculated using the Nernst equation for a hydrogen fuel cell as follows [119]:

$$V_{oc} = \frac{-\Delta G}{n_e F} = \frac{-\Delta G^0}{nF} - \frac{RT}{nF} \ln \left( \frac{P_{H_2O}}{P_{H_2} P_{O_2}^{0.5}} \right) \quad (3.15)$$

where  $\Delta G^0$  is the change of Gibbs free energy associated with reactions at the standard pressure (see Chapter 1).

The cell voltage is then calculated as follows [119]:

$$V = V_{oc} - \eta_{ohm} - \eta_{act,a} - \eta_{act,c} - \eta_{c,a} - \eta_{c,c} \quad (3.16)$$

where subscripts  $a$  and  $c$  refer to the anode and cathode, respectively,  $\eta_{ohm}$  is the ohmic polarization,  $\eta_{act}$  is the activation polarization,  $\eta_c$  is the concentration

polarization.

The ohmic polarization,  $\eta_{ohm}$ , occurs due to the resistance of the medium to the flow of the ions in the electrolyte and that of electrons in the electrodes, catalysts and interconnects and calculated by Ohm's law as follows [119]:

$$\eta_{ohm} = R_{ohm}I \quad (3.17)$$

$R_{ohm}$  is given by the following expression [119]:

$$R_{ohm} = \frac{l}{\sigma S} \quad (3.18)$$

where  $l$  is the length and  $S$  is the cross section of the conductor. Since in fuel cell modelling it is more convenient to use the current density "rather than the current, it is a more common practice to use an area resistance form as follows [119]:

$$r_{ohm} = \frac{l}{\sigma} \quad (3.19)$$

The concentration polarization is the voltage loss due to the rate of the mass transport of the gas species to the electrode and as a result due to the concentration difference between the reaction zone and the bulk. The concentration polarizations at the anode and cathode are calculated for example for a fuel cell with hydrogen and oxygen reactants on the anode and cathode, respectively as follows [105]:

$$\eta_{c.a} = \frac{RT}{2F} \ln \left( \frac{P_{H_2}^{TPB} P_{H_2O}^{bulk}}{P_{H_2}^{bulk} P_{H_2O}^{TPB}} \right) \quad (V) \quad (3.20)$$

$$\eta_{c.c} = \frac{RT}{2F} \ln \left( \frac{P_{O_2}^{bulk}}{P_{O_2}^{TPB}} \right) \quad (V) \quad (3.21)$$

where  $P_i^{TPB}$  and  $P_i^{bulk}$  are the partial pressures of the species  $i$  at the TPB and the bulk, respectively, and it is the multiplication of the mole fraction of the species  $i$  by the pressure, namely  $P_i = x_i P$ .

### 3.1.2 Numerical Model

To solve the governing balance equations, which are in the Partial Differential Equations (PDEs) form, numerically, the equations are first converted into a set of algebraic equations and then solutions are performed using either direct or iterative solution techniques. The conversion of the PDEs into algebraic equations can be made using one of the various numerical approaches, e.g. Finite Volume Method (FVM), Finite Element Method (FEM), etc. In the following section, the numerical solver software package, namely COMSOL which is a FE solver and which has been used in this study as a basis to model the solid oxide fuel cell will be introduced.

#### 3.1.2.1 Simulation tool - COMSOL Multiphysics

COMSOL Multiphysics (formerly known as FEMLAB) is a finite element CFD package. COMSOL is built on top of MATLAB, and it is an innovated extension of the multi-physics-coupling between logically distinct domains and models that permits simultaneous solution of the equations in different subdomains. On the other hand, the main disadvantage of COMSOL is its high memory requirements in the computations. It should be noted that the one of the commercial CFD packages, namely FLUENT which has a Finite Volume based Partial Differential

Equations solver has the fuel cell module. However in this study, the main reason for using COMSOL is its integrated modelling environment and the ease to modify the governing equations.

Although direct algorithms such as PARDISO [22] have capabilities to solve large problems in 3D in a fast and stable way, they are computationally more expensive and requires larger memory in comparison to the iterative algorithms. Therefore, in this thesis, an iterative solver, namely Generalized Minimal Residual Algorithm (GMRES) with a preconditioner incomplete Lower Upper (ILU) factorization was used. Lower and Upper (LU) triangular factorization is one of the most popular linear system solvers as it takes the advantage of the ease of inverting triangular matrices. However, LU method cannot take advantage of the sparseness of a matrix because the factors are not as sparse as the original matrix. Incomplete LU factorization of a matrix is a sparse approximation of the LU factorization which are used as the preconditioner [101]. GMRES is a Krylov based iterative method for the solution of linear systems associated to unsymmetric matrices. It has the property of minimizing at every step the norm of the residual vector over a Krylov subspaces [102]. The convergence criteria was set to  $10^{-7}$  for the mass species and velocity components. The interested reader can refer to [22] for the further details of the solver GMRES. The system of equations was solved iteratively. First the Navier Stokes equation, then the mass/species balance were solved. At each stage the solution was stored and used as an initial condition for the subsequent stage. The total computing time for all stages was approximately 12.46 min for the calculation of one value of concentration polarization in Windows XP 64 PC with 6 GB memory.

## **3.2 Neuro-Fuzzy Modelling Concept**

Soft computing includes Fuzzy Logic (FL), Neural Networks (NNs), probabilistic reasoning, and Genetic Algorithms (GAs). Today, techniques, or a combination of techniques, from all these areas are used to design an intelligence system. NNs provide algorithms for learning, classification and optimization, whereas FL deals with issues such as forming impressions and reasoning on a semantic or linguistic level. Probabilistic reasoning deals with uncertainty. Although there are substantial areas of overlap between NNs, FL and probabilistic reasoning, in general they are complementary rather than competitive. Recently, many intelligent systems, called neuro fuzzy systems, have been used. In this chapter, the methodology of a neuro-fuzzy technique, namely an Artificial Neuro Fuzzy Inference System (ANFIS), which has been used in this study will be presented. In order to understand the structure of ANFIS, it is necessary to understand the basic ideas in the design of NNs and FL techniques and in the following section, they will be introduced briefly.

### **3.2.1 Artificial Neural Network (ANN)**

Neural networks are massively parallel processors that have the ability to learn patterns through a training experience. This section will answer the important question of how neural networks are constructed and why they have the capacity to learn patterns.

#### **3.2.1.1 Structure**

Neural networks (NNs) consist of an input layer, one or more hidden layers and an output layer (see Fig. 3.1). Layers are interconnected to each other.

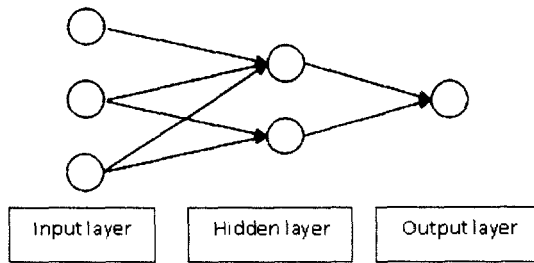


Figure 3.1: Typical structure of a neural network.

The function of an **input layer** is to receive input from the outside world.

The function of the **output layer** is to output the results of the NN predictions to the outside world.

The **hidden layer** links the input layer to the output layer. The role of the hidden layer is to extract and remember useful features and sub-features from the input patterns to predict the outcome of the network.

The training of the NNs is the process of adjusting the weights of connections until the network output matches the target output up to a desired degree of accuracy. Initially a random weight, usually in the range of -1 to +1, is assigned to each connection.

A process known as **back-propagation** accomplishes the adjustment of the weights to minimize the error between the network and the target output. Further, the error gradient is a computed gradient by moving from the output to the input.

Each input signal to a neuron in a layer from the neurons of the previous layer is multiplied by a weight factor and the product summed. The summation of the products is termed NET and can be calculated for each node in the network using the expression:

$$NET_i = \sum_{j=1}^l A_j w_{ji} \quad (3.22)$$

where  $NET_i$  is the net input to node  $i$  from the first sender  $f$  to the last sender  $l$  of the previous layer,  $A_j$  is the output of node  $j$  and  $w_{ji}$  is the weight of the connection between node  $j$  and  $i$ .

After  $NET_i$  is calculated, an activation function  $A_i$ , called the activation, is applied to modify it thereby producing the output signal. There are many functions that might be used as long as they are everywhere differentiable. If the activation function is a linear relationship, then the activation is equal to  $NET_i$ . However, for mapping nonlinear processes, then a nonlinear function is required, see [81].

**Advantages and Limitations of ANN:** A significant advantage of the ANN approach in system modelling is that one need not have a well-defined physical relationship for systematically converting an input to an output. Rather, all that is required for most networks is a collection of representative examples (input-output pairs) of the desired mapping. The ANN then adapts itself to reproduce the desired output when presented with a training sample input [86].

On the other hand, one of the criticisms of ANNs is that they are not able to provide explanations and justifications for their predictions. Another criticism

of ANNs is their lack of ability to extrapolate solutions for problems outside the network training domain. Research on these two areas is in progress [113].

### 3.2.2 Fuzzy Logic

Zadeh [134] introduced the term fuzzy logic and described the mathematics of fuzzy set theory. Fuzzy logic and fuzzy set theory are used to describe human thinking and reasoning in a mathematical framework. Fuzzy rule based modelling is a qualitative modelling scheme where the system behaviour is described using a natural language [109].

#### 3.2.2.1 Structure

**Membership Function (MF):** In fuzzy logic, the truth of any statement is a matter of degree. A fuzzy set  $A$  on a universe of discourse  $U^*$  is characterized by a membership function,  $\mu_A(x)$  that takes values in the interval  $[0,1]$ . A membership function is essentially a curve that defines how each point in the input space is mapped to a membership value (or degree of membership) between 0 and 1 [7].

There are different types of membership functions including triangular, trapezoidal, generalized bell shaped, Gaussian curves, polynomial curves, and sigmoid functions. As an example, triangular curves (see Fig. 3.2) depend on three parameters;  $a$ ,  $b$  and  $c$  [7]. The parameters  $a$ ,  $b$ , and  $c$  are the parameters that are adjusted to fit the desired membership data.

**Fuzzy if-then Rules:** The fuzzy if-then rules or fuzzy conditional statements are expressions of the form IF  $A$  THEN  $B$ , where  $A$  and  $B$  are labels of fuzzy sets characterized by appropriate membership functions. Due to their concise form, fuzzy if-then rules are often employed to capture the imprecise modes of

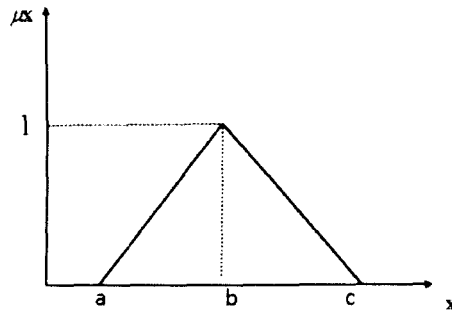


Figure 3.2: Triangular membership function

reasoning that play an essential role in the human ability to make decisions in an environment of uncertainty and imprecision [51].

An example that describes a simple if-then rule is the following:

*If the pressure is high, then the volume is small.*

where pressure and volume are linguistic variables and high and small are linguistic values or labels that are characterized by membership functions.

**Logical Operations:** In fuzzy logic, operators such as AND, OR, and NOT are implemented by intersection, union, and complement operators. There are various ways to define these operators. Commonly, AND, OR, and NOT operators are implemented by the min, max, and complement operators. The details can be found in [7].

**Fuzzy Inference System (FIS):** A fuzzy inference system (FIS) maps inputs to outputs. An FIS consists of four components: the fuzzifier, inference engine,

rule base, and defuzzifier (see Fig. 3.3).

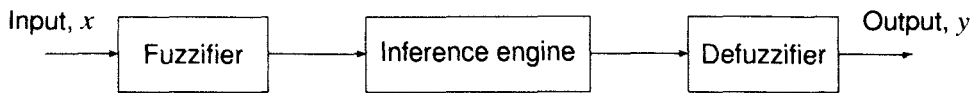


Figure 3.3: Block diagram of a fuzzy inference system.

The **fuzzifier** maps input numbers into corresponding fuzzy membership values.

The **inference engine** defines the mapping from input fuzzy sets to output fuzzy sets. It determines the degree to which the antecedent part is satisfied for each rule. If the antecedent part of the rule has more than one clause, then fuzzy operators are applied to obtain a number that represents the result of the antecedent part for that rule. Outputs of all rules are then aggregated.

The **defuzzifier** maps the output fuzzy sets into a number. Several methods for defuzzification are used in practice, including the centroid, maximum, mean of maxima, height, and modified height defuzzifier. The most popular defuzzification method is the centroid, which calculates and returns the centre of gravity of the aggregated fuzzy set. The commonly used defuzzification method is the centroid method [7].

The **rule base** contains linguistic rules that are provided by experts. Also it is possible to extract rules from the numerical data. Once the rules have been established, the FIS can be viewed as a system that maps an input vector to an output vector. Fuzzy rules are fired in parallel, and this is one of the most

important aspects of an FIS. In an FIS, the order in which rules are fired does not affect the output [7].

### 3.2.2.2 Advantages and Limitations of FL

The main advantage of FL is that one can describe a desired system by simple if-then relationship. In most applications, it decreases the design time of the problem. The main limitation of fuzzy logic is that a *priori* knowledge of the system to be designed is required to construct a relationship between the inputs and outputs with rules. Although in some applications, the knowledge that describes the system can be obtained from data sets, this can be quite difficult and time consuming, especially with large data sets.

### 3.2.3 Artificial Neuro-Fuzzy Inference System (ANFIS)

The ANFIS is an adaptive network based on a Sugeno type fuzzy inference system (FIS) which can simulate and analyze mapping relations between the input and output data through a learning algorithm to optimize the parameters of a given FIS ([52], [53]). It combines the benefits of artificial neural networks (ANNs) and FISs in a single model and yields fast and accurate learning and generalization capabilities with the explanation facilities in the form of semantically meaningful fuzzy rules.

To illustrate the ANFIS architecture, a FIS with two inputs ( $x_1$  and  $x_2$ ) and one output ( $y$ ) is considered where each input is assumed to have two fuzzy sets [123]. The associated first-order Sugeno type fuzzy rules are then as follows:

Rule 1: If ( $x_1$  is  $A_1$ ) and ( $x_2$  is  $B_1$ ) then  $f_{11} = p_{11}x_1 + q_{11}x_2 + r_{11}$

Rule 2: If ( $x_1$  is  $A_1$ ) and ( $x_2$  is  $B_2$ ) then  $f_{12} = p_{12}x_1 + q_{12}x_2 + r_{12}$

Rule 3: If ( $x_1$  is  $A_2$ ) and ( $x_2$  is  $B_1$ ) then  $f_{21} = p_{21}x_1 + q_{21}x_2 + r_{21}$

Rule 4: If ( $x_1$  is  $A_2$ ) and ( $x_2$  is  $B_2$ ) then  $f_{22} = p_{22}x_1 + q_{22}x_2 + r_{22}$

In Sugeno fuzzy rules, the consequent parts of the rules are the linear combination of input signals plus a constant term. These parameters,  $p_{ij}$ ,  $q_{ij}$ , and  $r_{ij}$  are determined during the training stage of ANFIS.

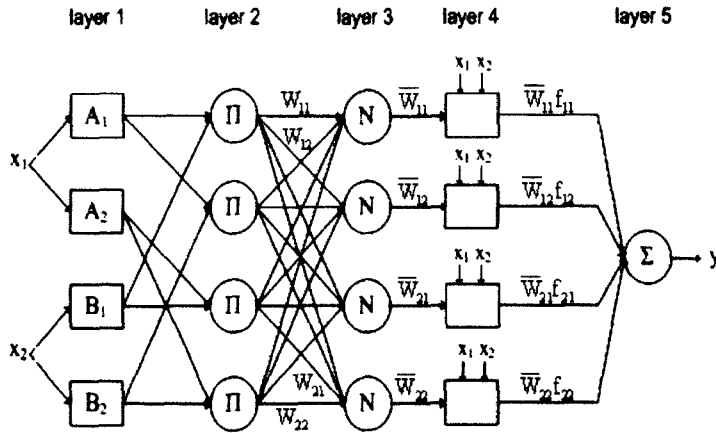


Figure 3.4: A typical ANFIS Architecture.

The ANFIS architecture to implement the FIS is schematically depicted in Fig. 3.4. It has five layers where nodes in each layer have different functionality. A circle indicates a fixed node whereas a square indicates an adaptive node whose parameters are changed during the training process.

Each node in the first layer is adaptive and generates a membership grade for each input variable. The node output in this layer is defined as follows:

$$Q_{A_i}^1 = \mu_A(x_1) \quad i = 1, 2; \quad Q_{B_j}^1 = \mu_B(x_2) \quad j = 1, 2 \quad (3.23)$$

where  $\mu_{A_i}$  (and  $\mu_{B_j}$ ) are fuzzy membership functions defined for linguistic labels  $A_i$  (and  $B_j$ ) for the corresponding input  $x_1$  (and  $x_2$ ). For example, if the bell-shaped membership function is employed,  $\mu_{A_i}(x_1)$  is given by

$$\mu_{A_i}(x_1) = \frac{1}{1 + \left[ \left( \frac{x_1 - c_i}{a_i} \right)^2 \right]^{b_i}} \quad (3.24)$$

where  $a_i, b_i$  and  $c_i$  are the parameters of bell-shaped membership functions which are also optimized during the training stage. Other continuous fuzzy membership functions can also be used to define linguistic labels.

In the second layer, every node is a fixed node in which the node function represents the firing strength of a rule and it is computed as follows:

$$Q_{i,j}^2 = W_{i,j} = \mu_{A_i}(x_1)\mu_{B_j}(x_2), \quad i, j = 1, 2 \quad (3.25)$$

In layer 3, each node is also a fixed node and is the ratio of the rules firing strength to the sum of all rules firing strengths:

$$q_{i,j}^3 = W_{i,j} = \frac{W_{i,j}}{W_{1,1} + W_{1,2} + W_{2,1} + W_{2,2}}, \quad i, j = 1, 2 \quad (3.26)$$

The output of each node in the fourth layer is the product of the normalized firing strength found in the previous step and the first-order polynomial of the rule:

$$Q_{i,j}^4 = W_{i,j}f_{i,j} = W_{i,j}(p_{ij}x_1 + q_{ij}x_2 + r_{ij}), \quad i, j = 1, 2 \quad (3.27)$$

In the fifth layer, a single node computes the overall output as the summation of all signals from layer 4:

$$Q^5 = \sum_{i=1}^2 \sum_{j=1}^2 W_{i,j} f_{i,j}, \quad i, j = 1, 2 \quad (3.28)$$

In the ANFIS architecture, there are two adaptive layers, namely layers 1 and 4. Adjustable parameters in layer 1 describe the shape of the membership functions and are referred to as premise parameters. The adjustable parameters in layer 4, related to the first-order polynomials, are called consequent parameters. The task of ANFIS in learning is to tune the premise and consequent parameters until the desired input-output mapping from the FIS is achieved. This learning task is accomplished by a hybrid algorithm combining the least squares method and the gradient descent method which is explained in the following section [52].

### 3.2.4 Hybrid Learning

The learning algorithm for ANFIS is a hybrid algorithm which is a combination between the gradient descent and least-squares methods. More specifically, in the forward pass of the hybrid learning algorithm, node outputs go forward until layer 4 and the consequent parameters are identified by the least-squares method. In the backward pass, the error signals propagate backwards and the premise parameters are updated by gradient descent. Table 3.1 summarizes the activities in each pass. The consequent parameters are identified as being optimal under the condition that the premise parameters are fixed. Accordingly, the hybrid approach converges much faster since it reduces the search space dimensions of the original pure backpropagation method [49].

Table 3.1: Forward and backward passes in the hybrid learning procedure for ANFIS [52].

	Forward pass	Backward Pass
Premise Parameters	Fixed	Gradient descent
Consequent Parameters	Least square estimate	Fixed
Signals	Node outputs	Error Rates

### 3.2.5 Performance Criteria

In this thesis, the mean absolute percentage error (MAPE) and the root mean square error (RMSE) are used to determine the error between the simulated and the experimental data. They are defined as follows:

$$MAPE = \frac{1}{n} \sum_{i=1}^n \left| \frac{a_i - p_i}{a_i} \right| \times 100 \quad (3.29)$$

$$RMSE = \sqrt{\frac{1}{n} \sum_{i=1}^n (a_i - p_i)^2} \quad (3.30)$$

where  $a_i$  and  $p_i$  are the actual and predicted values, respectively, and  $n$  is the number of training or testing samples. The smaller RMSE and MAPE values imply a better performance. A significance criteria for MAPE is also defined where 10 is regarded as excellent and 10-20 is considered as good [18].

# Chapter 4

## MULTICOMPONENT MASS TRANSFER IN POROUS MEDIA

In this chapter, the physical and mathematical concept of the multicomponent diffusion models developed to predict the flow in porous medium has been presented. This chapter starts with the physical concepts and the mathematical modelling of multicomponent gas diffusion in a porous medium. Then the different multicomponent, namely the FM, SMM, DGM, BFM diffusion models are theoretically evaluated and compared. The limitations and applicability of the models have been presented and the theoretical background and capabilities of the models have been discussed in detail.

### 4.1 Physical Definitions

In this section, the physical terms used in the mass transfer terminology are described briefly.

The **porosity**,  $\epsilon$ , is a macroscopic property of the medium which is the ratio of the volume of the pores to the total volume,

$$\epsilon = \frac{\text{Volume of pores}}{\text{Total volume}} \quad (4.1)$$

The **tortuosity**,  $\tau$ , is the ratio of actual pore length  $L$  to the average pore length,  $L_e$ . Since  $L > L_e$ , then  $\tau > 1.0$ .

**Diffusion** was first defined as the phenomena of the movement of the substance from high to low concentration and this mathematical concept was first known to have been developed by Adolf Fick in 1833 in analogy to Fourier's formulation of heat transfer. It was later realized that this is valid only for binary mixtures or dilute solutions. The movement of the substance in a mixture of more than two species, e.g. the movement of a substance from a low to a high concentration region has been well explained and formulated by Maxwell [77] and Stefan [108] at different times based on the molecular assumption and this has lead to the formula that we know today as the Stefan Maxwell (or Maxwell Stefan) formulation. Binary diffusion coefficient is the diffusion coefficient of a mixture consisting of two species. The diffusion in porous medium is discussed in detail in this chapter.

**Kinetic theory** or **kinetic theory of gases** explains the movement of gases on the molecular scale and it is based on the classical mechanics approach, i.e. the conservation of momentum, energy, etc. Hence, in the development of the kinetic theory of gases, the following hypotheses have been used: (i) molecular hypothesis, which is basically based on the idea that gases are composed of small units, known as molecules, (ii) the interaction of the molecules can be

treated by the classical mechanical theory (in spite of the developments in the quantum mechanics, this approach still remains valid in explaining the mass transport related phenomena), and (iii) the statistical mechanics hypothesis [94].

**Statistical Mechanics:** The kinetic theory of gases is a statistical theory. A statistical theory is required as the gases consist of a large number of molecules and the calculation of the position of each molecule is beyond the computational power. On the other hand we do not seek the information on the history of every molecule, and it is sufficient to know only about the molecular motions to predict the observable, macroscopic properties of the gas, such as pressure and viscosity [94]. For more information on statistical mechanics, please refer to [94] and [117].

**Multicomponent diffusion** is the transport process which occurs when the flux of one component is influenced by the concentration gradient of a second component [25].

**Knudsen (free molecule) flows** occur when the species mean free paths are much greater than the size of the container ( $Kn \gg 1$ ) so that wall collisions dominate over inter-molecular collisions and each gas component behaves independently [132].

**Normal (ordinary) diffusion** is the transfer of mass from one region to another because of a gradient in the concentration [43]. In some cases, the temperature and pressure gradient effects are considered.

**Knudsen number** is the dimensionless number which is the ratio of the path length to the diameter of the capillary tube ( $\lambda/2R$ ), and the gas transport in a porous media depends on the Knudsen number  $Kn$ . In SOFC operating conditions,  $\lambda$  typically lies in the range 0.1-1.0  $\mu m$ , or less, in the anode and catalyst layers [40].

Flow regimes are usually categorized as continuum ( $Kn < 0.1$ ), slip ( $0.1 < Kn < 1$ ), transition ( $1 < Kn < 10$ ) and free molecule ( $Kn > 10$ ). Therefore, in fuel cells, the flow is likely to be in the continuum or slip regimes in the porous support material, and in the slip or transition regimes in the anode and catalyst layers [40].

**Graham's Law:** Thomas Graham has formulated the law that is known as the Graham's law or Graham's law of effusion. According to this law, the rate of effusion of the species in a gas mixture is inversely proportional to the square root of molar mass of the species at a uniform pressure, i.e.  $N_1/N_2 = \sqrt{M_2/M_1}$  [47].

## 4.2 Mathematical Definitions

In this section, both the molar and mass fluxes are used. The conversion from one into another is important and is presented here for the convenience of the reader.

The species mass density,  $\rho_i$ , is related to the mixture mass density,  $\rho_T$ , as follows:

$$\rho_i = w_i \rho_T \quad (4.2)$$

$$\rho_T = \sum_{i=1}^N \rho_i \quad (4.3)$$

where  $\rho_T$  and  $\rho_i$  are the total and component mass density ( $kg/m^3$ ), respectively, while  $w_i$  is the mass fraction of the component  $i$  and  $N$  is the number of components in a mixture. Similarly for the total molar concentration:

$$c_i = x_i c_T \quad (4.4)$$

$$c_T = \sum_{i=1}^N c_i \quad (4.5)$$

where  $c_T$  and  $c_i$  are the total and component molar concentration ( $mol/m^3$ ), respectively, while  $w_i$  is the mass fraction of the component  $i$  and  $N$  is the number of components in a mixture.

In the literature, the total mass flux is defined as the sum of the diffusion flux and the convective flux:

$$\mathbf{n}_i = \mathbf{j}_i + \mathbf{n}_T w_i \quad (4.6)$$

Similarly for the total molar flux:

$$\mathbf{N}_i = \mathbf{J}_i + \mathbf{N}_T x_i \quad (4.7)$$

The species mass and mole fractions of the mixture sum to 1.0, i.e.

$$\sum_{i=1}^N x_i = 1.0 \quad (4.8)$$

$$\sum_{i=1}^N w_i = 1.0 \quad (4.9)$$

### 4.2.1 Special cases

For the equimolar diffusion assumption, where  $N_T = 0$  or  $\sum_{i=1}^N N_i = 0$ , then  $N_i = J_i$  and accordingly  $\sum J_i = 0$ .

### 4.2.2 Conversion from mole into mass fraction

The conversion from mass into mole fraction is calculated as follows:

$$x_i = \frac{\frac{w_i}{M_{w,i}}}{\sum_{k=1}^N \frac{w_k}{M_{w,k}}} \quad (4.10)$$

Similarly the conversion from mole into mass fraction is given as follows:

$$w_i = \frac{x_i M_{w,i}}{\sum_{k=1}^N x_k M_{w,k}} \quad (4.11)$$

### 4.2.3 Conversion from mole fraction gradient into mass fraction gradient

$M_{w,i}$  is the mean molar mass of the system defined as follows:

$$M_w = \sum_{k=1}^N x_k M_{w,k} = \left[ \sum_{k=1}^N w_k / M_{w,k} \right]^{-1} \quad (4.12)$$

After inserting Eqn. (4.12) into Eqn. (4.10) and by taking the derivative of both

sides with respect to special coordinates, and after some mathematical manipulations we obtain:

$$(\nabla x) = [B] (\nabla w) \quad (4.13)$$

where  $B$  is a  $(N - 1) \times (N - 1)$  matrix, with the components:

$$B_{ij} = \frac{M_w}{M_{w,i}} \delta_{ij} - x_i \left[ \frac{M_w}{M_{w,j}} - \frac{M_w}{M_{w,n}} \right] \quad (4.14)$$

where  $\delta$  is the Kronecker delta.

### 4.3 Mass Diffusion Model Approaches

There are different continuum approaches in the chemical engineering literature to predict multicomponent mass transfer in a porous media. The most widely used and applied models are listed as follows:

- i. Fick Model (FM)
- ii. Stefan Maxwell Model (SMM)
- iii. Dusty Gas Model (DGM)
- iv. Binary Friction Model (BFM)

In the following section, each of these models is explained in detail.

#### 4.3.1 Fick Model (FM)

The FM is the simplest approach developed to predict the species diffusion for a single component or dilute mixture where the diffusion of the components do

not have significant effects on the movement of each other. Three-dimensional, steady state multicomponent mass diffusion is given by

$$\mathbf{J}_i = -c_T D_{i,m} \nabla x_i \quad i = 1, \dots, n \quad (\text{mol}/\text{m}^2/\text{s}) \quad (4.15)$$

where  $\mathbf{J}_i$  is the molar diffusion flux of component  $i$  ( $\text{mol}/\text{m}^2/\text{s}$ ),  $x_i$  is the molar fraction of component  $i$ ,  $c_T$  is the total concentration of the gas mixture ( $\text{mol}/\text{m}^3$ ), and  $D_{i,m}$  is the mass diffusion coefficient for the component  $i$  in the mixture ( $\text{m}^2/\text{s}$ ).

The FM has been modified by Wilke [124] by changing the molecular diffusion coefficient,  $D_{i,m}$ , and writing it as a function of the Stefan-Maxwell Model  $D_{ij}$  so that it can be used for the multicomponent type of problem as follows:

$$D_{i,m} = \frac{1 - x_i}{\sum_{j,j \neq i} x_j / D_{ij}} \quad (4.16)$$

It should be noted that the thermal and pressure gradient effects on the diffusion can be added to Eqn. (4.15) if required. The conversion from bulk flow to flow in porous media is achieved simply by introducing the porosity ( $\epsilon$ ) and tortuosity ( $\tau$ ) terms. The  $\epsilon/\tau$  term is usually absorbed into the diffusivity coefficient term as follows:

$$D_{i,m}^e = \frac{\epsilon}{\tau} D_{i,m} \quad (4.17)$$

For the transition region, where both the ordinary and Knudsen diffusions are important, the FM are modified using the Bosanquet equations, i.e. modifying the term  $D_{i,m}^e$  as follows, see [95]:

$$\frac{1}{D_{i,m}^e} = \frac{\tau}{\varepsilon} \left( \frac{1}{D_{ij}} + \frac{1}{D_{i,Kn}} \right) \quad (4.18)$$

where  $D_{i,Kn}$  is the Knudsen diffusion coefficient ( $m^2/s$ ).

As stated in [132], Eqn. (4.18) has no physical basis and "the only evidence to suggest that it might provide accurate interpolation is the good agreement recorded by Pollard and Present with their mean free path theory for the self-diffusion coefficient" [132].

#### 4.3.1.1 Applicability of the FM

The FM can be used to predict the diffusion flux in a non-porous medium for dilute gases and binary mixtures.

#### 4.3.1.2 Limitations of the FM

Binary diffusion coefficients defined by the FM are remarkably independent of concentration [25]. Therefore, Eqn. (4.15) is valid only for dilute gases and cannot be used to model multicomponent diffusion. Originally, the FM is not applicable in the Knudsen diffusion region, i.e. in the regions of comparatively small pore sizes where molecule-wall interactions dominate. When collisions with the wall predominate, the diffusion flux is proportional to the square root of the concentration difference of the diffusing molecules. This square root dependence, which is most common for gases in porous catalysts, is in contrast with the linear relation of the flux and concentration gradient as suggested by Ficks law [25].

### 4.3.2 Stefan Maxwell Model (SMM)

The steady-state, isothermal multicomponent diffusion equation, according to Stefan-Maxwell, is given by [77], [108]:

$$c_T \nabla x_i = \sum_{j=1, j \neq i}^n \left[ \frac{\mathbf{J}_j x_i}{D_{ji}} - \frac{\mathbf{J}_i x_j}{D_{ij}} \right] \text{ for } i = 1, \dots, n \quad (4.19)$$

where  $c_T$  is the total concentration of gas mixture ( $kg/m^3$ ),  $\mathbf{J}_i$  is the molar diffusion flux of component  $i$  ( $mol/m^2/s$ ), and  $D_{ij}$  is the molecular binary diffusion coefficient ( $m^2/s$ ). The full derivation of Eqn (4.19) can be found in many multicomponent transfer books, for example [115], and therefore is not discussed further here. The calculation of the binary and Knudsen diffusion coefficient is discussed in chapter 5.2.2.8.

#### 4.3.2.1 Applicability of the SMM

The SMM can be applied to predict the diffusion flux of the species in a multicomponent mixture in a non-porous medium.

#### 4.3.2.2 Limitations of the SMM

Similar to the FM, originally the SMM did not include both the Knudsen diffusion and the diffusion in the transition region. For these types of problems, modified versions of the SMM equations using the Bosanquet formulation has been used and this is one of the most widely used equations for multicomponent mass transfer problems in the fuel cell literature and this is mainly due to its computational simplicity.

### 4.3.3 Dusty Gas Model (DGM)

The DGM ([29], [30], [81]) visualizes the porous medium as a collection of giant spherical molecules (dust particles) maintained in space by external forces and the movement of the gas molecules in the spaces between the dust particles is described by the kinetic theory of gases.

In the DGM, the diffusion flux is the extension of the Stefan-Maxwell equation with the Knudsen diffusion term. For steady state flow in the transition region in the porous medium, we have the following [81]:

$$c_T \nabla x_i = \sum_{j, j \neq i}^n \frac{\mathbf{J}_j x_i - \mathbf{J}_i x_j}{D_{ij}^e} + \frac{\mathbf{J}_i}{D_{i,Kn}^e} \quad \text{for } i = 1, \dots, n \quad (4.20)$$

where  $D_{i,Kn}^e$  is the effective Knudsen diffusion coefficient, i.e.  $D_{i,Kn}^e = (\epsilon/\tau)D_{i,Kn}$ .

From the kinetic theory, the Knudsen diffusion coefficient,  $D_{i,Kn}$  is given by [81]:

$$D_{i,Kn} = \frac{2}{3} r_0 \sqrt{\frac{8R_g T}{\pi M_{w,i}}} \quad (4.21)$$

where  $R_g$  is the universal gas constant ( $J/mol/K$ ),  $r_0$  is the mean pore radius ( $m$ ),  $M_{w,i}$  is the molar mass ( $kg/mol$ ),  $T$  is the temperature ( $K$ ).

If pressure gradients occur in a porous matrix, additional convective transport is taken into account using the Darcy's law [81]:

$$\mathbf{N}_i^c = \frac{B_o Y_i P}{\mu} \nabla c_T \quad (mol/m^2/s) \quad (4.22)$$

where  $B_o$  is the permeability of the porous medium ( $m^2$ ),  $P$  is the total pressure

of the system ( $Pa$ ), and  $B_o$  for cylindrical pores with radius  $R$  is  $R^2/8$ .

In the DGM, the net flux is calculated by adding the diffusion and the convection fluxes as follows:

$$\mathbf{N}_i = \mathbf{J}_i + \mathbf{N}_i^c \quad (4.23)$$

where  $\mathbf{N}_i$  is the total molar flux of species  $i$  ( $mol/m^2/s$ ),  $\mathbf{J}_i$  is the molar diffusive flux of species  $i$  ( $mol/m^2/s$ ), and  $\mathbf{N}_i^c$  is the molar convective flux of species  $i$  ( $mol/m^2/s$ ).

By combining Eqns. (4.20), (4.22) and (4.23), the general form of the DGM for isothermal flow in porous medium for the transitional region can be written as follows [47]:

$$-c_T \nabla x_i - x_i \nabla c_T \left( 1 + \frac{(B_o P)/\mu}{D_{i,Kn}^e} \right) = \sum_{j, j \neq i}^N \frac{N_j x_i - N_i x_j}{D_{ij}^e} + \frac{N_i}{D_{i,Kn}^e} \text{ for } i = 1, \dots, n \quad \left( \frac{kg}{m^4} \right) \quad (4.24)$$

where  $\mathbf{N}_i$  is the total flux of component  $i$  ( $mol/m^2/s$ ). At a uniform pressure, i.e.  $\nabla P = 0$ , the DGM equation reduces to the well-known and proven Graham's law, i.e.  $\sum_{i=1}^N \mathbf{N}_i \sqrt{M_{w,i}} = 0$ .

In the DGM equations, the addition of the flux terms, namely the diffusion flux and the viscous flux has later been criticized by Kerkhof [61]. He has used the example of the problem of water vapour transport in a capillary tube, namely the Stefan tube problem, in order to show that the additional viscous flux term is

extra in the final equations of the DGM and the viscous flux contribution is already accounted in the DGM equations. Then he reexamined the derivation of the DGM equations starting from Zhdanov type equations and concluded that "...the DGM which include the extra viscous term are incorrect due to derivational errors and double counting of the viscous terms". He then derived a new model, namely the Binary Friction Model (BFM) and this is discussed in section 4.3.4.

#### **4.3.3.1 Applicability of the DGM**

Since the DGM captures the Knudsen diffusion, it can be applied for multicomponent mass transfer problems in porous medium for the transition flow as well as free-molecule (Knudsen) and normal (ordinary, continuum) diffusion flows.

#### **4.3.3.2 Limitations of the DGM**

Recently Kerkhof [61] have highlighted some problems both with the physical model and mathematical development of the DGM. Young et al. [132] agree with Kerkhof's analysis and have rejected the DGM as a suitable foundation on which to construct a viable theory. For a detailed discussion of these problems, the reader is recommended to refer to [61].

#### **4.3.4 Binary Friction Model (BFM)**

The starting point of the BFM is the transport of species in a capillary tube and then averaging the velocities for a porous medium. The first main key difference in the BFM, in contrast to the previous models, namely the DGM and SMM, is that it takes into account the diffusion slip and this might have a significant effect in gas diffusion in porous medium. The second difference is

in the treatment of the porous medium. Although it was not reported previously in his early work ([61], in his later work [62], he followed the work of Epstein [28] and embedded the  $\tau^2/\varepsilon$  term into the whole equation instead of the classical absorption of the  $\varepsilon/\tau$  term into the binary and Knudsen diffusion coefficients.

The BFM equation is given as follows [62]:

$$\nabla P_i = -\frac{\tau^2}{\varepsilon} \left[ \sum_{j=1, j \neq i}^n \frac{RT}{D_{ij}} (x_j \mathbf{N}_i - x_i \mathbf{N}_j) - f_{im}^{BFM} RT \mathbf{N}_i \right] \quad (4.25)$$

$$f_{im}^{BFM} = \left( D_i^K + \frac{K_p}{\kappa_i} \right)^{-1} \quad (4.26)$$

where  $K_p$  is the channel permeability ( $m^2$ ), and  $D_i^K$  is the BFM Knudsen diffusion coefficient ( $m^2/s$ ), i.e.  $D_i^K = 0.89 D_{i,Kn}$ .  $\kappa_i$  is a function of the partial viscosity and the partial pressure and it is calculated as follows [124]:

$$\kappa_i = \frac{\eta_i}{x_i P} = \frac{1}{P} \frac{\eta_i^0}{\sum_{j=1}^n x_j \varepsilon_{ij}} \quad (4.27)$$

where  $P$  is the pressure (Pa),  $x_i$  is the mole fraction of species  $i$ ,  $\varepsilon_{ij}$  is the Wilke parameter,  $\eta_i$  is the dynamic viscosity of species  $i$  ( $kg/m/s$ ), and  $\varepsilon_{ij}$  is calculated as follows [124]:

$$\varepsilon_{ij} = \frac{\left[ 1 + (\eta_i^0/\eta_j^0)^{1/2} (M_{w,j}/M_{w,i})^{1/4} \right]^2}{\left[ 8(1 + M_{w,i}/M_{w,j}) \right]^{1/2}} \quad (4.28)$$

where  $\eta_i^0$  is the pure-component viscosity of the components at the prevailing temperature.

#### 4.3.4.1 Applicability of the BFM

The BFM can be applied to predict the multicomponent diffusion flux of the species in a multicomponent mixture.

## 4.4 Summary

In this chapter, different multicomponent diffusion models, namely the FM, SMM, DGM, BFM are theoretically evaluated and compared. The limitations and applicability of the models have been presented and their theoretical background and capabilities have been discussed in detail. There are a variety of differences between the diffusion models. In summary:

The **FM** is computationally the simplest model. The diffusion coefficient in the FM varies so rapidly with concentration that it cannot be treated as a constant. The rapid variations do not occur in dilute gases [25]. Therefore, the FM is valid only for dilute gases and cannot be used to model multicomponent diffusion. Originally, the FM was not applicable in the Knudsen diffusion region, i.e. in the regions of comparatively small pore sizes where molecule-wall interactions dominate. When collisions with the wall predominate, the diffusion flux is proportional to the square root of the concentration difference of the diffusing molecules. This square root dependence, which is most common for gases in porous catalysts, is in contrast with the linear relation of the flux and concentration gradient as suggested by Ficks law [25]. In the transition region between the ordinary and Knudsen diffusions, the FM are modified using the Bosanquet equations, i.e. modifying the  $D_{i,m}^e$ . As stated in [132], the formulation of the Eqn. (4.18) has no physical basis and "the only evidence to suggest that it might provide accurate

interpolation is the good agreement recorded by Pollard and Present with their mean free path theory for the self-diffusion coefficient"[132].

The **SMM** can be applied to multicomponent diffusion problems. However, similar to the FM, originally the SMM does not take into account both the Knudsen diffusion and the diffusion in the transition region. For these types of problems, modified versions of the SMM equation using the Bosanquet formulation are used and this is one of the most widely used equations for multicomponent mass transfer problems in the fuel cell literature and this is mainly due to its computational ease.

The **DGM** is computationally more demanding than the FM and SMM. Since the DGM captures the Knudsen diffusion, it can be applied for multicomponent mass transfer problems in porous medium for the transition flow as well as free-molecule (Knudsen) and normal (ordinary, continuum) diffusion flows. Recently Kerkhof [61] has highlighted some problems both with the physical model and the mathematical development of the DGM. In the DGM equations, the flux was split into two parts: namely pressure driven and diffusion fluxes. This causes a problem since diffusion fluxes of species do not sum to zero. At uniform pressure, the flux ratio satisfies the Graham's law of diffusion in gaseous mixtures. However, the DGM has problems in its derivation which have been analyzed by Kerkhof [61].

The **BFM** is derived in order to predict the multicomponent diffusion flux in the transition region after defining the erroneous terms in the derivation of the DGM. However, it is computationally more demanding than the DGM. Moreover, the final set of equations do not satisfy the Graham's law of diffusion at zero

pressure gradients.

The BFM takes into account the diffusion slip and this differentiates them from the FM, SMM and DGM. They argue that the diffusion velocity at the wall is not zero for flows where more than one component exists. Hence the effect of the diffusion slip should be taken into consideration. The BFM equations have been first formulated to predict the flow in a capillary tube and the treatment into the porous medium has been done by absorbing the factors  $\epsilon$  and  $\tau$  into the flux equations. In contrast to the previous models, namely the DGM and SMM which absorb the  $\epsilon/\tau$  term into the diffusivities, the BFM has followed the work of Epstein [28], and absorbs the effect of the porosity and tortuosity into the diffusion flux.

If the diffusion models are evaluated in terms of their computational ease, then FM appears to be the simplest model, whereas more computational effort is needed to solve the SMM, DGM and BFM. The closure equation of the SMM is total flux is zero. The DGM satisfies the Graham's law, while BFM does not satisfy neither the Graham's law nor the total zero flux condition.

If the diffusion models are evaluated in terms of the performance in the prediction of the species transport in the porous electrodes for the fuel cells, the models which take into account the effect of the molecule wall collisions are expected to give a better performance. This is because the wall-molecule interactions play an important role in the diffusion processes that occur in the porous electrodes of the fuel cells. The DGM and BFM, and the SMM and the FM modified with the Bosanquet equations, all take into account this phenomenon.

In this thesis, as the species transport in fuel cells are usually a multicomponent problem, only the multicomponent models are investigated. For that reason, the original FM and the modified version of the FM are not considered in this study. On the other hand, in addition to the SMM, the DGM and BFM are investigated as they are two competing theories and as yet, no practical study has been reported that compares and shows the differences in the DGM compared to the BFM and the possible effect of the so called "erroneous term" discussed in the BFM on the predictions in fuel cells.

## **Chapter 5**

# **PERFORMANCE OF DIFFUSION**

## **MODELS - 1D RESULTS**

This chapter discusses the prediction capabilities of the multicomponent diffusion models, namely the SMM, DGM and BFM to predict the multicomponent diffusion in porous anode of SOFCs. The three diffusion models are evaluated in 1D by comparing their capabilities in order to predict the concentration polarization with the experimental data of Yakabe et al. [130]. The concentration polarization is the loss of the cell voltage due to the limitations associated with the diffusion of the reactants to the reaction site, i.e. electrode-electrolyte-reactant triple phase boundary (TPB) and hence it is important to predict it accurately to assess the cell voltage. The effect of the main parameters that affect the diffusion in a porous medium such as the average pore diameter, current density and tortuosity on the concentration polarization predictions of the models is discussed. The model equations are solved for the one-dimensional case for both the uniform and non-uniform pressure terms in the BFM and the DGM.

## 5.1 Definition of the system

The experimental data of Yakabe et al. [130] has been used in this study. They measured the concentration polarization at 0.3, 0.7 and 1.0 A/cm<sup>2</sup> for the H<sub>2</sub>-H<sub>2</sub>O-Ar ternary gas system and the CO-CO<sub>2</sub> binary gas system. Fig. 5.1 is a schematic diagram of the anode supported SOFC system on which the experiments were performed.

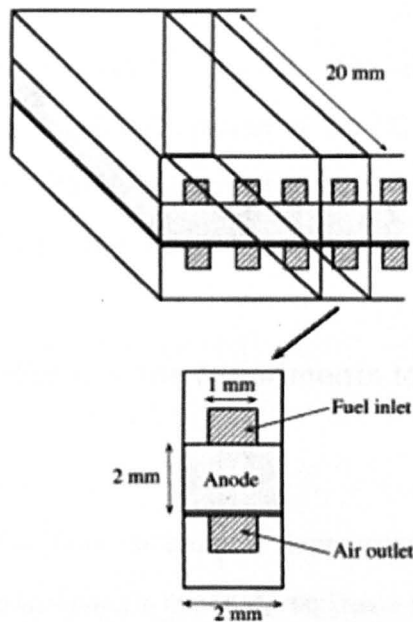


Figure 5.1: Schematic diagram of the one cell stack and the single-unit cell model for the anode-supported SOFC [130].

The SOFC configuration is a planar anode-supported SOFC with a channelled coflowing architecture. In the coflow configuration, the fuel and air is introduced in the same direction from anode and gas channel inlets, respectively. At the anode, a fuel mixture flows from the fuel channel inlet to the outlet, and it is then transported into the pores of the anode, by the combination of both

diffusive and convective flow. The catalyst particles are close to the interface of the anode and electrolyte and form a catalyst layer and within this catalyst layer, the fuel goes under reaction when it is combined with the oxygen ions (oxidizer) coming from the cathode layer. The layer where the fuel, oxidizer and catalyst are combined are referred to as Triple Phase Boundary (TPB), triple being the fuel, catalyst and oxidizer.

In the measurements, the cell operating temperature was maintained at  $750^{\circ}\text{C}$  and  $(\eta_c - \eta_0)$  values were measured at different inlet concentrations of reactants and current densities of the cell. The value of  $\eta_0$  is the concentration overpotential at  $\text{CO}/(\text{CO}+\text{CO}_2)=0.64$  for the  $\text{CO}-\text{CO}_2$  binary system and  $\text{H}_2/(\text{H}_2+\text{H}_2\text{O}+\text{Ar})=0.8$  for the  $\text{H}_2-\text{H}_2\text{O}-\text{Ar}$  ternary system. The measured  $\eta_c$  is the average value over the anode-electrolyte interphase.

### **5.1.1 Simplifications of the experiments to the 1D, 2D and 3D models**

The reduction of the three-dimensional experimental case into the one-dimensional model investigated in this study requires a number of simplifications. In this study, following the work of [130], the 3D system (Fig. 5.1) is simplified into a 1D system (Fig. 5.2), and the model equations are solved for the anode porous medium in the  $z$ -direction in Fig. 5.2. In the 1D model, the anode half cell has been considered in order to investigate the multicomponent mass diffusion in the porous medium because Yakabe et al. [130] conducted the experiments to measure the concentration polarization of the anode. The gas channel has not been taken into account where the main transport mechanism of the species is convection. Therefore the species distribution of the species in the gas channel

has been neglected, hence the experimentally measured values of the inlet  $H_2$  and  $H_2O$  mole fractions at the gas channel inlet have been assumed to be constant over the gas channel and taken as the boundary condition at the inlet of the porous anode. The effect of the species distribution in the gas channel on the mass diffusion mechanism and hence on the concentration polarization will be considered in the 2D and 3D analysis, see Chapter 6. Moreover, it was assumed that diffusion is the dominating flow mechanism in the porous anode and hence the convection term at the anode has been neglected. On the other hand, the current density, which was measured experimentally at the reaction site, was assumed constant over each computational cell since the current density distribution over the cell cannot be modelled using a half cell. This is due to the fact that the current density distribution over the cell is a function of both the anodic and cathodic reaction parameters (see the Butler-Volmer equations in Chapter 3).

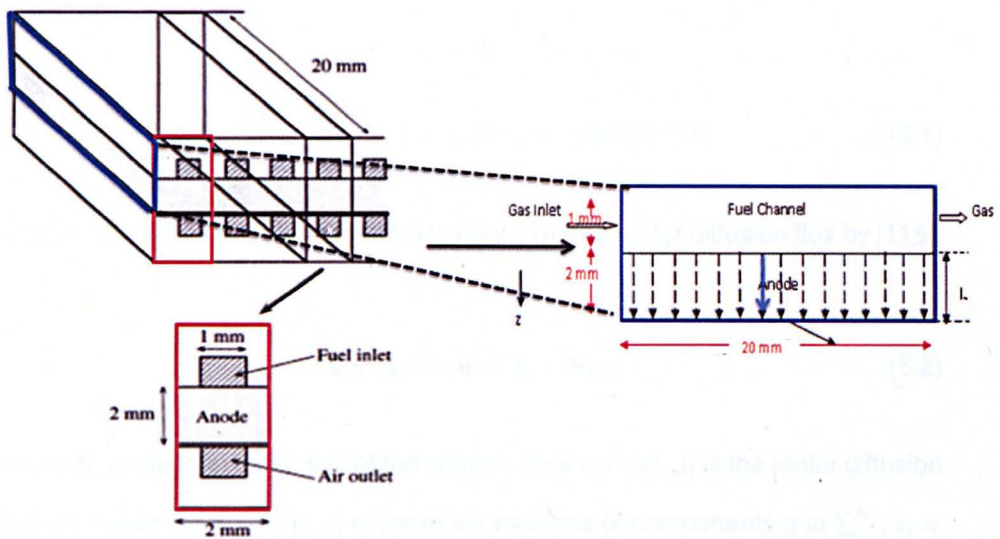


Figure 5.2: Schematic diagram of the 3D SOFC geometry used in the experiment of Yakabe et al. [130] (left) and its simplification to the 1D geometry used in this analysis (right).

In the two-dimensional model, the change of the variables in the direction transverse to the flow has been neglected. The experimental inlet fuel velocity to the fuel gas channel has been set as the inlet velocity boundary condition. The experimentally measured species mass fraction has been set as the boundary at the inlet of the gas channel. The current has been uniformly distributed by assuring the total current conservation in the cell. The species transport in the gas channel has been modelled by coupling the Navier-Stokes equations along with diffusion model equations.

## 5.2 Methodology

### 5.2.1 Conservation Equation

The molar conservation equation of species  $i$  in 1D at the steady state is given by:

$$\frac{\partial \mathbf{N}_i}{\partial z} = 0 \quad \text{for } i = 1, 2, \dots, n \quad [\text{mol}/\text{m}^3/\text{s}] \quad (5.1)$$

where  $\mathbf{N}_i$  is the total molar flux and it is related to the molar diffusion flux by [115]:

$$\mathbf{N}_i = \mathbf{J}_i + c_i \mathbf{u} = \mathbf{J}_i + \mathbf{N}_T x_i \quad (5.2)$$

where  $\mathbf{N}_i$  is the total molar flux of the species ( $\text{mol}/\text{m}^2/\text{s}$ ),  $\mathbf{J}_i$  is the molar diffusion flux of species ( $\text{mol}/\text{m}^2/\text{s}$ ),  $x_i$  is the molar fractions of components and  $\sum_{i=1}^N x_i = 1.0$ ,  $\mathbf{N}_T$  is the sum of the total molar flux of species ( $\text{mol}/\text{m}^2/\text{s}$ ) and  $\sum_{i=1}^N \mathbf{N}_i = \mathbf{N}_T$  and  $c_i$  is the molar density of species  $i$ . Inserting Eqn. (5.2) into Eqn. (5.1) and ignoring the viscous term  $c_i \mathbf{u}$ , we obtain the following:

$$\frac{\partial \mathbf{J}_i}{\partial z} = \frac{\partial \mathbf{N}_i}{\partial z} = 0 \quad (5.3)$$

In the following section, the models to solve for  $\mathbf{N}_i$  are presented and the solutions are discussed in detail.

## 5.2.2 Multicomponent Diffusion Models

### 5.2.2.1 1D SMM equations

The steady-state, isothermal multi-component diffusion equation according to Stefan-Maxwell is given by:

$$\sum_{j=1, j \neq i}^N \frac{\mathbf{N}_i x_j - \mathbf{N}_j x_i}{D_{ij}} = -c_T \frac{dx_i}{dz} \quad i = 1, 2, \dots, n \text{ [mol/m}^4\text{]} \quad (5.4)$$

where  $c_T$  is the total concentration of gas mixture ( $\text{kg/m}^3$ ),  $x_i$  is the molar fractions of components, and  $\mathbf{N}_i$  is the molar flux of species and  $D_{ij}$  is binary diffusion coefficient ( $\text{m}^2/\text{s}$ ).

For ideal gases,  $c_T = P/R_g/T$  where  $R_g$  is the universal gas constant ( $\text{J/mol/K}$ ),  $P$  is pressure ( $\text{Pa}$ ) and  $T$  is temperature ( $\text{K}$ ). A full derivation of Eqn. (5.4) can be found in any multicomponent transfer book, for example Ref. [115], and therefore this aspect is not discussed any further. Since the mole fractions sum to 1.0 (or  $\frac{d(\sum x_i)}{dz} = 0$ ), and the  $n^{\text{th}}$  component gradient is given by [115]:

$$\frac{dx_n}{dz} = -\frac{dx_1}{dz} - \frac{dx_2}{dz} - \dots - \frac{dx_{n-1}}{dz} \quad (5.5)$$

In the SOFC anode, the component fluxes at the catalyst layer are given by:

$$\mathbf{N}_1 = -\frac{\mathbf{i}}{nF}; \mathbf{N}_2 = \frac{\mathbf{i}}{nF} \text{ and } \mathbf{N}_3 = 0 \quad (5.6)$$

where 1, 2 and 3 refer to H<sub>2</sub>, H<sub>2</sub>O and Ar, respectively. Ignoring the viscous term, Eqn. (5.6) suggests that N<sub>i</sub> is constant over the anode domain and therefore the flux of each component written above are the flux at the catalyst layer. For example, for the SMM for the ternary mixture where N<sub>3</sub> = 0, Eqn. (5.4) reduces to:

$$\frac{\mathbf{N}_1 x_2 - \mathbf{N}_2 x_1}{D_{12}} + \frac{\mathbf{N}_1 x_3}{D_{13}} = -c_T \frac{dx_1}{dz} \quad (5.7)$$

$$\frac{\mathbf{N}_2 x_1 - \mathbf{N}_1 x_2}{D_{12}} + \frac{\mathbf{N}_2 x_3}{D_{23}} = -c_T \frac{dx_2}{dz} \quad (5.8)$$

$$-\frac{\mathbf{N}_1 x_3}{D_{13}} - \frac{\mathbf{N}_2 x_3}{D_{23}} = -c_T \frac{dx_3}{dz} \quad (5.9)$$

### 5.2.2.2 1D DGM equations

The 1D DGM equations are given by [47]:

$$\frac{\mathbf{N}_i}{D_{i,Kn}^e} + \sum_{j=1, j \neq i}^N \frac{\mathbf{N}_i x_j - \mathbf{N}_j x_i}{D_{ij}} = -c_T \frac{dx_i}{dz} - \frac{x_i}{RT} \left( 1 + \frac{B_o P}{\eta D_{i,Kn}^e} \frac{dP}{dz} \right) \quad i = 1, 2, \dots, n \quad (5.10)$$

At a uniform pressure where  $dP/dz = 0$ , the second term on the right hand side of Eqn. (5.10) cancels, which reduces the Eqn. (5.10) to Eqn. (5.4) with an additional  $N_i/D_{i,Kn}$  term on the left hand side of the Eqn. (5.10). DGM equations (Eqn. (5.10)) are then solved using the approach described for SMM in section 5.2.2.1. At a non-uniform pressure, we follow the same approach as Zhu and Kee [136]. By summing the Eqn. (5.10) over the  $n$  components, the second term on

the left-hand-side vanishes and the first term on the right hand side of Eqn. (5.10) is equal to zero since  $\frac{d(\sum x_i)}{dz} = 0$  and we obtain:

$$\frac{dP}{dz} = \frac{\sum \frac{N_i}{D_i^e}}{\frac{1}{RT} + \sum \frac{x_i}{RT} \frac{B_0 P}{\eta D_{i,Kn}^e}} \quad (5.11)$$

If Eqn. (5.11) is inserted into Eqn. (5.10), we obtain:

$$\begin{aligned} \frac{N_i}{D_{i,Kn}^e} + \sum_{j=1, j \neq i}^N \frac{N_i x_j - N_j x_i}{D_{ij}} &= -c_T \frac{x_i}{dz} \\ -\frac{x_i}{RT} \left( 1 + \frac{B_0 P}{\eta D_{i,Kn}^e} \right) \frac{\sum \frac{N_i}{D_i^e}}{\frac{1}{RT} + \sum \frac{x_i}{RT} \frac{B_0 P}{\eta D_{i,Kn}^e}} & \end{aligned} \quad (5.12)$$

If Eqn. (5.12) are written for ternary mixtures, the following final equations for each species are obtained:

$$\begin{aligned} \frac{dx_1}{dz} &= -\frac{RT}{P} \left( \frac{N_1}{D_{1,Kn}^e} + \frac{x_2 N_1 - x_1 N_2}{D_{12}^e} + \frac{x_3 N_1 - x_1 N_3}{D_{13}^e} \right) \\ -\frac{x_1}{RT} \left( 1 + \frac{B_0 P}{\eta D_{1,Kn}^e} \right) & \left( \frac{\frac{N_1}{D_{1,Kn}^e} \frac{N_2}{D_{2,Kn}^e} + \frac{N_3}{D_{3,Kn}^e}}{\frac{1}{RT} + \frac{x_1 B_0 P}{RT \eta D_{1,Kn}^e} + \frac{x_2 B_0 P}{RT \eta D_{2,Kn}^e} + \frac{x_3 B_0 P}{RT \eta D_{3,Kn}^e}} \right) \end{aligned} \quad (5.13)$$

$$\begin{aligned} \frac{dx_2}{dz} &= -\frac{RT}{P} \left( \frac{N_2}{D_{2,Kn}^e} + \frac{x_1 N_2 - x_2 N_1}{D_{21}^e} + \frac{x_3 N_2 - x_2 N_3}{D_{23}^e} \right) \\ -\frac{x_2}{RT} \left( 1 + \frac{B_0 P}{\eta D_{2,Kn}^e} \right) & \left( \frac{\frac{N_1}{D_{1,Kn}^e} + \frac{N_2}{D_{2,Kn}^e} + \frac{N_3}{D_{3,Kn}^e}}{\frac{1}{RT} + \frac{x_1 B_0 P}{RT \eta D_{1,Kn}^e} + \frac{x_2 B_0 P}{RT \eta D_{2,Kn}^e} + \frac{x_3 B_0 P}{RT \eta D_{3,Kn}^e}} \right) \end{aligned} \quad (5.14)$$

The solutions for  $x_1$  and  $x_2$  at the TPB is obtained with the given boundary conditions for  $x_1$  and  $x_2$  at the inlet (bulk) and known  $N_1$  and  $N_2$  (Eqn. 5.14). The final component,  $x_3$ , was calculated by using Eqn. (5.13). The solutions were obtained using an in-house code developed in MATLAB.

### 5.2.2.3 1D BFM equations

The final set of BFM equations in 1D is given by [61]:

$$-\frac{dP_i}{dz} = \frac{\tau^2}{\varepsilon} \left[ \sum RT \frac{N_i x_j - N_j x_i}{D_{ij}} + f_{im}^{BFM} RT N_i \right] \quad (5.15)$$

where  $f_{im}^{BFM}$  is the wall friction coefficient of the BFM and defined as follows:

$$f_{im}^{BFM} = \left( D_i^K + \frac{K_p}{\kappa_i} \right)^{-1} \quad (5.16)$$

$$\kappa_i = \frac{\eta_i}{x_i P} = \frac{1}{P} \frac{\eta_i^0}{\sum_{j=1}^n x_j \varepsilon_{ij}} \quad [s] \quad (5.17)$$

$$\eta_i = \frac{x_i \eta_i^0}{\sum_{j=1}^n x_j \varepsilon_{ij}} \quad (5.18)$$

$$\varepsilon_{ij} = \frac{[1 + (\eta_i^0 / \eta_j^0)^{1/2} (M_{w,j} / M_{w,i})^{1/4}]^2}{[8(1 + (M_{w,i} / M_{w,j}))^{1/2}]^{1/2}} \quad (5.19)$$

where  $K_p$  is the intrinsic permeability ( $m^2$ ),  $\kappa_i$  is the coefficient as a function of the partial viscosity and partial pressure ( $s$ ),  $D_i^K = 0.89 D_{i,Kn}$ , where  $D_{i,Kn}$  is the Knudsen diffusion coefficient.  $\eta_i^0$  is the pure-component viscosities of the components at the prevailing temperature.

It should be noted that the tortuosity and porosity terms in Eqn. (5.15) are introduced to define the flux in porous medium following the approach of Epstein [28]. This states that instead of multiplying the binary diffusion coefficient by  $\varepsilon/\tau$ , as in the SMM and DGM, the flux,  $\mathbf{N}$  is multiplied by  $\tau^2/\varepsilon$  to obtain the effective flux in porous medium. In fact, at uniform pressure, for the BFM, this means the multiplication of the binary diffusion coefficient with  $\varepsilon/\tau^2$  and hence  $\tau$  in the DGM and SMM corresponds to  $\tau^2$  in the BFM. For further details, see [28].

By definition, partial pressure of species  $i$ ,  $P_i$  is the multiplication of the species mole fraction and pressure, i.e.  $P_i = Px_i$ . By inserting this into the Eqn. (5.15), we obtain the following:

$$-x_i \frac{dP}{dz} - P \frac{dx_i}{dz} = \frac{\tau^2}{\varepsilon} \left[ \sum_{j=1}^N RT \frac{N_i x_j - N_j x_i}{D_{ij}} + f_{im}^{BFM} RT N_i \right] \quad (5.20)$$

When Eqn. (5.20) is added over each species  $i$ , the SMM term (first term on the right hand side of Eqn. (5.20)) cancel out and we obtain the following:

$$-\frac{dP}{dz} = \frac{\tau^2}{\varepsilon} \left[ \sum_{j=1}^N f_{im}^{BFM} RT N_i \right] \quad (5.21)$$

If Eqn. (5.21) is inserted into Eqn. (5.20), we obtain:

$$\frac{dx_i}{dz} = -\frac{1}{P} \left[ \frac{\tau^2}{\varepsilon} \left[ \sum_{j=1}^N RT \frac{N_i x_j - N_j x_i}{D_{ij}} + f_{im}^{BFM} RT N_i \right] + x_i \frac{dP}{dz} \right] \quad (5.22)$$

The solution procedure for the BFM at both uniform and the non-uniform pressure is the same as that described in the preceding section for the DGM.

#### 5.2.2.4 Calculation of the concentration polarization

The calculation of the concentration polarization is given here for the reader's convenience. After calculation of the mole concentrations of the species at the TPB using any of the models described above, the concentration polarization is calculated for example for the H<sub>2</sub>-H<sub>2</sub>O-Ar mixture [105]:

$$\eta_c = \frac{RT}{2F} \ln \left( \frac{P_{H_2}^{TPB} P_{H_2O}^{bulk}}{P_{H_2}^{bulk} P_{H_2O}^{TPB}} \right) \quad (5.23)$$

where  $P_i^{TPB}$  and  $P_i^{bulk}$  are the partial pressures of the species  $i$  at the TPB and the bulk, respectively, and it is the multiplication of the mole fraction of the species  $i$  by the pressure;  $P_i = x_i P$ .

### 5.2.2.5 Model Assumptions

The assumptions of the model are consistent with those of Suwanwarangkul et al. [110], except that in this investigation both the uniform and non-uniform model equations are used. These assumptions are listed as follows:

- Ideal gas assumption which is accurate at low pressures and high temperatures when the density is low.
- Isothermal system.
- Reaction kinetics are not rate limiting.
- Species concentrations were assumed constant along the gas channel and hence only a 1D model in the  $z$  direction of the porous anode was considered. This assumption is valid as the channel length, which is 20 mm, is very small (see also [110]).
- Steady state analysis.
- The electrochemical reactions are assumed to take place only at the anode-electrolyte interface. This assumption is valid as the electrochemical reactions occurs in the vicinity of the electrolyte-anode interface which is around 50  $\mu m$  in depth [74] and this is very small compared to the 2 mm anode thickness in the experiments.

### 5.2.2.6 Boundary conditions

In order to solve the Eqn. (5.5) along with the equation of each diffusion model (Eqns. (5.4), (5.10) and (5.15)), the appropriate boundary conditions should be supplied. Fig. (5.3) shows the domain of the 1D model investigated in this chapter. At the inlet to the porous anode (at  $z = 0$ ), the mole fractions of the species, e.g.  $x_{H_2}$ ,  $x_{H_2O}$  and  $x_{Ar}$  for the  $H_2$ - $H_2O$ - $Ar$  system are specified. At the anode-electrolyte interface ( $z = l$  in Fig. 5.3), the amount of flux is the function of the current density produced [110], i.e. for  $H_2$ - $H_2O$ - $Ar$  system,  $N_{H_2} = -i/nF$ ,  $N_{H_2O} = i/nF$  and  $N_{Ar} = 0$ . The boundary conditions for the  $H_2$ - $H_2O$ - $Ar$  system can be summarized as follows:

$$\text{At } z = 0, x_{H_2} = x_{H_2,in}, x_{H_2O} = x_{H_2O,in}, x_{Ar} = x_{Ar,in} \quad (5.24)$$

$$\text{At } z = L: N_{H_2} = -i/nF, N_{H_2O} = +i/nF, N_{Ar} = 0 \quad (5.25)$$

For the  $CO$ - $CO_2$  system, the boundary conditions are as follows:

$$\text{At } z = 0, x_{CO} = x_{CO,in}, x_{CO_2} = x_{CO_2,in}, \quad (5.26)$$

$$\text{At } z = L: N_{CO} = -i/nF, N_{CO_2} = +i/nF \quad (5.27)$$

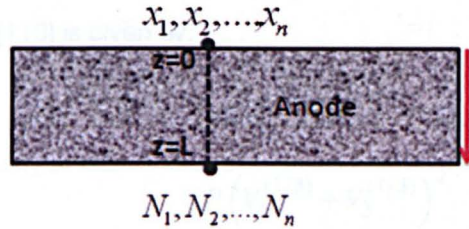


Figure 5.3: Schematic diagram of the 1D model domain.

Table 5.1: Model parameters [130].

Parameter	Value	Unit
Temperature	1023	$^{\circ}C$
Pressure	105	$Pa$
Universal Gas constant	8.314	$J/mol/K$
Average pore radius	$2.6 \times 10^{-6}$	$m$
Porosity	0.46	-
Anode thickness	$2 \times 10^{-3}$	$m$
Anode Permeability	$1.7 \times 10^{-10}$	$m^2/Pa/s$

### 5.2.2.7 Model Parameters

The model parameters are those as used in the experimental work of Yakabe et al. [130] and are given in Table 5.1. The tortuosity was initially set to be 4.5 as this was the value used in the previous studies, see [110], [118]. The effect of this parameter on the prediction of the concentration polarization is discussed in the subsequent sections. The estimation of the diffusion coefficients, pure component and mixture viscosity and permeability are discussed in the following section.

### 5.2.2.8 Estimation of the Governing Parameters

**Binary diffusion coefficient:** The binary diffusion coefficient according to the Fuller et al. theory [115] is given by:

$$D_{12} = CT^{1.75} \frac{\sqrt{(M_{w,1} + M_{w,2})/M_{w,1}M_{w,2}}}{P \left( V_1^{(1/3)} + V_2^{(1/3)} \right)^2} \quad (5.28)$$

where  $D_{12}$  is the binary diffusion coefficient ( $m^2/s$ ),  $C$  is a constant ( $=1.03 \times 10^{-2}$ ),  $T$  is the temperature ( $K$ ),  $P$  is the pressure ( $Pa$ ),  $M_{w,i}$  is the molar weight ( $g/mol$ ),

and  $V_i$  is the molecular diffusion volume of species  $i$ . The value of  $V_i$  is obtained from [115], Table 4.1.

The effective diffusion coefficient in the SMM and DGM is calculated by introducing the porosity ( $\epsilon$ ) and tortuosity ( $\tau$ ) terms as follows:

$$D_{ij}^e = \frac{\epsilon}{\tau} D_{ij} \quad (5.29)$$

**Knudsen Diffusion Coefficient:** From the kinetic theory of gases, the Knudsen diffusion coefficient,  $D_{i,Kn}$ , is given by [95]:

$$D_{i,Kn} = \frac{2}{3} r_o \sqrt{\frac{8R_g T}{\pi M_{w,i}}} \quad (5.30)$$

where  $D_{Kn,i}$  is the Knudsen diffusion coefficient ( $m^2/s$ ),  $r_o$  is the mean pore radius ( $m$ ), and  $M_{w,i}$  is the molar weight ( $kg/mol$ ). The Knudsen diffusion coefficient of each species calculated using Eqn. (5.30) for the given temperature, pore diameter and molecular weight are  $D_{H_2,Kn} = 0.0057$ ,  $D_{H_2O,Kn} = 0.0019$ , and  $D_{Ar,Kn} = 0.0013 \text{ m}^2/s$ .

**Permeability ( $K_i$ ) of anode:** The permeability of the anode was measured in Yakabe et al. [130] and it is given by  $1.7 \times 10^{-10} \text{ m}^2/Pa/s$ . In [130], it is stated that this value was measured using  $N_2$  gas at room temperature. To calculate the intrinsic permeability with units of  $m^2$ , the measured value must be calculated using the pure component viscosity of  $N_2$ . From the Chapman-Enskog equations,  $\eta_{N_2}$  is  $1.7393 \times 10^{-5}$  at 293 K. Hence  $B_0 = 1.7 \times 10^{-10} \times 1.7393 \times 10^{-5} = 2.96 \times 10^{-15} \text{ m}^2$ .

**Pure component viscosity and mixture viscosity:** For the calculation of the pure component viscosity,  $\eta_0$ , the first-order Chapman-Enskog theory is used in this thesis and the viscosity can be written as follows [95]:

$$\eta_i^0 = \frac{26.69(M_i T)^{1/2}}{\sigma^2 \omega_v} \quad (5.31)$$

where  $\eta_i^0$  is the pure component viscosity of component  $i$  ( $\mu P$ ),  $M_{w_i}$  is the molar weight of component  $i$  ( $g/mol$ ),  $T$  is the temperature ( $K$ ),  $\sigma$  is the hard sphere diameter ( $A^0$ ) and  $\omega_v$  is the temperature dependent collision integral.

To use the relation (5.31) to estimate the viscosities, the collision diameter  $\sigma$  and the collision integral  $\omega_v$  must be determined. Neufeld et al. [87] proposed an empirical equation which is convenient for computer application [95]:

$$\omega_v = |A(T^*)^{-B}| + C|\exp(-DT^*)| + E|\exp(-FT^*)| \quad (5.32)$$

where  $T^* = kT/\epsilon$ ,  $A=1.16145$ ,  $B=0.14874$ ,  $C=0.52487$ ,  $D=0.77320$ ,  $E=2.16178$  and  $F=2.43787$ .

The calculated viscosities of the components at the corresponding temperatures are presented in Table 5.2. Then the mixture viscosity was calculated using the Wilke formula [95]:

$$\eta_i = \frac{x_i \eta_i^0}{\sum_{j=1}^n x_j \epsilon_{ij}} \quad (5.33)$$

Table 5.2: Calculated viscosities of different gas components at different temperatures.

Substance	T (K)	Calculated (Pa.s)
CO	1023	$4.7630 \times 10^{-5}$
CO <sub>2</sub>	1023	$3.9761 \times 10^{-5}$
Ar	1023	$5.2899 \times 10^{-5}$
H <sub>2</sub>	1023	$1.9846 \times 10^{-5}$
H <sub>2</sub> O	1023	$3.6614 \times 10^{-5}$
N <sub>2</sub>	293	$1.7393 \times 10^{-5}$

$$\varepsilon_{ij} = \frac{\left[1 + (\eta_i^0/\eta_j^0)^{1/2}(M_{w,j}/M_{w,i})^{1/4}\right]^2}{\left[8(1 + M_{w,i}/M_{w,j})\right]^{1/2}} \quad (5.34)$$

where  $\eta_i^0$  is the pure-component viscosities of the components at the prevailing temperature.

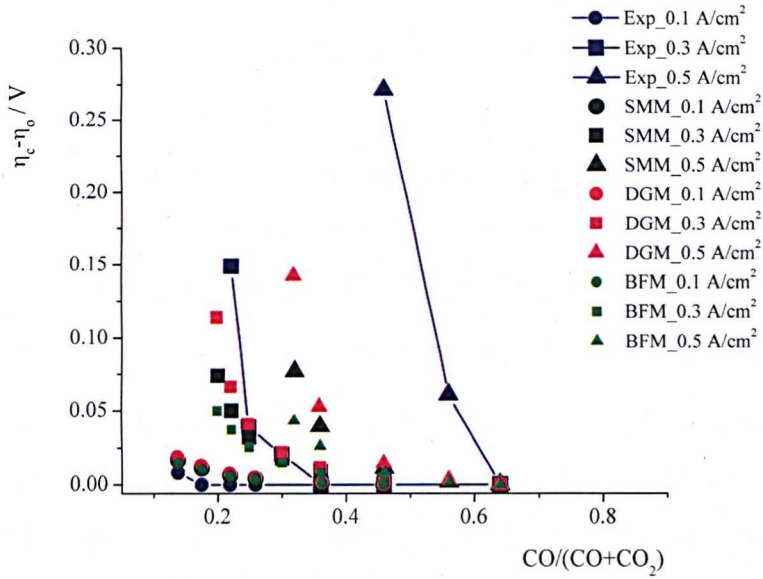
## 5.3 Results and Discussion

### 5.3.1 Results at Uniform Pressure

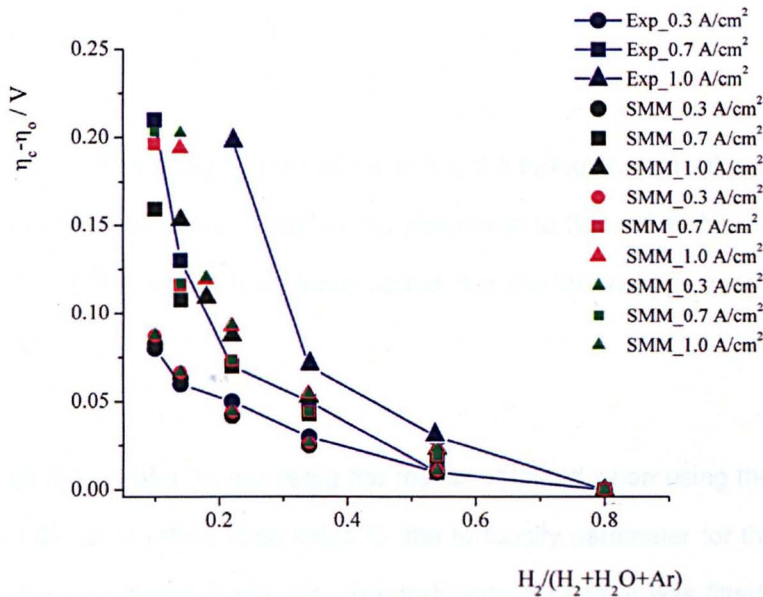
In Figures 5.4 (a) and (b), the predictions of the DGM, SMM and BFM are presented for the CO-CO<sub>2</sub> and H<sub>2</sub>+H<sub>2</sub>O+Ar systems, respectively.  $\eta_0$  is the concentration polarization where H<sub>2</sub>/(H<sub>2</sub>+H<sub>2</sub>O+Ar)=0.8 and CO/(CO+CO<sub>2</sub>)=0.64. As expected, a decrease in the concentration leads to an increase in the concentration polarization at all current densities due to the reactant concentration deficiencies at the TPB sites where the reactions take place. On the other hand, as the current densities increase, the concentration polarization increases proportionally. Again this is the result of the high reactant consumption at the reaction site associated with the high current density withdrawal. In general, it is

observed that the concentration polarization of the CO-CO<sub>2</sub> is higher than that of H<sub>2</sub>-H<sub>2</sub>O-Ar. This is due to the higher binary diffusion coefficient of CO-CO<sub>2</sub>. Therefore the limiting current density of the cell using CO-CO<sub>2</sub> is much smaller than that of the H<sub>2</sub>-H<sub>2</sub>O-Ar system. The tortuosity was kept constant at a value of 4.5 for all the cases considered. It should be noted that the tortuosity factor ( $\tau^2$ ) for the BFM corresponds to the tortuosity ( $\tau$ ) of the DGM and SMM. What is observed in the results is that for the CO-CO<sub>2</sub> system, in all the three models, the DGM predictions are best while the SMM is the worst, especially at high current densities and low reactant concentrations. For the H<sub>2</sub>-H<sub>2</sub>O-Ar system, the DGM and BFM results are quite similar, while their predictions are slightly better than the SMM prediction for the experimental data when the same tortuosity parameter (4.5) is used for all the models. These results are different from those presented by Suwanwarangkul et al. [110], especially for the ternary mixtures (see Fig. 3 in [110]). This is most probably due to the fact that the mole fraction of Ar is assumed constant over the anode. On the other hand, the results are comparatively more similar with the 1D solution of Tseronis et al. [118]. The slight differences may be due to the numerical solver as well as the differences in the permeability and the viscosity parameters used. In this thesis, the mixture viscosity was calculated using the Wilke formula and this value is dependent on the species mole fractions. The permeability of the medium was given in the experimental data of Yakabe et al. [130].

At the current density 0.1 A/cm<sup>2</sup>, the SMM, DGM and BFM fit the experimental data quite well. As the current density increases to 0.3 A/cm<sup>2</sup>, the DGM produces a better prediction than does the SMM and BFM. At 0.5 A/cm<sup>2</sup>, all the models fail to give an accurate prediction in 1D with the same or the fitted tortuosity values, since at high current densities, the reactant concentration



(a)



(b)

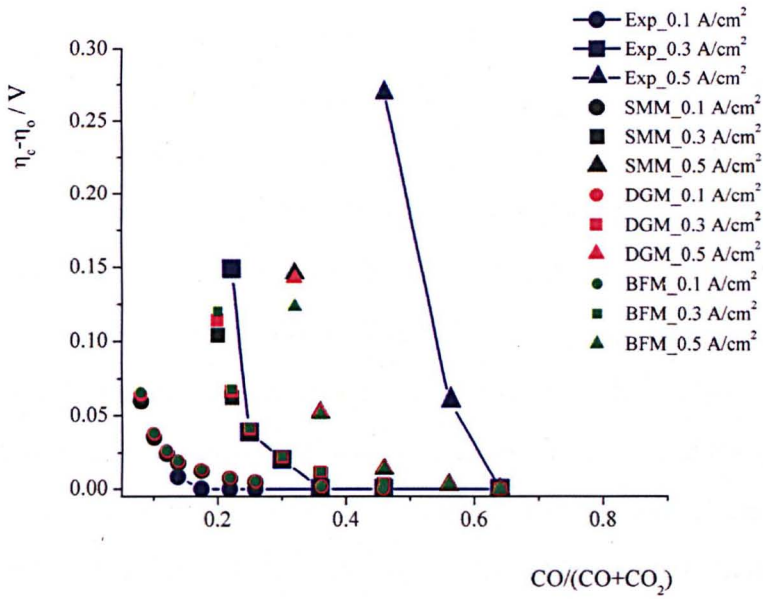
Figure 5.4: DGM, SMM and BFM predictions for (a) CO-CO<sub>2</sub> system at 0.1, 0.3 and 0.5  $A/cm^2$ , and (b) H<sub>2</sub>/(H<sub>2</sub>+H<sub>2</sub>O+Ar) system at 0.3, 0.7 and 1.0  $A/cm^2$ , and comparison with the experimental data ( $\tau$  is 4.5 in DGM and SMM, and  $\tau^2$  is 4.5 in the BFM).

along the anode length might also be significant due to the high consumption of the reactants. In general, between these three models, DGM gives a better prediction than does SMM and BFM at all the current densities for the set of parameters used in this particular system. On the other hand, at  $\tau$  is 4.5, BFM gives the worst prediction of all three models for the CO-CO<sub>2</sub> system. The BFM and DGM results are similar for the H<sub>2</sub>-H<sub>2</sub>O-Ar system.

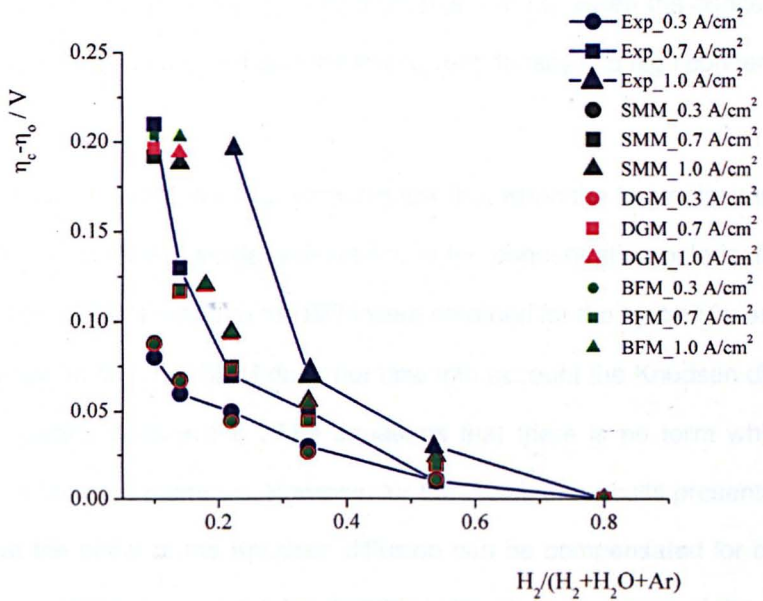
The difference between the BFM and DGM results is in the wall friction coefficient term,  $f_{im}^{BFM}$  in the BFM. This term, which is given by  $f_{im}^{BFM} = (0.89D_i^K + K_p/\kappa_i)^{-1}$ , corresponds to  $(D_i^{Kn})^{-1}$  in the DGM. The calculations in this study show that  $K_p/\kappa_i$  are relatively smaller compared to the values of  $0.89D_i^K$ . Hence the only difference between the BFM and DGM predictions is in the  $0.89D_i^K$  term.

The solutions have been obtained by setting the tortuosity to a value of 4.5 in all the models. The history of setting this parameter to that value dates back to Yakabe et al. [130], where it is clearly stated that the tortuosity is used as a fit parameter.

Figures 5.5 (a) and (b) represent the results obtained when using the SMM, DGM and the BFM with a fitted value for the tortuosity parameter for the same case as that considered in Fig. 5.4. The tortuosity parameter was fitted by trial and error for all the three models. By the fitted tortuosity parameter it is meant that the value of  $\tau$  in the DGM and SMM and  $\tau^2$  in the BFM equations. The fitted values for the models are shown in Table 5.3. It is noted that the fitted tortuosity parameter for the BFM is higher than that for the SMM and DGM and this is mainly due to the effect of the multiplier 0.89.



(a)



(b)

Figure 5.5: The DGM, SMM and BFM predictions for (a) CO-CO<sub>2</sub> system at 0.1, 0.3 and 0.5 A/cm<sup>2</sup> and (b) H<sub>2</sub>-H<sub>2</sub>O-Ar system at 0.3, 0.7 and 1.0 A/cm<sup>2</sup>, and comparison with the experimental data with fitted tortuosity values for each model.

It is observed in Figures 5.5 (a) and (b) that all the model curves are shifted to the right when the tortuosity increases. This means that the concentration polarization increases as the tortuosity increases at all current density values. This is due to the fact that an increase in the tortuosity obstructs the passage of the gas molecules, which results in a decrease in the concentration of the gas molecules at the TPB where the reactions take place. As a result, the concentration polarization increases and this leads to a decrease in the operational voltage. Similarly, when the tortuosity decreases, the concentration polarization decreases and the curves are shifted to the left. Also it can be seen in the Figs. 5.5 (a) and (b) that at high current densities and low concentrations, the same increase in tortuosity leads to a larger shift of the curves compared to low current densities and high concentration regions. This shows that the effect of the change in tortuosity is more severe, especially when the current density is high and the concentration is low, i.e. when the concentration polarization is high compared with the low current density and high concentration.

The results presented in this section show that when the tortuosity parameter is fitted for each model, similar predictions of the concentration polarization prediction of the SMM, DGM and the BFM were obtained for the system investigated in this study. In fact, the SMM does not take into account the Knudsen diffusion, and it is clearly seen in the SMM equations that there is no term which is a function of the pore diameter. However, for the SMM, the results presented here show that the effect of the Knudsen diffusion can be compensated for by fitting the tortuosity factor. It is postulated that this is the main weakness of the study of Suwanwarangkul et al. [110] and Tseronis et al. [118], where a single tortuosity factor is used for each model and comparisons have been performed accordingly.

Table 5.3: Tortuosity fitted values for the SMM, DGM and the BFM for CO-CO<sub>2</sub> and H<sub>2</sub>-H<sub>2</sub>O-Ar systems.

System	SMM	DGM	BFM
CO-CO <sub>2</sub>	4.79	4.5	5.49
H <sub>2</sub> -H <sub>2</sub> O-Ar	5.0	4.5	5.29

It must be noted that according to my opinion, the reason for the poor results at high current density is that solutions were solved in only one dimension. The solution in 2D or 3D is expected to predict even more accurate results at the high current densities where the reactant concentration varies not only along the anode thickness but also along the anode length due to the high consumption of the reactants.

As has been discussed previously in Suwanwarangkul et al. [110], the pore diameter and current density are two important factors and as the current density increases and the pore radius decreases, concentration polarization becomes dominant as the passage of the gases to the active reaction sites, i.e. TPB becomes more difficult. In fact, when the pore diameter is reduced, the Knudsen diffusion term becomes more dominant. Therefore, to investigate the extent of the validation of the results, we now extend the boundaries of the current density and the pore diameter to decide whether the model predictions are similar for a wide range of current densities and pore radii. The pore radius was decreased from 2.6, to 1.6, and then to 0.26  $\mu\text{m}$  with the range of current density being chosen to be 0.05, 1, and 1.5 A/cm<sup>2</sup>.

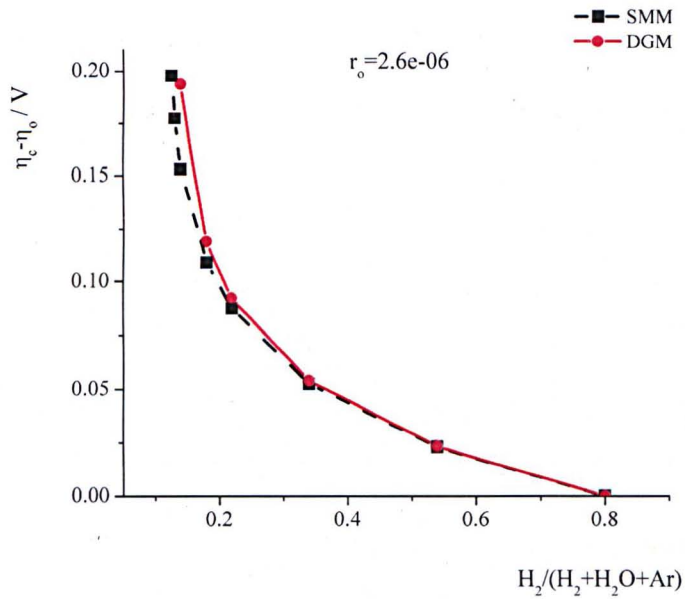
### 5.3.2 Effect of Pore Radius

The pore radius is one of the most important parameters that affects the diffusion in fuel cells. Physically, as pore diameter decreases, the diffusion path of the molecules to the reaction site increases, as a result it takes longer time for molecules to diffuse and the difference in the concentration of the reactant and product species at the inlet and reaction site increases and this result in an increase in the concentration polarization. Theoretically, this term is accounted for in the calculation of the Knudsen diffusion coefficient in the DGM and the BFM. In contrast, there is no term in the SMM that considers the effect of the pore radius, which means the change of the pore radius does not affect the results obtained when using the SMM.

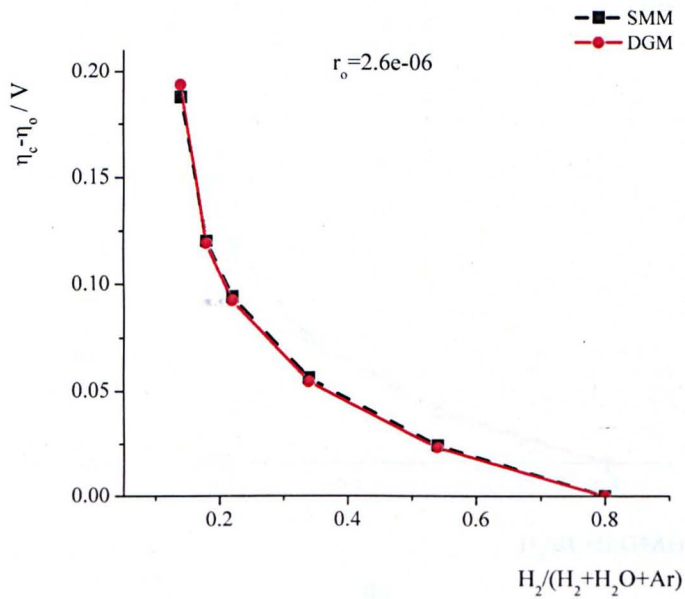
In this section, for convenience in the presentation of the results, first the DGM is compared with that of the SMM with the experimental data with different pore sizes and then the BFM and DGM comparison is presented.

#### 5.3.2.1 The SMM vs DGM

In Fig. 5.6, 5.7 and 5.8 the concentration polarization results obtained using the SMM and DGM for the  $H_2/(H_2+H_2O+Ar)$  system at  $1 A/cm^2$  are presented for (a) the initial tortuosity parameter of 4.5, and (b) the optimized tortuosity parameter, for the average pore radius decreases from 2.6 to 1.6 and  $0.26 \mu m$ , respectively. The highest current density used in the experiment is  $1 A/cm^2$ , and this value was selected and maintained for all the cases investigated during this analysis in order to perform the analysis in the most extreme situation. In fact when the pore diameter was decreased further to  $0.026 \mu m$ , we observed that the concentration polarization goes to infinity as there is no  $H_2$  at the reaction TPB site.

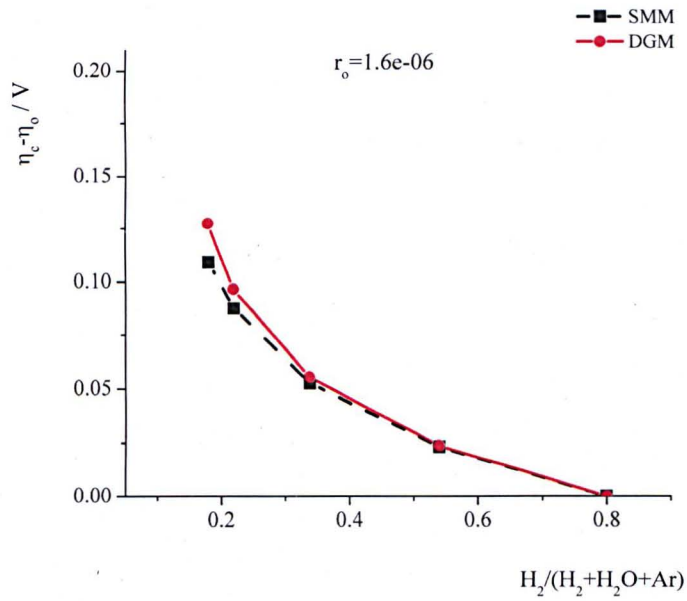


(a)

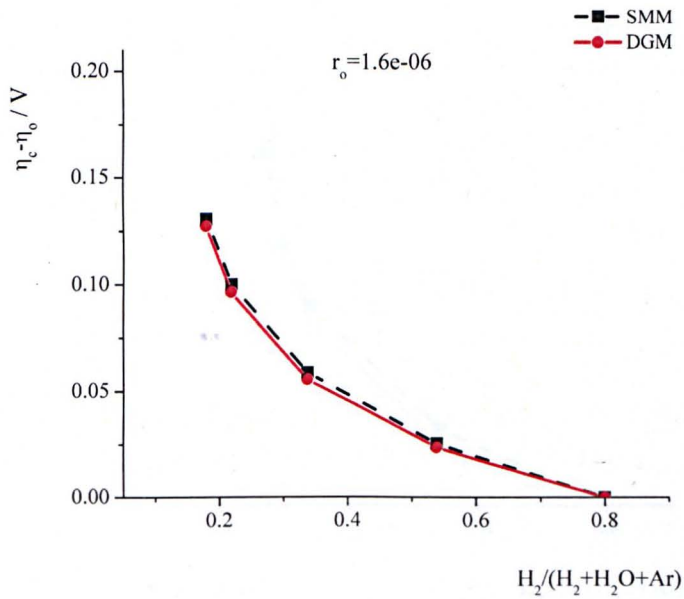


(b)

Figure 5.6: The  $(\eta_c - \eta_o)$  predictions of the SMM and the DGM for the  $H_2/(H_2+H_2O+Ar)$  system at  $1 \text{ A/cm}^2$ ; (a) for pore diameter  $2.6 \mu\text{m}$ , respectively, and  $\tau = 4.5$  and (b) same system for the optimized tortuosity parameters which are 5.0, 5.4 for the SMM and DGM, respectively.

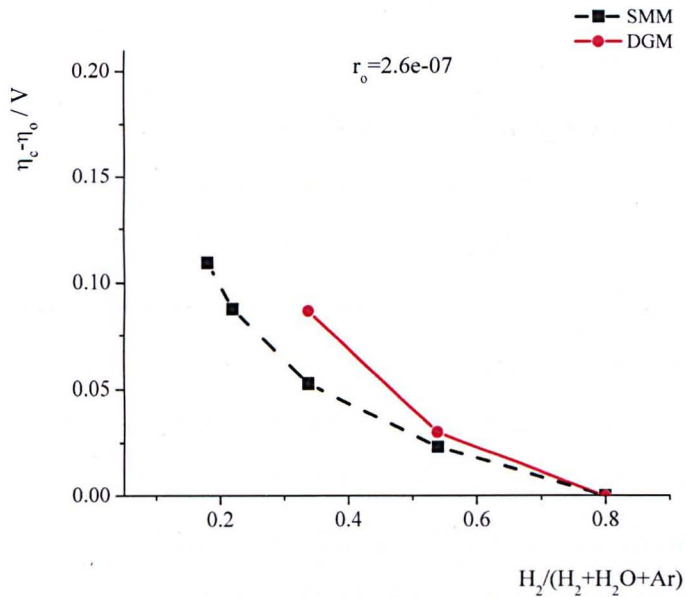


(a)

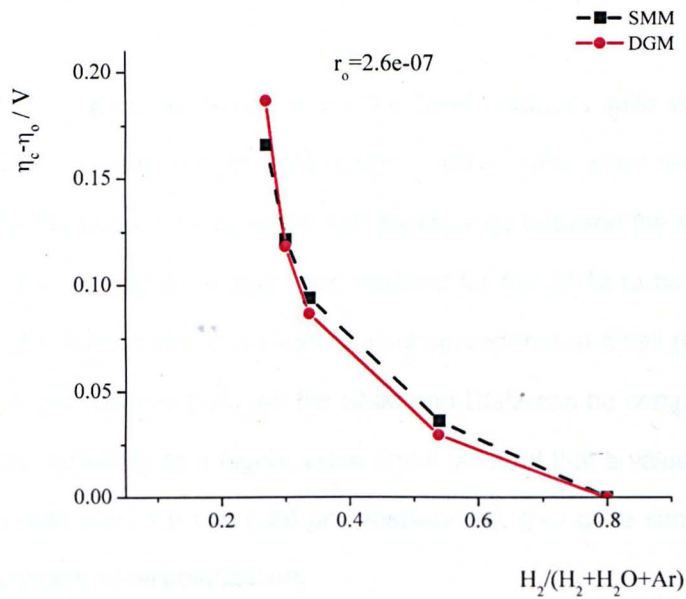


(b)

Figure 5.7: The  $(\eta_c - \eta_o)$  predictions of the SMM and the DGM for the  $H_2 / (H_2 + H_2O + Ar)$  system at  $1 A/cm^2$ ; (a) for pore diameter  $1.6 \mu m$ , respectively, and  $\tau = 4.5$  and (b) same system for the optimized tortuosity parameters which are 5.0, 5.4 for the SMM and DGM, respectively.



(a)



(b)

Figure 5.8: The  $(\eta_c - \eta_o)$  predictions of the SMM and the DGM for the  $H_2 / (H_2 + H_2O + Ar)$  system at  $1 A/cm^2$ ; (a) for pore diameter  $0.26 \mu m$ , respectively, and  $\tau = 4.5$  and (b) same system for the optimized tortuosity parameters which are 5.0, 5.4 for the SMM and DGM, respectively.

It is observed that as the pore size decreases, the difference between the results obtained using the SMM and DGM increases, a result which is in agreement with the theory. The flux equations of the SMM are independent of the pore radius, and hence there is no change in the prediction of the SMM with the pore radius. On the other hand, when the pore diameter increases, the Knudsen term in the DGM becomes more significant. These are the initial results that we obtained with the tortuosity parameter set at a value of 4.5. In Fig. 5.6, 5.7, and 5.8 (b), the results are presented when the tortuosity parameter is fitted for each model separately. The tortuosity for the DGM was kept constant at a value of 4.5 and the SMM was increased to 5.0, 5.4 and 10. The results show that the difference between the DGM and SMM in predicting the concentration polarization can be compensated for by increasing the tortuosity factor to be as high as twice the value as set for the DGM.

At an average pore radius  $2.6 \mu\text{m}$ , the SMM produces quite similar results to the DGM, especially at high mole fractions of  $\text{H}_2$ . Only when the mole fraction is smaller than about 0.2 does a small discrepancy between the models appear. When the tortuosity parameter was modified for the SMM to be 5.4, the SMM and DGM results match quite well. It is observed that at small pore diameters, the larger discrepancy between the SMM and DGM can be compensated for by setting the tortuosity to a higher value and it is found that a value of 5.4 and 10 for pore diameters  $1.6$  and  $0.26 \mu\text{m}$ , respectively, give quite similar predictions for the concentration polarization.

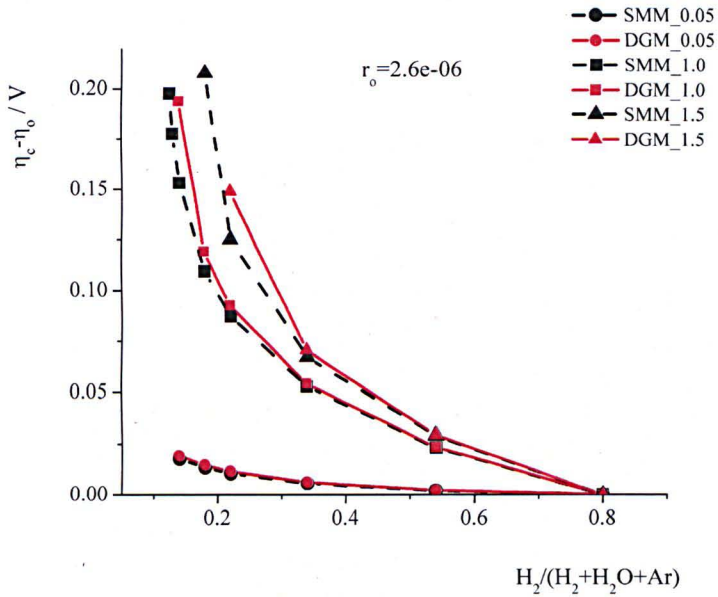
As stated in the study of Suwanwarangkul et al. [110], the current density also has an important effect on the concentration polarization. That is when the current density increases, the concentration at the TPB decreases. In Figs. 5.9, 5.10, and

5.11 the results are presented for each average pore radius as in Fig. 5.6, 5.7, and 5.8 but for a wide range of current densities, namely 0.05, 1, and 1.5 A/cm<sup>2</sup>. The results show that, even at the small pore radius, there is still a probability that the SMM produces comparatively similar results to those obtained when using the DGM by fitting the tortuosity parameter. As the pore radius decreases, and the current density increases, then the tortuosity parameter fitted for the SMM increases. Overall, for the pore diameter as small as 0.26 μm and current density as large as 1.5 A/cm<sup>2</sup>, comparatively similar agreement can be obtained for both the SMM and the DGM for the calculation of the concentration polarization.

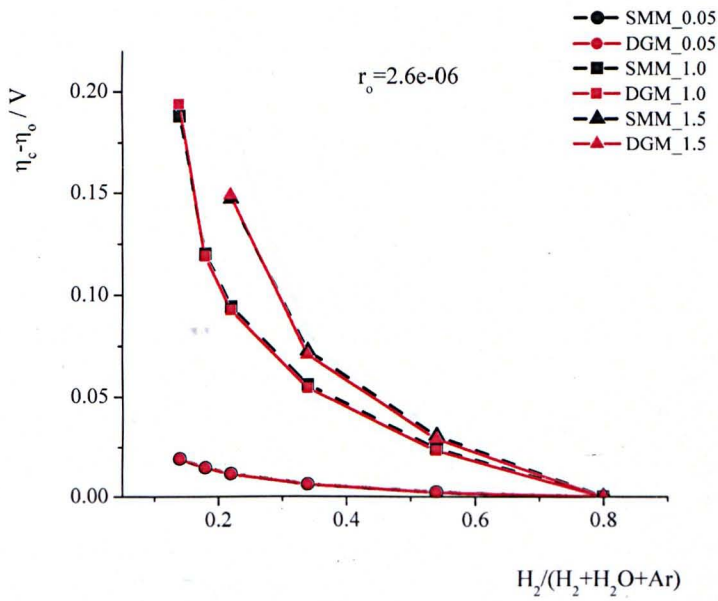
### 5.3.2.2 The DGM vs BFM

In Fig. 5.12 (a) and 5.13 (a), the predictions of the DGM and BFM has been represented for the H<sub>2</sub>/(H<sub>2</sub>+H<sub>2</sub>O+Ar) system at 0.05, 1, and 1.5 A/cm<sup>2</sup>, for pore diameters 2.6 and 0.26 μm, respectively at τ = 4.5. In Fig. 5.12 (b) and 5.13 (b) the results for the optimized tortuosity parameters were presented.

In modelling the transport in porous medium at a uniform pressure, the theoretical difference between the DGM and the BFM is in the term called the wall friction coefficient, namely  $f_{im}^{BFM}$ . The results indicate that,  $\kappa_i/K$  is very small compared to the 0.89  $D_{i,Kn}$  value and that is be the reason for the similar predictions of the DGM and the BFM. The concentration polarization predictions of the DGM and BFM are quite similar, especially at small pore diameters and the fitted tortuosity parameters, see Fig. 5.12(b) and 5.13 (b).



(a)



(b)

Figure 5.9: The  $(\eta_c - \eta_0)$  predictions of the SMM and the DGM for the  $H_2/(H_2+H_2O+Ar)$  system at 0.05, 1, and 1.5  $A/cm^2$  and average pore diameter =  $2.6 \mu m$  (a) for  $\tau = 4.5$  and (b) the same system for the optimized tortuosity parameters.

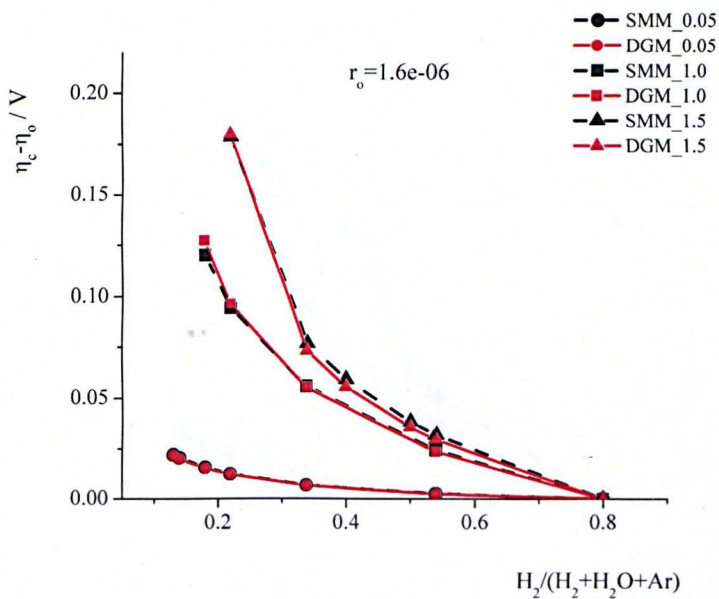
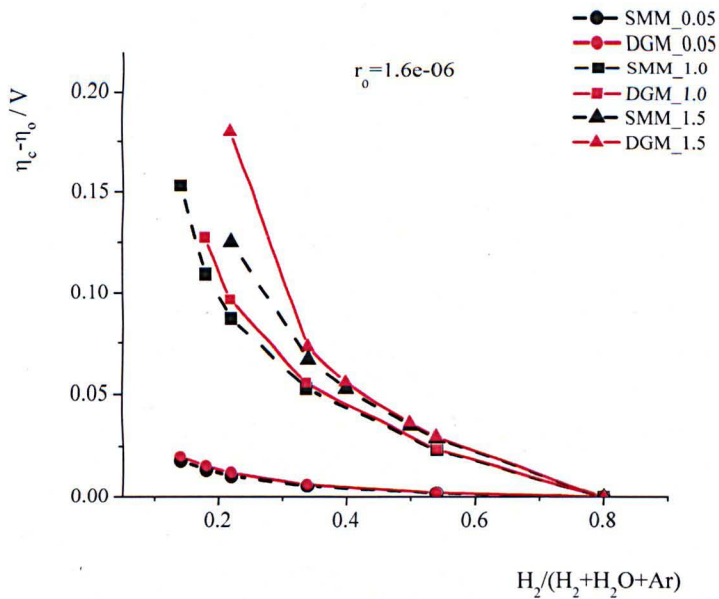
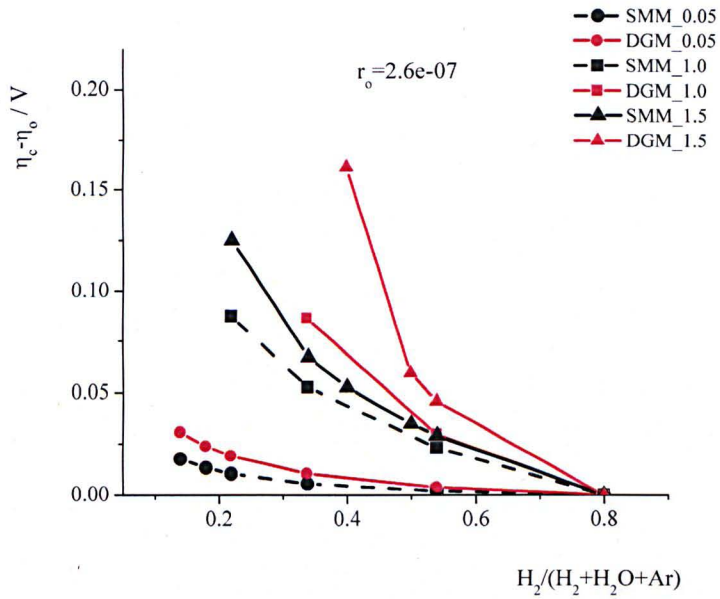
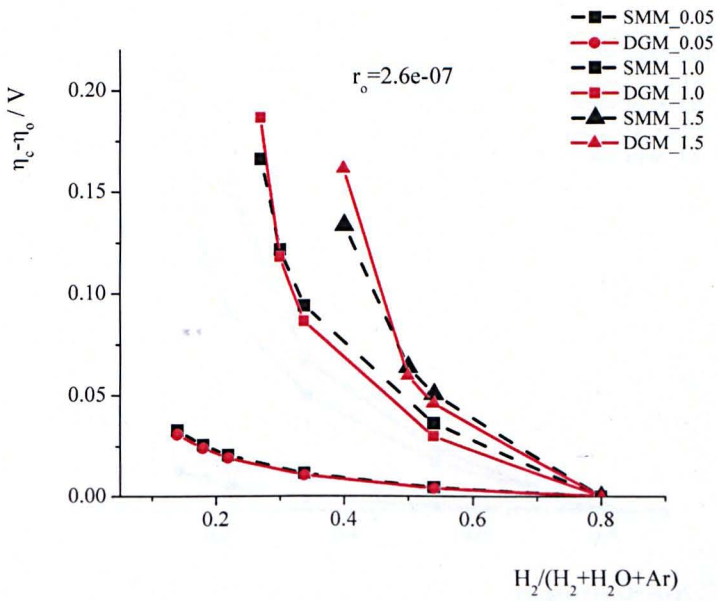


Figure 5.10: The  $(\eta_c - \eta_0)$  predictions of the SMM and the DGM for the  $H_2/(H_2+H_2O+Ar)$  system at 0.05, 1, and 1.5  $A/cm^2$  and average pore diameter =  $1.6 \mu m$  (a) for  $\tau = 4.5$  and (b) the same system for the optimized tortuosity parameters.

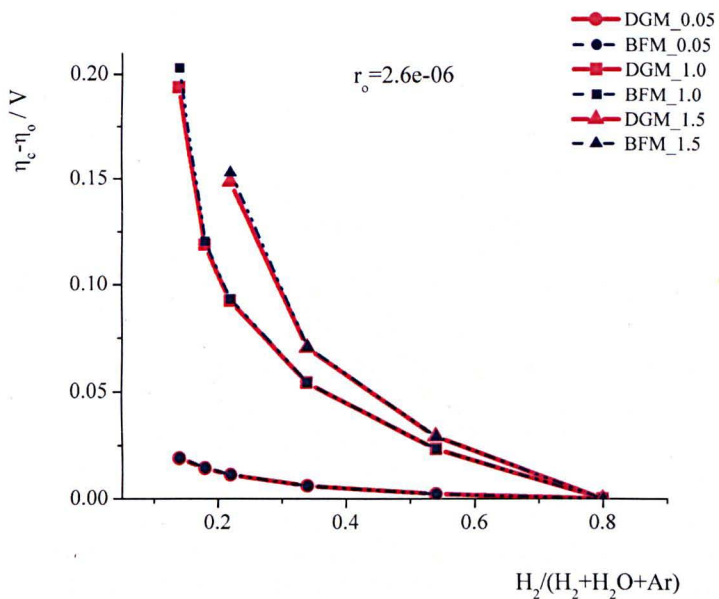


(a)

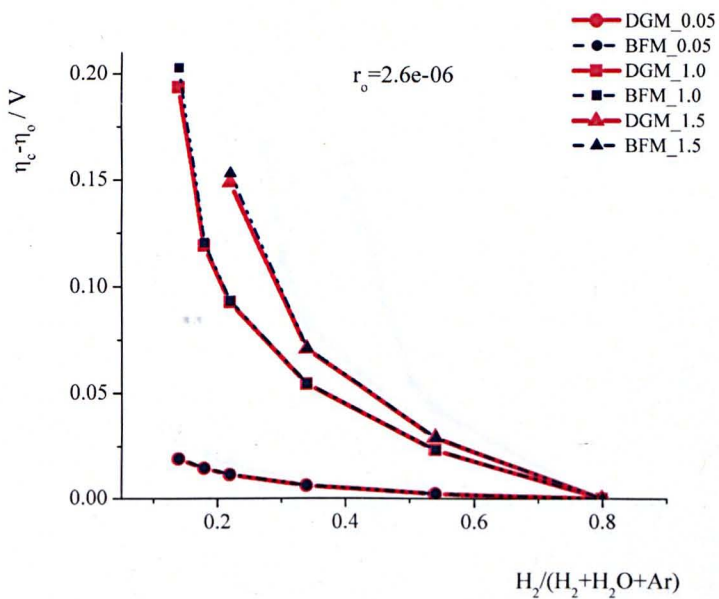


(b)

Figure 5.11: The  $(\eta_c - \eta_0)$  predictions of the SMM and the DGM for the  $H_2 / (H_2 + H_2O + Ar)$  system at 0.05, 1, and 1.5 A/cm<sup>2</sup> and average pore diameter = 0.26  $\mu\text{m}$  (a) for  $\tau = 4.5$  and (b) the same system for the optimized tortuosity parameters.

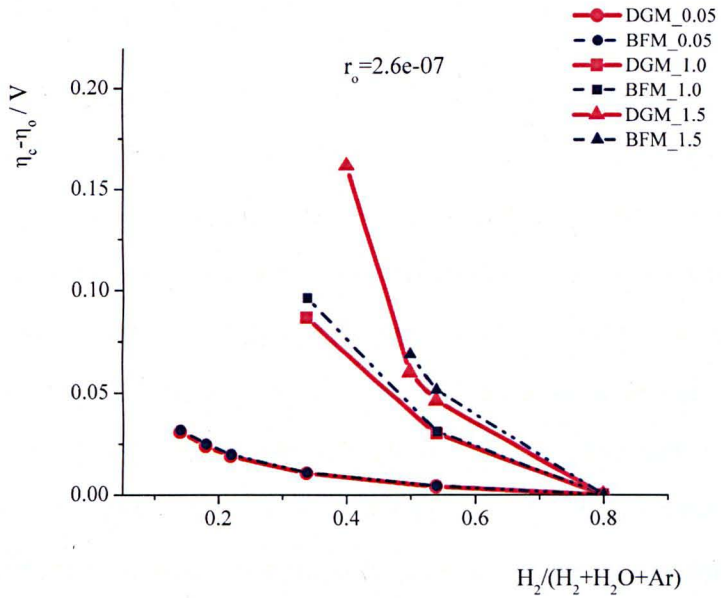


(a)

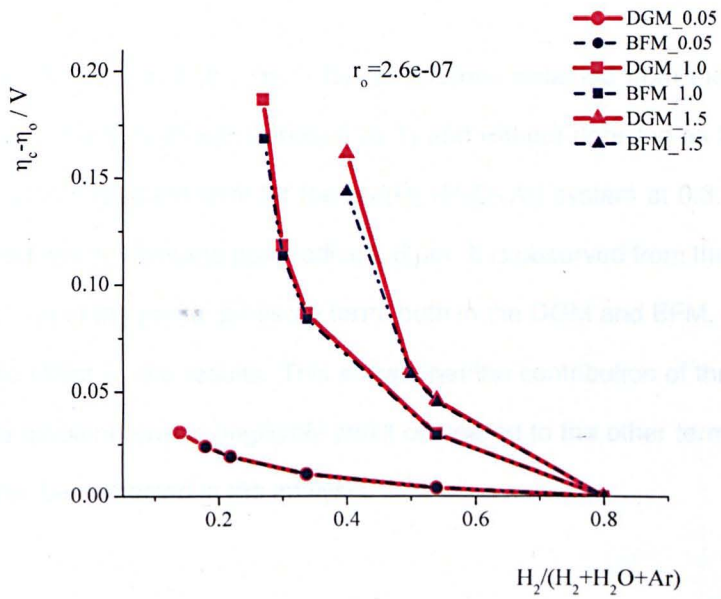


(b)

Figure 5.12: The  $(\eta_c - \eta_0)$  predictions of the DGM and the BFM for the  $H_2/(H_2+H_2O+Ar)$  system at 0.05, 1, and 1.5  $A/cm^2$  for pore diameters 2.6  $\mu m$  (a) for  $\tau=4.5$  (b) for the optimized tortuosity parameter.



(a)



(b)

Figure 5.13: The  $(\eta_c - \eta_0)$  predictions of the DGM and the BFM for the  $H_2/(H_2+H_2O+Ar)$  system at 0.05, 1, and 1.5  $A/cm^2$  for pore diameters  $0.26 \mu m$  (a) for  $\tau=4.5$  (b) for the optimized tortuosity parameter.

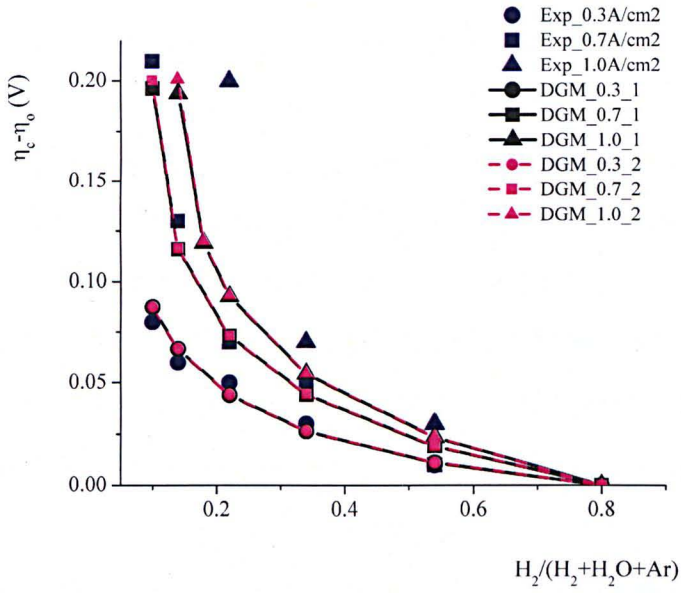
### 5.3.3 Results at a non-uniform pressure (Effect of the partial pressures in the DGM and the BFM)

In the previous sections, calculations have been performed by excluding the pressure gradient in the DGM and BFM equations. This is because this term has a negligible effect when diffusion is the dominating mechanism, as in the case under investigation. In fact, in the literature, Ni et al. [90] have shown that the inclusion of this term improves the predictions of the fuel cell performance. Also one of the differences between the work of Suwanwarangkul et al. [110] and Tseronis et al. [118] is that the pressure gradient term was included in the latter. In this section, the effect of the inclusion of the pressure gradient on the predictions of the DGM and the BFM in the 1D analysis are presented by calculating the predictions using Eqn. (5.10) and Eqn. (5.22) for the DGM and the BFM, respectively.

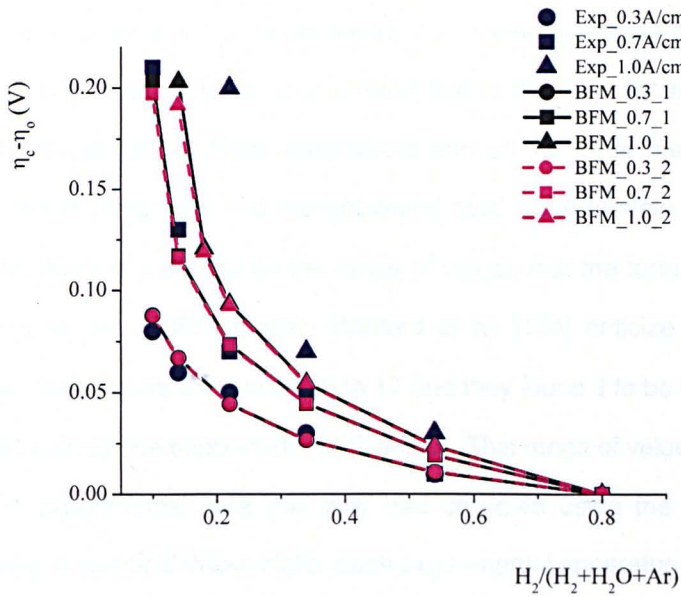
In Fig. 5.14 (a) and (b),  $(\eta_c - \eta_0)$  predictions obtained from the DGM and BFM, respectively, both with (labelled as 1) and without (labelled as 2) the additional pressure gradient term for the  $H_2/(H_2+H_2O+Ar)$  system at 0.3, 0.7, and 1  $A/cm^2$  and with an average pore radius 2.6  $\mu m$ . It is observed from the figure that the inclusion of the partial pressure term, both in the DGM and BFM, produces a negligible effect on the results. This shows that the contribution of the additional pressure gradient term is negligibly small compared to the other terms and can, in general, be neglected in the analysis.

### 5.3.4 Further Remarks and Discussions on the tortuosity

Tortuosity is, in its broadest sense, the ratio of the actual path that a particle follows due the tortuous nature of the medium over the length of the medium,



(a)



(b)

Figure 5.14:  $(\eta_c - \eta_0)$  predictions of the (a) DGM and (b) BFM with and without the additional pressure gradient term, labelled as (1) and (2), respectively for the  $H_2/(H_2+H_2O+Ar)$  system at 0.3, 0.7, and 1  $A/cm^2$ ; for pore diameter  $2.6 \mu m$ .

and by definition it is always greater than 1.0. In other words, due to the tortuous nature of the medium, the path that is travelled by a particle increases and as a result flux in porous medium increases. Simply this effect is taken into account by introducing the porosity,  $\epsilon$  and the tortuosity,  $\tau$ . In a porous medium, the diffusion coefficient is usually multiplied by the factor  $\epsilon/\tau$ , which is then called the effective diffusion coefficient. On the other hand, Epstein [28] states that the diffusivity of a species in a porous medium should be obtained by multiplication of the diffusion flux of the species by the factor  $\tau^2/\epsilon$  to obtain the effective diffusion flux, where  $\tau^2$  is referred to as the tortuosity factor.

In fact, the measurement of tortuosity is not as straightforward as that of the porosity. In a real system, the tortuosity and pore size are spatially varying parameters. However in the model equations an averaged value for tortuosity and pore size was used. This is on one hand due to the difficulty in experimentally obtaining the details of these parameters and on the other hand due to need to reduce the complexity and computational cost of the models. In the fuel cell literature, there is a debate on the range of values that the tortuosity parameter may take for the SOFC anode. Williford et al. [124] criticize the use of the tortuosity parameters as high as 10 to 17 and they found it to be in the range 2.0 and 3.0 for an anode supported SOFC anode. This range of values was obtained from the experimental data that they had collected using the Stefan-Maxwell formalism. A classical Wicke-Kallenbach experimental apparatus was assembled and used to determine the tortuosity for porous anode materials in counter diffusion, where the gases diffuse in opposite directions. This is the case in an SOFC anode: the fuels e.g.  $H_2$  and CO diffuse toward the anode/electrolyte interface, and the oxidation products, e.g.  $H_2O$  and  $CO_2$ ) diffuse away from that interface. Since an equal number of moles diffuse in each direction, there is no

localized gas accumulation to cause internal pressure gradients. Consequently, a near-zero pressure gradient was maintained across the sample by balancing the flow rates of the gas supplies, thus eliminating Darcian fluxes. Diffusion of gases through the porous anode material was considered to be dominated by bulk gas diffusion and Knudsen diffusion mechanisms. Data were collected using mass flow controllers and a gas chromatograph, and subsequently analyzed using a Maxwell-Stefan formalism to extract the tortuosities. Moreover, it was noted that the tortuosity values will depend on the definition of the diffusion coefficients Fickian or Maxwellian, how they are applied, and the intended use of the resulting model - interpretive or predictive. Further, they noted that, depending on whether the Knudsen diffusion is taken into consideration or not, the tortuosity value might vary between 2.0 and 6.0. In Jiang and Virkar [54], for different gas compositions and limiting current densities, the tortuosity varies between 5.0 and 9.0.

In fact, as stated in [124], accounting for Knudsen diffusion or not can result in different values of the tortuosity. Failure to properly account for the Knudsen effect can result in fitted tortuosities that are about a factor two higher than the ones that take this effect into account [124]. However, Cussler [25] also states that it is hard to justify the measured quantities using geometrical arguments alone and the main advantage of using this factor is its simplicity. In fact, in this thesis the fitted tortuosity is in the range of 4.5 to 10 and thus these values are comparable to previous studies. However, it must be noted that the fluctuations in the definition of this parameter indicates that in addition to its physical meaning, the tortuosity is a convenient fit parameter used to overcome the uncertainties associated with the diffusion models. For example, in the models investigated in this study, the effect of the pore size distribution that might have an important effect in highly

heterogeneous medium is not considered. Further, the surface diffusion and adsorption have been ignored and this has been mainly due to the complexity of including them and insufficient accuracy in defining these phenomena.

## 5.4 Conclusions

In this chapter, the performance of the SMM, DGM and the BFM have been compared in terms of their prediction capabilities of the concentration polarization in the anode of a SOFC fuel cell in 1D.

Based on this study, the following conclusions are drawn:

- Apart from the pore diameter and the current density, the tortuosity (or porosity/tortuosity) has a substantial effect on the predictions of concentration polarizations. Even at very high current densities ( $1.5 \text{ A/cm}^2$ ) and small pore radius ( $0.27 \mu\text{m}$ ), for the fitted tortuosity parameter, the SMM, DGM and BFM predictions are similar, and this contradicts some of the previous studies reported in the fuel cell literature. The results show that the SMM provides a quite similar prediction of the concentration polarization (in fact at least as accurate as the DGM) with the fitted tortuosity values so it may be preferred over the DGM when considering the comparative computational ease in comparison to the DGM.
- The effect of the partial pressure has been investigated and it is concluded that the pressure gradient term in the DGM and the BFM have a very small effect on the concentration polarization predictions for the conditions investigated and hence does not need to be included in this study.
- The importance of model validation against experimental data over a wide

range of conditions is demonstrated. The model appears to give a good fit in the range of the experimental operating conditions investigated but might not be appropriate at other conditions due to the empirical parameters found by fitting the model to the experimental data. Therefore the models must be validated for a large range of operating conditions before being used as a prediction tool.

- None of the 1D models give good predictions of the concentration polarization at high current densities and low fuel concentrations. The solution in 2D or 3D is expected to predict even more accurate results at high current densities where the reactant concentration varies not only along the anode thickness but also along the anode length due to the high consumption of the reactants.

It should be noted that the reduction of the 3D experimental case into the 1D model investigated in this study requires a number of simplifications. First of all, it was assumed that diffusion is the dominant flow mechanism in the porous anode and hence the convection term at the anode has been neglected. Moreover the transport of the species in the gas channel has been neglected and it was assumed that the inlet species concentration into the gas channel, which are measured experimentally, is constant over the gas channel and was taken as the boundary condition at the inlet of the anode. The validity of this simplification will be investigated in the 2D and 3D model investigations in the next chapter (Chapter 3.1.1.3) where the transport of the species in the gas channel will be considered by coupling the Navier-Stokes equations with the species mass balance equations in the model. On the other hand, the current density, which was measured experimentally at the reaction site, was assumed as constant over each computational cell since the current density distribution over the cell cannot be modelled using a half cell. This is due to the fact that the current density distribution over

the cell is a function of both the anodic and cathodic reaction parameters (see the Butler-Volmer equations in chapter 3). Although the constant current density assumption might be an oversimplification of the real case in order to predict the distribution of the species mass fractions, it was reported in the literature that with this assumption the average species concentration at the TPB which is ultimately used in the concentration polarization predictions can be predicted accurately (see [118]). The validity of the constant current density assumption for the prediction of the concentration polarization for the case investigated in this study will also be investigated in the next chapter.

## Chapter 6

# TWO AND THREE DIMENSIONAL RESULTS

In this chapter, the 2D and 3D solutions of the case presented in Chapter 5 in 1D is investigated and discussed using three multicomponent diffusion models, namely the SMM, DGM and BFM. In order to solve the equations in 2D and 3D, the DGM and the BFM has been implemented into COMSOL which is a Finite Element based PDE solver software. The following section starts with a description of the implementation steps of the DGM and BFM into COMSOL. Then, the verification of the implementation procedure using another set of diffusion experimental data is presented. After validation of the implementation, the solution domains and the boundary conditions of the 2D and 3D solid oxide fuel cell models are presented and the prediction performance of the SMM, DGM and the BFM in 2D and 3D are compared. The predictions of the three model are investigated under different operating conditions and the effect of the boundary conditions on the concentration polarization of the models are discussed. The 1D, 2D and 3D model results are compared and the reasons for the differences and similarities between the diffusion models' predictions are discussed in detail.

## 6.1 Implementation of the diffusion models into COMSOL

In this section, implementation of the diffusion models, namely the DGM and the BFM into COMSOL is discussed.

In COMSOL, in order to model the multi-component diffusion, the Stefan Maxwell model is used as the species mass conservation equations as follows:

$$\nabla w_i \rho u - \rho w_i \left( \sum_{j=1}^N D_{ij} \frac{M_w}{M_{w,j}} (\nabla w_j + w_j \nabla \frac{M_w}{M_{w,i}} + (x_j - w_j) \frac{\nabla P}{P}) \right) = R_i \quad i = 1, \dots, N \quad (6.1)$$

where  $w_i$  is the weight fraction of species  $i$ ,  $D_{ij}$  represents the  $ij$  component of the multicomponent Fick diffusivity, which is calculated from the Maxwell-Stefan diffusivities ( $m^2/s$ ),  $\rho$  is the density of the fluid ( $kg/m^3$ ),  $P$  is the pressure ( $Pa$ ), and  $R_i$  is the reaction source term for species  $i$  ( $kg/m^3/s$ ), and  $x_j$  is the molar fraction of species  $j$ . The term in the bracket in Eqn. (6.1) is the Stefan Maxwell diffusion mass flux,  $\mathbf{j}_i$ . The first term on the left hand side of the Eqn. (6.1) is the convective term, while the second term on the left hand side is the diffusion term. The term on the right hand side of the equation is the source term. The average molecular weight  $M_w$  is calculated as follows:

$$M_w = \sum_{j=1}^k x_j M_{w,j} \quad (6.2)$$

where  $M_{w,j}$  is the molar mass of species  $j$  ( $kg/mol$ ). If we assume that the gas is ideal, the density is given by

$$\rho = \frac{PM_w}{RT} \quad (6.3)$$

For the implementation of the DGM and the BFM the Stefan Maxwell Module of COMSOL has been modified by changing the  $\mathbf{j}$  term in Eqn. (6.1) which is shown in the box. The required form of the DGM and the BFM equations for the modification are discussed in the following section.

### 6.1.1 DGM

In this section, it is convenient to work with the total mass flux of the species,  $\mathbf{N}_i$  since the conversion of the total mole flux into mass flux can be obtained by multiplying the total mole flux by the molar mass of the species  $i$ . However, this is not the case for the conversion of the diffusion flux, for more details see [68], [115], [132].

In Chapter 2, the complete set of dusty gas model flux equations have been presented. In order to couple this equation with the species mass conservation equation, the flux,  $\mathbf{N}_i$  should be obtained as a function of  $\nabla x_i$ . If the DGM equations are written by taking into account the pressure gradient, the following set of equations are obtained for a ternary mixture [47]:

$$\mathbf{N}_1 = -\frac{\Delta_{12}\Delta_{23}\Delta_{31}}{(x_1\Delta_{23} + x_2\Delta_{31} + x_3\Delta_{12})} \left( \frac{\frac{A_1}{\Delta_{23}} \left( \frac{x_2}{D_{2,Kn}^e} + \frac{x_3}{D_{3,Kn}^e} \right) - x_1 \left( \frac{A_2}{D_{2,Kn}^e\Delta_{31}} + \frac{A_3}{D_{3,Kn}^e\Delta_{12}} \right)}{\frac{x_1}{D_{1,Kn}^e} + \frac{x_2}{D_{2,Kn}^e} + \frac{x_3}{D_{3,Kn}^e}} \right) - \left( \frac{x_1}{RT} \right) \left( \frac{B_o P}{\mu} + \frac{1}{\frac{x_1}{D_{1,Kn}^e} + \frac{x_2}{D_{2,Kn}^e} + \frac{x_3}{D_{3,Kn}^e}} \right) \nabla P \quad (6.4)$$

$$\frac{1}{\Delta_{ij}} = \frac{1}{D_{ij}^e} + \frac{1}{D_{i,Kn}^e D_{j,Kn}^e} \left( \sum_t x_t / D_{t,Kn}^e \right) \quad (6.5)$$

The quantities,  $\Delta_{13}$  and  $\Delta_{23}$  can be found by the cyclic permutation of the suffices in Eqn. (6.5). It is seen from Eqn. 6.5 that  $\Delta_{ij}$  is symmetric, i.e.  $\Delta_{ij}=\Delta_{ji}$  and  $A_{ij}$  in the Eqn. (6.4) is defined as follows:

$$\mathbf{A}_i = \frac{P}{RT} \nabla x_i + \frac{x_i}{RT} \left( 1 - \frac{\frac{1}{D_{i,Kn}^e}}{\frac{x_1}{D_{1,Kn}^e} + \frac{x_2}{D_{2,Kn}^e} + \frac{x_3}{D_{3,Kn}^e}} \right) \nabla P \quad (6.6)$$

When Eqn. (6.6) is inserted into Eqn. (6.4) and after some mathematical manipulations,  $\mathbf{N}_1$  may be obtained as follows:

$$\begin{aligned} \mathbf{N}_1 = & - \frac{\Delta_{12}\Delta_{31}}{(x_1\Delta_{23} + x_2\Delta_{31} + x_3\Delta_{12}) \left( \frac{x_1}{D_{1,Kn}^e} + \frac{x_2}{D_{2,Kn}^e} + \frac{x_3}{D_{3,Kn}^e} \right)} \left( \frac{x_2}{D_{2,Kn}^e} + \frac{x_3}{D_{3,Kn}^e} \right) \\ & \left( \frac{P}{RT} \nabla x_1 + \frac{x_1}{RT} \left( 1 - \frac{\frac{1}{D_{1,Kn}^e}}{\frac{x_2}{D_{2,Kn}^e} + \frac{x_3}{D_{3,Kn}^e}} \right) \nabla P \right) \\ & \left( \frac{x_1}{D_{2,Kn}^e} \right) \left( \frac{P}{RT} \nabla x_2 + \frac{x_2}{RT} \left( 1 - \frac{\frac{1}{D_{2,Kn}^e}}{\frac{x_2}{D_{2,Kn}^e} + \frac{x_3}{D_{3,Kn}^e}} \right) \nabla P \right) \\ & + \frac{\Delta_{23}\Delta_{31}}{(x_1\Delta_{23} + x_2\Delta_{31} + x_3\Delta_{12}) \left( \frac{x_1}{D_{1,Kn}^e} + \frac{x_2}{D_{2,Kn}^e} + \frac{x_3}{D_{3,Kn}^e} \right)} \\ & \left( \frac{x_1}{D_{3,Kn}^e} \right) \left( \frac{P}{RT} \nabla x_3 + \frac{x_3}{RT} \left( 1 - \frac{\frac{1}{D_{3,Kn}^e}}{\frac{x_2}{D_{2,Kn}^e} + \frac{x_3}{D_{3,Kn}^e}} \right) \nabla P \right) \\ & - \frac{x_1}{RT} \left( \frac{B_0 P}{\mu} + \frac{1}{\frac{x_1}{D_{1,Kn}^e} + \frac{x_2}{D_{2,Kn}^e} + \frac{x_3}{D_{3,Kn}^e}} \right) \nabla P \end{aligned} \quad (6.7)$$

In order to write Eqn. (6.7) in the form given in COMSOL, Eqn. (6.7) is divided

and multiplied by the  $\rho w_1$ , and to convert  $N_1$  into the mass flux form, it is multiplied by the factor  $M_{w,1}$  so that:

$$\mathbf{n}_1 = \mathbf{N}_1 \left( \frac{M_{w,1}}{\rho w_1} \right) \rho w_1 \quad (6.8)$$

By inserting Eqn. (6.7) into Eqn. (6.8), total mass flux of species 1,  $n_1$  is obtained.  $D_{11}$ ,  $D_{12}$ ,  $D_{13}$  are the coefficient of the  $\nabla x_1$ ,  $\nabla x_2$  and  $\nabla x_3$ , respectively, and they are given as follows:

$$D_{11} = \frac{\Delta_{12}\Delta_{31}}{(x_1\Delta_{23} + x_2\Delta_{31} + x_3\Delta_{12}) \left( \frac{x_1}{D_{1,Kn}^e} + \frac{x_2}{D_{2,Kn}^e} + \frac{x_3}{D_{3,Kn}^e} \right)} \left( \frac{x_2}{D_{2,Kn}^e} + \frac{x_3}{D_{3,Kn}^e} \right) \frac{1}{x_1} \quad (6.9)$$

$$D_{12} = \frac{\Delta_{12}\Delta_{23}}{(x_1\Delta_{23} + x_2\Delta_{31} + x_3\Delta_{12}) \left( \frac{x_1}{D_{1,Kn}^e} + \frac{x_2}{D_{2,Kn}^e} + \frac{x_3}{D_{3,Kn}^e} \right)} \frac{1}{D_{2,Kn}^e} \rho w_1 \quad (6.10)$$

$$D_{13} = \frac{\Delta_{23}\Delta_{31}}{(x_1\Delta_{23} + x_2\Delta_{31} + x_3\Delta_{12}) \left( \frac{x_1}{D_{1,Kn}^e} + \frac{x_2}{D_{2,Kn}^e} + \frac{x_3}{D_{3,Kn}^e} \right)} \frac{1}{D_{3,Kn}^e} \rho w_1 \quad (6.11)$$

Likewise,  $\mathbf{N}_2$  and  $\mathbf{N}_3$  can be obtained by a cyclic permutation of Eqn. (6.7) and thus the other  $D_{ij}$  terms may be obtained accordingly. Their values can be found in Appendix A.

## 6.1.2 BFM

The general form of the BFM is given by Kerkhof [61]:

$$-x_i \nabla P - P \nabla x_i = \frac{\tau^2}{\varepsilon} \left[ \sum_{j=1, j \neq i}^n RT \frac{N_i x_j - N_j x_i}{D_{ij}} + f_{im}^{BFM} RT N_i \right] \quad i = 1, \dots, n \quad (6.12)$$

In this part, the general equation and determination of the coefficient of the diffusion matrix is presented for a ternary mixture as follows:

$$\left[ \frac{N_1 x_2 - N_2 x_1}{D_{12}} + \frac{N_1 x_3 - N_3 x_1}{D_{13}} + f_{1m}^{BFM} N_1 \right] = \frac{\varepsilon}{\tau^2 RT} [-P \nabla x_1 - x_1 \nabla P] \quad (6.13)$$

After some mathematical manipulation of Eqn. (6.13) to obtain  $N_i$  as a function of  $\nabla x_i$ , we obtain the following:

$$\begin{pmatrix} N_1 \\ N_2 \\ N_3 \end{pmatrix} = [B]^{-1} \left( \frac{\varepsilon}{\tau^2 RT} \right) \left[ -P \begin{pmatrix} \nabla x_1 \\ \nabla x_2 \\ \nabla x_3 \end{pmatrix} - \nabla P \begin{pmatrix} x_1 \\ x_2 \\ x_3 \end{pmatrix} \right] \quad (6.14)$$

where  $[B]$  is a 3 x 3 matrix and it is given by:

$$\begin{aligned} B_{ii} &= \sum_{j=1, j \neq i}^n -x_j / D_{ij} + f_{im}^{BFM} \\ B_{ij} &= -x_i / D_{ij} \end{aligned} \quad (6.15)$$

From here,  $D_{ij}$  is the coefficient term of the  $\nabla x_j$  for each species  $i$ . In other words,  $D_{11}, D_{12}$  and  $D_{13}$  are the coefficient of  $\nabla x_1, \nabla x_2$  and  $\nabla x_3$ , respectively in the Eqn. (6.14).

## 6.2 Verification of the implementation of diffusion models into COMSOL

Before using the diffusion models' codes implemented into COMSOL for modeling the mass transport in SOFC, in order to check the correctness of the implementation procedure, first the codes have been used to simulate the experimental data of Evans et al. [29]. The main property of this experimental data is that it has been used by the developers of the DGM and the BFM in order to verify their diffusion models. Therefore the solution obtained in this section using COMSOL can be compared to their solutions. In the following section, the experimental data will be explained in detail.

The counter flow of the binary mixtures of two inert gases, namely Helium (He) and Argon (Ar) over a porous septum of thickness  $4.47\text{ mm}$  and length  $0.98\text{ m}$  was measured at the uniform pressure medium. Fig. 6.1 demonstrates the set-up of the experimental data. The pore radius of septum is around  $0.3\text{ }\mu\text{m}$ . The pressure difference across the septum was kept equal to zero while the total system pressure was varied between  $1$  and  $7.6\text{ atm}$ . The mole fraction driving force,  $\Delta x$  was maintained at  $0.9628$ , with a mean composition  $x_{He} = 0.5$ . The fluxes of He and Ar were then measured at different pressure values.

In the solutions obtained using COMSOL in this thesis, the parameters used in the original study of the Kerkhof [61] and Krishna [67] have been used for (see Table 6.1). In Kerkhof [61], the solution was obtained using a direct numerical solution of their model equation (Eq. (191) [61]) in 1D. Krishna made the calculations using a simplified linearized method that was introduced in Krishna [67] in 1D. The solutions in this study has been obtained in 1D using the Finite Element

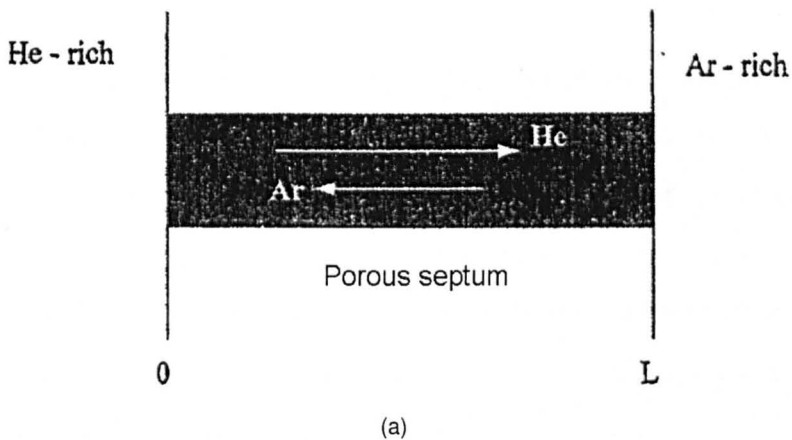


Figure 6.1: The experimental set-up of Evans et al. [29] that is used to measure the counter diffusion flux of He and Ar in a porous septum.

PDE solver COMSOL.

Table 6.1: Parameters used in Kerkhof [61] (DGM) and Krishna [67] (DGM) to predict the flux of He and Ar in the porous septum at uniform pressure.

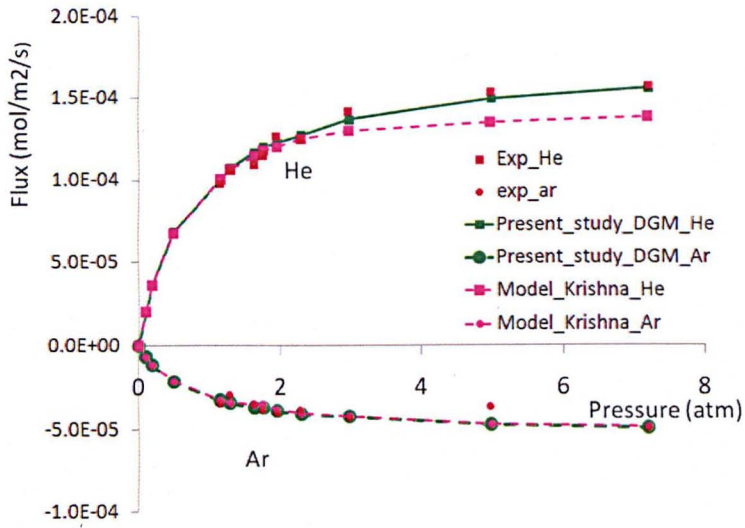
Parameters	Krishna [67] (DGM)	Kerkhof [61] (BFM)
$D_{HeAr}(m^2/s)$	$1.06 \times 10^{-5}/P$ (effective)	$7.29 \times 10^{-5}$
$D_{Kn,He}(m^2/s)$	$3.93 \times 10^{-8}$ (effective)	$\times 10^{-5}$
$D_{Kn,Ar}(m^2/s)$	$1.24 \times 10^{-8}$ (effective)	$\times 10^{-5}$
$K(m^2)$	$2.13 \times 10^{-18}$	$1.66 \times 10^{-14}$
$\varepsilon/\tau$	-	$1.28 \times 10^{-4}$

Fig. 6.2 (a) presents the predictions of the  $N_{He}$  and  $N_{Ar}$  for the uniform pressure system at different pressures using the DGM predicted by (a) COMSOL in this study and (b) Krishna [67]. Although at low pressures, the fluxes of both He and Ar fit to the experimental data well, the predictions of Krishna [67] do not fit to the experimental data at high pressures. On the other hand, the predictions obtained for COMSOL is better at high pressure. The lack of accuracy in the predictions of Krishna [67] at high pressures may be due to the inaccuracy in their simplified solution algorithm.

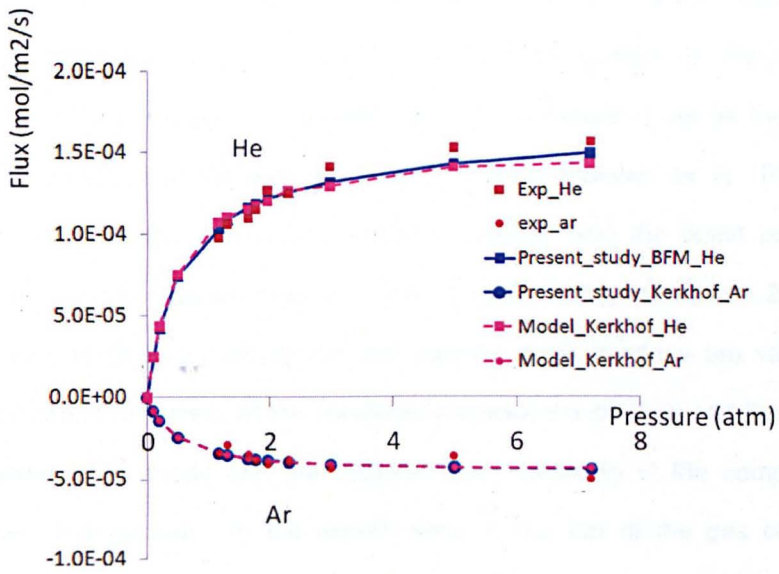
Figures 6.2 (b) show the solution obtained for the BFM using COMSOL and the solution of the BFM as obtained by Kerkhof [61]. It appears that the predictions obtained in this study, and those of Kerkhof [61] are very similar. As a result, it can be concluded that the predictions obtained using COMSOL for the implemented DGM and the BFM match the experimental data and the previous model predictions performed by Krishna [67] and Kerkhof [61] quite well. Thus this verifies the implementation procedure of the multicomponent diffusion models performed in this thesis.

### **6.3 Simplification of the 2D model**

In the 2D model, the variations of the variables, such as the species concentration, velocity and pressure along the thickness of the cell ( $y$ -direction in Fig. 6.4) was ignored. In contrast to the 1D model, in the 2D model the convection flow in the gas channel and the porous anode and catalyst layer has been taken into account. The experimentally measured species mole fractions at the inlet of the gas channel and the velocity of inlet gas mixture have been used as the boundary conditions at the inlet of the gas channel and flow and species mass fraction distributions along the fuel cell in the direction of the flow have been predicted. The differences between the 2D model and the 1D model are as follows; (i) in the 2D model, the transport processes in the gas channel has been taken into account, and (ii) the Navier-Stokes equations have been coupled with the species mass transfer equations in the gas channel, anode and cathode subdomains.



(a)



(b)

Figure 6.2: A comparison of the predictions of the  $N_{He}$  and  $N_{Ar}$  for the uniform pressure system at different pressure between the experimental data and (a) present study, and Krishna [67] for the DGM and (b) present study, and Kerkhof et al.[61] for the BFM.

## 6.4 Two-Dimensional Model Domain and Boundary Conditions

The domain consists of three sub domains, namely the gas channel, porous anode and catalyst; the experimentally measured dimensions are given in Table 6.2.

Table 6.2: Dimensions of the SOFC anode.

	Length [mm]	Thickness [mm]	Width [mm]
Anode diffusion layer	20	2	1
Anode reaction site (catalyst)	20	0.02	1
Anode gas channel	20	1	0.5

Fig. 6.4 (a) shows the domain of the two-dimensional SOFC model. At the inlet of the gas channel (labelled as I), the composition of the species and mixture fluid velocity are specified while the pressure is set as the outlet boundary condition at the exit of the gas channel (labelled as II). The inlet species concentration and the mixture fluid velocity and the outlet pressure are experimentally measured values. The velocity and pressure are  $2.0 \text{ m/s}$  and  $1 \text{ atm}$ , respectively, while the inlet species mole fractions are varied at different current densities. At the interfaces between the channel and the anode and between the anode and the catalyst layer, continuity in the composition and mass flux applies. In the experiments, at the top of the gas channel, a solid conductive layer exists which has not been considered in this thesis due to the fact that it does not contribute to the mass flow transfer and it is only important for the electronic conduction processes which have not been considered in this thesis. Therefore, the mass flux is set to zero at the the upper wall of the gas channel, i.e. it was considered as wall in the simulations.

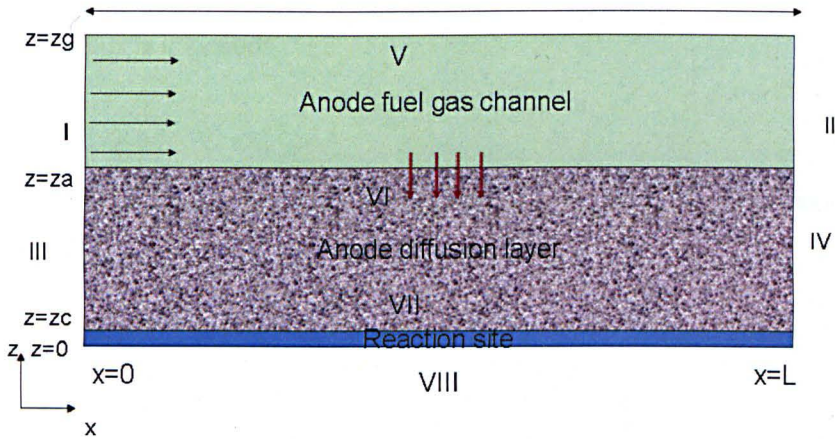


Figure 6.3: The domain for the 2D SOFC model.

In summary, the boundary conditions are as follows:

- (I) At the inlet of the fuel channel ( $x = 0$   $z \in (z_a, z_g)$ ), the mole fraction of each species,  $x_i$ , and the inlet mixture velocity,  $\mathbf{u}_{in}$  are prescribed:

$$x_i = x_{i,0}, \quad i = 1, 2, \dots, n \quad (6.16)$$

$$\mathbf{u}_{in} = 2.0 \text{ m/s} \quad (6.17)$$

- (II) At the fuel channel outlet ( $x = L$   $z \in (z_a, z_g)$ ), the pressure is atmospheric pressure:

$$P = P_{atm} \quad (6.18)$$

- (III) At the diffusion layer at  $x = 0$  and  $z \in (z_c, z_a)$ , the boundaries are impermeable, and hence zero mass flux is imposed:

$$\mathbf{N}_i = 0, \quad i = 1, 2, \dots, n \quad (6.19)$$

- (IV) At the diffusion layer,  $x = L$ , and  $z \in (z_c, z_a)$ , due to the solid wall boundaries

zero flux is imposed:

$$\mathbf{N}_i = 0, \quad i = 1, 2, \dots, n \quad (6.20)$$

- (V) At the top boundary of the fuel channel  $x \in (0, L)$  and  $z = z_g$ , the boundary is impermeable solid, and therefore zero mass flux is imposed:

$$\mathbf{N}_i = 0, \quad i = 1, 2, \dots, n \quad (6.21)$$

- (VI) At the interface between the fuel channel with the porous electrode,  $x \in (0, L)$  and  $z = z_a$ , the flux terms for the fuel channel are the same to the porous electrode flux.

- (VII) At the interface of the fuel channel with the porous electrode  $x \in (0, L)$  and  $z = z_c$ , the flux terms for the anode are equal to the porous catalyst flux.

- (VIII) At the bottom end of the catalyst layer,  $x \in (0, L)$  and  $z = 0$ , a zero flux is defined for the species, due to the impervious nature of the layer.

At the catalyst layer, the species flux source term due to the production and consumption of products and reactants, respectively, is calculated according to Faraday's law:

$$\mathbf{N}_i = \frac{\mathbf{i}}{n_e F} M_{w,i} \quad i = 1, 2, \dots, n \quad (6.22)$$

where  $n_e$  is the mole of electrons in the reaction. The parameters of the models are same as those given in the previous chapter in Table 5.1.

## 6.5 Three-Dimensional Model Domain and Boundary Conditions

Fig. 6.4 (b) shows the domain of the three-dimensional SOFC model. As in the two-dimensional model, at the inlet of the gas channel (II in Fig. 6.4 (b)), the composition of the species and mixture fluid velocity are specified while pressure is set as the outlet boundary condition at the exit of the gas channel (III). The velocity and pressure are  $2.0 \text{ m/s}$  and  $1 \text{ atm}$ , respectively while the inlet species mole fractions are varied at different current densities. At the interfaces between the channel and anode (XI) and between the anode and catalyst layer (IX), continuity in composition and flux applies. The upper boundary of the gas channel (I) and the half section between the anode and gas channel are solid and the sides of the gas channel and hence flux is set to zero. At the sides of the anode and reaction layers (IV, V, VI and VII), no flux boundary was set assuming that these parts are perfectly sealed to prevent gas migration. At the reaction layer (VIII), the flux source term has been added for the production and consumptions due to the electrochemical reaction. In summary, the boundary conditions are as follows:

(I) The top boundary of the gas channel,  $x \in (0, L)$ ,  $y \in (y_g, y_e)$  and  $z = z_g$ , the due to the solid wall, the zero flux is imposed.

(II) At the inlet of the fuel channel,  $x = 0$ ,  $y \in (y_g, y_e)$ , and  $z \in (z_a, z_g)$ , the mole fraction of every component,  $x_i$ , and inlet mixture velocity,  $u_{in}$ , are prescribed:

$$x_i = x_{i,0}, \quad i = 1, 2, \dots, n \quad (6.23)$$

$$\mathbf{u}_{in} = 2.0 \text{ m/s} \quad (6.24)$$

(III) At the channel outlet,  $x = L$ ,  $y \in (y_g, y_e)$ , and  $z \in (z_a, z_g)$ , the pressure

is specified to be the atmospheric pressure:

$$P = P_{atm} \quad (6.25)$$

(IV) At the anode diffusion layer,  $x = 0, y \in (0, y_e)$  and  $z \in (z_c, z_a)$ , due to the solid wall boundaries a zero species mass flux is imposed:

$$\mathbf{N}_i = 0, \quad i = 1, 2, \dots, n \quad (6.26)$$

(V) At the end of the anode diffusion layer,  $x = L, y \in (0, y_e)$ , and  $z \in (z_c, z_a)$ , due to the solid wall boundaries, a zero mass flux is imposed:

$$\mathbf{N}_i = 0, \quad i = 1, 2, \dots, n \quad (6.27)$$

(VI) At  $(x = 0, y \in (0, y_e))$  and  $z \in (0, z_c)$ , due to the solid wall boundaries, a zero mass flux is imposed:

$$\mathbf{N}_i = 0, \quad i = 1, 2, \dots, n \quad (6.28)$$

(VII) At  $x = L, y \in (0, y_e)$  and  $z \in (0, z_c)$ , due to the solid wall boundaries, a zero mass flux is imposed:

$$\mathbf{N}_i = 0, \quad i = 1, 2, \dots, n \quad (6.29)$$

(VIII) At  $x \in (0, L), y \in (0, y_e), z = 0$ , due to the solid wall boundaries, a mass zero flux is imposed:

$$\mathbf{N}_i = 0, \quad i = 1, 2, \dots, n \quad (6.30)$$

(IX) At the interface between the diffusion layer and catalyst,  $x \in (0, L), y \in (0, y_e)$ , and  $z = z_c$ , the flux in the diffusion layer is equal to the flux in the catalyst layer.

(X) At the diffusion layer,  $x \in (0, L), y \in (0, y_g), z = z_a$ , the boundary is impermeable, and hence zero mass flux is imposed:

$$N_i = 0, \quad i = 1, 2, \dots, n \quad (6.31)$$

(XI) At the interface between the gas channel and porous anode diffusion layer,  $x \in (0, L), y \in (y_g, y_e)$ , and  $z = z_a$ , the flux in the gas channel is the same as the flux in the anode diffusion layer.

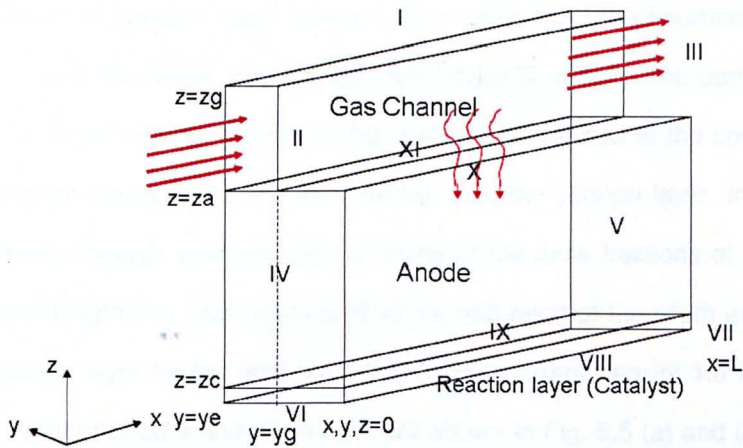


Figure 6.4: The domain of the 3D SOFC model.

## 6.6 Pre-processing

### 6.6.1 Grid Independency Analysis

In order to ensure the balance between the number of cell sizes and computational accuracy, a grid independency study has been performed for both the 2D and 3D analyse. In 2D, the domain has been divided into 60,120, 240, 480, 960 unstructured rectangular meshes. Since the purpose of this study is to predict the concentration polarization, which uses average mass fractions of  $H_2$  and  $H_2O$  at the catalyst layer, the average  $w_{H_2}$  and  $w_{H_2O}$  predictions have been compared for different mesh sizes. As an example, in Table 6.3 and 6.4, the comparison using the DGM at highest experimental polarization where current density is  $1.0 \text{ A/cm}^2$  and inlet  $H_2$  mole fraction is 0.0145 has been presented. It is seen that the difference in the average mass fractions after 1200 and 13600 number of grids for the 2D and 3D model, respectively, are negligibly small. The convergence obtained at small number of cells in this study might be due to the comparison of the average values of the  $H_2$  mole fraction over the catalyst layer. In order to make a more through analysis, the variations of the mole fractions of  $H_2$  along the catalyst length has been compared at the mid point of the width and height of the catalyst layer for the inlet  $w_{H_2}=0.0202$  and current density  $1.0 \text{ A/cm}^2$  for different number of cells and the results are shown in Fig. 6.5 (a) and (b) for the 2D and 3D models, respectively. In Fig. 6.5 (a), it is observed that the difference in the variation of the mass fraction is negligibly small between different number of grids. The main variation is observed in the mass fraction distribution throught the end of the catalyst length where  $0.018 < x < 0.02$ . On the other hand, for the 3D analysis, the difference in the mass fractions become negligible after 2720 number of cells. As a result, considering the balance between the computational time and accuracy, 960 and 2720 number of cells have been selected for the 2D

and 3D models, respectively.

Table 6.3: The average mass fraction of  $H_2$  and  $H_2O$  at the anode-electrolyte interface for different number of cells for the 2D model.

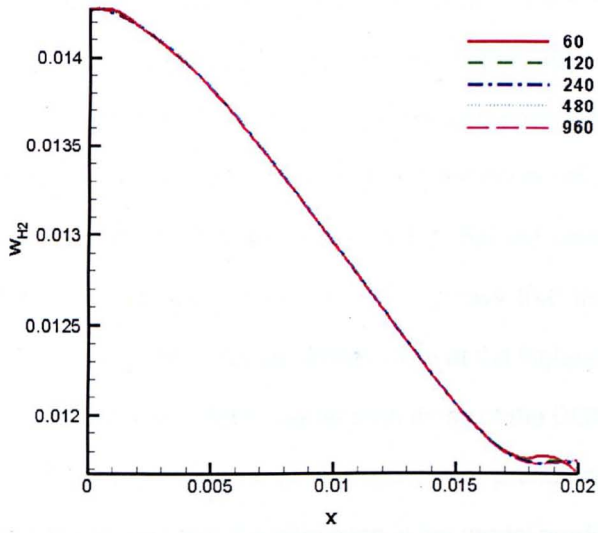
Number of cells	$w_{H_2}$	$w_{H_2O}$
60	$2.695 \times 10^{-5}$	$7.50 \times 10^{-2}$
120	$2.592 \times 10^{-5}$	$9.035 \times 10^{-2}$
240	$2.591 \times 10^{-5}$	$9.045 \times 10^{-2}$
480	$2.591 \times 10^{-5}$	$9.045 \times 10^{-2}$
960	$2.591 \times 10^{-5}$	$9.048 \times 10^{-2}$

Table 6.4: The average mass fraction of  $H_2$  and  $H_2O$  at the anode-electrolyte interface for different number of cells for the 3D model.

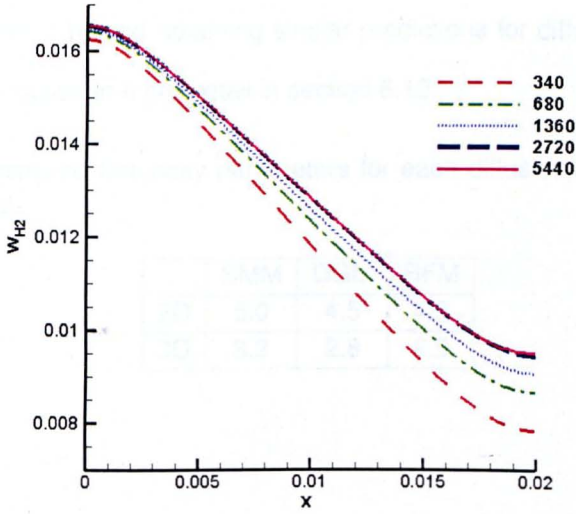
Number of cells	$w_{H_2}$	$w_{H_2O}$
340	$2.335 \times 10^{-7}$	$4.753 \times 10^{-6}$
680	$2.478 \times 10^{-7}$	$4.702 \times 10^{-6}$
1360	$2.531 \times 10^{-7}$	$4.642 \times 10^{-6}$
2720	$2.573 \times 10^{-7}$	$4.611 \times 10^{-6}$
5440	$2.574 \times 10^{-7}$	$4.604 \times 10^{-6}$

## 6.7 Two-Dimensional Results

Figure 6.6 shows the 2D model predictions of the SMM, DGM and the BFM with the experimental data at (a) 0.3, (b) 0.7 and (c) 1.0  $A/cm^2$  with a single tortuosity parameter ( $=4.5$ ) used for all the models. According to these figures, at 0.3  $A/cm^2$ , the BFM overpredicts the concentration polarization, while the DGM and the SMM fit better to the experimental data at this current density. On the other hand at 0.7  $A/cm^2$  and especially at 1.0  $A/cm^2$ , the BFM predictions are better than that of the DGM and those of the DGM is better than the SMM. The fact that the BFM predictions are worse than the SMM and the DGM at the low current density,



(a)



(b)

Figure 6.5: The variations of the  $w_{H_2}$  along the catalyst length ( $x$ -direction) for the inlet  $w_{H_2}=0.0202$  and current density  $1.0 \text{ A/cm}^2$  for different number of cells for the (a) 2D, and (b) 3D model.

while it is better at high current density, has inconsistencies in itself. In order to investigate whether the differences between the predictions from the models are due to using the same single tortuosity parameter for all models, the models have been run with the optimized tortuosity parameters. Optimization of the tortuosity value has been performed using a trial and error approach and the optimized tortuosity values are given in Table 6.5. In Fig. 6.7, the concentration polarization predictions are shown for the same case as in Fig. 6.6 but using the optimized value of the tortuosity for each model. Fig. 6.7 shows that the predictions of the SMM, DGM and the BFM are quite similar, even at the highest current density while the BFM predictions are slightly better than those of the DGM and the SMM. These results are consistent with the 1D predictions, presented in Chapter 5. Thus, it is clearly understood that the difference in the model predictions observed in Fig. 6.6 are due to the single tortuosity value used. Also, it is important to assess the reason behind obtaining similar predictions for different models and this will be discussed in more detail in section 6.10.

Table 6.5: Optimized tortuosity parameters for each diffusion model for the 2D and 3D analysis.

	SMM	DGM	BFM
2D	5.0	4.5	4.0
3D	3.2	2.8	2.5

## 6.8 Three Dimensional Results

Figure 6.8, 6.9, 6.10 present a comparison of the predictions of the concentration polarization,  $(\eta_c - \eta_0)$ , in 3D using the SMM, DGM and the BFM at 0.3, 0.7, 1.0 A/cm<sup>2</sup>, respectively, for (a) a constant tortuosity value, and (b) an adjusted tortuosity value for each model. When a single tortuosity value is used in the

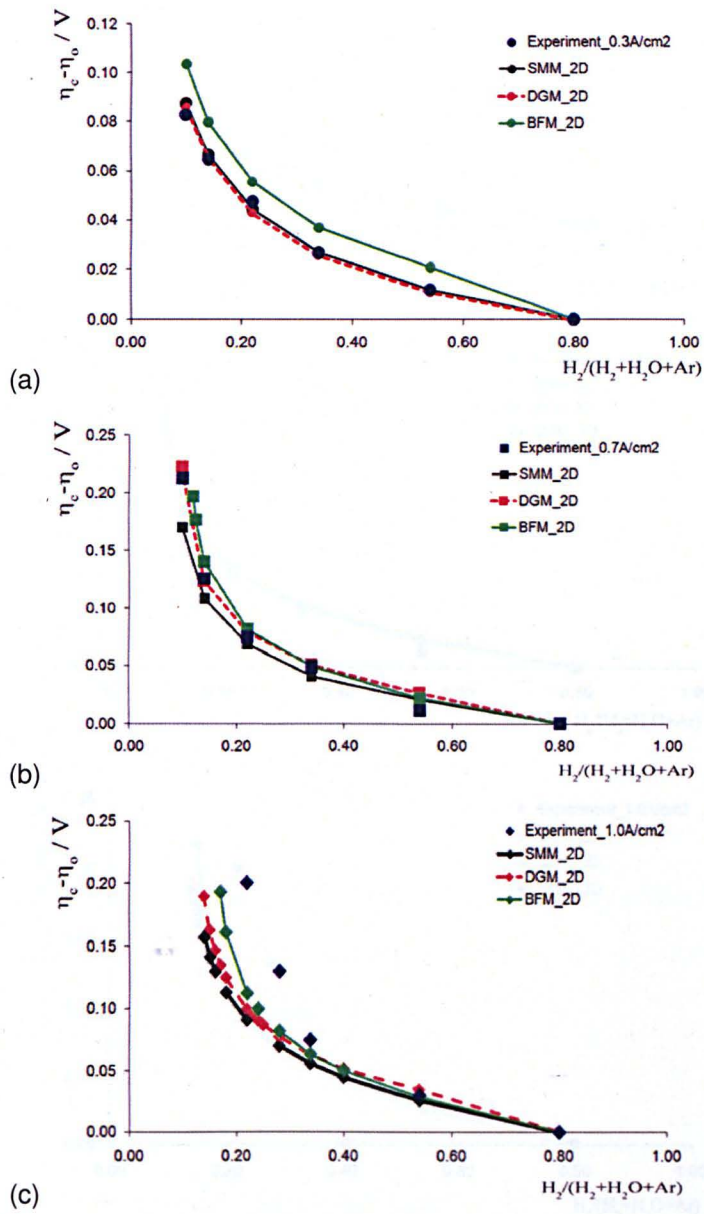


Figure 6.6: A comparison of the 2D models of the SMM, DGM and the BFM and the comparison with the experimental data at (a) 0.3, (b) 0.7 and (c) 1.0 A/cm<sup>2</sup>.

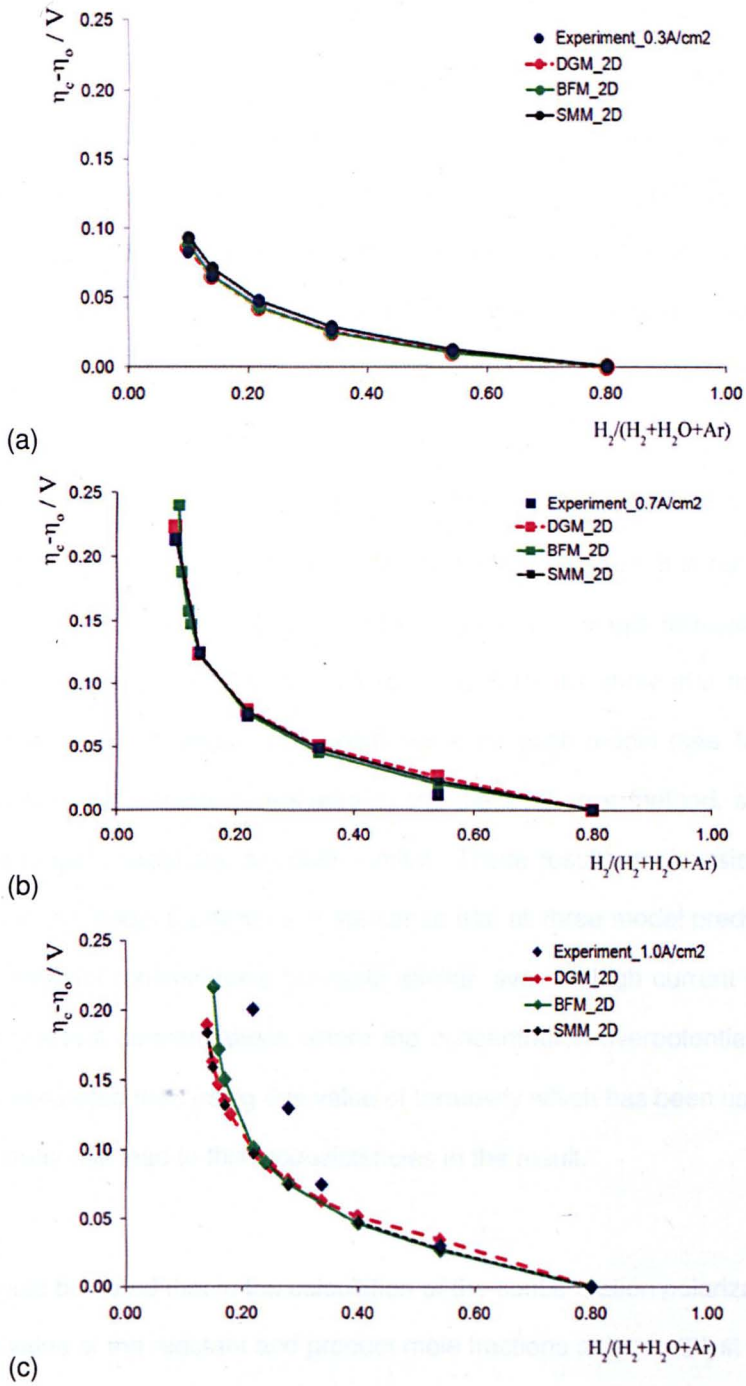
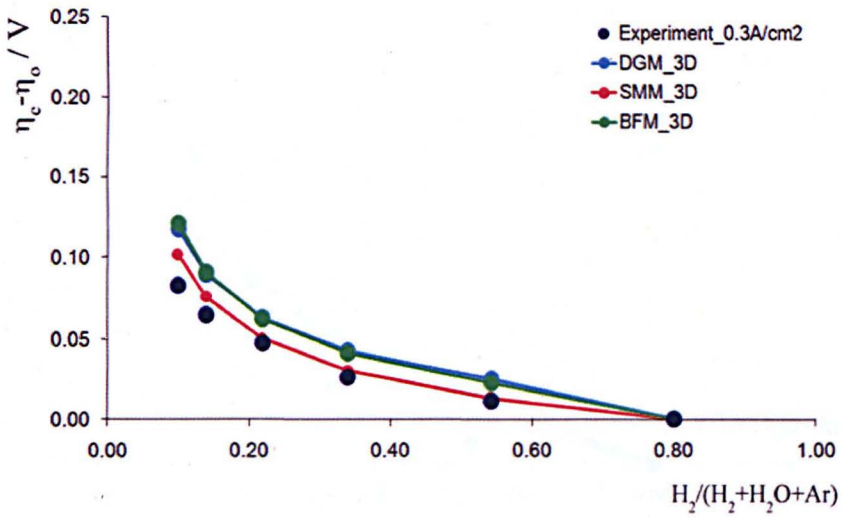


Figure 6.7: The 2D concentration polarization predictions of the SMM, DGM and the BFM for different inlet mole fractions of H<sub>2</sub> with the adjusted tortuosity parameter at (a) 0.3 (b) 0.7 (c) 1.0 A/cm<sup>2</sup>.

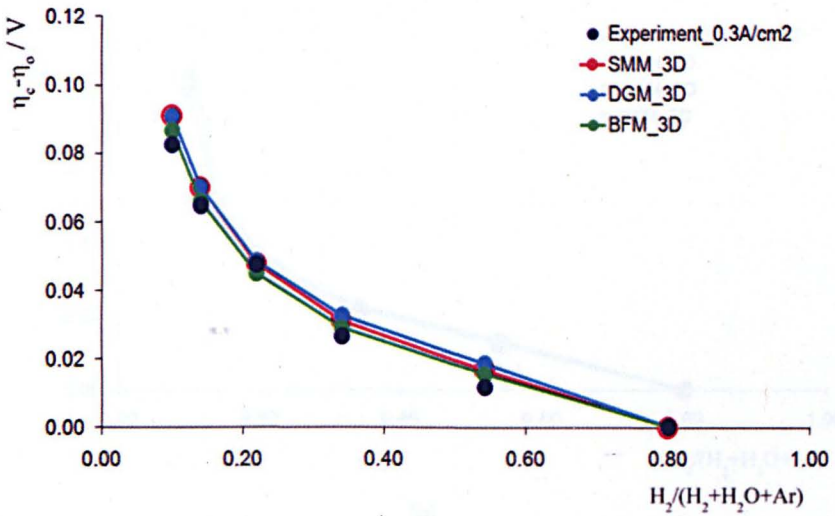
models, see Figs. 6.8 (a), 6.9 (a), and 6.10 (a), all the model overpredicts the experimental data. Also, it is observed that for the specific tortuosity value used, the model predictions fit better at high current densities and less well at low current densities. A comparison of Figs. 6.8 (b) with 6.9 (b) and 6.10 (b) show that the BFM predictions are better at the high current densities ( $1.0 \text{ A/cm}^2$ ) than those of the DGM and SMM, while the SMM predictions are better at the current densities  $0.3$  and  $0.7 \text{ A/cm}^2$  than those of the DGM and SMM.

As in the 2D results, the results shows alone the contradiction of using a single tortuosity value for the SMM, DGM and BFM. Therefore, it is not possible to assess which model predictions are best by using a single tortuosity value. On the other hand, Figs. 6.8 (b), 6.9 (b), and 6.10 (b) show that the model comparisons with the adjusted tortuosity value for each model (see Table 6.5) for the tortuosity parameters, adjusted by the trial and error method, show that the three model predictions are quite similar. These results are consistent with the 1D and 2D model predictions in the sense that all three model predictions of the concentration polarizations are quite similar, even at high current densities and low reactant concentrations where the concentration overpotential is high. As has been noted that, using one value of tortuosity which has been used in the original study has lead to this inconsistencies in the result.

It should be noted that in the calculation of the concentration polarization, the average value of the reactant and product mole fractions at the catalyst layer are used. Hence a significant change in the distribution of the species' concentration might result in a less significant change in the average value of the species concentration and, this, in turn, in the concentration polarization. Therefore, it is important to evaluate and compare the species concentration distribution

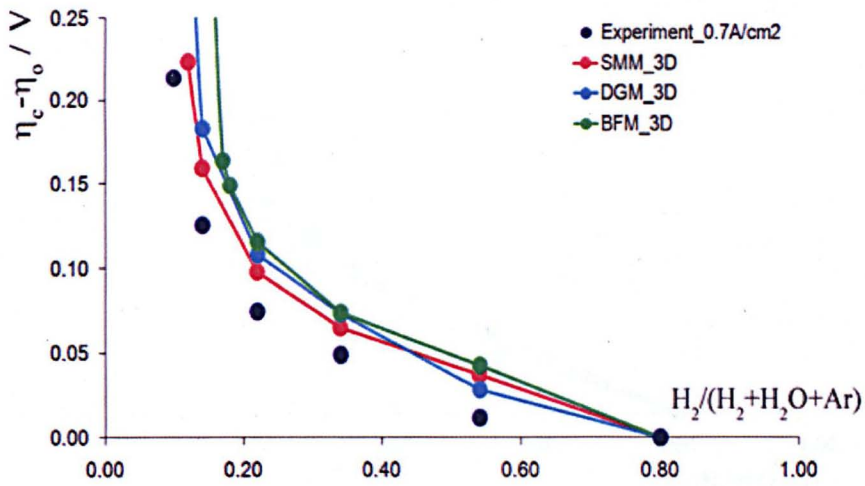


(a)

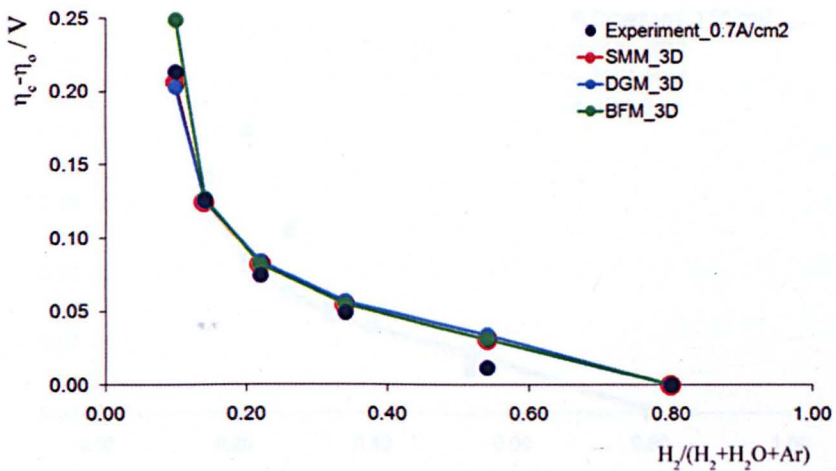


(b)

Figure 6.8: A comparison of the 3D predictions of the concentration polarization,  $(\eta_c - \eta_0)$ , of the SMM, DGM and the BFM when using a constant tortuosity parameter at  $0.3 \text{ A/cm}^2$  for (a)  $\tau=4.5$  and (b) the adjusted tortuosity parameter (see Table 6.5).

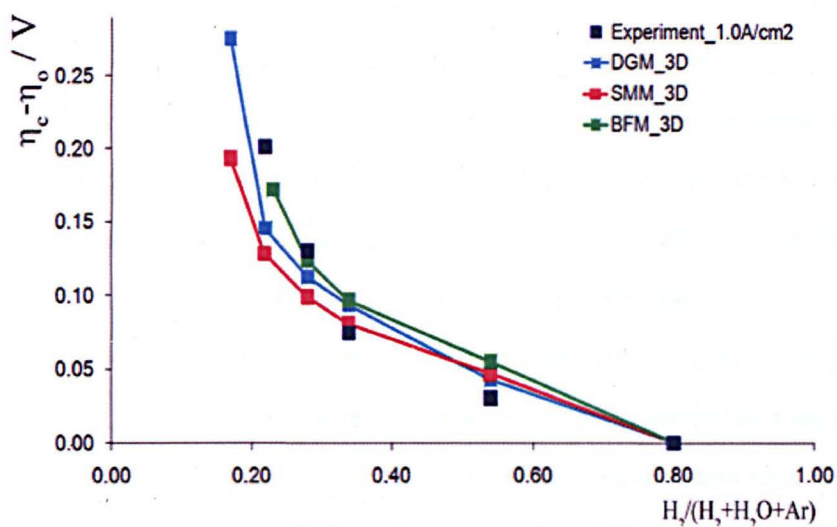


(a)

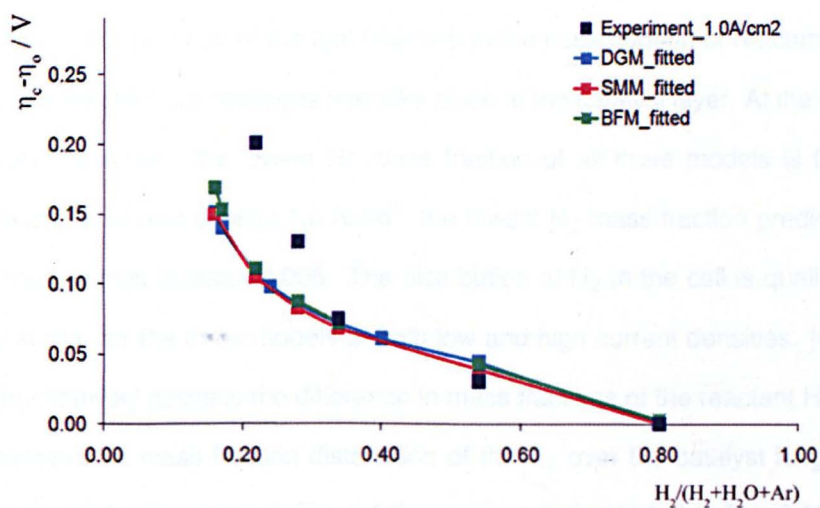


(b)

Figure 6.9: A comparison of the 3D predictions of the concentration polarization,  $(\eta_c - \eta_0)$  of the SMM, DGM and the BFM with using a constant tortuosity parameter at  $0.7 \text{ A/cm}^2$  for (a)  $\tau=4.5$  and (b) adjusted tortuosity parameter (see Table 6.5).



(a)



(b)

Figure 6.10: A comparison of the 3D predictions of the concentration polarization,  $(\eta_c - \eta_0)$  of the SMM, DGM and the BFM with using a constant tortuosity parameter at  $1.0 \text{ A/cm}^2$  for (a)  $\tau=4.5$  and (b) adjusted tortuosity parameter (see Table 6.5).

predictions over the cell for the different diffusion models to make a more thorough comparison even if there is no experimental data on the species concentration over the cell. It should be noted that the main difficulty in conducting the experiments to measure the species concentration in the cell is the high operating cell temperature. Figs. 6.11 (a), (c), and (e) show the  $H_2$  species mass fraction distribution over the anode side fuel channel, gas diffusion layer and catalyst for the SMM, DGM and BFM, respectively at  $0.3 \text{ A/cm}^2$  and inlet  $H_2$  mass fraction,  $w_{H_2} = 0.0202$ . Fig. 6.11 (b), (d) and (f) present the  $H_2$  species mass fraction distribution at  $1.0 \text{ A/cm}^2$  and inlet  $H_2$  mass fraction,  $w_{H_2} = 0.0202$ . The chosen low value of inlet  $H_2$  mass fraction represents a high concentration polarization region at high current density and low concentration polarization region for the low current density. At both high and low current densities, it is seen in Figs. 6.11 (a)-(f) that the mass fraction of  $H_2$  decreases in the fuel channel, anode layer and catalyst in the direction of the fuel flow due to the consumption of reactants as a result of the chemical reactions that take place at the catalyst layer. At the current density  $0.3 \text{ A/cm}^2$ , the lowest  $H_2$  mass fraction of all three models is 0.0165, while at the current density  $1.0 \text{ A/cm}^2$ , the lowest  $H_2$  mass fraction predicted by all three models is about 0.008. The distribution of  $H_2$  in the cell is qualitatively very similar for the three models at both low and high current densities. In order to quantitatively assess the difference in mass fractions of the reactant  $H_2$  more accurately, the mass fraction distribution of the  $H_2$  over the catalyst length and width ( $x$ - and  $z$ -directions in Fig. 6.11) has been demonstrated in Fig. 6.12 at (a)  $0.3 \text{ A/cm}^2$ , and (b)  $1.0 \text{ A/cm}^2$  and inlet  $w_{H_2} = 0.0202$ . Fig. 6.12 shows that at  $0.3 \text{ A/cm}^2$  and at the beginning of the catalyst layer where  $y = 0$ ,  $z = 0$ , and  $x = 0 \text{ m}$ , the  $H_2$  mass fractions are predicted as 0.0187, 0.0188, 0.0185 by the SMM, DGM and BFM, respectively. The relative difference between the SMM and DGM prediction is 0.4815% and between the SMM and BFM is 0.803%, and between

DGM and BFM is 1.278%. At  $0.3 \text{ A/cm}^2$  and at the end of the TPB, where  $y = 0$ ,  $z = 0$  and  $x = 0.02 \text{ m}$ , the relative difference between the SMM and DGM mass fraction predictions is 0.608%, the relative difference between the SMM and BFM is 0.912% and the relative difference between DGM and BFM is 1.510%. The results show the highest difference of the models has been observed between the DGM and BFM while the lowest difference has been observed between the SMM and DGM predictions. At  $1.0 \text{ A/cm}^2$ , the SMM, DGM and BFM predictions of the  $\text{H}_2$  mass fraction at the inlet of the TPB ( $x = 0$ ,  $y = 0$  and  $z = 0$ ) are 0.016, 0.016, and 0.015, respectively. The relative difference between the predictions of the SMM and DGM is 2.804%, between the SMM and DGM the difference is 7.649% and between the DGM and BFM the difference is 10.167%. At  $1.0 \text{ A/cm}^2$ , and at the end of the catalyst layer ( $y = 0$ ,  $z = 0$  and  $x = 0.02 \text{ m}$ ), the relative difference between the SMM and DGM mass fraction predictions is 4.563%, between the SMM and BFM it is 13.872% and between DGM and BFM it is 17.630%. The fact that the difference between the model predictions of the DGM and the BFM both at  $0.3 \text{ A/cm}^2$  and  $1.0 \text{ A/cm}^2$  is highest in comparison to the difference between the SMM and the DGM and between the SMM and BFM points out the fact that the differences are not due to the Knudsen diffusion effect but rather due to the tortuosity parameter, in turn the effective diffusivity effect. Moreover, the high difference observed in the mass fraction predictions between the models have not been observed in the concentration polarization calculations. This may be due to the fact that averaging of the values and taking logarithm of those in the concentration polarization calculation smears out the differences in the predictions of the mass fraction in the models.

Fig. 6.13 shows the distribution of the mass fraction of  $\text{H}_2$  along the height of the anode ( $z$ -direction in Fig. 6.11 (a)) at the mid-point of the anode plane

( $x=0.01\text{ m}$ ,  $y=0$ ) for (a)  $0.3\text{ A/cm}^2$  and (b)  $1.0\text{ A/cm}^2$ , and the inlet  $w_{H_2}=0.0202$ . According to the predictions of all the three models, the  $H_2$  mass fraction decreases nonlinearly from  $z=0.00202\text{ m}$  (see Fig. 6.11 (a)), i.e. the top of the anode layer, to  $z=0$ , where the catalyst layer ends. It is observed that at  $0.3\text{ A/cm}^2$ , and at the top of the anode layer where  $x=0.001$ ,  $y=0\text{ m}$ , and  $z=0.0202\text{ m}$ , the  $H_2$  mass fractions are predicted to be 0.01856, 0.0186, 0.01856 by the SMM, DGM and BFM, respectively. The difference between the SMM and DGM prediction is 0.215% and between the SMM and BFM is 0.005%, and between the DGM and BFM is 0.22%. At  $0.3\text{ A/cm}^2$ , and at the end of the catalyst layer where  $x=0.001$ ,  $y=0\text{ m}$ , and  $z=0\text{ m}$ , the  $H_2$  mass fractions predicted are 0.0178, 0.0179, 0.0176 by the SMM, DGM and BFM, respectively. The relative difference between the SMM and DGM prediction is 0.281% and between the SMM and BFM is 1.124%, and between the DGM and BFM is 1.401%. The highest relative difference has been observed between DGM and BFM which is 1.4001.

At  $1.0\text{ A/cm}^2$  and at the top of the anode layer where  $x=0.001$ ,  $y=0\text{ m}$ , and  $z=0.0202\text{ m}$ , the  $H_2$  mass fractions are predicted to be 0.0146, 0.0150, 0.0146 by the SMM, DGM and BFM, respectively. The relative difference between the SMM and DGM prediction is 2.88% and between SMM and BFM is 0.069%, and between DGM and BFM is 2.87%. At  $1.0\text{ A/cm}^2$ , and at the end of the catalyst layer where  $x=0.001$ ,  $y=0\text{ m}$ , and  $z=0\text{ m}$ , the  $H_2$  mass fractions predicted are 0.0125, 0.0130, 0.0112 by the SMM, DGM and BFM, respectively. The relative difference between the SMM and DGM predictions is 4% and between the SMM and BFM is 10%, and between the DGM and BFM is 13.84%.

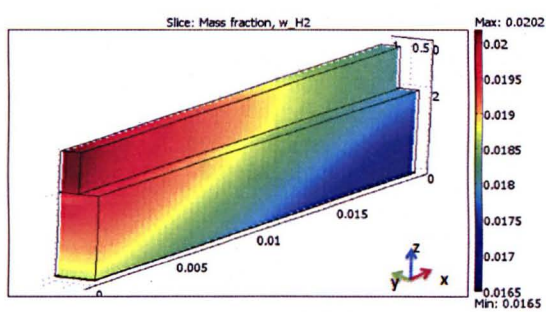
It can be concluded that the predictions between the models is highest at 1.0

$\text{A/cm}^2$  and at the end of the catalyst layer where the electrochemical reactions occur. The DGM predictions are higher than the SMM and the BFM and the BFM predictions are the lowest. In the concentration polarization calculations, the values at the catalyst layer is used. However a comparison of the results at  $1.0 \text{ A/cm}^2$  show that the difference in the  $\text{H}_2$  mass fraction predictions of the models result in a less significant difference in the concentration polarization predictions.

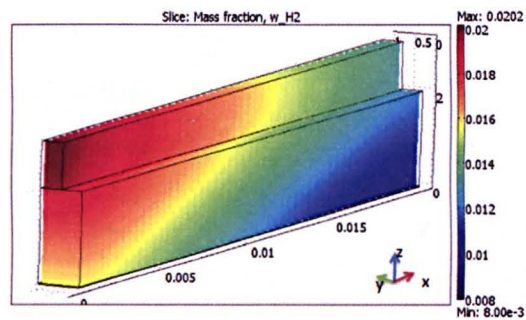
## 6.9 Comparison of the 1D, 2D and 3D Results

Figure 6.14 (a), (b) and (c) show the predictions of the concentration polarization of the SMM in 2D and 3D and a comparison with 1D at 0.3, 0.7, and  $1.0 \text{ A/cm}^2$ , respectively. From these figures, it is observed that the 3D simulations match the experiments better than do the 1D and 2D predictions at high current densities. However it slightly overpredicts the experimental data at low current densities. Overall, the 3D predictions make only a slight improvement in the prediction at  $1.0 \text{ A/cm}^2$  in comparison to the 1D and 2D predictions.

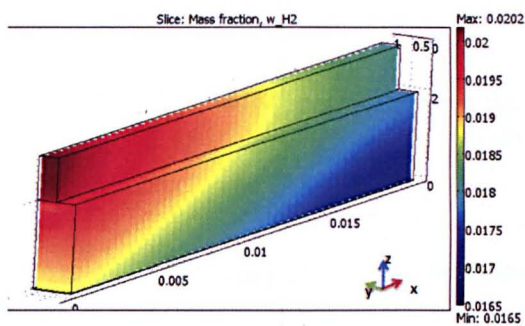
In Figs. 6.15 (a) - (c) and Figs. 6.16 (a) - (c), a comparison of the 1D, 2D and 3D concentration polarization predictions at different current densities are shown for the DGM and BFM, respectively. As in the predictions of the SMM, especially at high current densities, a slight improvement in the 3D predictions of the DGM and BFM are seen in comparison to 1D and 2D predictions, the 1D and 2D predictions are similar. At low current densities, the 3D predictions of the DGM and BFM slightly overpredict the experimental data, especially at high inlet  $\text{H}_2$  concentrations. This is due to the fact that, in 3D analysis, the width of the gas channel which is in size half the width of the anode are considered while in 1D and



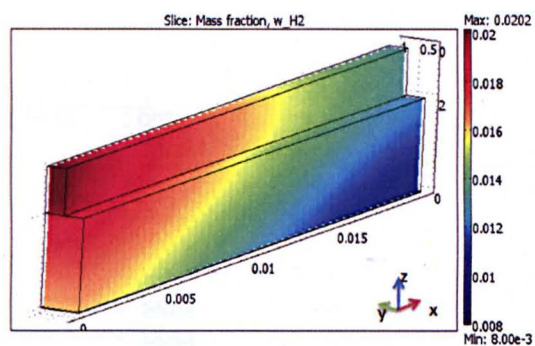
(a) SMM



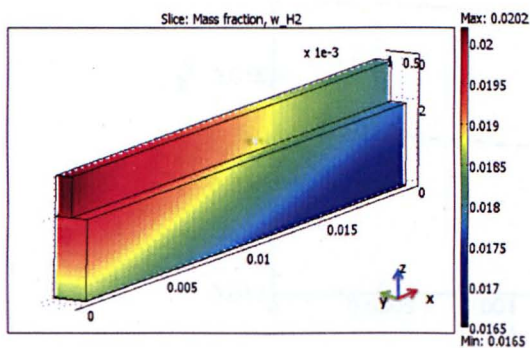
(b) SMM



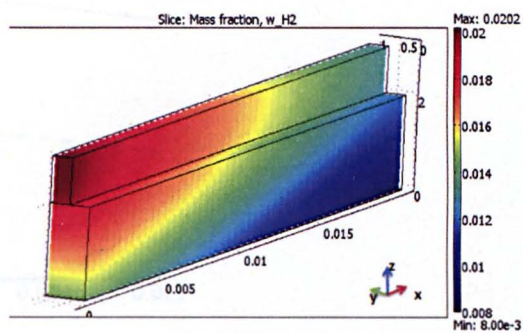
(c) DGM



(d) DGM

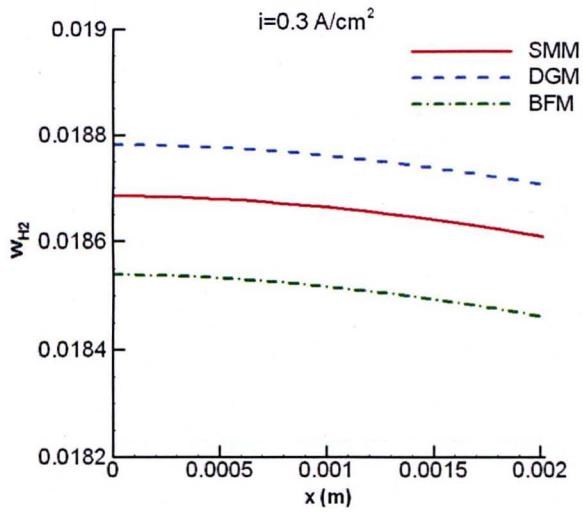


(e) BFM

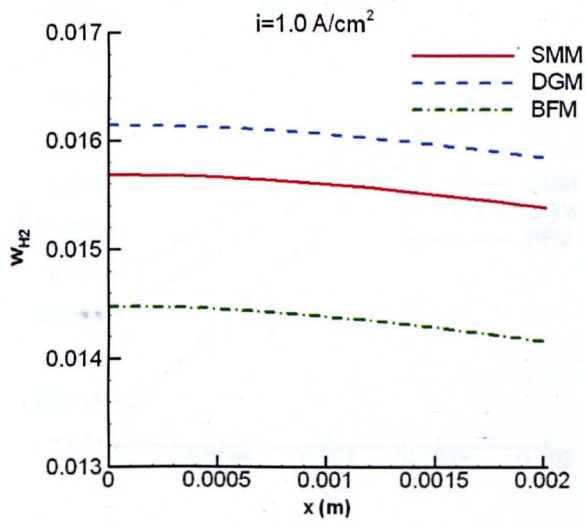


(f) BFM

Figure 6.11: The  $H_2$  mass fraction distribution over the SOFC anode for at  $0.3 \text{ A/cm}^2$  for (a) SMM, (c) DGM and (e) BFM, and at  $1.0 \text{ A/cm}^2$  for (b) SMM, (d) DGM, and (f) BFM. The inlet  $w_{H_2}$  is 0.0202.

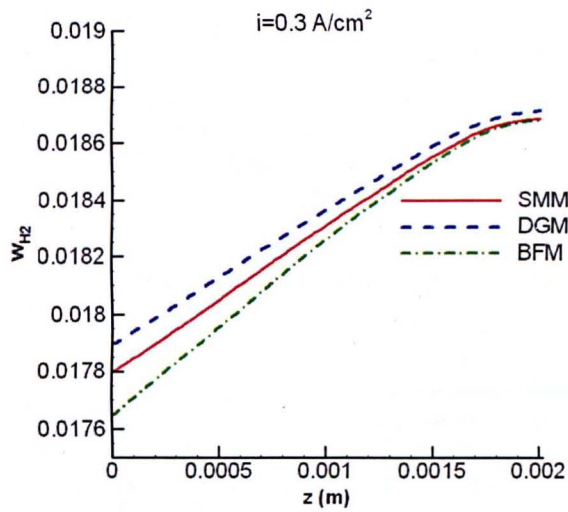


(a)

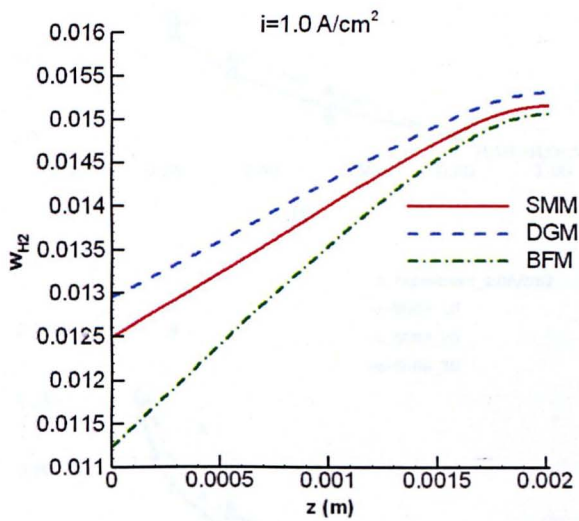


(b)

Figure 6.12: A comparison of the SMM, DGM and BFM predictions of the  $H_2$  mass fraction distribution over the length of the catalyst layer at  $y = 0, z = 0$  at (a)  $0.3 \text{ A/cm}^2$ , and (b)  $1.0 \text{ A/cm}^2$ , and  $w_{H_2}=0.0202$ .

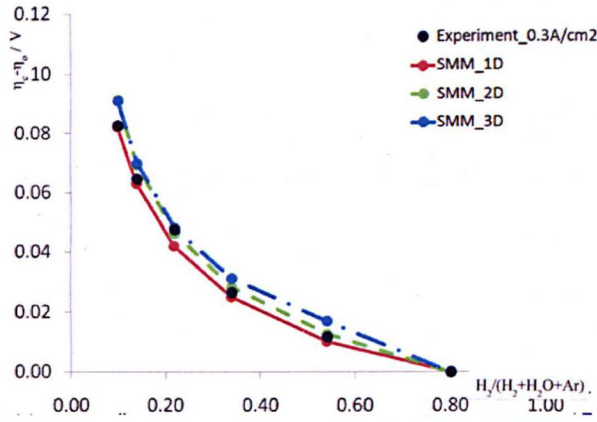


(a)

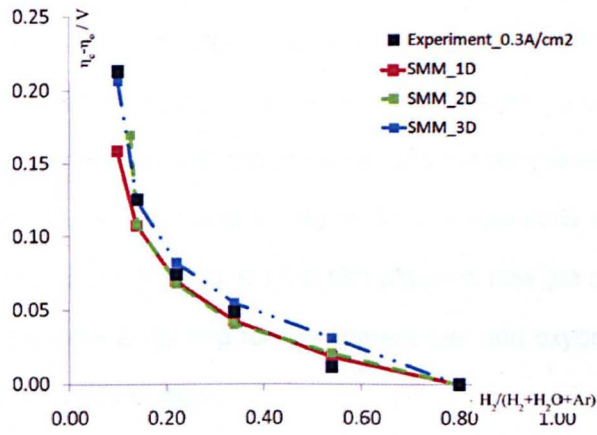


(b)

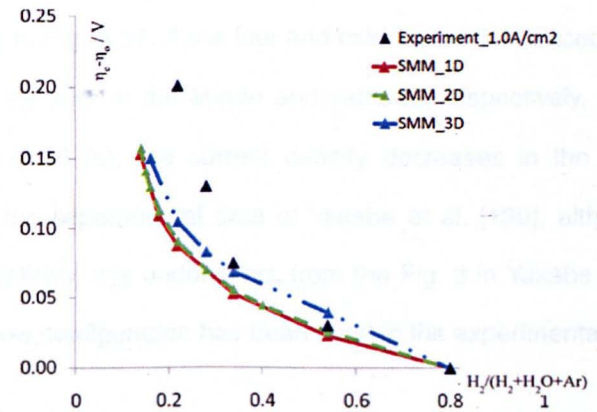
Figure 6.13: A comparison of the SMM, DGM and BFM predictions of the  $H_2$  mass fraction distribution over the height of the anode and catalyst at the midpoint of the length of the anode ( $x = 0.01, y = 0$ ) at (a)  $0.3 \text{ A/cm}^2$ , and (b)  $1.0 \text{ A/cm}^2$ , and  $w_{H_2}=0.0202$ .



(a)



(b)



(c)

Figure 6.14: A comparison of the 1D, 2D and 3D concentration polarization predictions of the SMM at the current densities (a) 0.3, (b) 0.7, and (c) 1.0 A/cm<sup>2</sup>.

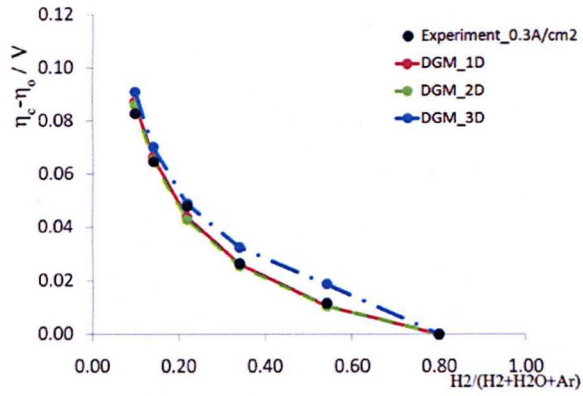
2D analyse the width of the gas channel and anode are same. On the other hand, the difference between the results obtained from the 1D and 2D models is that the mass transport processes in the fuel gas channel has been taken into account in the later, hence the similarities between the 1D and 2D predictions show that taking into account the convective dominated mass transport processes in the gas channel has a negligible effect on the prediction of the concentration polarization.

### **6.9.1 Evaluation of the Constant Current Density Assumption**

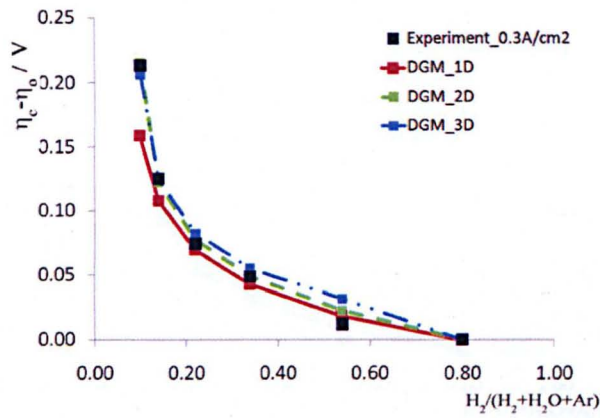
In this thesis, it has been assumed that current is distributed uniformly over each cell. In fact, physically the distribution of the current density is dependent on the mass fractions of the reactants and products, and the temperature. Usually this relationship is calculated by using the Butler-Volmer equations which have been discussed in section 3.1.1.3. Fig. 6.17 of [98] presents how the current density is distributed in the cells according to the different fuel and oxygen inlet direction configurations for a SOFC stack.

According to Fig. 6.17, if the fuel and oxidant are introduced in the opposite directions at the inlet of the anode and cathode, respectively, i.e. counter-flow configuration (3.10 (c)), the current density decreases in the direction of the fuel flow. In the experimental data of Yakabe et al. [130], although it was not mentioned explicitly, it is understood, from the Fig. 3 in Yakabe et al. [130], that the counter-flow configuration has been used in the experimental investigation.

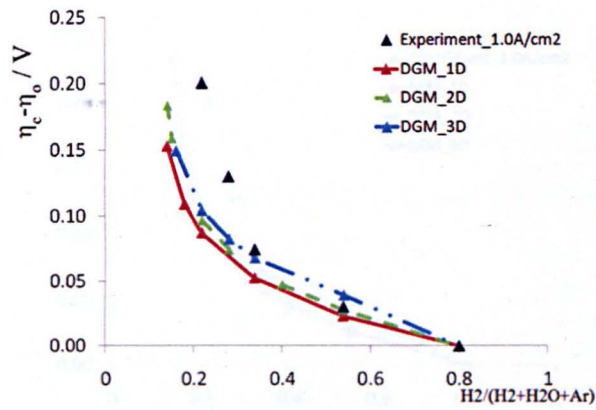
In order to calculate the distribution of the current in the cell, the cathode side activation overpotential is required and hence the Butler-Volmer type of relation cannot be used for a half fuel cell model. However, the effect of the current



(a)

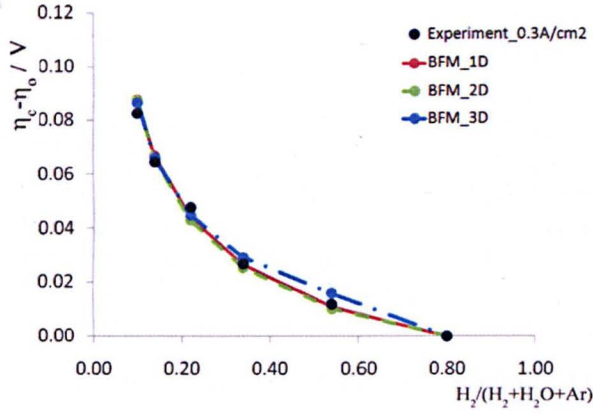


(b)

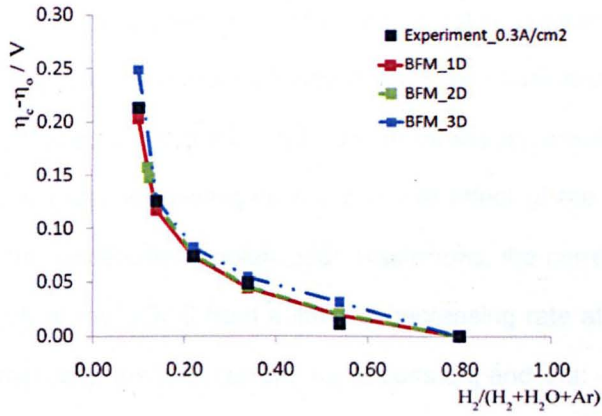


(c)

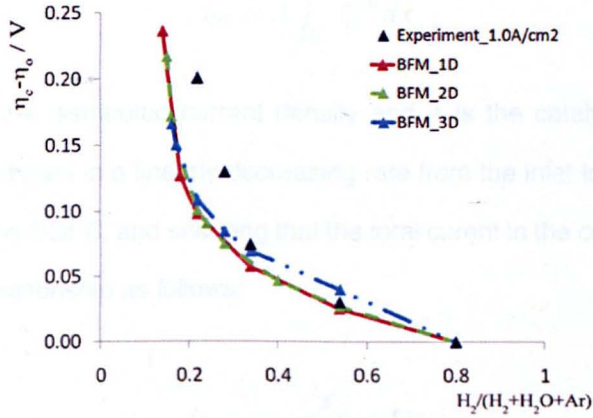
Figure 6.15: A comparison of the 1D, 2D and 3D concentration polarization predictions of the DGM at the current densities at (a) 0.3, (b) 0.7, and (c) 1.0 A/cm<sup>2</sup>.



(a)



(b)



(c)

Figure 6.16: A comparison of the 1D, 2D and 3D concentration polarization predictions of the BFM at the current densities at (a) 0.3, (b) 0.7, and (c) 1.0 A/cm<sup>2</sup>.

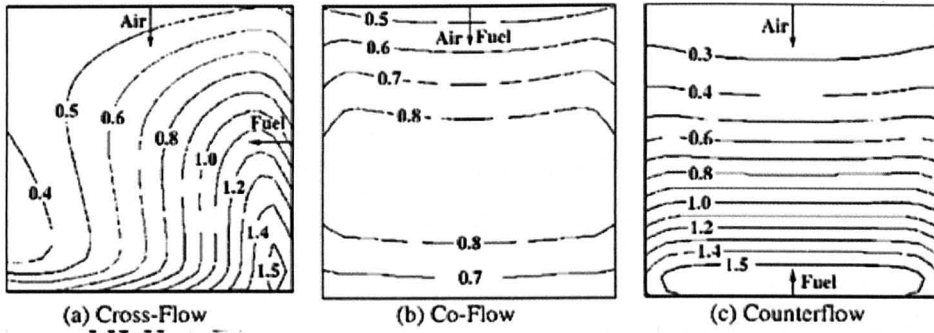


Figure 6.17: Current density distribution in the active area of a cross flow planer SOFC stack [98].

density distribution on the prediction of the concentration polarization can still be investigated by setting the current density in every computational cell according to Fig. 6.17 and ensuring that the total current density is conserved in the cell. In this thesis, in order to investigate the possible effect of the current density distribution on the concentration polarization predictions, the current is distributed along the length of the SOFC from a linearly decreasing rate at the inlet to the outlet. Mathematically, the total current,  $i_{tot}$  is constant and it is:

$$i_{tot} = A \int_0^L i_0^{dist} dx \quad (6.32)$$

where  $i_0^{dist}$  is the distributed current density and  $A$  is the catalyst area. If the current is distributed in a linearly decreasing rate from the inlet to the outlet over the length of the SOFC, and ensuring that the total current in the cell is conserved, we obtain a relationship as follows:

$$i_{0,tot} = -a \frac{x}{L} i_0 + b i_0 \quad (6.33)$$

where  $a$  and  $b$  are the empirical constants. The values of 1 and 3/2 for  $a$  and  $b$ , respectively, are consistent with the current density distribution shown in Fig.6.17

(c).

Figs. 6.18 (a) and (b) present a comparison of the concentration polarization prediction,  $(\eta_c - \eta_o)$ , of the SMM at different inlet concentrations of  $H_2$  at  $0.3 A/cm^2$  and  $1.0 A/cm^2$ , respectively. It is observed that there is no significant difference in the concentration polarization predictions of the models with the linearly and uniformly distributed current density assumptions at both  $0.3$  and  $1.0 A/cm^2$ . However, it is important to compare the mass fraction distribution of the species in order to assess the difference in the predictions of the two different approaches. Figs. 6.19 (a) and (b) show the  $H_2$  mass fraction distribution over the length of the TPB at  $0.3 A/cm^2$  and  $1.0 A/cm^2$ , respectively. At  $0.3 A/cm^2$ , at the beginning of the catalyst, the  $H_2$  mass fraction predicted by the model with a constant current density assumption is 2.67 % higher than the linear density model, while at the outlet constant model predictions with a constant current density is 3.43% below that of the model predictions with a linear current density assumption. However, when the area under the curves -which is the average mass fraction- are compared, it is observed that the difference between the area is about 0.41% and that is the main reason for the insignificant difference observed in the concentration polarization predictions of the two models. On the other hand, at  $1.0 A/cm^2$ , at the beginning of the catalyst, the  $H_2$  mass fraction predicted by the model with a constant current density assumption is 2.67% higher than the linear density model, while at the outlet the constant model predictions with the constant current density is 3.43% below that of the model predictions with a linear current density assumption. However, the difference between the areas under the curves is about 0.6% and that is slightly higher than the predictions at  $0.3 A/cm^2$ .

Figs. 6.20 (a) and (b) show a comparison of the concentration polarization prediction,  $(\eta_c - \eta_o)$ , of DGM at different inlet concentrations of  $H_2$  at 0.3  $A/cm^2$  and 1.0  $A/cm^2$ , respectively. It is observed that there is no significant difference in the concentration polarization predictions of the models with the linearly and uniformly distributed current density assumptions at both 0.3 and 1.0  $A/cm^2$ . Figs. 6.23 (a) and (b) show the distribution of the mass fraction of  $H_2$  at 0.3  $A/cm^2$  and 1.0  $A/cm^2$ , respectively with the inlet  $w_{H_2}$  0.0202. Again it is observed that although there is a difference in the the distribution of the mass fraction, the average mass fraction predicted by the linearly and uniformly distributed current density assumptions are similar. At 0.3  $A/cm^2$ , at the beginning of the TPB, the  $H_2$  mass fraction predicted by the model with a constant current density assumption is 3.74% higher than the linear density model, while at the outlet the constant model predictions with the constant current density is 2.86% below that of the model predictions with a linear current density assumption. However, when the area under the curves -which is the average mass fraction- are compared, it is observed that the difference in the areas is about 0.32% and that is the main reason for the insignificant difference observed in the concentration polarization predictions of the two models. On the other hand, at 1.0  $A/cm^2$ , and at the beginning of the TPB, the  $H_2$  mass fraction predicted by the model with a constant current density assumption is 8.64% higher than that of the linear density model, while at the outlet the constant model predictions with the constant current density is 13.04% below that of the model predictions with a linear current density assumption. However, the difference between the areas under the curves is about 0.65%, and this is slightly higher than the area difference under the curves for the models at 0.3  $A/cm^2$ , which is only 0.13%.

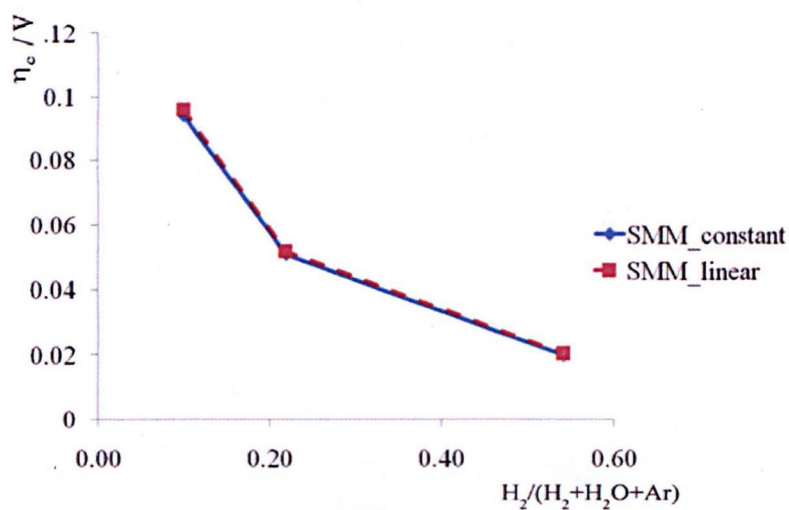
Figs. 6.20 (a) and (b) show a comparison of the concentration polarization

prediction,  $(\eta_c - \eta_o)$ , of BFM at different inlet concentrations of  $H_2$  at  $0.3 \text{ A/cm}^2$  and  $1.0 \text{ A/cm}^2$ , respectively. The difference in of the mass fraction of  $H_2$  at the inlet at  $0.3 \text{ A/cm}^2$  and  $1.0 \text{ A/cm}^2$  is 7.85%. At the beginning of TPB, the  $H_2$  mass fraction predicted by the model with a constant current density assumption is 5.64% higher than that of the linear density model, while at the outlet the model predictions with the constant current density is 10.04% below than that of the model predictions with a linear current density assumption. However, the difference between the areas under the curves is about 0.53%, and this is slightly higher than the area difference under the curves for the models at  $0.3 \text{ A/cm}^2$ , which is about 0.22%.

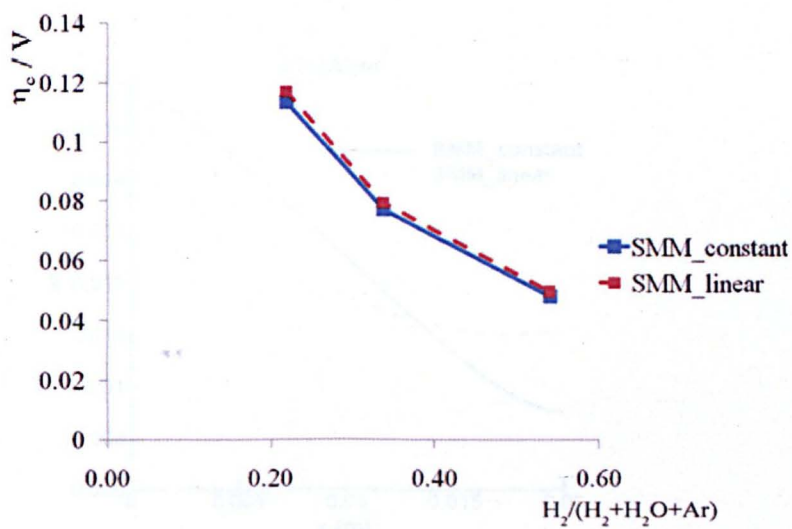
It should be noted, in the analysis presented in this section the constant current density assumption has been compared with the linearly distributed current density assumption. The effect of the nonlinear distribution of the current density assumption has been investigated by Tsenoris et al. [118] and therefore it has not been addressed here. Their analysis also shows that as long as the average of the distributed current density is equal to the total current, the actual current density is not significant in the computation of the concentration polarization for both high and low fuel utilization [118]. Therefore constant current density can be taken as a satisfactory assumption for the analysis presented in this chapter.

## 6.10 Further Discussion

It is of importance to discuss why the predictions of the SMM, DGM and the BFM are quite similar for the cases investigated in this thesis. Again it should be



(a)



(b)

Figure 6.18: A comparison of the 3D concentration polarization predictions of the SMM with the constant and the linear variations in the current density distribution at (a)  $i=0.3 \text{ A/cm}^2$ , and (b)  $1.0 \text{ A/cm}^2$ .

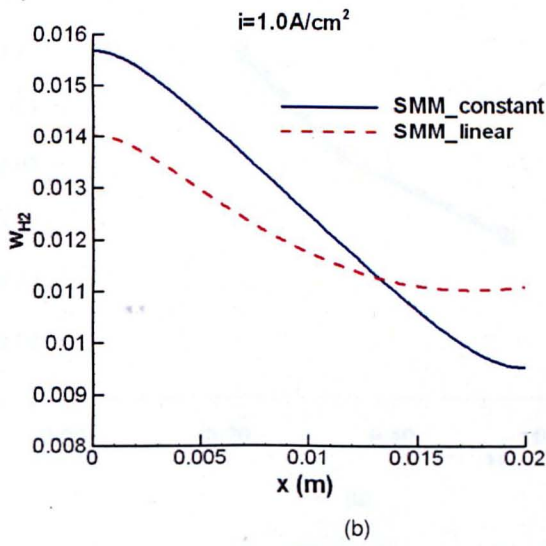
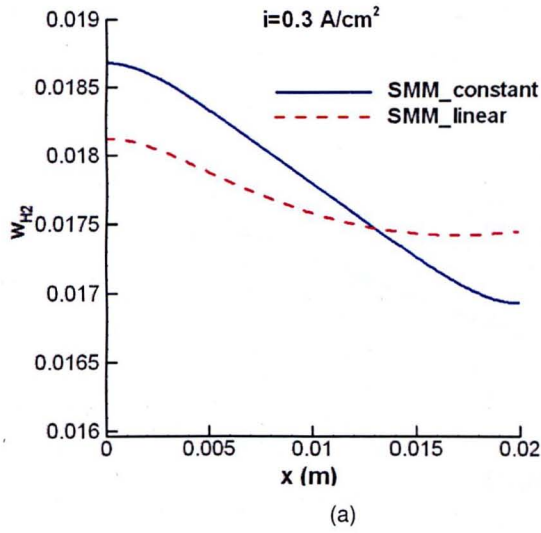
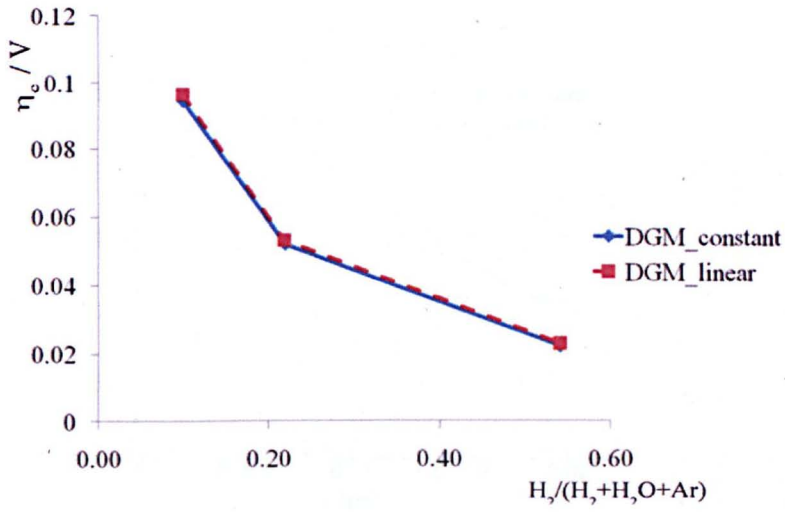
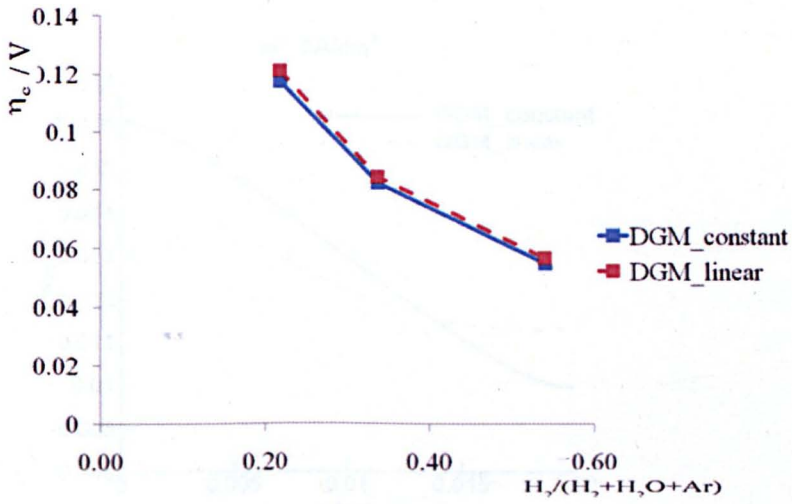


Figure 6.19: A comparison of the distribution of mass fraction of  $H_2$  along the length of the catalyst layer with the constant and linear variations in the current density distribution at (a)  $i=1.0 \text{ A/cm}^2$ , and (b)  $0.3 \text{ A/cm}^2$ , for the SMM.

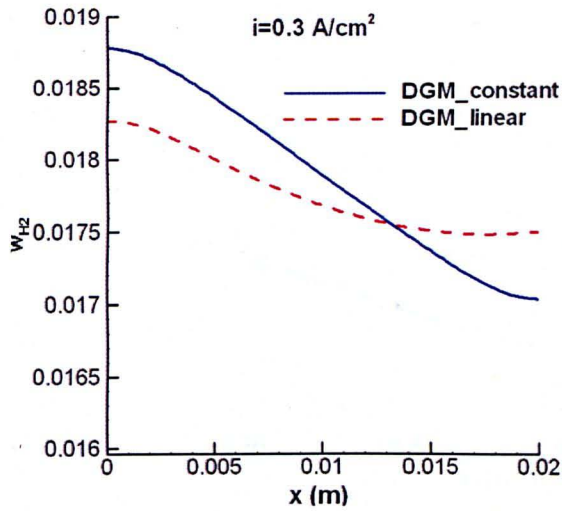


(a)

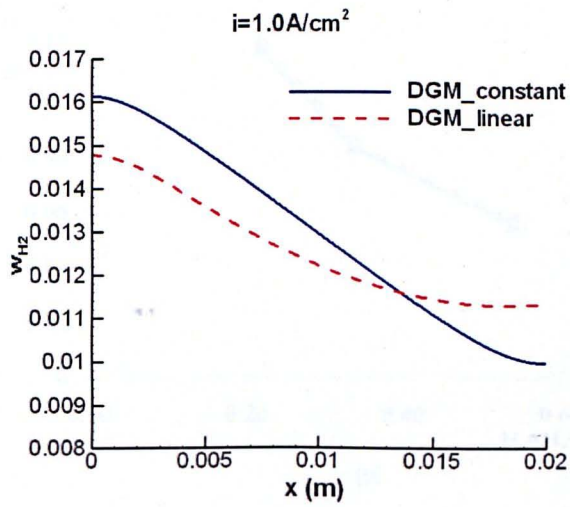


(b)

Figure 6.20: A comparison of the 3D concentration polarization predictions of the DGM with the constant and the linear variations in the current density distribution at (a)  $i=0.3 \text{ A/cm}^2$ , and (b)  $1.0 \text{ A/cm}^2$ .

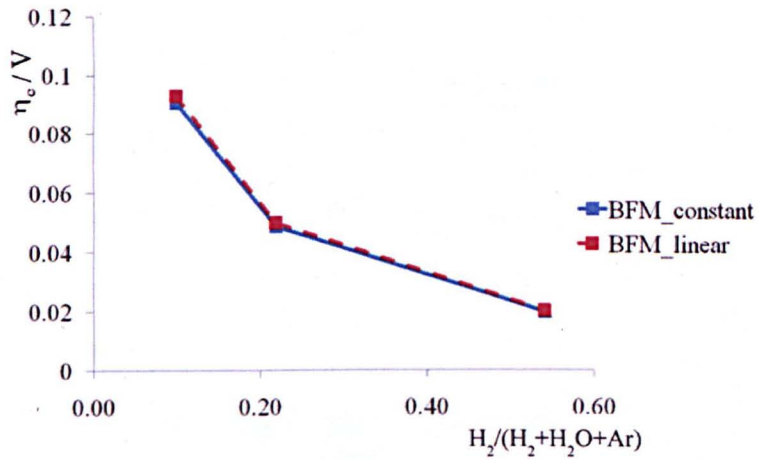


(a)

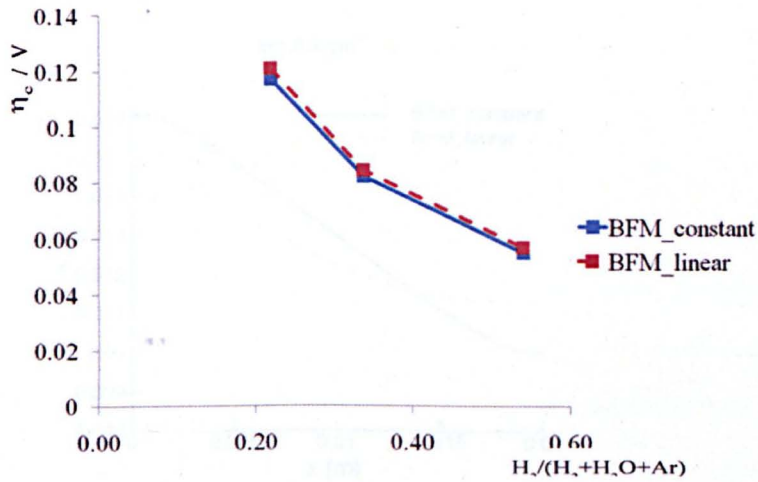


(b)

Figure 6.21: A comparison of the distribution of mass fraction of  $\text{H}_2$  along the length of the catalyst layer with the constant and linear variations in the current density distribution at (a)  $i=1.0 \text{ A/cm}^2$ , and (b)  $0.3 \text{ A/cm}^2$ , for the DGM.

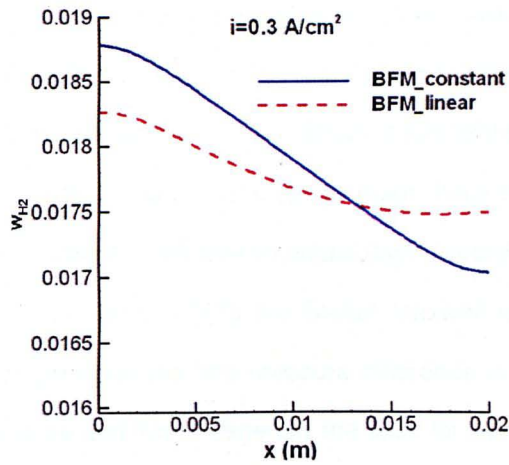


(a)

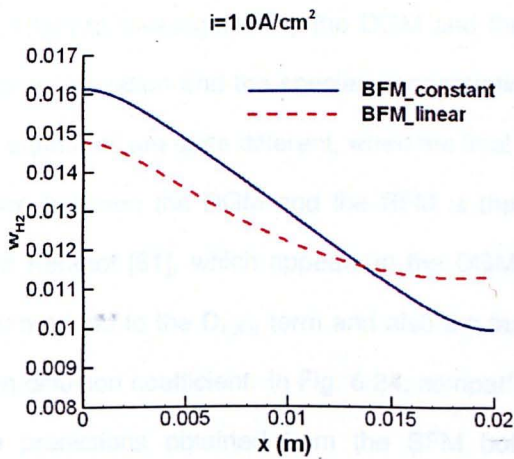


(b)

Figure 6.22: A comparison of the 3D concentration polarization predictions of the BFM with the constant and the linear variations in the current density distribution at (a)  $i=0.3 \text{ A/cm}^2$ , and (b)  $1.0 \text{ A/cm}^2$ .



(a)



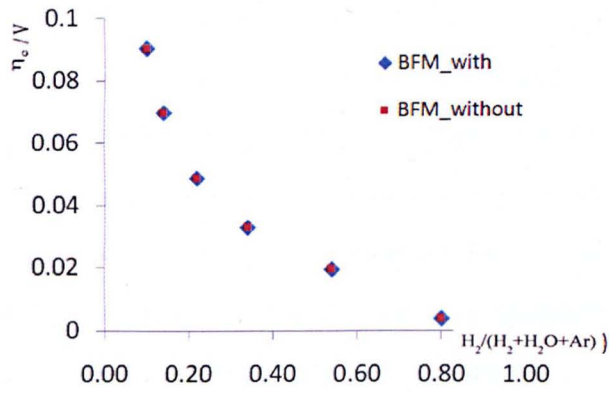
(b)

Figure 6.23: A comparison of the distribution of mass fraction of H<sub>2</sub> along the length of the catalyst layer with the constant and linear variations in the current density distribution at (a)  $i = 1.0 \text{ A/cm}^2$ , and (b)  $0.3 \text{ A/cm}^2$ , for the BFM.

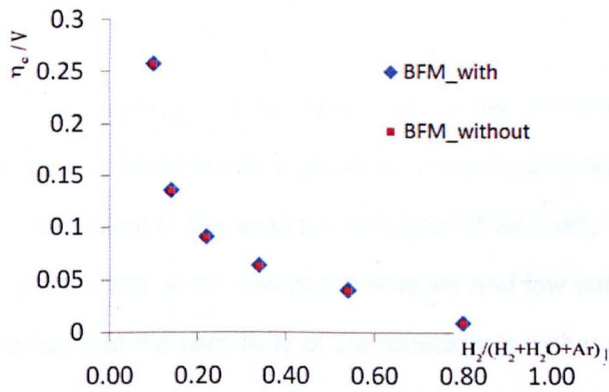
noted that the difference between the SMM and the DGM is that while the former does not take into account the Knudsen diffusion, the later does. As a result, at a uniform pressure the relationship between the molar flux of the SMM, namely  $\sum \mathbf{N}_i = 0$ , but the DGM obeys the Graham's law, i.e.  $\sum \mathbf{N}_i \sqrt{M_{w,i}} = 0$ . On the other hand, the condition of the conservation of mass in a chemically reacting system requires that  $\sum \mathbf{N}_i M_{w,i} = 0$ . At a uniform pressure, the existence of a relation between the species fluxes, which is Graham's law, is inconsistent with the demand of stoichiometry. In order to meet these two requirements, usually the pressure gradient is left free to adjust itself accordingly. In such a case, as also discussed in Jackson [47], the Stefan Maxwell equations are still a good approximation provided that the pressure difference is small compared with the absolute pressure and this is generally the case for solid oxide fuel cells.

It is important to investigate why the DGM and the BFM predictions of the concentration polarization and the species concentrations are similar. Although the starting equations are quite different, when the final equations are compared, the difference between the DGM and the BFM is the 'extra viscous term', as discussed in Kerkhof [61], which appears in the DGM but not in the BFM and the  $\kappa/K_i$  term added to the  $D_{i,Kn}$  term and also the factor 0.89 which multiplies the Knudsen diffusion coefficient. In Fig. 6.24, comparisons of the concentration polarization predictions obtained from the BFM both with and without the  $\kappa/K_i$  term, at current densities 0.3, 0.7, and 1.0 A/cm<sup>2</sup> have been presented. The results show that the inclusion of this term has a negligible effect on the predictions of concentration polarization at all the current densities and inlet H<sub>2</sub> concentrations investigated in this thesis.

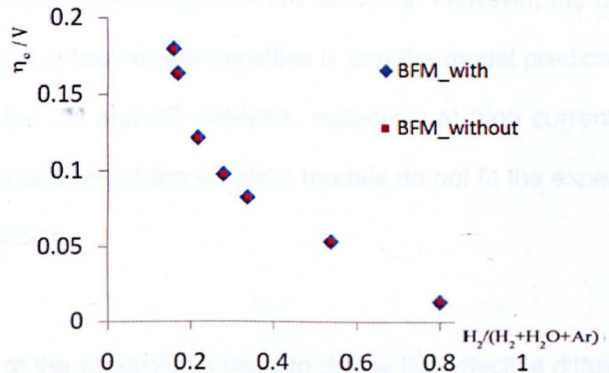
In my view, the final set of equations for the BFM can be criticized on the fact



(a)



(b)



(c)

Figure 6.24: A comparison of the 3D concentration polarization predictions of the BFM, both with and without  $\kappa/K_i$ , at the current densities (a) 0.3 (b) 0.7, and (c) 1.0 A/cm<sup>2</sup>.

that the  $\kappa/Ki$  term already accounts for the effect of the intermolecular collisions of the species and the addition of the Stefan-Maxwell type of relations to the Binary Friction Model may result in an additional accountment for the same term in the governing equations. Moreover, the factor 0.89 in the Knudsen diffusion has been found by fitting the predictions for one set of experimental data and the validity of this value over a large range of conditions has not been investigated. Moreover, the BFM equations do not satisfy Graham's relationship at a uniform pressure which has been experimentally well established and well validated relation.

Moreover, in this analysis, as we have seen in the previous chapter, the tortuosity plays a very important role in deciding which model predictions are the best. It must be noted that in this analysis, the value of tortuosity was chosen in order to fit the parameters at the low concentrations and low current densities. Considering the fact that the sensitivity of the tortuosity is higher at high current densities than at the low current densities, its value can be chosen so that the model predictions fit well at high current densities. However, the main reason for fitting the models at low current densities is that the model prediction is expected to improve in the 2D and 3D analysis, especially at high current densities. In general, the predictions of the diffusion models do not fit the experiments well at all current densities.

The value of the tortuosity is used to define the effective diffusion coefficient and hence a discussion on the tortuosity is in fact associated with the determination of the effective diffusion coefficient. The effective diffusion coefficient is usually determined by using the Wicke-Kellenbach cell. As discussed in Jackson [47], the experimentally measured effective diffusivity would incorrectly predict the

system consisting of the chemical reactions. This is an important point to note and, in general, it has been ignored mostly in the experimental measurements.

## 6.11 Conclusions

Based on the findings of this chapter, the following conclusions may be drawn:

- The two- and three-dimensional results show that the predictions of the SMM, DGM and the BFM are quite similar, even at the highest current density, while the BFM predictions are slightly better than those of the DGM and the SMM. These results are consistent with the 1D predictions obtained in Chapter 5 in the sense that the tortuosity has an important effect on the predictions of the concentration polarization, in other words, the mass diffusion dominated processes, and the three diffusion models produce almost similar concentration polarization predictions.
- The species mass fraction distribution along the catalyst length has been compared and evaluated for each model in the high and low current concentration regions. The results show that, at low concentration polarization regions, there is an almost insignificant difference between the three model predictions. The highest differences in the model predictions has been observed between the DGM and BFM, while the lowest differences have been observed between the SMM and DGM predictions. In high concentration polarization regions, the differences between the model predictions may be up to 10.17% for the DGM and SMM, and 17.63% between the DGM and BFM. Moreover, the large difference observed in the percentage of the mass fraction predictions between the models have not been observed in the concentration polarization predictions for the models. This is be due

to the fact that the averaging for the mass fraction values over the catalyst layer as required in the concentration polarization calculation results gives rise to a smaller difference in the prediction of the concentration polarization of the models.

- A comparison of the constant current density assumption and the linear distributed current density shows that the concentration polarization difference between these two model assumption is insignificantly small at both low and high current densities for the three models. When the mass distribution is compared along the catalyst layer, it is observed that the linear distributed current density assumption results in a more uniform distribution of the  $H_2$  mass fraction in comparison to the predictions of the model with a constant current density assumption. However, when the area under the curves - which is the average mass fraction- are compared, it is observed that the difference between the area is very small and this is the main reason for the insignificant difference observed in the concentration polarization predictions of the two assumptions for the SMM, DGM and BFM.
- A comparison of the 1D, 2D and 3D models show that the 1D and 2D predictions are quite similar, while the 3D model is slightly better. Even in the 3D model, the models do not fit the experimental data very well at all current densities. This may be due to the uncertainties associated with the simplified electrochemistry used in the models. The main differences between the 1D and 2D model predictions is that the mass transport processes in the fuel gas channel has been taken into account in the later. Hence the similarities between the 1D and 2D predictions points out the fact that taking into account the convective dominated mass transport processes in the gas channels has a negligible effect on the prediction of the concentration

polarization.

- As discussed in Kerkhof [61], the difference between the DGM and the BFM are the 'extra viscous term' which appears in the DGM but not in the BFM and the  $\kappa/K_i$  term added to the  $D_{i,Kn}$  which represents the viscous type of flux and also the factor of 0.89 which is multiplied by the Knudsen diffusion coefficient. It has been shown that the inclusion of  $\kappa/K_i$  in the BFM has a negligible effect on the predictions of the concentration polarization at all the current densities and inlet H<sub>2</sub> concentrations.

# Chapter 7

## NEURO-FUZZY MODELLING

### RESULTS

In this chapter, an Adaptive Neuro-Fuzzy Inference System has been employed in order to predict the performance of a circular-planar type IT-SOFC and a PEMFC. The main aim of this study is building and verifying the capability of the model in order to understand the combined effect of various operational conditions on the performance of the fuel cells which can assist in reducing the experimentation and associated cost of the cells.

Firstly, the input data selection, optimal use of the data, the training and test data division and the selection of the type and number of the membership functions required for the ANFIS modelling of the SOFC and the PEMFC are presented and discussed. Secondly, the capabilities of the model for the prediction of the training data set and the unseen test data set are presented and the model capabilities to predict the performance of the cells is discussed. The further issues such as the prediction capability of the ANFIS model out of the boundaries of its training domain are also addressed in this chapter.

## 7.1 ANFIS Modelling of SOFC

### 7.1.1 Experimental Data

In this study, the experimental data of Begodni et al. [13] is used. They conducted several experimental tests on circular-planar IT-SOFC single cells to obtain a complete characterization of the fuel cell behaviour through voltage current measurements.

In Fig. 7.1, the fuel cells are shown which are made of an annulus shaped membrane. On both sides parallelepiped type separators with edge of  $1.5\text{ mm}$  and height of  $0.8\text{ mm}$  are placed. Internal and external diameters of the cells are  $10\text{ mm}$  and  $78\text{ mm}$ , respectively. Separators are required in order to identify two distinct zones where air and fuel flow. The inlet air is first preheated and fed externally (see Fig. 7.2). Fuel enters from the centre of the annulus, then flows radially to the external side of the fuel cell.

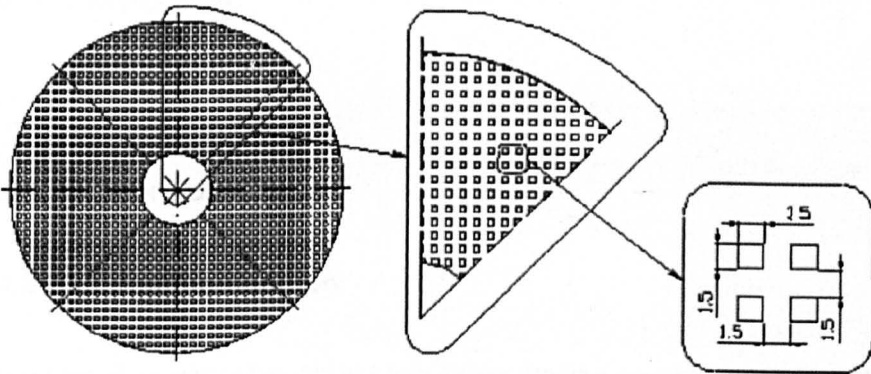


Figure 7.1: Fuel cell geometry (view from the top; lengths in mm) [13].

For the different operating conditions presented in Table 7.1, the cell voltage

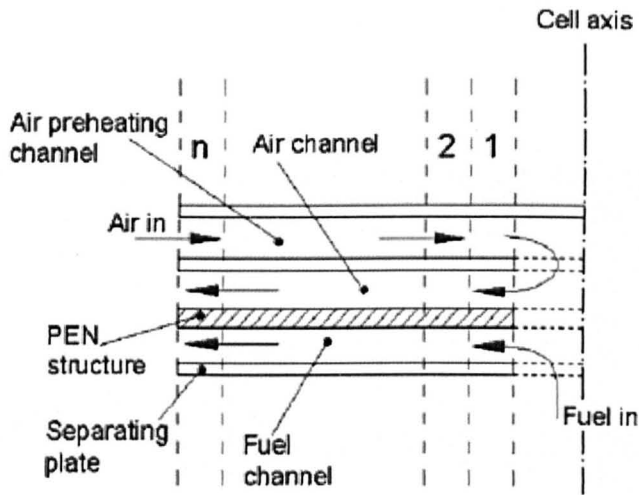


Figure 7.2: The IT-SOFC cross section [13].

was measured against the current to obtain the performance curve of the fuel cell. For each case listed in Table 7.1, measurements were made at 1A intervals at currents smaller than 10 A while at currents higher than 10 A, the voltage was measured every 5 A increments of the current. The cell temperature and air mass flow rate were maintained at constant values, namely 800°C and 0.0324 g/s, respectively throughout the experiments. In this way, a total of 166 data points were produced.

## 7.1.2 Preprocessing

### 7.1.2.1 Input Data Selection

An excessive number of inputs not only impair the transparency of the underlying model, but also increases the complexity of the computations necessary for building the model. Therefore it is necessary to do input selection that finds the priority of each input [51]. The approach employed in this study is based on that

Table 7.1: Fuel mass flow rate and fuel composition (the water content is complimentary to 100%) used for the experimental characterization of the fuel cell [13].

Case	Fuel mass flow rate (g/s)	H <sub>2</sub> vol (%)	N <sub>2</sub> vol (%)
1	0.00342	76	20
2	0.00514	60	36
3	0.00626	50	46
4	0.00737	40	56
5	0.00850	30	66
6	0.00757	31	65
7	0.00755	51	45
8	0.00748	74	22
9	0.00589	48	48
10	0.00783	48	48
11	0.01170	48	48

proposed by Jang [51], which is based on the assumption that the ANFIS model with the smallest RMSE after one epoch of training has the greater potential of achieving a lower RMSE when given more epochs of training.

In this thesis, to find the most influential inputs by removing all antecedent clauses associated with a particular input variable from the rules, 4 candidate inputs for our case were reduced to 3, 2 and 1 using all the possible combinations of inputs. For example, if we have a problem with 4 inputs and we want to find the most influential 2 inputs as the inputs to ANFIS, we can construct combinations of the ANFIS model and train them with a single pass of the least square method [51]. In this way, in our model, the ANFIS models were constructed. The ANFIS model with the smallest RMSE is then selected for further training using hybrid learning to tune the membership functions.

Table 7.2 presents the test RMSE values for the 15 ANFIS models. I, M, H<sub>2</sub>

and  $N_2$  stand for the current, mass flow rate, volumetric hydrogen content and volumetric nitrogen content, respectively. It is seen in Table 7.2, when only one input is used to predict the voltage (scenarios 1,2,3, and 4), the smallest RMSE is obtained with the one when the only current is used as input and this shows that current has the most significant effect on the output while the effect of volumetric content of  $H_2$  and  $N_2$  are same, which is due to the fact that in the experiments  $N_2$  is complementary to  $H_2$  and they sum up to 96 %. When only two input parameters are used (scenarios 5,6,7 and 8) the smallest RMSE is obtained with the inputs  $I, H_2$  and  $I, N_2$  with RMSE values of 0.0241 and their values are same due to the reason mentioned above. Using two input data gives more accurate voltage predictions in comparison to the using of one input parameter. On the other hand scenarios with the three input parameters with  $I, M, H_2$  (or  $I, M, N_2$ ) (scenarios 11 and 12) give the smallest RMSE of all the scenarios tested. This is due to the fact that parameters  $I, M$  and  $H_2$  or  $N_2$  has important effects on the voltage predictions. On the other hand, from the scenario 15 with RMSE of 0.0159 which is higher than RMSE of the scenarios 11 and 12, it can be concluded that the excessive number of inputs impairs the transparency of the underlying model, and increases the complexity of the model. Therefore, elimination of either  $H_2$  or  $N_2$  makes the model more transparent and concise and hence improves the performance of the model. Therefore, in this thesis,  $N_2$  was excluded and  $I, M$  and  $H_2$  were used as inputs to the model.

#### **7.1.2.2 Optimal Use of Data**

The experimental data of Bedogni et al. [13] involves the measurement of the quantities that are close to each other. The distribution of the original input data is presented in Fig. 7.3 (a). In particular, at current values between 0-10 A, for each case excessive measurements were performed. In order to decrease the

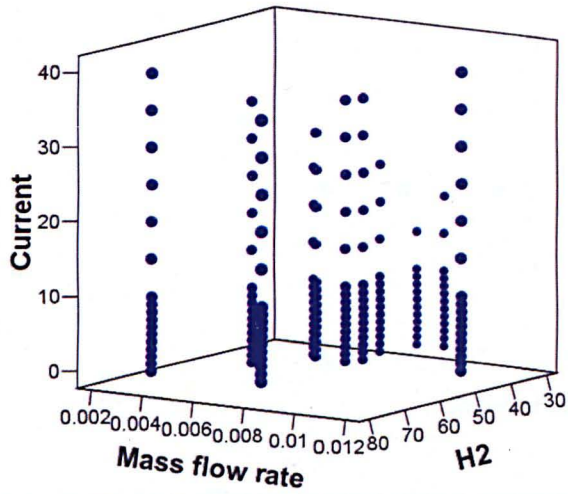
Table 7.2: Performance of the ANFIS model for the SOFC using fifteen different input combinations.

Scenarios	Inputs	RMSE (test)
1	I	0.0338
2	M	0.1028
3	H <sub>2</sub>	0.1049
4	N <sub>2</sub>	0.1049
5	I,M	0.0345
6	I,H <sub>2</sub>	0.0241
7	I,N <sub>2</sub>	0.0241
8	M,H <sub>2</sub>	0.1046
9	M,N <sub>2</sub>	0.1046
10	H <sub>2</sub> ,N <sub>2</sub>	0.1046
11	I,M,H <sub>2</sub>	0.0128
12	I,M,N <sub>2</sub>	0.0128
13	I,H <sub>2</sub> ,N <sub>2</sub>	0.0197
14	M,H <sub>2</sub> ,N <sub>2</sub>	0.1050
15	I,M,H <sub>2</sub> ,N <sub>2</sub>	0.0159

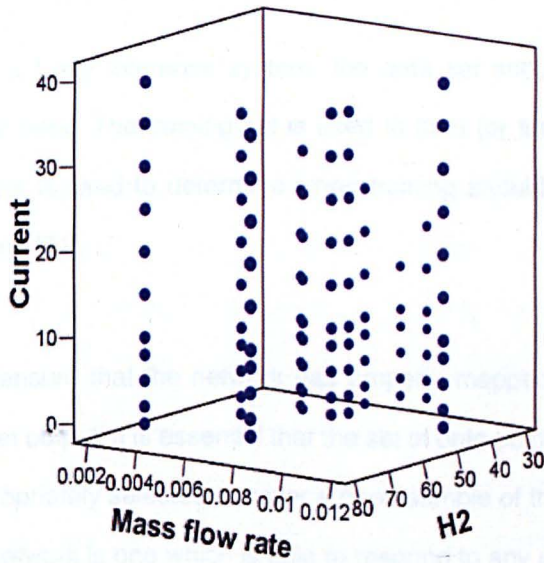
computational time, unnecessarily repeated data should be removed.

It is noted that there is still no formula for estimating the number of data points required to train a neural network. The number can vary greatly depending on the complexity of the problem, and the quality of the data. An optimization of the number of data sets that is really needed is still a challenge in the field of neural network [97].

In this thesis, in order to find the optimum data, an analysis was made by gradually removing data points from 166 to 130, 100, 70, 40, and comparing the RMSE of each model. As seen in Fig. 7.4, a substantial increase in RMSE is not observed up to about 100 data points but at 70 data points the RMSE increases considerably. Therefore, 100 data points were used in this study in ANFIS. The



(a)



(b)

Figure 7.3: The input data distribution (a) before and (b) after, the data reduction.

distribution of the data points after the reduction is presented in Fig. 7.3 (b).

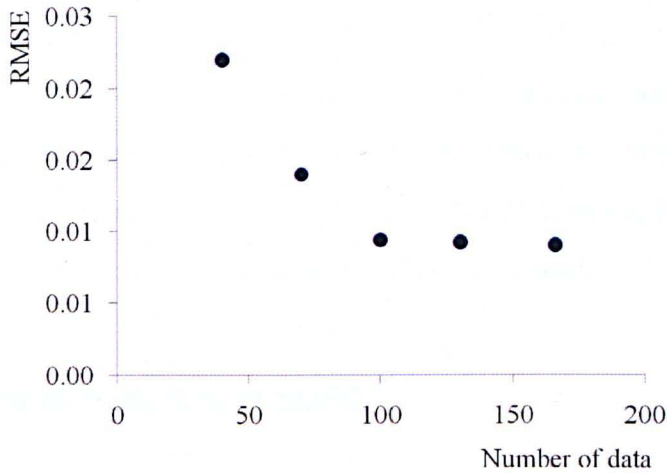


Figure 7.4: RMSE for a different number of experimental data.

### 7.1.2.3 Training and Test Data Division

Before training a fuzzy inference system, the data set should be divided into training and test sets. The training set is used to train (or tune) a fuzzy model, while the test set is used to determine when training should be terminated, to prevent overfitting [51].

In order to ensure that the network has properly mapped the input training data to the target output, it is essential that the set of data points presented to the network is appropriately selected to cover a good sample of the training domain. A well trained network is one which is able to respond to any unseen data points within an appropriate domain.

In this thesis, in order to find the optimum division of test and training data sets, the following approach was followed. First, the 100 data sets were decided to be divided into data sets of 50%, 60% and 70% training data. Second, 10 different test and training data sets were created for each 70%, 60% and 50%

training sets automatically using a programming code. In total 30 data sets, and hence 30 ANFIS models were built. They were then compared with respect to their test RMSE. It was found out that the smallest RMSE was obtained for the ANFIS model which corresponds to a division of the 70% training and 30% test data. This trained and test data sets were used for the model.

### **7.1.3 ANFIS modelling of SOFC**

Since the purpose of this study is to predict the fuel cell voltage under different operating conditions, the voltage was set as an output parameter of the model, while the current density, fuel cell temperature, anode and cathode humidification temperature and operating pressures were set as input parameters.

In order to run the ANFIS model, the number and type of the Membership Functions (MFs) should be determined by the user. The performance of the model depends on the combination of these different parameters. It should be noted that as the number of the membership functions increases for each input, the computational time increases. The ANFIS models with the different number of membership function for each input with the Gaussian membership functions, which is the most widely used and effective MF for fuel cell systems [128] has been constructed. It was found out that the Gaussian membership with 2 MFs for each input provided the best prediction, i.e. the smallest RMSE after one epoch of training and hence this configuration is used in the modelling of SOFC. Since there are three inputs with 2 membership functions for each input,  $2^3 = 8$  rules are constructed in the model.

## 7.1.4 Results and Discussion

### 7.1.4.1 Performance of the ANFIS model

The predicted output of the ANFIS model was compared to the experimental data for the training, see Fig. 7.5, and the test data set, see Fig. 7.6. The MAPE value of the test set is 1.04 %, and this indicates a very good performance although it is slightly higher than those of the training, which is 0.73 %. In order to compare the performance of the ANFIS model, the linear regression equation was also built for the same data. The RMSE value of the test set and the linear regression model is 0.013 and 0.024 and this indicates that the ANFIS model yields a lower error when compared to the regression model. Thus the principal advantage of using ANFIS in this study is that it performs better than the regression analysis. These results show that the ANFIS model predicts the voltage to be a good match with the experimental data for all the data points.

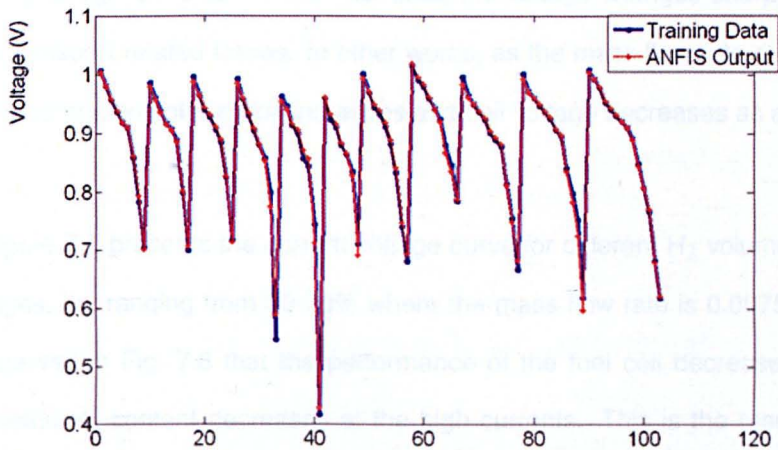


Figure 7.5: Training data versus the ANFIS output.

The trained and the tested model can be used to predict the performance

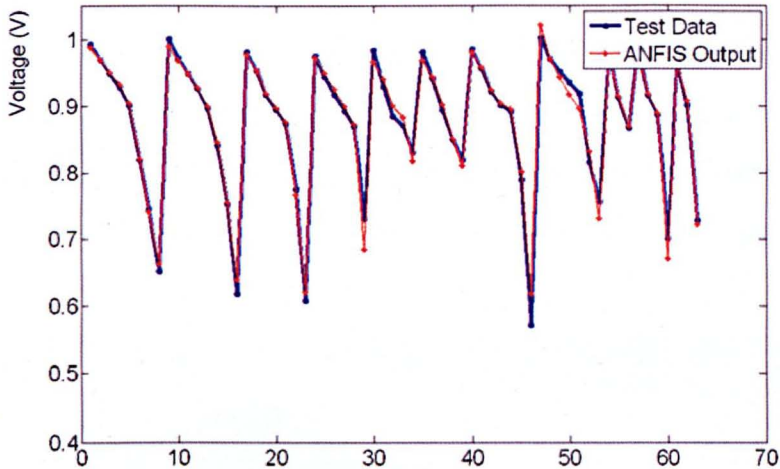


Figure 7.6: Test data versus the ANFIS output.

of the fuel cell under different operational conditions. As an example, Fig. 7.7 presents the 3D visualization of the current-voltage curve as a function of fuel mass flow rate when the  $H_2$  volumetric rate is maintained at 53%. In this figure, it is seen that the voltage increases as the fuel mass flow rate increases both at low and high currents. At high currents, the voltage changes sharply due to mass transport related losses. In other words, as the mass flow rate decreases, the concentration polarization increases and cell voltage decreases as a result.

Figure 7.8 presents the current-voltage curve for different  $H_2$  volumetric percentages, i.e. ranging from 30-70% where the mass flow rate is 0.00756 g/s. It is observed in Fig. 7.8 that the performance of the fuel cell decreases as the volumetric  $H_2$  content decreases at the high currents. This is the result of the concentration over potential, i.e. the performance decreases due to the fuel deficiency at the reaction site of the fuel cell. One important point to note is that in the region where the volumetric ratio of  $H_2$  goes below 40%, the voltage decreases to unrealistically low values. This is mainly due to the experimental data deficiency

in this region which hinders the model to construct realistic fuzzy rules for this region. One way to overcome this problem might be to obtain detailed information on the performance of the fuel cell for this region and create and add additional rules into the model. Alternatively the missing data points can be predicted using a well validated physical model, which is then given as an input to the ANFIS model.

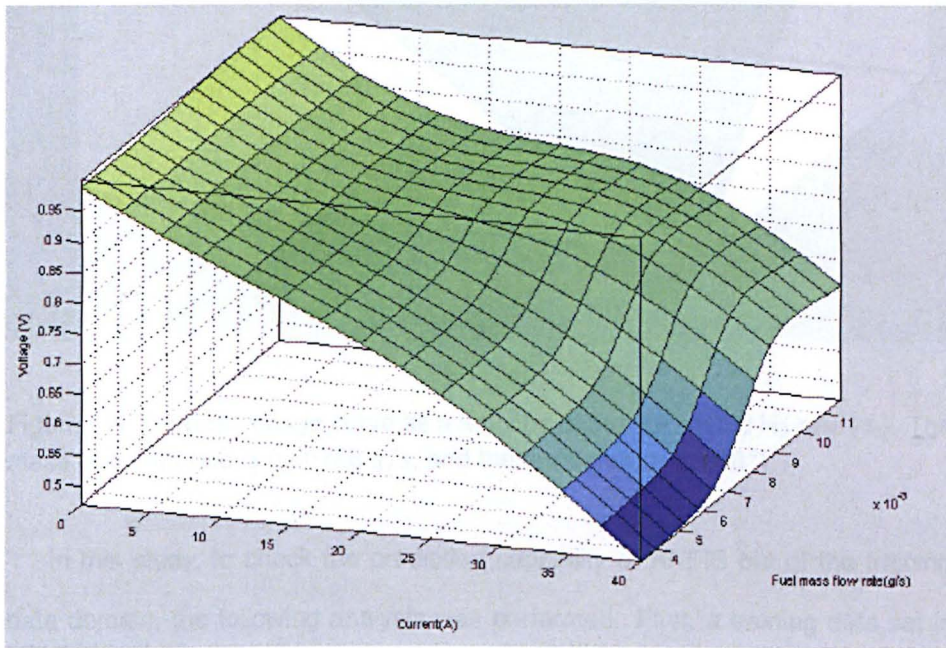


Figure 7.7: Current-voltage curve as a function of the fuel mass flow rate. The volumetric  $H_2$  content is 53%, and the temperature is  $800^\circ C$ .

### 7.1.5 Extrapolation capability of the ANFIS model

The extrapolation capability of a neural network depends on several factors, such as the training domain range, as well as the distance of the points to be extrapolated to the training domain. At present, neural networks are not good at extrapolating information outside of the training domain [97].

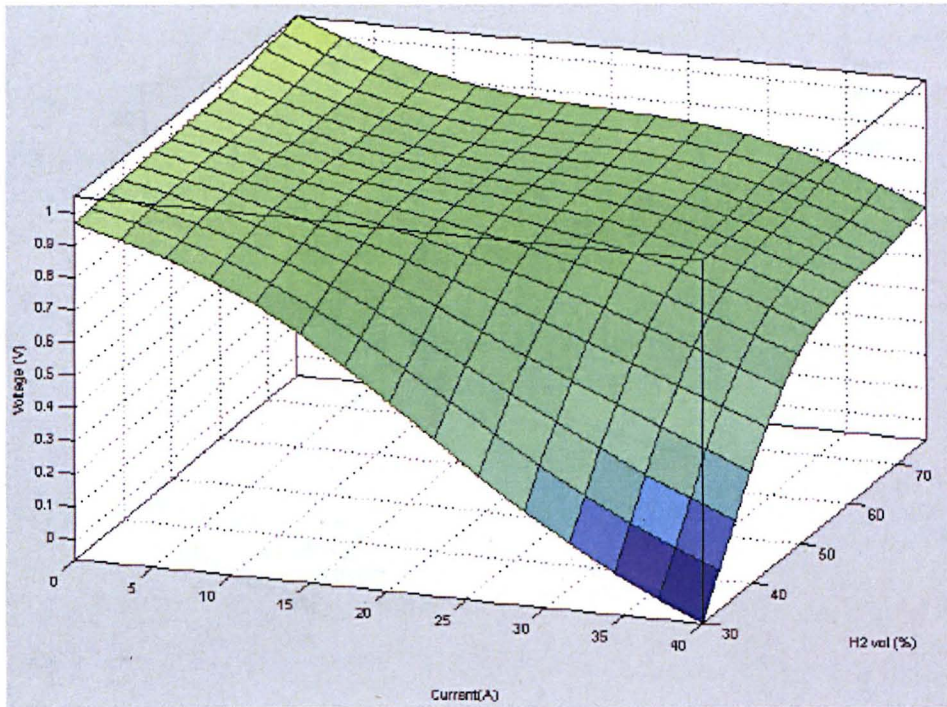


Figure 7.8: Current-voltage curve as a function of the volumetric H<sub>2</sub> rate (%). The mass flow inlet rate is 0.00756 g/s, and the temperature is 800 °C.

In this study, to check the prediction capability of ANFIS out of the training data domain, the following analysis was performed. First, a training data set is selected inside the original experimental domain (labelled as Train in Fig. 7.9) , second, three different test data sets were selected out of the training domain (labelled as Test 1, Test 2 and Test 3 in Fig. 7.9). From Test 1 to Test 3 the distance of the test data to the training data set increases. The model is trained within the domain and then its predictive capability is tested outside of the training domain by comparing its RMSEs.

It is seen from Table 7.3 that, the training and Test 1 RMSE values are very low, namely 0.014 and 0.016, respectively, while Test 2 and Test 3 RMSEs are comparatively higher, namely 0.761 and 2.561, respectively. This shows that

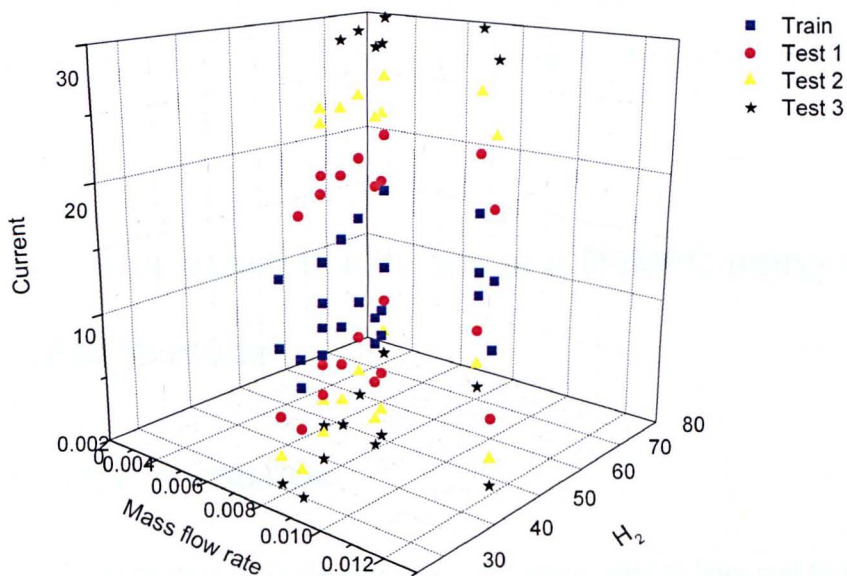


Figure 7.9: The training and test data distribution chosen to test the extrapolation capability of ANFIS.

although the model was trained and tested well, its prediction capability outside of the training domain decreases considerably, and the decrease is higher as the selected test data points are taken further from the selected training data set domain.

Table 7.3: RMSE of the training and test data sets chosen to test the extrapolation capability of ANFIS.

Training	Test1	Test2	Test 3
0.014	0.016	0.761	2.561

It must be noted that although this analysis gives a general indication, it is not enough to come to a general conclusion on the predictive capability of ANFIS outside of the training domain. A comprehensive analysis is needed with an

additional experimental data set to reach a firm conclusion. However, a detailed analysis is outside the scope of this thesis and hence the problem will not be addressed any further.

## **7.2 Performance Prediction of a PEMFC using the ANFIS model**

### **7.2.1 Experimental Data**

The experimental data of Wang et al. [122] has been used to train and test the ANFIS model. Wang et al. [122] performed various experiments with a single PEMFC which has a  $7.2 \times 7.2 \text{ cm}^2$  active surface area. The performance prediction through current voltage measurements was performed at cell temperatures ranging from 50 to 80 °C with the anode and cathode humidification temperatures kept at 70 °C. Then the anode and cathode humidification temperatures were varied between 50 and 90 °C. The backpressure was varied between 1 to 3.72 atm at intervals of 0.34 atm. During the experiments, the flow rates were kept the same and set to be 1200 sccm and 2200 sccm on the anode and cathode sides, respectively.

### **7.2.2 Preprocessing**

In this section, the preprocessing of the ANFIS model in order to select the training and test data set and determine the number of the MFs are presented. In order to find the optimum division of test and training data sets for the PEMFC, the same approach as in the ANFIS modelling of SOFC was followed. First, the experimental data sets were divided into data sets of 50%, 60% and 70% training

data sets. Second, 10 different test and training data sets were created for each 70 %, 60% and 50% training sets automatically using a programming code. In total 30 data sets, and hence 30 ANFIS models were built. They were then compared with respect to their test RMSE. The smallest RMSE which was obtained for the ANFIS model which corresponds to a division of the 60% training and 40% test data. This trained and test data sets were used for the modelling of PEMFC.

### **7.2.3 ANFIS modelling of the PEMFC**

Since the purpose of this study is to predict the fuel cell voltage under different operating conditions, the voltage was set as an output parameter, while the current density, fuel cell temperature, anode and cathode humidification temperature and operating pressures were set as input parameters. The ANFIS model with different number of the Gaussian membership function for each input has been tested. It was found out that the best model predictions have been obtained with the 2 numbers of Gaussian MFs for the input numbers 1, 2, 3, 4, and 5 respectively. In the model, for the selected number and type of the membership functions, a total number of 212 parameters were optimized, 192 being linear and 20 nonlinear. Fig. 7.10 presents the structure of the ANFIS procedure with 5 inputs, where each node presents an input, 32 rules and one output (voltage) of the model. The premise parameters;  $a, b, c$  and the consequent parameters;  $p, q, r$  of the membership functions are optimized through the learning algorithm.

Table 7.4: The training and test performances of ANFIS.

MAPE	MAPE	RMSE	RMSE
ANFIS	ANFIS	ANFIS	Linear regression
Training	Test	Test	Test
1.858	2.061	0.015	0.032

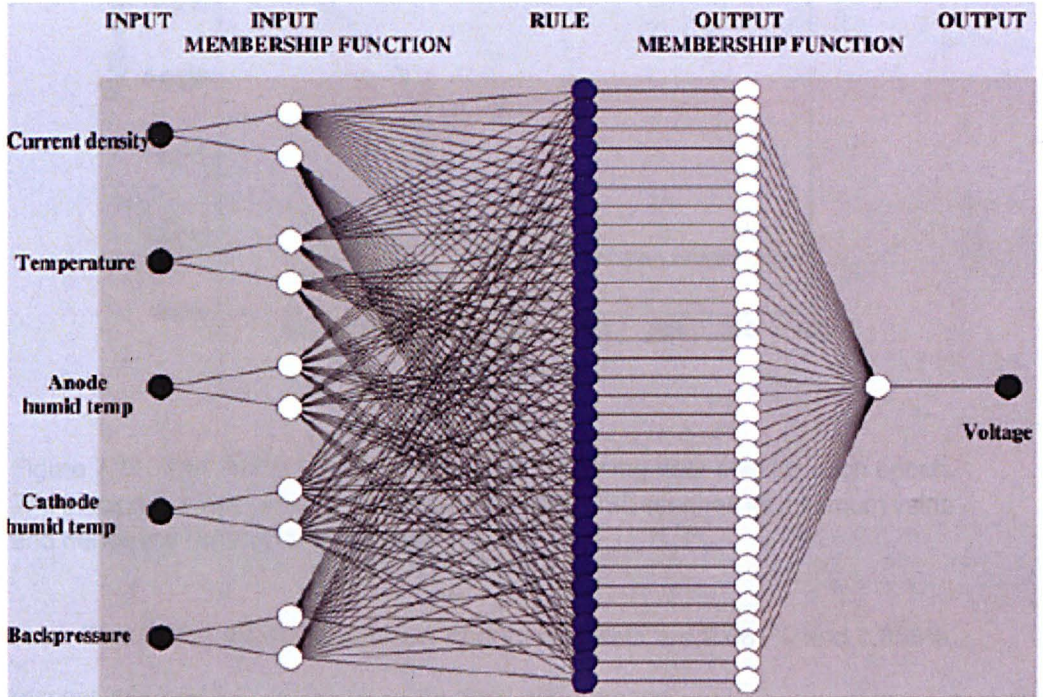


Figure 7.10: The structure of the ANFIS for the PEMFC model with 5 inputs, 2 input membership functions for each input, constructed 32 rules and the output of the model.

## 7.2.4 Results and Discussion

### 7.2.4.1 Performance of the ANFIS Model for PEMFC

The prediction of the ANFIS model has been compared with the experimental data for the training (see Fig. 7.12 (a)) and the test data (see Fig. 7.12(b)). It is observed from a comparison of the correlation coefficients that the predictions match quite well with the experimental data for both the training and test data

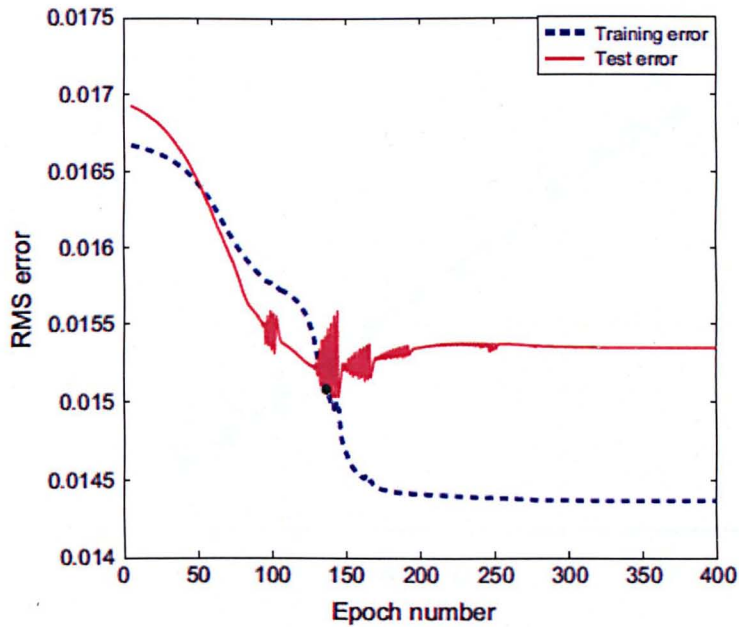


Figure 7.11: The RMSE values of the test and training data sets for each epoch. The black dot indicates the point where the test RMSE reaches its minimum value and hence the training is terminated.

sets. The MAPE values for the test and training sets are 2.061% and 1.858%, respectively, and this indicates a very good performance.

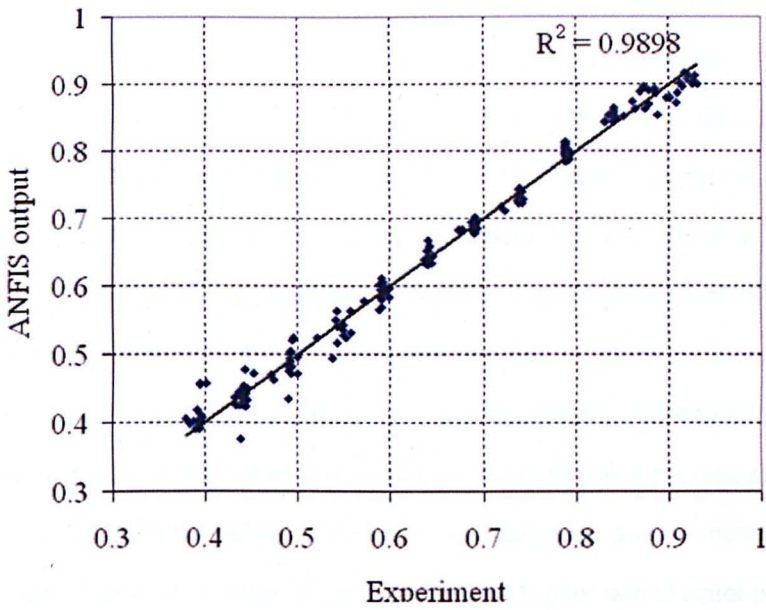
## 7.2.5 Performance of ANFIS at various operational conditions

In this section, the PEM fuel cell performance curve prediction of the ANFIS at different operational conditions is presented and discussed.

### 7.2.5.1 Effect of cell temperature

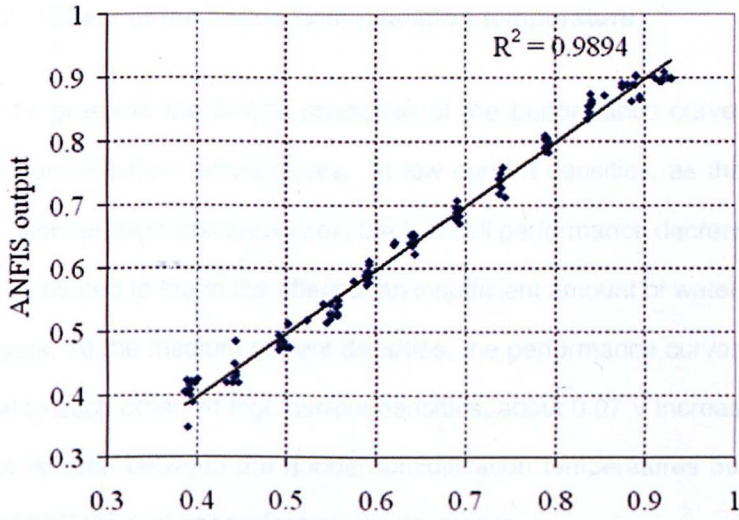
Fig. 7.13 shows the cell performance curve prediction of the ANFIS model at different temperatures. It is seen that, at low current densities, the cell performance decreases with increasing temperature. This may be related to the decrease in

Training data



(a)

Test Data



(b)

Figure 7.12: Scatter diagrams showing the correlation between the ANFIS output and (a) the training data, and (b) the test data.

the theoretical cell voltage with an increase in the temperature. On the other hand, at high current densities, the cell performance increases with increasing temperature. The increased temperature results in an exponentially higher exchange current density and this significantly improves the mass transport properties [9] which may explain this phenomenon. Moreover, as seen in Fig. 7.13, the changes in the performance for both low and high current densities are more severe for the cell temperature above 70°C, which is the anode and cathode humidification temperature. This indicates the possible effect of the humidification temperature on the cell performance. In Wang et al.[121], this was explained by the poor hydration of the catalyst layers which could cause a decrease in the active surface area of the catalysts at low current densities, and an increase in the active surface area of the catalyst layers due to the higher rate of water production at high current densities.

#### **7.2.5.2 Effect of the anode humidification temperature**

Fig. 7.14 presents the ANFIS prediction of the performance curve at different anode humidification temperatures. At low current densities, as the anode humidification temperature decreases, the fuel cell performance decreases and this might be related to the effect of an insufficient amount of water in the catalyst layers. At the medium current densities, the performance curves are almost parallel to each other. At high current densities, about 0.07 V increase in the cell voltage is seen between the anode humidification temperatures 30-50°C, and above 50°C the fuel cell performances decreases.

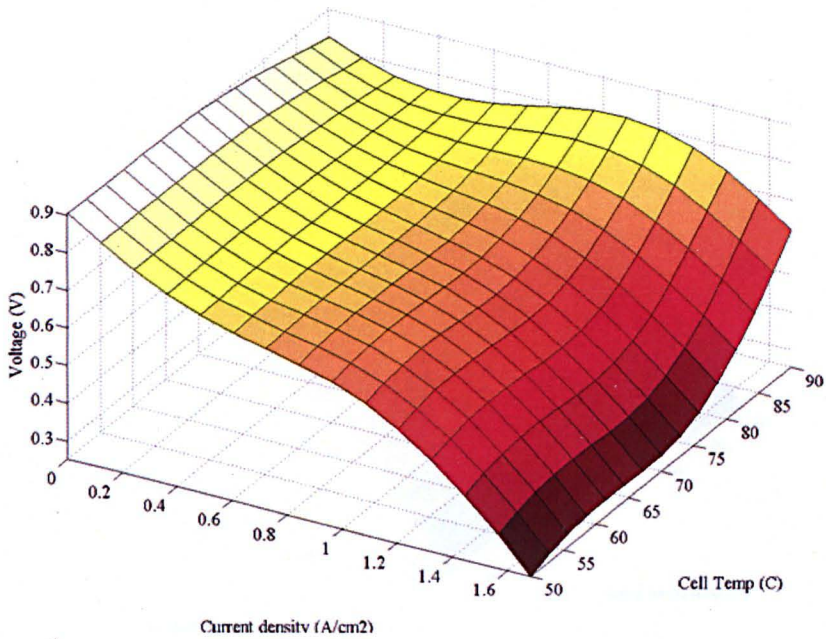


Figure 7.13: The ANFIS prediction of the voltage-current density curve as a function of the cell temperature. The anode and cathode humidification temperatures are 70 °C, backpressures are 3 atm on both the anode and cathode sides, and the flow rates are 1200 sccm on the anode side and 2200 sccm on the cathode side.

### 7.2.5.3 Effect of the cathode humidification temperature

At low current densities, there is almost no apparent change in the performance of the fuel cell with the change in the cathode humidification temperature (see Fig. 7.15). At the high current densities, e.g. at current densities between 1.4 and 1.6  $A/cm^2$ , as the cathode temperature change from 40-70°C, about 0.5 V decrease in the cell voltage is observed. This can be explained by the possible effects of the decrease in the effective porosity and gas diffusion layers and the decrease in the reactant contribution.

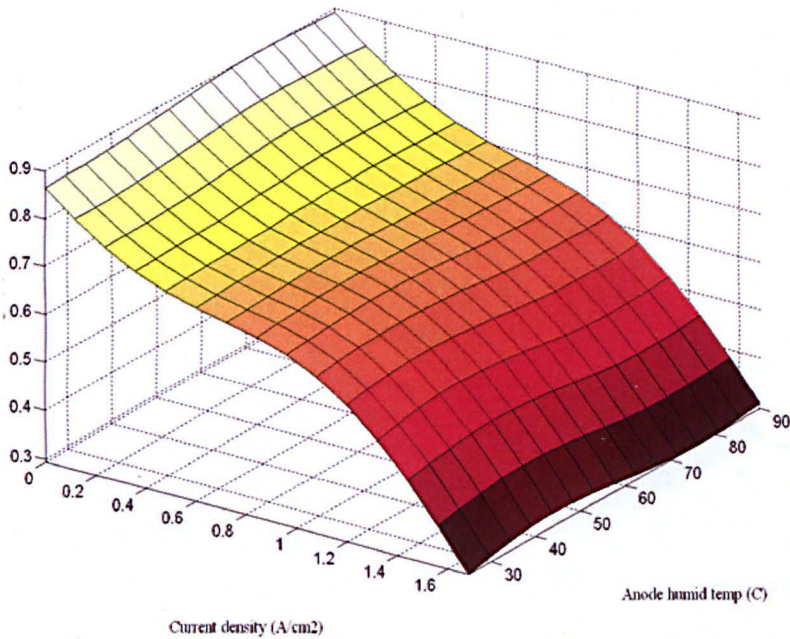


Figure 7.14: The ANFIS prediction of the voltage-current density curve as a function of the anode humidification temperature. The cell temperature and cathode humidification temperatures are 70 °C, backpressures are 3 atm on the both anode and cathode sides, and the flow rates are 1200 sccm on the anode side and 2200 sccm on the cathode side.

#### 7.2.5.4 Effect of pressure

Fig. 7.16 presents the ANFIS prediction of the voltage-current density curve as a function of the backpressure. The fuel cell temperature and anode and cathode humidification temperatures are 70 °C, and the flow rates are 1200 sccm on the anode side and 2200 sccm on the cathode side. As seen in Fig. 7.16, the performance of the fuel cell increases as the operational pressure increases. It is observed that there is a significant increase at high current densities. This might be explained by the increase in the partial pressures of the reactant gases, which in turn results in the decrease of the mass transfer related overpotential.

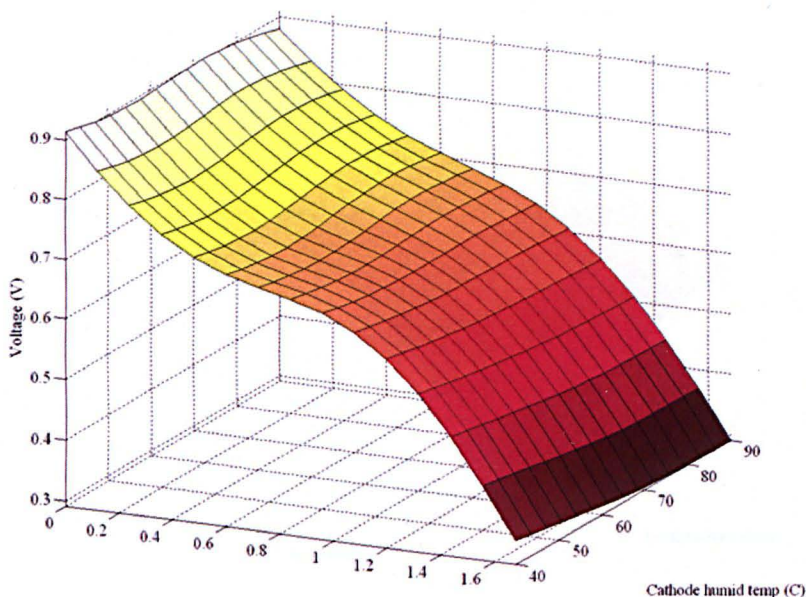


Figure 7.15: The ANFIS prediction of the voltage-current density curve as a function of the cathode humidification temperature. The cell temperature and anode humidification temperatures are 70°C, backpressures are 3 atm on both the anode and cathode sides, and the flow rates are 1200 sccm on the anode side and 2200 sccm on the cathode side.

## 7.2.6 Further Remarks on the ANFIS Model

In general, the main practical advantage of the ANFIS model over physical models is that the predictions can be performed in an easy, fast and accurate manner and this is valuable for practical purposes in the design of fuel cells. However, unlike the physical models, if the effect of any other variables, other than the given or measured experimentally is desired to be investigated on the cell performance, e.g. cathode and anode mass flow rate for the case investigated in this study, the model must be reconstructed including the information related to the new variables. This information can be obtained either from real experiments or an explicit knowledge can be obtained from a human expert to be used to build the model. Alternatively, physical models can be coupled

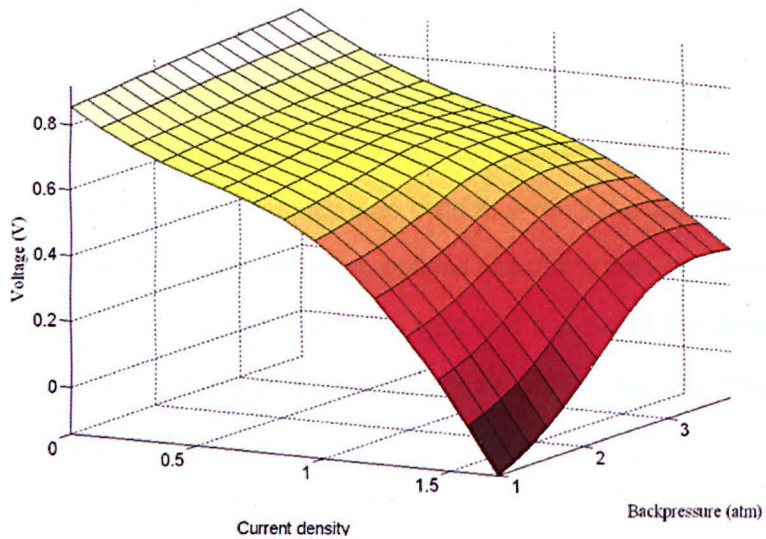


Figure 7.16: The ANFIS prediction of the voltage-current density curve as a function of the backpressure. The fuel cell temperature and anode and cathode humidification temperatures are 70 °C, and the flow rates are 1200 sccm on the anode side and 2200 sccm on the cathode side.

with the neuro-fuzzy models. This can be achieved by identifying the effect of the additional input parameters on the output by using the physical model and modifying the ANFIS output.

Unlike a conventional fuzzy system, where the rules of the model is constructed using the expert knowledge, in ANFIS, the neural network identifies and adjusts the parameters of the membership functions and the fuzzy rules of the fuzzy system from the data it is modelling. Hence it is important to know the features of the training and the test data sets that are selected. They must be representative of the domain chosen. In any case, the best way to assess the performance of the model, and also to prevent the overfitting of the model by an excessive number of rules, is to check the test data predictions.

## 7.2.7 Conclusions

In this chapter, an Adaptive Neuro-Fuzzy Inference System has been employed in order to predict the performance of a circular-planar type IT-SOFC and a PEMFC. The main aim of this study is to build and verify the capabilities of the model. Firstly, the input data selection, optimal use of the data, the training and test data division and the selection of the type and number of the membership functions required for the ANFIS modelling of the SOFC and the PEMFC are presented and discussed.

The predicted output of the ANFIS model of the SOFC was compared to the experimental data of Bedogni [13] for the training and the test data sets. The MAPE value of the test (1.04 %) and training data sets (0.73 %) indicates a very good model performance. These results show that the ANFIS model predicts the voltage to be a good match with the experimental data for SOFC modelling. From the analysis, it is seen that the prediction capability of the unseen data of ANFIS decreases when both the training and test data sets are not selected within the same domain, i.e. the test data is selected outside of the training domain.

For the prediction of the ANFIS model for PEMFC, it is seen from the comparison of the correlation coefficients that the predictions match well with the experimental data of Wang et al. [121] for both the training and test data sets. The MAPE values for the test and training sets are 2.061% and 1.858%, respectively, and this indicates a very good performance. Moreover, the PEM fuel cell performance curve prediction of ANFIS at different operational conditions are presented. The effect of the cell temperature, anode, cathode humidification temperatures and pressure on the cell performance has been discussed.

Overall, it is seen that ANFIS has the capability of predicting the performance curves in a very good and accurate manner for different operational temperatures and pressures (see Fig. 1 in [121]). Hence, it can be concluded that a well trained and tested ANFIS model can be used as a viable tool to predict the performance of the fuel cell at different operational conditions. In this way, it can facilitate the understanding of the combined effect of various operational conditions on the performance of the fuel cell.

In the analysis of the SOFC, depending on the availability of the experimental data, only the effect of the volumetric  $H_2$  and mass flow rate on the cell performance of a SOFC has been investigated. Other operational conditions, such as temperature, the structure of the materials and geometry used for the model, is expected to have a substantial effect on the cell performance. In the analysis of the PEMFC, depending on the availability of the experimental data, the cell temperature, anode and cathode humidification temperature and pressure, which are the main variables that affect the PEMFC performance, have been used to build the model and validate its predictions. However, the anode and cathode air mass flow rates and the structure of the fuel cells also might have important effects on the PEM cell performance. The extension of the capability of the model through combination with a physical model such as CFD might be an interesting area to search to develop a hybrid model that improves the capabilities of both the physical models and ANFIS.

## **Chapter 8**

# **GENERAL CONCLUSIONS AND FUTURE WORK**

### **8.1 General Conclusions**

This thesis presents model developments for the simulation and optimization of the design of fuel cells, in particular for the SOFC and PEMFC. However, the approaches and models presented can be easily applied to any type of fuel cell.

In this thesis, the multicomponent diffusion processes in porous medium of a solid oxide fuel cells anode has been investigated through a comparison of the Stefan Maxwell Model, Dusty Gas Model and Binary Friction Model in terms of their prediction performance of the concentration polarization of a SOFC anode to mainly investigate the effect of the Knudsen diffusion on the predictions. The model equations are first solved in 1D using an in-house code developed in MATLAB. Then the diffusion models have been implemented into a PDE solver, namely COMSOL to obtain 2D and 3D solutions. The model predictions have

been evaluated for different parameters and operating conditions.

The model predictions in 1D show that apart from the pore diameter and the current density, the tortuosity (or porosity/tortuosity) has a substantial effect on the predictions of concentration polarizations. Even at very high current densities ( $1.5 \text{ A/cm}^2$ ) and small pore radius ( $0.27 \mu\text{m}$ ), for the fitted tortuosity parameter, the SMM, DGM and BFM predictions are similar, and this contradicts some of the previous studies reported in the fuel cell literature. The results show that the SMM provides a quite similar prediction of the concentration polarization (in fact at least as accurate as the DGM) with the fitted tortuosity values so it may be preferred over the DGM when considering the comparative computational ease in comparison to the DGM. The effect of the partial pressure has been investigated and it is concluded that the pressure gradient term in the DGM and the BFM have a very small effect on the concentration polarization predictions for the conditions investigated and hence does not need to be included in this study. The importance of model validation against experimental data over a wide range of conditions is demonstrated. The model appears to give a good fit in the range of the experimental operating conditions investigated but might not be appropriate at other conditions due to the empirical parameters found by fitting the model to the experimental data. Therefore the models must be validated for a large range of operating conditions before being used as a prediction tool. None of the 1D models gives good predictions of the concentration polarization at high current densities and low fuel concentrations. The solution in 2D or 3D is expected to predict even more accurate results at high current densities where the reactant concentration varies not only along the anode thickness but also along the anode length due to the high consumption of the reactants.

The two- and three-dimensional results show that the predictions of the SMM, DGM and the BFM are quite similar, even at the highest current density, while the BFM predictions are slightly better than those of the DGM and the SMM. These results are consistent with the 1D predictions obtained in Chapter 5 in the sense that the tortuosity has an important effect on the predictions of the concentration polarization, in other words, the mass diffusion dominated processes, and the three diffusion models produce almost similar concentration polarization predictions. The species mass fraction distribution along the catalyst length has been compared and evaluated for each model in the high and low current concentration regions. The results show that, at low concentration polarization regions, there is an almost insignificant difference between the three model predictions. The highest differences in the model predictions has been observed between the DGM and BFM, while the lowest differences have been observed between the SMM and DGM predictions. In high concentration polarization regions, the differences between the model predictions may be up to 10.17% for the DGM and SMM, and 17.63% between the DGM and BFM. Moreover, the large difference observed in the percentage of the mass fraction predictions between the models have not been observed in the concentration polarization predictions for the models. This is be due to the fact that the averaging for the mass fraction values over the catalyst layer as required in the concentration polarization calculation results gives rise to a smaller difference in the prediction of the concentration polarization of the models. A comparsion of the constant current density assumption and the linear distributed current density shows that the concentration polarization difference between these two model assumption is insignificantly small at both low and high current densities for the three models. When the mass distribution is compared along the catalyst layer, it is observed that the linear distributed current density assumption results in a more uniform

distribution of the  $H_2$  mass fraction in comparison to the predictions of the model with a constant current density assumption. However, when the area under the curves - which is the average mass fraction- are compared, it is observed that the difference between the area is very small and this is the main reason for the insignificant difference observed in the concentration polarization predictions of the two assumptions for the SMM, DGM and BFM. A comparison of the 1D, 2D and 3D models show that the 1D and 2D predictions are quite similar, while the 3D model is slightly better. Even in the 3D model, the models do not fit the experimental data very well at all current densities. This may be due to the uncertainties associated with the simplified electrochemistry used in the models. The main differences between the 1D and 2D model predictions is that the mass transport processes in the fuel gas channel has been taken into account in the later. Hence the similarities between the 1D and 2D predictions points out the fact that taking into account the convective dominated mass transport processes in the gas channels has a negligible effect on the prediction of the concentration polarization. As discussed in Kerkhof [61], the difference between the DGM and the BFM are the 'extra viscous term' which appears in the DGM but not in the BFM and the  $\kappa/K_i$  term added to the  $D_{i,Kn}$  which represents the viscous type of flux and also the factor of 0.89 which is multiplied by the Knudsen diffusion coefficient. It has been shown that the inclusion of  $\kappa/K_i$  in the BFM has a negligible effect on the predictions of the concentration polarization at all the current densities and inlet  $H_2$  concentrations.

An Adaptive Neuro-Fuzzy Inference System has been employed in order to predict the performance of a circular-planar type IT-SOFC and a PEMFC. The main aim of this study is to build and verify the capabilities of the model. The predicted output of the ANFIS model of the SOFC was compared to the

experimental data of Bedogni [13] for the training and the test data sets. The MAPE value of the test (1.04 %) and training data sets (0.73 %) indicates a very good model performance. These results show that the ANFIS model predicts the voltage to be a good match with the experimental data for SOFC modelling. From the analysis, it is seen that the prediction capability of the unseen data of ANFIS decreases when both the training and test data sets are not selected within the same domain, i.e. the test data is selected outside of the training domain.

For the prediction of the ANFIS model for PEMFC, the MAPE values for the test and training sets are 2.061% and 1.858%, respectively, and this indicates a very good model performance. Moreover, the PEM fuel cell performance curve prediction of ANFIS at different operational conditions are presented. The effect of the cell temperature, anode, cathode humidification temperatures and pressure on the cell performance has been discussed. Overall, it is seen that ANFIS has the capability of predicting the performance curves in a very good and accurate manner for different operational temperatures and pressures (see Fig. 1 in [121]). Hence, it can be concluded that a well trained and tested ANFIS model can be used as a viable tool to predict the performance of the fuel cell at different operational conditions. In this way, it can facilitate the understanding of the combined effect of various operational conditions on the performance of the fuel cell.

## **8.2 Future Work**

The work presented in the thesis can be extended in the future in the following directions:

- The performance of the models which take into account the Knudsen diffusion can be investigated for the micro or nano fuel cells of which porous electrode has an average pore size smaller than a micrometer. In the SOFC investigated in this study, average pore radius of the anode electrode is of the order of a micrometer. The prediction of the models show that the Knudsen diffusion is not predominant in this range on the multicomponent diffusion processes in the porous medium of the fuel cell electrode. However, at the pore scale which is smaller than a micrometer, the Knudsen diffusion effect is expected to be predominant over the ordinary diffusion. This is evident from the fact at the smaller pore diameter, the collision of the molecules with the wall will be more frequent than the collision of the molecules with each other. In the micro and nano fuel cells, the average pore size of the electrodes are smaller than micrometer and hence it might be interesting to investigate and compare the diffusion model's performances for the micro and nano fuel cells.
- The diffusion models should be theoretically re-evaluated. As emphasized in this study, at the uniform pressure, the requirements of the Graham's law of diffusion is inconsistent with the requirements of the stoichiometry of the reacting medium. First, the validity of the Graham's law of diffusion should be experimentally retested in a medium that consists of the chemically reacting species.
- In the analysis of the IT-SOFC, depending on the availability of the experimental data, only the effect of the volumetric  $H_2$  and mass flow rate on the cell performance of an IT-SOFC has been investigated. Other operational conditions, such as temperature, the structure of the materials and geom-

entry used for the model, is expected to have a substantial effect on the cell performance. In the analysis of the PEMFC, depending on the availability of the experimental data, the cell temperature, anode and cathode humidification temperature and pressure, which are the main variables that affect the PEMFC performance, have been used to build the model and validate its predictions. The neuro fuzzy model can be coupled with the physical models in order to increase the applicability of the model for a large range of operating conditions where experimental data is not available. This can be done by identifying the effect of the additional input parameters on the output by using the physical model and modifying the ANFIS output accordingly. This might be an interesting area to search to develop a hybrid model that improves the capabilities of both the physical models and ANFIS.

# Bibliography

- [1] Achenbach E. Three-dimensional and time-dependent simulation of a planar solid oxide fuel cell stack. *J. Power Sources*, 49 (1994), 333-348.
- [2] Ackmann T., Haart L. G. J. de, Lehnert W., Stolten D. Modeling of Mass and Heat Transport in Planar Substrate Type SOFCs. *J. Electrochem. Soc.*, 150 (2003), A783-A789.
- [3] Aguiar P., Adjiman C.S., Brandon N.P. Anode supported intermediate temperature direct internal reforming solid oxide fuel cell. I: Model-based steady-state performance. *J. Power Sources*, 138 (2004), 120-136.
- [4] Akhtar N., Decent S.P., Loghin D., Kendall K. A three-dimensional numerical model of a single-chamber solid oxide fuel cell. *Int. J. Hydrogen Energ.*, 34 (2009), 8645-8663.
- [5] Andreassi L. Ubertini S., Bove R., Sammes N.M. CFD based results for planar and micro-tubular single cell designs. In R.Bove and S. Ubertini (eds.), *Modeling Solid Oxide Fuel Cells*, 97-122, Springer, Berlin, 2008.
- [6] Arriagada J., Olausson P., Selimović A. Artificial neural network simulator for SOFC performance predictions. *J. Power Sources*, 112 (2002), 5460.

- [7] Bai Y. and Wang D. Fundamentals of Fuzzy Logic Control - Fuzzy Sets, Fuzzy Rules and Defuzzifications, in *Advanced Fuzzy Logic Technologies in industrial Applications*, 17-36, Springer, 2006.
- [8] Autissier N., Larrain D., Van herle J., Favrat D. CFD simulation tool for solid oxide fuel cells. *J. Power Sources*, 131 (2004) 313-319.
- [9] Barbir F. *PEM Fuel Cells*, Elsevier, New York, 2005.
- [10] Bazylak A.M.J. Liquid water transport in fuel cell gas diffusion layers. PhD Thesis, University of Victoria, 2008.
- [11] Bhattacharyya D., Raghunathan R. A Review of Solid Oxide Fuel Cell (SOFC) Dynamic Models. *Ind. Eng. Chem. Res.*, 48 (2009), 6068-6086.
- [12] Bessette II N.F., Wepfer W.J., Winnick J. A mathematical model of a solid oxide fuel cell. *J. Electrochem. Soc.*, 142 (1995), 3792-3800.
- [13] Bedogni S., Campanari S., Iora P., Montelatici L., Silva P. Experimental analysis and modeling for a circular-planar type IT-SOFC. *J. Power Sources*, 171 (2007), 617-625.
- [14] Bird R.B. Five decades of Transport Phenomena, *AIChE J.*, 50 (2004), 273-287.
- [15] Buragohain M., Mahanta C. A novel approach for ANFIS modeling based on full factorial design. *App. Soft Comput.*, 8 (2008), 609-625.
- [16] Burt A.C., Celik I.B., Gemmen R.S., Smirnov A.V. A numerical study of cell-to-cell variations in a SOFC stack. *J. Power Sources*, 126 (2004), 76-87.
- [17] Celik I.B., Pakalapati S.R. From a single cell to a stack modeling. In R.Bove and S.Ubertini (eds.), *Modeling Solid Oxide Fuel Cells*, 123-182, Springer, Berlin, 2008.

- [18] Chang P.C., Liu C.H., Lai R.K. A fuzzy case-based reasoning model for sales forecasting in print circuit board industries. *Exp. Sys. Appl.*, 34 (2008), 2049-2058.
- [19] Chan S.H., Khor K.A., Xia Z.T. A complete polarization model of a solid oxide fuel cell and its sensitivity to the change of cell component thickness. *J. Power Sources*, 93 (2001), 130-140.
- [20] Colpan O., Dincer I., Hamdullahpur F. A review on macro-level modeling of planar solid oxide fuel cells. *Int. J. Energ. Res.*, 32 (2007), 336-355.
- [21] Colpan O., Dincer I., Hamdullahpur F. Thermodynamic modeling of direct internal reforming solid oxide fuel cells operating with syngas. *Int. J. Hydrogen Energ.*, 32 (2007), 787-795.
- [22] COMSOL Multiphysics User's Guide, Version 3.5a, 2008.
- [23] Ciucci F., Goodwin. D.G. Nonlinear modeling of mixed ionic electronic conductors. In: *ECS Transactions*. 2007 (7), 2075-2082.
- [24] Curtiss C.F., Bird R.B., Multicomponent Diffusion, *Ind. Eng. Chem. Res.*, 38 (1999), 2515-2522.
- [25] Cussler E. *Diffusion: Mass Transfer in Fluid Systems*, third ed., Cambridge University Press, 2009.
- [26] Djilali N., Transport phenomena in fuel cells: from microscale to macroscale. *Int. J. Comp. Fluid Dynamics*, 22 (2008), 115-133.
- [27] Entchev E., Yang L. Application of adaptive neuro-fuzzy inference system techniques and artificial neural networks to predict solid oxide fuel cell performance in residential microgeneration installation. *J. Power Sources*, 170 (2007), 122-129.

- [28] Epstein N. On tortuosity and the tortuosity factor in flow and diffusion through porous media. *Chem. Eng. Sci.*, 44 (1989), 777-779.
- [29] Evans R.B., Watson G.M., Mason E.A. Gaseous diffusion in porous media at uniform pressure. *J. Chem. Phys.* 35 (1961) 2076-2083.
- [30] Evans R.B., Watson G.M., Mason E.A. Gaseous diffusion in porous media II - effect of pressure gradients. *J. Chem. Phys.*, 39 (1962), 1894-1902.
- [31] Fuzzy Logic Toolbox Users Guide. The MathWorks, Inc.; 2001. Version 2.
- [32] Fimrite J., Structrup H., Djilali N. Transport Phenomena in Polymer Electrolyte Membranes I. Modeling Framework, *J. Electrochem. Soc.*, 152 (2005), A1804-A1814.
- [33] Fimrite J., Carnes B., Structrup H., Djilali N. Transport Phenomena in Polymer Electrolyte Membranes II. Binary Friction Membrane Model. *J. Electrochem. Soc.*, 152 (9) A1815-A1823.
- [34] Gardner F.J., Day M.J., Brandon N.P., Pashley M.N. and Cassidy M. SOFC technology developments at Roll-Royce. *J. Power Sources*, 86 (2000), 122-129.
- [35] Gemmen and Trembly. On the mechanism and behavior of coal syngas transport and reaction within the anode of a solid oxide fuel cell. *J. Power Sources*, 161 (2006), 1084-1095.
- [36] Ghadamian H., Saboohi Y. Quantitative analysis of irreversibilities causes voltage drop in fuel cell (simulation and modeling). *Electrochem. Acta*, 50 (2004), 699-704.
- [37] Gorzalczany M.B. Computational intelligence systems and applications. Heidelberg: Physica-Verlag; 2002.

- [38] Goodwin D.G., in Chemical Vapor Deposition XVI and EUROCV D 14, M.Allendorf, F. Maury, and F. Teyssandier, Editors, PV 2003-08, p.155, the Electrochem.Soc., Proceed. Series, Pennington, NJ.
- [39] Gubner A., Froning D., Haart B.de, Stolten D. Complete modeling of kW-range SOFC stacks. SOFC VIII, Proc. of the Int. Symposium, Electrochem. Soc., 2003, 1436-1441.
- [40] Haberman B.A., Young J.B. Diffusion and Chemical Reaction in the porous Structures of Solid Oxide Fuel Cells. J. Fuel Cell Sci. Tech., 3 (2006), 312321.
- [41] Hao Y., Goodwin D.G. Numerical study of heterogeneous reactions in an SOFC anode with oxygen addition. In: ECS Transactions. 2007 (7), 1859-1867.
- [42] Hernandez-Pacheco Eduardo et al. A macro level model for determining the performance characteristics of solid oxide fuel cell. J. Power Sources, 138 (2004), 174-186.
- [43] Hirschfelder, J.O., Curtiss C.F., Bird R.B. Molecular Theory of Gases and Liquids. Wiley, New York, 1964.
- [44] Huayang, Kee R.J., Janardhanan V.M., Deutschmann O., Goodwin D. Modeling Elementary Heterogeneous Chemistry and Electrochemistry in Solid-Oxide Fuel Cells. J. Electrochem. Soc., 152 (2005), A2427-A2440.
- [45] Hussain M.M., Li X., Dincer I. Multi-component mathematical model of solid oxide fuel cell anode. Int. J. Energ. Res., 29 (2005), 1083-1101.
- [46] Hussain M.M., Li X., Dincer I. Mathematical modeling of transport phenomena in porous SOFC anodes. Int. J. Thermal Sci., 46 (2007), 48-56.
- [47] Jackson R., Transport in Porous Catalysts, Elsevier, Amsterdam, 1977.

- [48] Janardhanan V.M., Deutschmann O. CFD analysis of a solid oxide fuel cell with internal reforming: Coupled interactions of transport, heterogeneous catalysis and electrochemical processes. *J. Power Sources*, 162 (2006), 1192-1202.
- [49] Jang J.S.R. Fuzzy modeling using generalized neural networks and Kalman filter algorithm, in *Proc. Ninth Nat. Conf. Artificial Intell. (AAAI-91)*, 1991, 762-767.
- [50] Jang J.S.R., Sun C.T. Neuro-fuzzy modeling and control. *Proc IEEE* 1995.
- [51] Jang J.S.R. Input Selection for ANFIS Learning, *Proc. IEEE Int. Conf. on Fuzzy Systems*, 1996.
- [52] Jang J.S.R. ANFIS: Adaptive network-based fuzzy inference system. *IEEE Transactions on Systems, Man and Cybernetics*, 23 (1993), 665-685.
- [53] Jang J.S.R., Sun C.T., Mizutani E. *Neuro-fuzzy and soft computing: a computational approach to learning and machine intelligence*. Upper Saddle River: Prentice-Hall, 1997.
- [54] Jiang Y., Virkar A.V., *J. Electrochem. Soc.* 150 (2003) A942A951.
- [55] Jurado F. Predictive control of solid oxide fuel cells using fuzzy Hammerstein model. *J Power Sources* 2006;158:24553.
- [56] Jiang W., Fang R.X., Dougal R.A., Khan J.A. Thermoelectric model of a tubular SOFC for dynamic simulation. *J. Energ. Res. Tech-Trans. ASME*, 130 (2008).
- [57] Juhl M., Primdahl S., Manon C. and Mogensen M. Performance/structure correlation for composite SOFC cathodes. *J. Power Sources*, 61 (1996), 173-181.

- [58] Jurado F. Predictive control of solid oxide fuel cells using fuzzy Hammerstein models. *J. Power Sources*, 158 (2006), 245-253.
- [59] Kakac S., Pramuanjaroenkij A., Zhou X.Y. A review of numerical modeling of solid oxide fuel cells. *Int. J. Hydrogen Energ.*, 32 (2007), 761-786.
- [60] Kenney and Karan. Mathematical micro-model of a solid oxide fuel cell composite cathode. In: *Proceedings Hydrogen and Fuel Cells*. Toronto, Canada, 2004.
- [61] Kerkhof P.J.A.M. A modified Maxwell-Stefan model for transport through inert membranes: the binary friction model. *Chem. Eng. J.*, 64 (1996), 319-343.
- [62] Kerkhof P.J.A.M., Goebbers M.A.M. Analysis and extension of the theory of multicomponent fluid diffusion. *Chem. Eng. Sci.*, 60 (2005), 3129-3167.
- [63] Khaleel M., Reknagle K., Deibler J., C. L.A, Stevenson J. Thermo-mechanical and electrochemistry modeling of planar SOFC stack. in H.Yokokawa and S. Singhal, editors, *SOFC VII, Proc. of the Int.Symposium, Electrochem. Soc.* 2001, 1032-1041.
- [64] Kramers H.A., J. Kistemaker. On the slip of a diffusing gas mixture along a wall. *Physica*, 10 (1943), 699-713.
- [65] Krishna. A simplified procedure for the solution of the Dusty Gas Model equations for steady state transport in nonreacting system", *Chem. Eng. J.*, 35 (1987), 75-81.
- [66] Kim J., Virkar A.V., Fung K., Mehta K., Singhal S.C. Polarization effects in intermediate temperature, anode-supported solid oxide fuel cells. *J. Electrochem. Soc.* 1999; 146(1): 69-78.

- [67] Krishna R. and Wesselingh J.A. The Maxwell-Stefan approach to mass transfer. *Chem. Eng. Sci.*, 52 (6), 861-911, 1997.
- [68] Konstogeornis G. Multicomponent Diffusion. in *Computer Aided Design*, McGraw-Hill Inc., 2003.
- [69] Lee S., Bae J., Lim S., Park J. Improved configuration of supported nickel catalysts in a steam reformer for effective hydrogen production from methane. *J. Power Sources*, 180 (2008), 506-515.
- [70] Wang L., Husar A., ZXhou T., Liu H. A parametric study of PEM fuel cell performances. *Int J. Hydrogen Energ.*, 28 (2003), 12631272.
- [71] Li P.W., Chyu M.K. Simulation of the chemical/electrochemical reactions and heat/mass transfer for a tubular SOFC stack. *J. Power Sources*, 124 (2003), 487-498.
- [72] Lu Y., Schaefer L., Li P., Numerical study of a flat-tube high power density solid oxide fuel cell. Part I: Heat/mass transfer and fluid flow. *J. Power Sources*, 140 (2005), 331-339.
- [73] Larminie J. and Dicks A. *Fuel Cell Systems Explained*. John Wiley and Sons, 2000.
- [74] Lehnert W., Meusinger J., Thom F. modeling of gas transport phenomena in SOFC anodes. *J. Power Sources*, 87 (2000), 57-63.
- [75] Lin and Beale. Performance predictions in solid oxide fuel cells. In *App. Math. Model.*, 3rd International Conference on CFD in Minerals and Process Industries, 30 (2006), 1485-1496.

- [76] Lu Y., Schaefer L., Li P. Numerical study of a flat-tube high power density solid oxide fuel cell. Part I: Heat/mass transfer and fluid flow. *J. Power Sources*, 140 (2005), 331-39.
- [77] Maxwell J.C. On the dynamical theory of gases. In: Niven, W.D. (Ed), 1965, *The Scientific Papers of James Clerk Maxwell. Part II.* Dover Publications, New York, 26-78. *Phil.I Trans. R. Soc.*, 157, 1860.
- [78] Ma L., Ingham D.B., Pourkashanian M., Carcadea E. Review of Computational Fluid Dynamics Modeling of Fuel Cells. *J. Fuel Cell Sci. and Technol.*, 2 (2005), 246- 257.
- [79] Malkow T. SOFC in brief. In R. Bove, S. Ubertini (eds.), *Modeling Solid Oxide Fuel Cells*, 3-12, Springer, 2008.
- [80] Mandin P., Bernay C., Tran-Dac S., Broto A., Abes D., Cassir M. SOFC modeling and numerical simulation of performances. *Fuel Cells*, 1 (2005), 71-78.
- [81] Mason E.A, Malianuskas A.P., *Gas Transport in Porous Media: The Dusty Gas Model*, Elsevier, Amsterdam, 1983.
- [82] Massie D. Neural network fundamentals for scientists and engineers. In: *Proceedings, ECOS 2001, Int. Conf. Efficiency, Cost, Optimisation, Simulation and Environmental Aspects of Energy and Process Systems*, ASME, Istanbul, Turkey, July 46, 2001.
- [83] Merk, H.J. The Macroscopic Equations for Simultaneous Heat and mass Transfer in Isotropic, Continuous and Closed Systems. *Appl. Sci. Res.*, 8 (1959), 73-99.
- [84] Muhl P. Mathematical and numerical modeling of solid oxide fuel cell. *J. Power Sources*, 131 (1960), 345-354.

- [85] Nauck D., Klawonn F., Kruse R. Foundations of neuro-fuzzy systems. Wiley, Chichester, 1997.
- [86] Nayak P. C., Sudheer K.P., Rangan D.M., Ramasastry K.S.. A neuro-fuzzy computing technique for modeling hydrological time series. J. Hydrol., 291 (2004), 52-66.
- [87] Neufeld P.D., Aziz R.A., Janzen A.R. Empirical equations to calculate 16 of the transport collision integrals  $\sigma^{(l,s)*}$  for the Lennard-Jones (12-6) Potential. J. Chem. Phys. 57 (1972), 1100-1102.
- [88] Nehter P. Two-dimensional transient model of a cascaded micro-tubular solid oxide fuel cell fed with methane. J. Power Sources, 157 (2006), 325-334.
- [89] Ni M., Leung D.Y.C., Leung M.K.H. Mathematical modeling of ammonia-fed solid oxide fuel cells with different electrolytes. Int. J. Hydrogen Energ., 33 (2008), 5765-5772.
- [90] Ni M., Leung M.K.H., Leung D.Y.C. Mathematical modeling of the coupled transport and electrochemical reactions in solid oxide steam electrolyzer for hydrogen production. Electrochem. Acta, 52 (2007), 6707-6718.
- [91] Ou S., Achenie L.E.K. A hybrid neural network model for PEM fuel cells. J. Power Sources, 140 (2005), 319-330.
- [92] Pasaogullari U, Wang C. Computational fluid dynamics modeling of solid oxide fuel cells. Proceedings of SOFC VIII, Paris, France, 2003.
- [93] Pramuanjaroenkij A, Kakac S, Zhou XY. Mathematical analysis of planar solid oxide fuel cells. Int. J. Hydrogen Energ., 33 (2008), 2547-2565.
- [94] Present R.D. Kinetic Theory of gases. McGraw-Hill Book Company, Inc., New York, 1954.

- [95] Poling B.E., Prausnitz J.M. and OConnell J.P. *The Properties of Gases and Liquids* (5th ed.), McGraw-Hill, New York, 2000.
- [96] Pollard W.G., Present R.D. On gaseous self-diffusion in long capillary tubes. *Phys. Rev.*, 73 (1948), 762-774.
- [97] Rafiq M.Y., Bugmann G., Easterbrook D.J. Neural network design for engineering applications. *Comput. Struc.*, 79 (2001), 1541-1552.
- [98] Recknagle K.P., Williford R.E., Chick L.A., Rector D.R., and Khaleel M.A. Three-dimensional thermo-fluid electrochemical modeling of planar SOFC stacks. *J. Power Sources*, 113 (2003), 109-114.
- [99] Reid, R.C., Prausnitz J.M. and Poling B., "The properties of gases and liquids", 4th ed., McGraw-Hill, New York, 1987.
- [100] Rumelhart D.E., Hinton G.E., Williams R.J. Learning representations by back-propagation errors. *Nature*, 323 (1986), 533-536.
- [101] Saad, Yousef, "Iterative methods for sparse linear systems", 1st ed., Boston, 1996.
- [102] Saad Y. and Schultz M.H. GMRES: A Generalized Minimal Residual Algorithm for solving Nonsymmetric Linear Systems, *SIAM J. Scientific and Stat. Comp.*, 7 (1986), 856-869.
- [103] Schneider P. Multicomponent isothermal diffusion and forced flow of gases in capillaries. *Chem. Eng. Sci.*, 33 (1978), 1311-1319.
- [104] Shapiro A.A., Davis P.K., and Duda J.L. Diffusion in Multicomponent Mixtures. In *Computer Aided Property Estimation for Process and Product Design* by Kontogeorgis and Gani, Elsevier, 2004.

- [105] Singhal S.C., Kendall K. High Temperature Solid Oxide Fuel Cells: Fundamentals, Design and Applications. Elsevier, New York, 2003.
- [106] Solcova O., Snajdaufova H., Schneider P. Multicomponent counter-current gas diffusion in porous solids: the Grahams law diffusion cell. Chem. Eng. Sci., 56 (2001), 5231-5237.
- [107] Steele B.C.H. Material science and engineering: The enabling technology for the commercialisation of fuel cell systems. J. Mate. Sci., 36 (2001), 1053-1068.
- [108] Stefan J. Ueber das Gleichgewicht und die Bewegung, insbesondere die Diffusion von Gasgemengen. Sitzungsber. Osterr. Akademie der Wissensch., 1871, 63-124.
- [109] Sugeno M., Yasukawa T. A fuzzy logic based approach to qualitative modeling. IEEE Transac. Fuzzy Sys., 1 (1993), 7-31.
- [110] Suwanwarangkul R., Croiset E., Fowler M.W., Douglas P.L., Entchev E., Douglas M.A. Performance comparison of Fick's, dusty-gas and Stefan-Maxwell models to predict the concentration overpotential of a SOFC anode. J. Power Sources, 122 (2003), 9-18.
- [111] Suwanwarangkul R., Croiset E., Pritzker M.D., Fowler M.W., Douglas P.L., Entchev E., Douglas M.W. Mechanistic modelling of a cathode-supported tubular solid oxide fuel cell. J. Power Sources, 154 (2006), 74-85.
- [112] Sun T, Yan S, Cao G, Zhu X. Modeling and control PEMFC using fuzzy neural networks. Zhejiang Univ. Press, 10 (2005), 1084-1089.
- [113] Swingler K. Applying neural networks a practical guide. New York: Academic Press; 1996.

- [114] Takagi T. and Sugeno M. Derivation of fuzzy control rules from human operators control actions. In Proc. IFAC Symp. Fuzzy Inform. Knowledge Representation and Decision Analysis, 1983, 55-60.
- [115] Taylor R., Krishna R. Multicomponent Mass Transfer. Wiley, New York, 742, 1993.
- [116] Todd B. and Young J.B. Thermodynamic and transport properties of gases for use in solid oxide fuel cell modeling. J. Power Sources, 110 (2002), 186-200.
- [117] Tolman R.C. The principle of similitude entropy of polyatomic gases. J. Am. Chem. Soc., 43 (1921), 866875.
- [118] Tseronis K., Kookos I.K., Theodoropoulos C. Modeling mass transport in solid oxide fuel cell anodes: a case for a multidimensional dusty-gas-based model. Chem. Eng. Sci., 63 (2008), 5626-5638.
- [119] Ubertini S., Bove R. Mathematical models: a general overview. In R.Bove and S.Ubertini (eds.), Modeling Solid Oxide Fuel Cells, 51-93, Springer, 2008.
- [120] Veldinsk J.W., Van Damme R.M.J., Versteeg G.F., Van Swaaij. The use of the dusty-gas model for the description of mass transport with chemical reaction in porous media. Chem. Eng. J., 57 (1995), 115-125.
- [121] Wang R., Qi L., Xie X., Ding Q., Li C., Ma C.M. Modeling a 5-cell direct methanol fuel cell using adaptive-network based fuzzy inference systems., J. Power Sources, (2008), 1201-1208. xx
- [122] Wang L., Husar A., Zhou T., Liu H. A parametric study of PEM fuel cell performances. Int. J. Hydrogen Energ., 28 (2003), 1263-1272.

- [123] Wang Y.M., Elhag T.M.S. An adaptive neuro-fuzzy inference system for bridge risk assessment. *Expert Syst. Appl.*, 34 (2008), 3099-3106.
- [124] Williford R.E., Chick L.A., Maupin G.D., Simner S.P., Stevenson J.W. Diffusion limitations in the porous anodes of SOFCs. *J. Electrochem. Soc.*, 150 (2003), A1067A1072.
- [125] Winkler W. Thermodynamics. In *High Temperature Solid Oxide Fuel Cells-Fundamentals, Design and Applications*, Chapter 3, Singhal SC, Kendall K (eds). Elsevier: London, U.K., 2002.
- [126] Wu X.J., Zhu X.J., Cao G.Y., Tu H.Y. Modeling a SOFC stack based on GA-RBF neural networks identification. *J. Power Sources*, 167 (2007), 145-150.
- [127] Wu X.J., Zhu X.J., Cao G.Y., Tu H.Y. Nonlinear modelling of a SOFC stack by improved neural networks identification. *J. Zhejiang Uni. Sci. A*, 8 (2007), 1505-1509.
- [128] Wu X.J., Zhu X.J., Cao G.Y., Tu H.Y. Predictive control of SOFC based on a GA-RBF neural network model. *J. Power Sources*, 179 (2008), 232-239.
- [129] Wu X., Zhu X., Cao G., Tu H. Nonlinear modeling of a SOFC based on ANFIS identification. *Simul Model Pract Theor.*, 16 (2008), 399409.
- [130] Yakabe H., Hishinuma M., Uratani M., Matsuzaki Y., Yasuda I. Evaluation and modeling of performance of anode-supported solid oxide fuel cell. *J. Power Sources* (2000), 423-431.
- [131] Yakabe H, Ogiwara T, Hishinuma M, Yasuda I. 3-D model calculation for planar SOFC. *J. Power Sources*, 102 (2001), 144-154.
- [132] Young J.B. and Todd B. Modeling of multi-component gas flows in capillaries and porous solids. *Int. J. Heat and Mass Transfer*, 48 (2005), 5338-5353.

- [133] Young J.B. Thermofluid Modeling of Fuel Cells. *Annu. Rev. Fluid Mech.*, 39 (2007), 193-215.
- [134] Zadeh L.A. Fuzzy sets. *Information and Control*, 8 (1965), 338-353.
- [135] Zadeh L.A. Outline of a new approach to the analysis of complex systems and decision processes. *IEEE Trans. Syst., Man., Cybern.*, 3 (1973), 28-44.
- [136] Zhu H., Kee R.J. A general mathematical model for analyzing the performance of fuel cell membrane-electrode assemblies. *J. Power Sources*, 117 (2003), 6174.
- [137] Zhu H., Kee R.J., Janardhanan V.M., Deutschmann O. and Goodwin D.G. Modeling Elementary Heterogeneous Chemistry and Electrochemistry in Solid-Oxide Fuel Cells, *J. Electrochem. Soc.*, 152 (2005), A2427-A2440.

# Appendix A

## Source codes

### A.1 IMPLEMENTATION OF THE DGM AND BFM INTO COMSOL

#### A.1.1 Implementation of the DGM into COMSOL

(The parameters are shown in the form of the COMSOL code)

**Parameters for the binary mixtures for the porous domains**

$DE_{11} = Dh_{2h2}oeff / x_w_{H2\_chms} / Dh_{2o\_Kn\_eff} / Se$

$DE_{12} = 0$

$DE_{21} = 0$

$DE_{22} = Dh_{2h2}oeff / x_w_{H2O\_chms} / Dh_{2\_Kn\_eff} / Se$

$Se = x_w_{H2\_chms} / Dh_{2\_Kn\_eff} + x_w_{H2O\_chms} / Dh_{2o\_Kn\_eff}$

## Parameters for the Ternary Mixtures for the porous domains

DE\_11=Delta\_h2h2o\*Delta\_h2ar\*(x\_w\_H2O\_chms/Dh2o\_Kn\_eff...

+x\_w\_Ar\_chms/Dar\_Kn\_eff)/Delta\_e/Se/x\_w\_H2\_chms

DE\_12=-Delta\_h2h2o\*Delta\_h2oar/Dh2o\_Kn\_eff/Delta\_e/Se

DE\_13=-Delta\_h2ar\*Delta\_h2oar/Dar\_Kn\_eff/Delta\_e/Se

DE\_21=-Delta\_h2ar\*Delta\_h2h2o/Dh2\_Kn\_eff/Delta\_e/Se

DE\_22=Delta\_h2h2o\*Delta\_h2oar\*(x\_w\_H2\_chms/Dh2\_Kn\_eff...

+x\_w\_Ar\_chms/Dar\_Kn\_eff)/Delta\_e/Se/x\_w\_H2O\_chms

DE\_23=-Delta\_h2oar\*Delta\_h2oar/Dar\_Kn\_eff/Delta\_e/Se

DE\_31=-Delta\_h2ar\*Delta\_h2h2o/Dh2\_Kn\_eff/Delta\_e/Se

DE\_32=-Delta\_h2h2o\*Delta\_h2oar/Dh2o\_Kn\_eff/Delta\_e/Se

DE\_33=Delta\_h2ar\*Delta\_h2oar\*(x\_w\_H2O\_chms/Dh2o\_Kn\_eff...

+x\_w\_H2\_chms/Dh2\_Kn\_eff)/Delta\_e/Se/x\_w\_Ar\_chms

## Diffusion Fluxes

dflux\_w\_H2\_x=

-rho\_chms\*w\_H2\*(DE11\_chms\*d(w\_H2/(M\_w\_H2\_chms...

\*(w\_H2/M\_w\_H2\_chms...

+w\_H2O/M\_w\_H2O\_chms+(1-w\_H2-w\_H2O)/M\_w\_Ar\_chms)),x)...

+DE12\_chms...d(w\_H2O/(M\_w\_H2O\_chms...

\*(w\_H2/M\_w\_H2\_chms+w\_H2O/M\_w\_H2O\_chms+(1-w\_H2-w\_H2O)...

/M\_w\_Ar\_chms)),x)...

+DE13\_chms\*d((1-w\_H2-w\_H2O)/(M\_w\_Ar\_chms...

\*(w\_H2/M\_w\_H2\_chms+w\_H2O...

/M\_w\_H2O\_chms...+(1-w\_H2-w\_H2O)/M\_w\_Ar\_chms)),x)...

```

+DE11_chms...
*(x_w_H2_chms)*(1-1/ Dh2_Kn_eff/Se)*d(P_chms,x)/P_chms...
-DE12_chms*...
(x_w_H2O_chms)*(1-1/ Dh2o_Kn_eff/Se)*d(P_chms,x)/P_chms...
-DE13_chms*...
(x_w_Ar_chms)*(1-1/ Dar_Kn_eff/Se)*d(P_chms,x)/P_chms...
+((perm_a...
* P_chms /mu)+1/Se) ...
*d(P_chms,x)/P_chms) -DiT_w_H2_chms*d(T_chms,x)/T_chms

dflux_w_H2_y=
-rho_chms*w_H2*(DE11_chms*d(w_H2/(M_w_H2_chms...
*(w_H2/M_w_H2_chms..
.+w_H2O/M_w_H2O_chms+(1-w_H2-w_H2O)/M_w_Ar_chms)),y)...
+DE12_chms*d(w_H2O/(M_w_H2O_chms*(w_H2...
/M_w_H2_chms+w_H2O/M_w_H2O_chms+(1-w_H2-w_H2O)...
/M_w_Ar_chms)),y)...
+DE13_chms*d((1-w_H2-w_H2O)/(M_w_Ar_chms...
*(w_H2/M_w_H2_chms...
+w_H2O/M_w_H2O_chms+(1-w_H2-w_H2O)/M_w_Ar_chms)),y)...
+DE11_chms*(x_w_H2_chms)*(1-1/ Dh2_Kn_eff/Se)...
*d(P_chms,y)/P_chms-DE12_chms...
*(x_w_H2O_chms)*(1-1/ Dh2o_Kn_eff/Se)...
*d(P_chms,y)/P_chms-DE13_chms...
*(x_w_Ar_chms)*(1-1/ Dar_Kn_eff/Se)*d(P_chms,y)/P_chms ...
+(perm_a* P_chms /mu+1/Se) *d(P_chms,y)/P_chms)-DiT_w_H2_chms...
*d(T_chms,y)/T_chms

```

```

dflux_Wh2_z=
-rho_chms*w_H2*(DE11_chms*d(w_H2/(M_w_H2_chms...
*(w_H2/M_w_H2_chms...
+w_H2O/M_w_H2O_chms+(1-w_H2-w_H2O)...
/M_w_Ar_chms),z)+DE12_chms...
*d(w_H2O/(M_w_H2O_chms...
*(w_H2/M_w_H2_chms+w_H2O/M_w_H2O_chms...
+(1-w_H2-w_H2O)/M_w_Ar_chms),z)+DE13_chms...
*d((1-w_H2-w_H2O)/(M_w_Ar_chms...
*(w_H2/M_w_H2_chms...
+w_H2O/M_w_H2O_chms+(1-w_H2-w_H2O)/M_w_Ar_chms),z)...
+ DE11_chms*(x_w_H2_chms)*(1-1/Dh2_Kn_eff/Se)...
*d(P_chms,z)/P_chms...
-DE12_chms*(x_w_H2O_chms)*(1-1/Dh2o_Kn_eff/Se)...
*d(P_chms,z)/P_chms...
-DE13_chms*(x_w_Ar_chms)*(1-1/Dar_Kn_eff/Se)...
*d(P_chms,z)/P_chms...
+(perm_a* P_chms /mu+1/Se) *d(P_chms,z)/P_chms)...
-DiT_w_H2_chms*d(T_chms,z)/T_chms

```

```

dflux_wH2O_x= -rho_chms*w_H2O*(DE21_chms...
*d(w_H2/(M_w_H2_chms...
*(w_H2/M_w_H2_chms...+w_H2O/M_w_H2O_chms...
+(1-w_H2-w_H2O)/M_w_Ar_chms),x)+DE22_chms...
*d(w_H2O/(M_w_H2O_chms...
*(w_H2/M_w_H2_chms+w_H2O/M_w_H2O_chms+...

```

$(1-w_{H2}-w_{H2O})/M_{w\_Ar\_chms}), x) + DE23\_chms...$   
 $*d((1-w_{H2}-w_{H2O})/(M_{w\_Ar\_chms}*(w_{H2}...$   
 $/M_{w\_H2\_chms}+w_{H2O}/M_{w\_H2O\_chms}...$   
 $+ (1-w_{H2}-w_{H2O})/M_{w\_Ar\_chms}), x) ...$   
 $+ DE22\_chms*(x_{w\_H2O\_chms})*(1-1/Dh2o\_Kn\_eff/Se)...$   
 $*d(P\_chms, x)/P\_chms...$   
 $- DE23\_chms*(x_{w\_Ar\_chms})*(1-1/Dar\_Kn\_eff/Se)...$   
 $*d(P\_chms, x)/P\_chms...$   
 $- DE21\_chms*(x_{w\_H2\_chms})*(1-1/Dh2\_Kn\_eff/Se)...$   
 $*d(P\_chms, x)/P\_chms ...$   
 $+ (perm\_a* P\_chms /mu+1/Se)*d(P\_chms, x)/P\_chms)-...$   
 $DiT_{w\_H2O\_chms}*d(T\_chms, x)/T\_chms$

$dflux_{wH2O\_y} = -rho\_chms*w_{H2O}*(DE21\_chms...$   
 $*d(w_{H2}/(M_{w\_H2\_chms}...$   
 $*(w_{H2}/M_{w\_H2\_chms}+w_{H2O}/M_{w\_H2O\_chms}...$   
 $+ (1-w_{H2}-w_{H2O})/M_{w\_Ar\_chms}), y) ...$   
 $+ DE22\_chms*d(w_{H2O}/(M_{w\_H2O\_chms}...$   
 $*(w_{H2}/M_{w\_H2\_chms}+w_{H2O}/M_{w\_H2O\_chms}...$   
 $+ (1-w_{H2}-w_{H2O})/M_{w\_Ar\_chms}), y) ...$   
 $+ DE23\_chms*d((1-w_{H2}-w_{H2O})/(M_{w\_Ar\_chms}...$   
 $*(w_{H2}/M_{w\_H2\_chms}...$   
 $+w_{H2O}/M_{w\_H2O\_chms}+...$   
 $(1-w_{H2}-w_{H2O})/M_{w\_Ar\_chms}), y) + DE22\_chms...$   
 $*(x_{w\_H2O\_chms})*(1-1/Dh2o\_Kn\_eff/Se)...$   
 $*d(P\_chms, y)/P\_chms-DE23\_chms...$   
 $*(x_{w\_Ar\_chms})*(1-1/Dar\_Kn\_eff/Se)*d(P\_chms, y)/P\_chms-DE21\_chms...$

$$*(x\_w\_H2\_chms) * (1 - 1 / Dh2\_Kn\_eff / Se) * d(P\_chms, y) / P\_chms \dots$$

$$+ (perm\_a * P\_chms / \mu + 1 / Se) * \dots$$

$$d(P\_chms, y) / P\_chms - DiT\_w\_H2O\_chms * d(T\_chms, y) / T\_chms$$

dflux\_wH2O\_z=

$$-rho\_chms * w\_H2O * (DE21\_chms * d(w\_H2 / (M\_w\_H2\_chms \dots$$

$$* (w\_H2 / M\_w\_H2\_chms + w\_H2O / M\_w\_H2O\_chms \dots$$

$$+ (1 - w\_H2 - w\_H2O) / M\_w\_Ar\_chms), z) + DE22\_chms \dots$$

$$* d(w\_H2O / (M\_w\_H2O\_chms * (w\_H2 / M\_w\_H2\_chms \dots$$

$$+ w\_H2O / M\_w\_H2O\_chms \dots$$

$$+ (1 - w\_H2 - w\_H2O) / M\_w\_Ar\_chms), z) \dots$$

$$+ DE23\_chms * d((1 - w\_H2 - w\_H2O) / (M\_w\_Ar\_chms \dots$$

$$* (w\_H2 / M\_w\_H2\_chms \dots$$

$$+ w\_H2O / M\_w\_H2O\_chms + (1 - w\_H2 - w\_H2O) \dots$$

$$/ M\_w\_Ar\_chms), z) \dots$$

$$+ DE22\_chms * (x\_w\_H2O\_chms) * (1 - 1 / Dh2o\_Kn\_eff / Se) \dots$$

$$* d(P\_chms, z) / P\_chms \dots$$

$$- DE23\_chms * (x\_w\_Ar\_chms) * (1 - 1 / Dar\_Kn\_eff / Se) \dots$$

$$* d(P\_chms, z) / P\_chms \dots$$

$$- DE21\_chms * (x\_w\_H2\_chms) * (1 - 1 / Dh2\_Kn\_eff / Se) \dots$$

$$* d(P\_chms, z) / P\_chms \dots$$

$$+ (perm\_a * P\_chms / \mu + 1 / Se) * d(P\_chms, z) / P\_chms \dots$$

$$- DiT\_w\_H2O\_chms * d(T\_chms, z) / T\_chms$$

$$Se = x\_w\_H2\_chms / Dh2\_Kn\_eff + x\_w\_H2O\_chms / Dh2o\_Kn\_eff \dots$$

$$+ x\_w\_Ar\_chms / Dar\_Kn\_eff$$

## A.1.2 Implementation of the BFM into COMSOL

### Parameters for the Binary Mixtures

$$DE_{11} = (p_{atm} * e_{por} / \tau_{or} / R_g / T / D_{mtrx}) * (x_{w\_H2\_chms} / Dh_{2h2o} \dots + f_{h2o\_BFM} + x_{w\_H2O\_chms} * f_{h2o\_BFM}) * (M_{h2} / \rho_{H2} / w_{H2})$$

$$DE_{12} = (p_{atm} * e_{por} / \tau_{or} / R_g / T / D_{mtrx}) * (x_{w\_H2\_chms} / Dh_{2h2o} \dots - x_{w\_H2\_chms} * f_{h2o\_BFM}) * (M_{h2} / \rho_{H2} / w_{H2})$$

$$DE_{21} = (p_{atm} * e_{por} / \tau_{or} / R_g / T / D_{mtrx}) * (x_{w\_H2O\_chms} / Dh_{2h2o} \dots - x_{w\_H2O\_chms} * f_{h2\_BFM}) * (M_{h2o} / \rho_{H2O} / w_{H2O})$$

$$DE_{22} = (p_{atm} * e_{por} / \tau_{or} / R_g / T / D_{mtrx}) * (x_{w\_H2O\_chms} / Dh_{2h2o} \dots + f_{h2\_BFM} + x_{w\_H2\_chms} * f_{h2\_BFM}) * (M_{h2o} / \rho_{H2O} / w_{H2O})$$

$$f_{h2\_BFM} = 1 / (Dh_{2\_Kn\_BFM} + perm_a / K_1)$$

$$f_{h2o\_BFM} = 1 / (Dh_{2o\_Kn\_BFM} + perm_a / K_2)$$

$$Dh_{2\_Kn\_BFM} = 0.89 * Dh_{2\_Kn}$$

$$Dh_{2o\_Kn\_BFM} = 0.89 * Dh_{2o\_Kn}$$

$$K_1 = (1 / p_{atm}) * (n_{h2\_0} / (x_{w\_H2\_chms} * e_{11} + x_{w\_H2O\_chms} * e_{12}))$$

$$K_2 = (1 / p_{atm}) * (n_{h2o\_0} / (x_{w\_H2\_chms} * e_{21} + x_{w\_H2O\_chms} * e_{22}))$$

### Fluxes

$$dflux_{wH2\_x} =$$

$$- \rho_{chms} * w_{H2} * (DE_{11\_chms} * d(w_{H2} / (M_{w\_H2\_chms} \dots$$

$$\begin{aligned}
& * (w_{H2}/M_{w_{H2\_chms}} \dots \\
& + (1-w_{H2})/M_{w_{H2O\_chms}}), x) + DE12\_chms \dots \\
& * d((1-w_{H2})/(M_{w_{H2O\_chms}} \dots \\
& (w_{H2}/M_{w_{H2\_chms}} + (1-w_{H2})/M_{w_{H2O\_chms}}), x) \dots \\
& + (DE11\_chms * (x_{w_{H2\_chms}}) * d(P\_chms, x) / P\_chms \dots \\
& + DE12\_chms * (x_{w_{H2O\_chms}}) * d(P\_chms, x))) \dots \\
& - DiT_{w_{H2\_chms}} \dots * d(T\_chms, x) / T\_chms
\end{aligned}$$

$$\begin{aligned}
dflux_{wH2\_y} = & \\
& -rho\_chms * w_{H2} * (DE11\_chms * d(w_{H2}/(M_{w_{H2\_chms}} \dots \\
& * (w_{H2}/M_{w_{H2\_chms}} \dots \\
& + (1-w_{H2})/M_{w_{H2O\_chms}}), y) + DE12\_chms \dots \\
& * d((1-w_{H2})/(M_{w_{H2O\_chms}} \dots \\
& (w_{H2}/M_{w_{H2\_chms}} + (1-w_{H2})/M_{w_{H2O\_chms}}), y) \dots \\
& + (DE11\_chms * (x_{w_{H2\_chms}}) * d(P\_chms, y) / P\_chms \dots \\
& + DE12\_chms * (x_{w_{H2O\_chms}}) * d(P\_chms, y))) \dots \\
& - DiT_{w_{H2\_chms}} * d(T\_chms, y) / T\_chms
\end{aligned}$$

$$\begin{aligned}
dflux_{wH2O\_x} = & \\
& -rho\_chms * w_{H2O} * (DE21\_chms * d(w_{H2}/(M_{w_{H2\_chms}} \dots \\
& * (w_{H2}/M_{w_{H2\_chms}} \dots \\
& + (1-w_{H2})/M_{w_{H2O\_chms}}), x) + DE22\_chms \dots \\
& * d((1-w_{H2})/(M_{w_{H2O\_chms}} \dots \\
& (w_{H2}/M_{w_{H2\_chms}} + (1-w_{H2})/M_{w_{H2O\_chms}}), x) \dots \\
& + (DE21\_chms * (x_{w_{H2\_chms}}) * d(P\_chms, x) / P\_chms \dots \\
& + DE22\_chms * (x_{w_{H2O\_chms}}) * d(P\_chms, x))) \dots \\
& - DiT_{w_{H2O\_chms}} * d(T\_chms, x) / T\_chms
\end{aligned}$$

$$\begin{aligned}
& \text{dflux\_wH2O\_y=} \\
& -\text{rho\_chms} * \text{w\_H2O} * (\text{DE21\_chms} * \text{d}(\text{w\_H2} / (\text{M\_w\_H2\_chms} \dots \\
& * (\text{w\_H2} / \text{M\_w\_H2\_chms} + (1 - \text{w\_H2}) / \text{M\_w\_H2O\_chms}), \text{y}) \dots \\
& \backslash + \text{DE22\_chms} * \text{d}((1 - \text{w\_H2}) / (\text{M\_w\_H2O\_chms} * \dots \\
& (\text{w\_H2} / \text{M\_w\_H2\_chms} + (1 - \text{w\_H2}) / \text{M\_w\_H2O\_chms}), \text{y}) \dots \\
& + (\text{DE21\_chms} * (\text{x\_w\_H2\_chms}) \dots \\
& * \text{d}(\text{P\_chms}, \text{y}) / \text{P\_chms} + \text{DE22\_chms} * (\text{x\_w\_H2O\_chms}) \dots \\
& * \text{d}(\text{P\_chms}, \text{y})) \dots \\
& - \text{DiT\_w\_H2O\_chms} * \text{d}(\text{T\_chms}, \text{y}) / \text{T\_chms}
\end{aligned}$$

### Parameters for the Ternary Mixtures

$$\begin{aligned}
& \text{a11} = \text{x\_w\_H2O\_chms} / \text{Dh2h2o} + \text{x\_w\_Ar\_chms} / \text{Dh2ar} \dots \\
& + \text{f\_h2\_BFM} \dots \\
& + \text{x\_w\_H2\_chms} * \text{f\_h2\_BFM} \\
& \text{a12} = -\text{x\_w\_H2\_chms} / \text{Dh2h2o} + \text{x\_w\_H2\_chms} * \text{f\_h2o\_BFM} \\
& \text{a13} = -\text{x\_w\_H2\_chms} / \text{Dh2ar} + \text{x\_w\_H2\_chms} * \text{f\_ar\_BFM} \\
& \text{a21} = -\text{x\_w\_H2O\_chms} / \text{Dh2h2o} + \text{x\_w\_H2O\_chms} \dots \\
& * \text{f\_h2\_BFM} \\
& \text{a22} = \text{x\_w\_H2\_chms} / \text{Dh2h2o} + \text{x\_w\_Ar\_chms} / \text{Dh2oar} \dots \\
& + \text{f\_h2\_BFM} \dots \\
& + \text{x\_w\_H2O\_chms} * \text{f\_h2o\_BFM} \\
& \text{a23} = -\text{x\_w\_H2O\_chms} / \text{Dh2oar} + \text{x\_w\_H2O\_chms} \dots \\
& * \text{f\_ar\_BFM}
\end{aligned}$$

$a_{31} = -x_{w\_Ar\_chms}/Dh_{2ar} + x_{w\_Ar\_chms} * f_{h2\_BFM}$   
 $a_{32} = -x_{w\_Ar\_chms}/Dh_{2oar} + x_{w\_Ar\_chms} * f_{h2o\_BFM}$   
 $a_{33} = x_{w\_H2\_chms}/Dh_{2ar} + x_{w\_H2O\_chms}/Dh_{2oar} \dots$   
 $+ f_{ar\_BFM} \dots$   
 $+ x_{w\_Ar\_chms} * f_{ar\_BFM}$

$Det: a_{11} * (a_{33} * a_{22} - a_{32} * a_{23}) - a_{21} * (a_{33} * a_{12} - a_{32} * a_{13}) \dots$   
 $+ a_{31} * (a_{23} * a_{12} - a_{22} * a_{13})$

$DE_{11} = (p_{atm} * e_{por}/tor/Rg/T/ Det) * (a_{33} * a_{22} - a_{32} * a_{23}) \dots$   
 $* (Mh_2 / rho/w_{H2})$

$DE_{12} = -(p_{atm} * e_{por}/tor/Rg/T/ Det) * (a_{33} * a_{12} - a_{32} * a_{13}) \dots$   
 $* (Mh_2 / rho/w_{H2})$

$DE_{13} = (p_{atm} * e_{por}/tor/Rg/T/ Det) * (a_{23} * a_{12} - a_{22} * a_{13}) \dots$   
 $* (Mh_2 / rho/w_{H2})$

$DE_{21} = -(p_{atm} * e_{por}/tor/Rg/T/ Det) * (a_{33} * a_{21} - a_{31} * a_{23}) \dots$   
 $* (Mh_{2o} / rho/w_{H2O})$

$DE_{22} = (p_{atm} * e_{por}/tor/Rg/T/ Det) * (a_{33} * a_{11} - a_{31} * a_{13}) \dots$   
 $* (Mh_{2o} / rho/w_{H2O})$

$DE_{23} = -(p_{atm} * e_{por}/tor/Rg/T/ Det) * (a_{23} * a_{11} - a_{21} * a_{13}) \dots$   
 $* (Mh_{2o} / rho/w_{H2O})$

$DE_{31} = (p_{atm} * e_{por}/tor/Rg/T/ Det) * (a_{32} * a_{21} - a_{31} * a_{22}) \dots$   
 $* (Mar / rho/w_{Ar})$

$DE_{32} = -(p_{atm} * e_{por}/tor/Rg/T/ Det) * (a_{32} * a_{11} - a_{31} * a_{12}) \dots$

\* (Mar /rho/w\_Ar)

DE\_33=(p\_atm\*e\_por/tor/Rg/T/ Det)\*(a22\*a11-a21\*a12)...

\* (Mar /rho/w\_Ar)

e\_11=1

e\_12= (1+(n\_h2\_0/n\_h2o\_0)^(1/2)\*(Mh2o/Mh2)^(1/4))^2...

/((8\*(1+ Mh2/Mh2o))^1/2)

e\_13=(1+(n\_h2\_0/n\_ar\_0)^(1/2)\*(Mar/Mh2)^(1/4))^2...

/((8\*(1+ Mh2/Mar))^1/2)

e\_21=(1+(n\_h2o\_0/n\_h2\_0)^(1/2)\*(Mh2/Mh2o)^(1/4))^2...

/((8\*(1+ Mh2o/Mh2))^1/2)

e\_22=1

e\_23=(1+(n\_h2o\_0/n\_ar\_0)^(1/2)\*(Mar/Mh2o)^(1/4))^2...

/((8\*(1+ Mh2o/Mar))^1/2)

e\_31=(1+(n\_ar\_0/n\_h2\_0)^(1/2)\*(Mh2/Mar)^(1/4))^2...

/((8\*(1+ Mar/Mh2))^1/2)

e\_32=(1+(n\_ar\_0/n\_h2o\_0)^(1/2)\*(Mh2o/Mar)^(1/4))^2...

/((8\*(1+ Mar/Mh2o))^1/2)

e\_33=1

K\_h2=(1/p\_atm)\*(n\_h2\_0/( x\_w\_H2\_chms\*e\_11+ x\_w\_H2O\_chms...

\*e\_12+ x\_w\_Ar\_chms\*e\_13))

K\_h2o=(1/p\_atm)\*(n\_h2o\_0/( x\_w\_H2\_chms\*e\_21...

+ x\_w\_H2O\_chms\*e\_22+ x\_w\_Ar\_chms\*e\_23))

$$K_{ar} = (1/p_{atm}) * (n_{ar_0} / (x_{w_H2\_chms} * e_{31} \dots \\ + x_{w_H2O\_chms} * e_{32} \dots \\ + x_{w\_Ar\_chms} * e_{33}))$$

$$f_{h2\_BFM} = 1 / (Dh2\_Kn\_BFM + perm\_a / K_{h2})$$

$$f_{h2o\_BFM} = 1 / (Dh2o\_Kn\_BFM + perm\_a / K_{h2o})$$

$$f_{ar\_BFM} = 1 / (Dar\_Kn\_BFM + perm\_a / K_{ar})$$

$$Dh2\_Kn\_BFM = 0.89 * Dh2\_Kn$$

$$Dh2o\_Kn\_BFM = 0.89 * Dh2o\_Kn$$

$$Dar\_Kn\_BFM = 0.89 * Dar\_Kn$$

## Diffusion Fluxes

$$dflux_{wH2\_x} =$$

$$-rho_{chms} * w_{H2} * (DE11_{chms} * d(w_{H2} / (M_{w\_H2\_chms} \dots$$

$$* (w_{H2} / M_{w\_H2\_chms} \dots$$

$$+ w_{H2O} / M_{w\_H2O\_chms} + (1 - w_{H2} - w_{H2O}) / M_{w\_Ar\_chms}), x) + \dots$$

$$DE12_{chms} * d(w_{H2O} / (M_{w\_H2O\_chms} \dots$$

$$* (w_{H2} / M_{w\_H2\_chms} \dots$$

$$+ w_{H2O} / M_{w\_H2O\_chms} + (1 - w_{H2} - w_{H2O}) / M_{w\_Ar\_chms}), x) \dots$$

$$+ DE13_{chms} * d((1 - w_{H2} - w_{H2O}) / (M_{w\_Ar\_chms} * (w_{H2} / M_{w\_H2\_chms} \dots$$

$$+ w_{H2O} / M_{w\_H2O\_chms} + (1 - w_{H2} - w_{H2O}) / M_{w\_Ar\_chms}), x) \dots$$

$$+ DE11_{chms} * (x_{w\_H2\_chms}) * d(P_{chms}, x) / P_{chms} \dots$$

$$+ DE12_{chms} * (x_{w\_H2O\_chms}) * d(P_{chms}, x) / P_{chms} \dots$$

$$+ DE13_{chms} * (x_{w\_Ar\_chms}) \dots$$

$$* d(P_{chms}, x) / P_{chms} - DiT_{w\_H2\_chms} * d(T_{chms}, x) / T_{chms}$$

```

dflux_wH2_y=
-rho_chms*w_H2*(DE11_chms*d(w_H2/(M_w_H2_chms...
*(w_H2/M_w_H2_chms...
+w_H2O/M_w_H2O_chms+(1-w_H2-w_H2O)/M_w_Ar_chms)),y)...
+DE12_chms...
*d(w_H2O/(M_w_H2O_chms*(w_H2/M_w_H2_chms...
+w_H2O/M_w_H2O_chms...
+(1-w_H2-w_H2O)/M_w_Ar_chms)),y)...+DE13_chms...
*d((1-w_H2-w_H2O)/(M_w_Ar_chms*...
(w_H2/M_w_H2_chms+w_H2O/M_w_H2O_chms...
+(1-w_H2-w_H2O)/M_w_Ar_chms)),y)...
+DE11_chms*x_w_H2_chms*...
d(P_chms,y)/P_chms+DE12_chms*x_w_H2O_chms...
*d(P_chms,y)/P_chms+...
DE13_chms*x_w_Ar_chms*d(P_chms,y)/P_chms)...
-DiT_w_H2_chms*d(T_chms,y)/T_chms

```

```

dflux_wH2_z=
-rho_chms*w_H2*(DE11_chms*d(w_H2/(M_w_H2_chms...
*(w_H2/M_w_H2_chms...
+w_H2O/M_w_H2O_chms+(1-w_H2-w_H2O)...
/M_w_Ar_chms)),z)...
+DE12_chms*d(w_H2O/(M_w_H2O_chms...
*(w_H2/M_w_H2_chms...
+w_H2O/M_w_H2O_chms+...
(1-w_H2-w_H2O)/M_w_Ar_chms)),z)+DE13_chms...

```

$*d((1-w_{H2}-w_{H2O}) / (M_w_{Ar\_chms} * (w_{H2}/M_w_{H2\_chms}...$   
 $+w_{H2O}/M_w_{H2O\_chms}...$   
 $+(1-w_{H2}-w_{H2O}) / M_w_{Ar\_chms})), z) + DE11\_chms * x_{w_{H2\_chms}}...$   
 $*d(P\_chms, z) / P\_chms... + DE12\_chms * x_{w_{H2O\_chms}}...$   
 $*d(P\_chms, z) / P\_chms...$   
 $+ DE13\_chms * x_{w_{Ar\_chms}} * d(P\_chms, z) / P\_chms)...$   
 $- DiT_{w_{H2\_chms}} * d(T\_chms, z) / T\_chms$

$dflux_{wH2O\_x} =$   
 $-rho\_chms * w_{H2O} * (DE21\_chms * d(w_{H2} / (M_w_{H2\_chms}...$   
 $* (w_{H2}/M_w_{H2\_chms}...$   
 $+w_{H2O}/M_w_{H2O\_chms} + (1-w_{H2}-w_{H2O}) / M_w_{Ar\_chms})), x)...$   
 $+ DE22\_chms * d(w_{H2O} / (M_w_{H2O\_chms} * (w_{H2}/M_w_{H2\_chms}...$   
 $+w_{H2O}/M_w_{H2O\_chms}...$   
 $+(1-w_{H2}-w_{H2O}) / M_w_{Ar\_chms})), x)...$   
 $+ DE23\_chms * d((1-w_{H2}-w_{H2O}) / (M_w_{Ar\_chms}...$   
 $* (w_{H2}/M_w_{H2\_chms}...$   
 $+w_{H2O}/M_w_{H2O\_chms} + (1-w_{H2}-w_{H2O})...$   
 $/M_w_{Ar\_chms})), x)...$   
 $+ DE21\_chms * x_{w_{H2\_chms}} * d(P\_chms, x) / P\_chms...$   
 $+ DE22\_chms * x_{w_{H2O\_chms}} * d(P\_chms, x) / P\_chms...$   
 $+ DE23\_chms * x_{w_{Ar\_chms}} * d(P\_chms, x) / P\_chms)...$   
 $- DiT_{w_{H2O\_chms}} * d(T\_chms, x) / T\_chms$

$dflux_{wH2O\_y} =$   
 $-rho\_chms * w_{H2O} * (DE21\_chms * d(w_{H2} / (M_w_{H2\_chms}...$   
 $* (w_{H2}/M_w_{H2\_chms} + w_{H2O}/M_w_{H2O\_chms}...$

$$\begin{aligned}
& + (1-w_{H2}-w_{H2O}) / M_{w\_Ar\_chms})), y) \dots \\
& + DE22\_chms * d(w_{H2O} / (M_{w\_H2O\_chms} \dots \\
& * (w_{H2} / M_{w\_H2\_chms} \dots \\
& + w_{H2O} / M_{w\_H2O\_chms} + (1-w_{H2} \dots \\
& - w_{H2O}) / M_{w\_Ar\_chms})), y) \dots \\
& + DE23\_chms * d((1-w_{H2}-w_{H2O}) / (M_{w\_Ar\_chms} \dots \\
& * (w_{H2} / M_{w\_H2\_chms} + w_{H2O} / M_{w\_H2O\_chms} \dots \\
& + (1-w_{H2}-w_{H2O}) / M_{w\_Ar\_chms})), y) \dots \\
& + DE21\_chms * (x_{w\_H2\_chms}) \dots \\
& * d(P_{chms}, y) / P_{chms} + DE22\_chms * (x_{w\_H2O\_chms}) * d(P_{chms}, y) \dots \\
& / P_{chms} + DE23\_chms * (x_{w\_Ar\_chms}) * d(P_{chms}, y) / P_{chms} \dots \\
& - DiT_{w\_H2O\_chms} * d(T_{chms}, y) / T_{chms}
\end{aligned}$$

dflux\_wH2O\_z=

$$\begin{aligned}
& -rho\_chms * w_{H2O} * (DE21\_chms * d(w_{H2} / (M_{w\_H2\_chms} \dots \\
& * (w_{H2} / M_{w\_H2\_chms} \dots \\
& + w_{H2O} / M_{w\_H2O\_chms} + (1-w_{H2}-w_{H2O}) \dots \\
& / M_{w\_Ar\_chms})), z) \dots \\
& + DE22\_chms * d(w_{H2O} / (M_{w\_H2O\_chms} \dots \\
& * (w_{H2} / M_{w\_H2\_chms} + w_{H2O} / M_{w\_H2O\_chms} \dots \\
& + (1-w_{H2}-w_{H2O}) / M_{w\_Ar\_chms})), z) + DE23\_chms \dots \\
& * d((1-w_{H2}-w_{H2O}) / (M_{w\_Ar\_chms} * (w_{H2} / M_{w\_H2\_chms} \dots \\
& + w_{H2O} / M_{w\_H2O\_chms} \dots \\
& + (1-w_{H2}-w_{H2O}) / M_{w\_Ar\_chms})), z) + DE21\_chms \dots \\
& * (x_{w\_H2\_chms}) * d(P_{chms}, z) / P_{chms} \dots + DE22\_chms \dots \\
& * (x_{w\_H2O\_chms}) * d(P_{chms}, z) / P_{chms} \dots \\
& + DE23\_chms * (x_{w\_Ar\_chms}) * d(P_{chms}, z) / P_{chms} \dots
\end{aligned}$$

```
-DiT_w_H2O_chms*d(T_chms,z)/T_chms  
}
```